# Integrated photonics for mid-infrared stellar interferometry

By

Thomas Gretzinger

A thesis submitted to Macquarie University
for the degree of Doctor of Philosophy
Department of Physics and Astronomy
August 2019

Typeset in $\LaTeX\,2_\varepsilon$.

# Declaration of authorship

Throughout my candidature, I developed and fabricated optical waveguides as well as optical devices in gallium lanthanum sulphide glass using the femtosecond laser direct-writing facility at Macquarie University. I pre- and post-processed the glass material and developed the test beds for determining the waveguide propagation losses and the spectral response of optical devices.

The micro-reflectivity setup used in this thesis to retrieve the refractive index contrast of optical waveguides was built by Dr. Simon Gross who also conducted the measurements. The electron probe micro-analysis was carried out at the Department of Earth and Planetary Sciences at Macquarie University and The University of New South Wales with the support of Dr. Timothy Murphy and Karen Privat, respectively from each institution. The asymmetric directional couplers and multimode interference couplers were characterised interferometrically for their extinction ratio at the University of Cologne. Due to a short period of time in July 2017 when I worked with the group of Lucas Labadie, I was familiar with the equipment and able to supervise the measurements remotely. The measurements were conducted by Dr. Jan Tepper and his Master's student Dominik Strixner.

The development and characterisation of low-loss optical waveguides and key components for an on-chip nulling interferometer presented in this thesis represent my original work.

This thesis is submitted in fulfilment of the requirements for the degree of Doctor of Philosophy in Physics at Macquarie University and has not been submitted for a higher degree to any other university or institution. I certify that to the best of my knowledge, all sources used and assistance received in the preparation of this thesis have been acknowledged. This thesis does not contain any material which is defamatory of any person, form or corporation and is not in breach of copyright or breach of other rights which shall give rise to any action at Common Law or under Statute.

| Sydney, 28/08/2019 | |
|---|---|
| Place, Date | Thomas Gretzinger |

# Acknowledgements

After having spent my six month M.Sc. thesis project at Macquarie University, it was not a difficult decision to return to Sydney. My thanks go first to both my supervisors Simon Gross and Michael Withford and also to Alex Arriola who all encouraged me to come back and join the MQ photonics group for my PhD degree. Having limited funds after travelling the world for one year, this would not have been possible without the great support from the university and an International Macquarie Research Excellence Scholarship.

I want to express my deepest thanks to Mick for leading this research group with such an amazing work atmosphere. To Simon, who continuously inspired me with his passion for details that let me grow as a researcher, for his excellent mentorship, for good advice and of course for constantly maintaining and upgrading the HPO facility. To Alex Arriola, for always having an open ear and for the adventures working many times at the Anglo-Australian Telescope commissioning new instruments and testing optical setups together with Barnaby Norris and Tiphaine Lagadec from the University of Sydney.

My colleagues I had the pleasure working with Toney Fernandez who helped me to understand the EPMA and Raman analysis, Ben Johnston, Martin Ams, Peter Dekker, Robert Woodward, Darren Hudson and Alex Fuerbach who helped and supported me whenever they could as well Lucas Labadie and Jan Tepper from the University of Cologne. Furthermore, I want to thank our administrative staff Lisa Pesavento, Megha Patel and especially Anita Verinder - we would all be lost without her. I would also like to acknowledge Dan Hewak from the University of Southampton for providing me with my working material GLS glass free of charge.

I would also like to extend thanks to my fellow peers who accompanied me during my candidature: Andrew Ross-Adams, Christoph Wieschendorf, Sergei Antipov, Gayathri Bharathan, Blake Entwisle and Saurabh Bhardwaj both my officemates and friends Alex Stokes and Glen Douglass for getting me into rock climbing and for endless chats in the office and the updates on the newest anime releases. I also hold a special place for my friends Michelle Whitford, Daniel Blay, Yameng Zheng, Atiyeh Zarifi, Luke Mckay and Yang Lui for being part of the organising commitee for IONS KOALA 2018. Organising this big international conference would not have been possible and such a great success without their dedication and thousands of hours of volunteering work over the entire year of 2018, even though most of us were in the final stage of our PhD candidature.

Finally and most importantly, I wish to thank my family and loved ones. I am most grateful for my beautiful partner Michelle Demers for her limitless support, boundless love and for being my best friend. To my brother Richard Jr. and my parents Maria and Richard Gretzinger, who always motivated me to follow my dreams, love me unconditionally and left no stone unturned to support me. It is to them that I dedicate this thesis. Ich danke meinem Bruder Richard Jr. und meinen Eltern Maria und Richard Gretzinger, die mich immer dazu motiviert haben, meinen Träumen zu folgen, mich bedingungslos lieben und mir immer zur Seite standen. Ihnen widme ich diese Arbeit.

Cheers,

Thomas

# Abstract

Nulling-interferometry is a powerful tool to advance beyond the resolving power of ground-based observatories with the prospect of directly detecting exoplanets. By suppressing the radiation of the host star through destructive interference, the emission from a young planet can be observed. A favourable contrast between a planet and a star as well as reduced atmospheric disturbances are found centered around 4 $\mu$m wavelength. For high stability and robustness, it is preferable to deploy integrated optics devices based on waveguide technology. Their advancement however is hindered in the mid-infrared wavelength range due to the lack of suitable host materials as well as compatible manufacturing techniques to fabricate low-loss photonic devices.

This thesis details the development of mid-infrared optical waveguides and the key components for an integrated nulling interferometer chip in gallium-lanthanum-sulphur glass, utilising femtosecond laser direct-writing. By combining the multiscan technique with the cumulative heating fabrication, single-mode waveguides with a propagation loss of 0.22$\pm$0.02 dB/cm at 4 $\mu$m were realised. Evidence of structural changes and ion migration in these positive refractive index waveguides are presented using Raman spectroscopy and electron probe micro-analysis (EPMA), respectively. 2-D Raman maps revealed full-width at half maximum variations and a peak shift in the symmetric vibrations of the $GaS_4$ main Raman band. The 2-D spectral map of the Boson peak band was used to understand and identify the material densification profile in a high refractive index glass waveguide. EPMA provided evidence of sulphur ion migration and the observation of an anion ($S^{2-}$) migration causing material modification.

These low-loss waveguides were the foundation of S-bends with a negligible bending loss and Y-splitters with a 50/50 power division across a 600 nm wavelength window. Directional couplers were developed from symmetric into asymmetric directional couplers with a 50/50 power splitting ratio over a broad wavelength range (3.8 - 4.05 $\mu$m). Furthermore, multimode interference couplers are presented with an even splitting capability between 3.75 - 4.25 $\mu$m with no polarisation dependency. Both types of couplers feature a high broadband extinction ratio. These main building blocks are developed to create a future compact nulling interferometer with a total projected intrinsic loss of $< 1$ dB, a value that is sufficient to perform future on-sky experiments in relatively short observation runs on ground based telescopes.

# Contents

# List of Figures

# 1 Introduction

The search for extrasolar planets is a rather young astronomical field where the first confirmed detections appeared in 1992 and the first planet orbiting a sun-like star was reported in 1995 [1]. As of January 2019, ∼4000 planets have been found [2] primarily by NASA's space telescope Kepler [3]. Kepler uses radial velocity [1] and photometric transit [4] to find these planets, techniques that are of an indirect nature. These and other indirect methods including astrometric positioning [5], gravitational microlensing [6] and pulsar timing [7] are responsible for 97% of all findings. Each of these methods is based on the change of the star's observables due to the presence of a planet rather than measuring the flux of a planet directly. This flux however carries valuable information that is indispensable for identifying biosignatures such as water vapour or oxygen. Some of Kepler's discoveries are planets in the habitable zone that are 0.8 - 2.2× of the Earth's radius and 0.5 - 10× of the Earth's mass [8]. The habitable zone is defined as a region around the star where the surface temperature of the planet lies between the freezing and the boiling point of water. Planets that fall into this category are called Earth-like planets and usually revolve a sun-like star at distances of <1 astronomical units (AU).

Kepler's space location is ideal to avoid light pollution and atmospheric turbulences that distort the captured light. These severe problems are encountered by telescopes on Earth and require advanced adaptive optics to compensate for atmospheric disturbances [9]. Nevertheless, space missions are expensive and less flexible when it comes to telescope maintenance and upgrading.

Ground-based observations can only be performed in the transmission windows of the Earth's atmosphere (Fig. 1.1). Water vapour is largely responsible for the absorption of infrared radiation including the largest transmission gap spanning from ~5.5 - 8 $\mu$m. Other gases such as carbon dioxide and ozone contribute to this absorption.

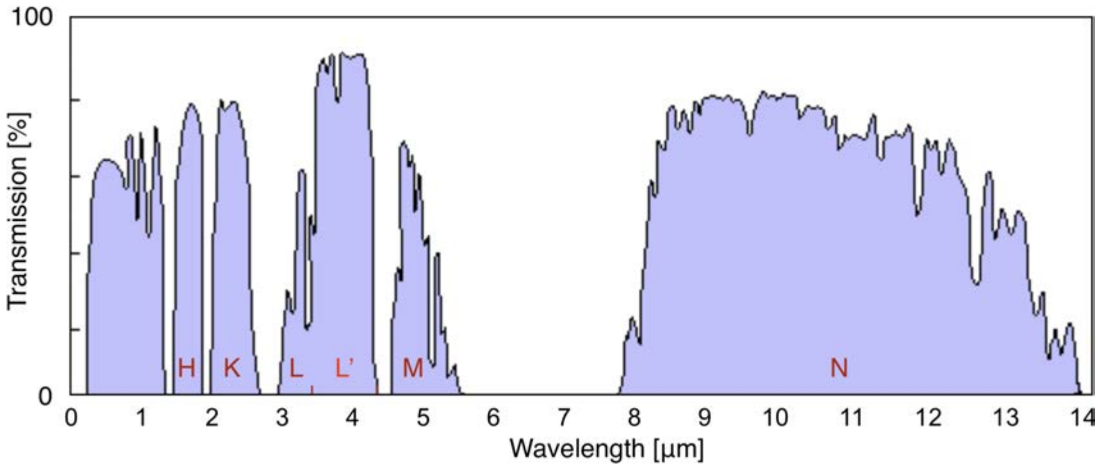


FIGURE 1.1: Transmission window of the Earth's atmosphere. Due to strong absorption of atmospheric gases, observations can only be performed in transmission windows called astronomical bands (H - N). Image derived from [10].

The observed flux for Earth-like planets varies at each transmission window and becomes even more important in close vicinity to the star (Fig. 1.2). The small separation between star and planet leads to two main issues for direct detection with ordinary telescopes: the dynamic range of flux and the angular resolution between star and planet. The first issue is attributed to the brightness contrast between both an Earth-like planet and a solar-type star. The contrast reaches the order of $5\times10^9$ in the visible and near-infrared wavelength range (0.4 - 3 $\mu$m) since the planet almost exclusively reflects the light from a star. The mid-infrared wavelength range (3 - 20 $\mu$m) by contrast is a rather interesting observing regime as it allows for probing young planets with a surface that is still relatively hot but colder than the stellar photosphere. These young planets are of great interest as they offer the physical conditions for liquid water [11]. The astronomical L'-band (3.6 - 4.26 $\mu$m) is best suited for their detection since it offers the highest transmission in a wavelength region where the black body radiation of young planets peaks (Fig. 1.2). Here the atmospheric disturbances and thermal background noise of our Earth is relatively low. An additional decrease in stellar flux for longer wavelengths leads to a significantly improved brightness contrast of up to $10^7$ [12].

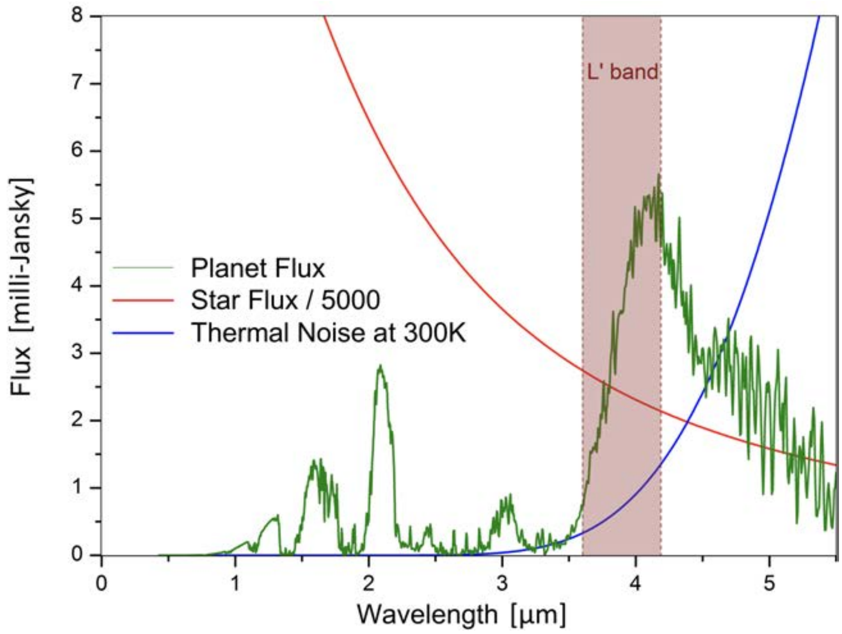


FIGURE 1.2: The mid-infrared emission of young planets (green) peaks in the astronomical L-band [13] while a simultaneous decrease in stellar flux (red) is observed. This leads to a favourable contrast between star and planet. The Earth's thermal background noise is relatively low and favours observations in this wavelength window. Image courtesy of Dr. Alexander Arriola.

The second issue for direct detection methods is the small angular separation between star and planet that is typically only a fraction of an arcsec when observed from Earth. The resolution $1.22\lambda/D$ rad of a telescope is diffraction-limited by the diameter $D$ and would require an enormous primary mirror for observations in the mid-infrared. This problem can be overcome with applied interferometry operating with two or more apertures. The resolution of the interferometer fringes $\lambda/2b$ rad depends on the apertures separation $b$ that is called baseline. Apertures can either be provided by multiple telescopes or a single telescope with appropriate masking [14]. Such a mask divides the main mirror into smaller subapertures that form an interferometric array, increasing the resolution to half of the diffraction limit.

Combining the light of the apertures with an artificial 180° phase shift results in alternating constructive and destructive interference. Basically, destructive interference is applied across the star while faint off-axis objects can be revealed. This so-called nulling interferometry can significantly improve the dynamic range between star and planet (Fig. 1.3) while the interferometric aspect improves the angular resolution. This technique therefore helps to overcome the two main challenges of exo-planet direct detection.

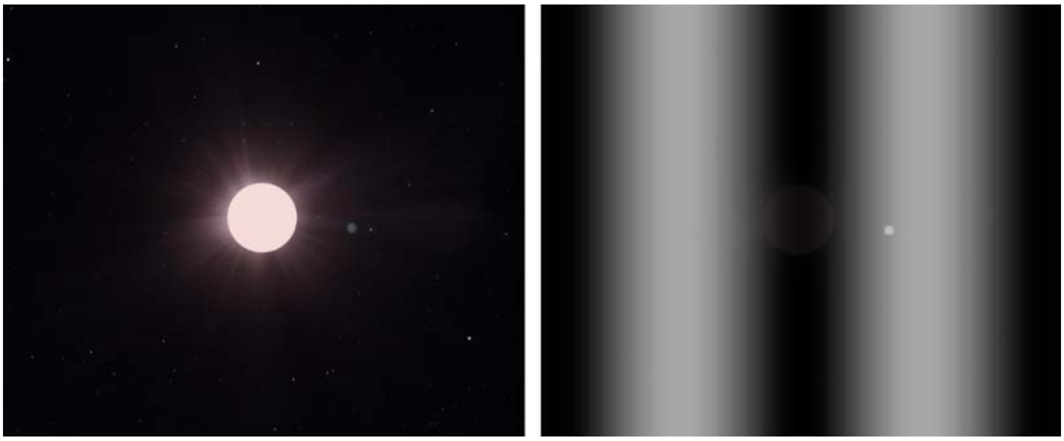

FIGURE 1.3: Left: The image shows a star and its faint companion. Right: Applied nulling interferometry utilises destructive interference across that star to diminish the overwhelming flux and reveal faint objects in its vicinity.

The concept of nulling interferometry was proposed by Bracewell [15] in 1978 and is the foundation of the largest ground-based nulling projects at the two-telescope interferometer KECK, located at Mauna Kea, Hawaii (2001 - 2012) [16–18]. NASA and ESA both invested more than a decade to develop mid-infrared space telescopes using nulling interferometry as the main measurement principle. Both programs, DARWIN (ESA) and Terrestrial Planet Finder (NASA), were eventually cancelled in 2007 and 2011 due to a lack of funding. The focus was subsequently redirected to the ground-based Large Binocular Telescope Interferometer (LBTI) and the Palomar Telescope where this powerful method was developed into instruments. A bulk optics instrument was implemented at the LBTI [19] and operates at wavelengths between 1.5 - 13 $\mu$m. The nulling interferometer at the Palomar Telescope, on the other hand, is optical fiber-based and covers a near-infrared window of 1.5 - 1.8 $\mu$m, and is known as the Palomar Fiber Nuller (PFN) [20].

Optical fibers were first introduced in the early 1980s to transport and combine light within the telescope network or to reformat the captured light onto an optical spectrograph. In particular, single-mode fibers have shown excellent spatial and modal filtering characteristics that remove any phase defects associated with the incoming wave front. This improves the extinction ratio of the star light in interferometric measurements [21]. By specifically propagating only the fundamental mode, a deformed wave front only affects the amount of energy coupled into the waveguide [22]. Optical waveguides also improve the long-term stability of white light interferograms [23] as well as minimising any thermal background otherwise seen by the detector.

Optical fibers and photonic integrated optics are well matured technologies for the near-infrared wavelength range, in particular around 1.3 and 1.55 $\mu$m due to pioneering work in telecommunication. The translation of this knowledge into astronomical applications has led to the completely new field of astrophotonics as a powerful alternative to classical bulk optics [24]. Astrophotonic devices are compact and inherently more robust against environmental influences like temperature and vibration. They have the potential to reduce the complexity of astronomical instruments by implementing a broad range of optical functions on a single chip.

Components for interferometric beam combination based on single-mode waveguides range from Y-splitters, directional couplers or zig-zag couplers (Fig. 1.4 left to right). Y-splitters can be operated in reverse to combine light from two telescopes. For this type, the waveguides merge in the coupling region, hence the name zero-gap coupler. Such a device is based on two-mode interference and is admittedly achromatic but inherently lossy since at minimum, 50% of the light is lost as radiation modes. A directional coupler on the other hand relies on evanescent coupling of two parallel waveguides in close vicinity. The energy transfers gradually from one waveguide to the other over a certain length. This makes this coupler sensitive to the design parameters such as separation and length of the waveguides in the coupling region. The fundamental chromaticity of the coupler for instance can be overcome by introducing asymmetry in one of the arms which makes the fabrication more challenging. The last beam combiner design is called a zig-zag coupler and is a discrete beam combiner that consists of an array of straight evanescently coupled waveguides [26]. Due to discrete diffraction, the modes at the entrance waveguides spread into the neighbouring waveguides and superimposed at the waveguide outputs.

In 1996, Kern *et al.* [27] proposed conceptional designs for on-chip beam combiners based on Michelson and Fizeau type interferometers for the astronomical K-band. These ideas were developed into the first astrophotonic beam combiner chips and incorporated Y-splitters/zero-gap and directional couplers based on telecommunication technology. These chips were installed as part of the IONIC instrument at the Infrared Optical Telescope Array (IOTA) at Mt Hopkins, U.S. in 2001. After rigorous instrumental tests, the devices were successfully commissioned and operated on-sky [28, 29] to combine light from two telescopes. Both chips showed similar, very stable interferograms of 14 different stars. An advanced photonic chip (IONIC-3 [30]) combining three telescopes was tested in 2004 and delivered results of spectroscopic binary stars using closure phase measurements [31] for the first time.

These pioneering results were followed by a photonic chip based four-telescope configuration, this time at Very Large Telescope (VLT) in the Atacama Desert, Chile, operated by the European Southern Observatory (ESO). The experience gained with the IONIC-3 chip was translated into the visiting instrument PIONIER that uses the VLT interferometer (VLTI). The instrument combines the light from four 1.8 m or four 8 m telescopes [32] to permit high angular resolution. PIONIER was commissioned in 2011 and paved the way for the flagship

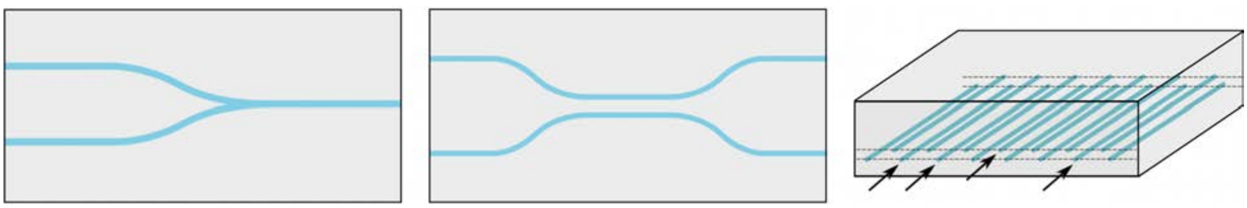

FIGURE 1.4: Optical function such as power dividing Y-splitters (left), 2×2 directional couplers (middle) or zig-zag couplers (right) can be implemented on a single chip in different variations and combinations to form interferometric circuits. Image courtesy of [25].

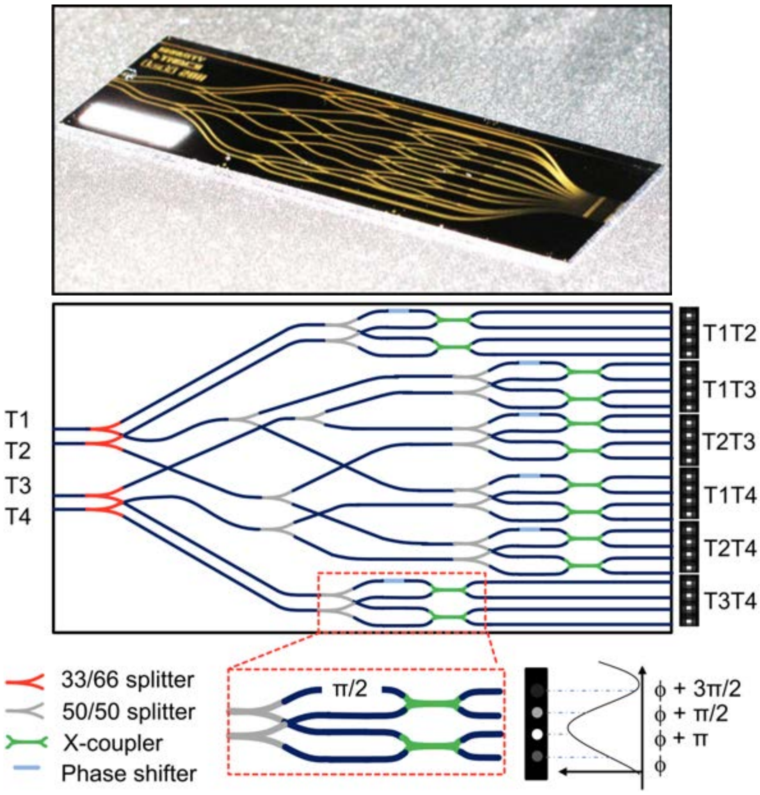


FIGURE 1.5: Photonic chip used in the GRAVITY instrument installed at the VLTI. The schematic below the photograph shows the circuit design of the chip including all major functions such as waveguides, Y-splitters, X-couplers and phase-shifters. This sophisticated chip combines light from four telescopes (T1 - T4) interferometrically with six different combinations. The interferometric fringe is sampled, and four phase states can be extracted from the output signals [33]. Image courtesy of [34].

project GRAVITY [33] that saw first light in 2016 [34]. Both instruments are dedicated to the near-infrared astronomical H- and K-band.

GRAVITY is to date the most sophisticated photonic instrument in operation and combines the most common optical functions on one interferometric chip (Fig. 1.5). Functions such as phase shifting devices, Y-splitters with 50/50 and 33/66 power division capability and 50/50 couplers have been utilised to combine light from four telescopes (T1 - T4) in six different ways.

At its basic principle (Fig. 1.5 bottom), light from one telescope is spilt into two beams (grey) and combined with light from another telescope (green). The phase in one of the four arms is phase-shifted by 90° (teal). The four output beams are hence measured with relative phase shifts of 0°, 90°, 180° and 270°. This allows for the retrieval of the visibility amplitude, phase and signal-to-noise ratio of the fringe for each of the six baselines applying the ABCD method [35]. This way a high accuracy in angular resolution is obtained, combining all four 8 m telescopes with an equivalent of a 130 m baseline. The chip obtains a high throughput of 65% with high and stable instrumental contrasts. The contrast reaches up to ∼100% for a narrow bandwidth and decreases to ∼80% for a higher bandwidth due to spectral dispersion. Such photonic chips are fabricated with well-established technologies such as ion-exchange and wet or dry-etching based on classic micro-lithography in silica-based devices. Waveguides in these glasses have been engineered to offer high performance with a minuscule propagation loss in the near-infrared. This is an indispensable feature for astronomical devices, as the loss of collected photons has typically made longer on-sky observation runs necessary, consequently also having increased operational costs.

A mid-infrared interferometric chip therefore needs to as well feature a low propagation loss to keep the intrinsic losses of the chip to a minimum where 1 dB is set to be the benchmark. Operating the chip at a broad wavelength window allows for more photons to be used and thus leads to a further reduction in observation time. This on the other hand requires an almost perfectly broadband splitting capability of either of the arms of the interferometer. These conditions have to be in place to perform a high suppression of the star light where the contrast of an Earth-like planet and a sun-like star is around $10^{-6} - 10^{-7}$.

The transparency of silica-based glasses however, decreases rapidly beyond 2 $\mu$m which makes them unsuitable for mid-infrared applications involving exo-planet hunting. Mid-infrared platforms that have proven to deliver waveguides with low propagation loss of <1 dB/cm include $Si/SiO_2$ [36] and arsenic-based chalcogenide glasses [37]. Still, lithography requires uniquely tailored masks and a multitude of fabrication steps carried out in clean-room facilities. The fact that lithography is inherently limited to two dimensions hampers the development of more complex devices, especially with the intention to combine light interferometrically from several apertures at the same time.

The still young but meanwhile well-established technology of femtosecond laser direct-writing (FLDW) can overcome the planar circuitry restriction and also allows for 3-dimensional waveguide architecture. Davis *et al.* [38] discovered in 1996 that a permanent refractive index change can be induced in a dielectric material around the focal volume of a tightly focused femtosecond laser due to nonlinear absorption processes. By translating the material through the focus in any direction, a continuous wave-guiding structure can be inscribed. This fast and simple technique is compatible with a wide range of exotic materials that are transparent in the mid-infrared wavelength range such as germanate, fluoride and chalcogenide glasses [39].

The chalcogenide glass known under its trade name GLS has become one of the most studied mid-infrared glasses for FLDW. It consists of three elements: gallium, lanthanum and sulphur, and features a high transparency of up to 9 $\mu$m wavelength. Waveguide fabrication in this high refractive index glass is challenging since its high nonlinearity can distort the inscribing laser beam and change the focusing conditions. In general, neither the waveguide formation in GLS glass nor their refractive index profile are clearly understood to date. Previous attempts using quantitative phase microscopy or ellipsometric measurements were unsuccessful [40] and makes the engineering of complex devices more challenging.

This thesis presents the development of a platform for a mid-infrared waveguide nulling interferometer in GLS glass with a total projected intrinsic loss of <1 dB. This target loss value is sufficient to perform future on-sky experiments on ground-based telescopes in relatively short observation runs.

The breakdown of this thesis into its main components is presented below.

Chapter 2 gives a detailed introduction into the topic of femtosecond laser direct-writing and various aspects of waveguide fabrication. It provides deeper understanding of the general interaction between femtosecond laser pulses and dielectrics and illustrates the underlying structural changes in the materials.

Chapter 3 outlines the experimental methods used throughout this project. This ranges from pre- and post-processing of the material to the fabrication facility and the device characterisation setups and instrumentation.

Chapter 4 first reviews the operating principle of optical fibers, then presents the study of waveguide fabrication in GLS glass using the multiscan and cumulative heating methods. The fabricated waveguides are characterised at a wavelength of 3.39 $\mu$m and the results are contrasted against each other. A further extension to 4 $\mu$m is undertaken for waveguides developed using the cumulative heating regime.

In Chapter 5, Raman spectroscopy lays the foundation for investigating the role of ion migrations and structural reorganisations in cumulative heating waveguides developed in Chapter 4. Electron probe microanalysis helps to deepen the understanding of the material modification. The resulting refractive index change of the modification is investigated in detail.

In Chapter 6, the experiments developing optimised S-bend shaped waveguides, Y-splitters, multimode interference and directional couplers are presented. The latter was further developed from symmetric to asymmetric couplers in order to achieve a wavelength-flattened response and hence a broadband 50/50 power splitting behaviour.

Chapter 7 concludes the project by summarising the findings on femtosecond laser direct written waveguides and integrated components for a mid-infrared nulling interferometer in GLS glass and gives an outlook on future research.

# 2

# Femtosecond laser direct-writing

Many optical materials are being utilised for optical integrated circuits such as silicon-on-insulator and indium phosphate as well as a variety of different glasses. Glass is an excellent material for optical waveguide technologies due to a high transmission in both the visible as well as the infrared wavelength range. The advent of ultrashort pulsed lasers enabled the in-volume processing of transparent dielectrics by utilising nonlinear optical breakdown triggered by intense laser pulses. This universal technique enables the formation of light guiding structures and entire circuits inside transparent materials without damaging the surface, starting from fused silica [41] and borosilicate [42], to more exotic glasses such as fluoride [43], chalcogenide [44] and tellurite glasses [45] and even polymers [46] and crystals [47]. The process of laser-induced optical breakdown describes the transfer of optical energy to the material leading to ionisation of the material. The electrons can then transfer their energy to the material lattice that creates a permanent material modification. These non-linear absorption processes occur when the electric field of the bound valence electron equals the electric field strength of the incident laser pulse. Such a high electric field strength can be achieved inside the material at the focal volume of a tightly focused laser beam. The absorption of two or more photons causes a localised deposition of energy that is converted into thermal energy. The glass undergoes a structural or phase modification that results in a permanent refractive index change.

Lasers with picosecond pulse durations generally reach the peak intensity for optical break-down with a relatively large pulse energy. This energy causes the modification to extend far beyond the focal volume. With the development of femtosecond lasers in the late 1980s, it became possible to achieve the required peak intensity with a much lower pulse energy. Modifications in the bulk can thus obtain sub-micrometer precision since the excitation remains within the focal volume, mainly caused by multiphoton excitation. An excited electron transfers its energy on a time scale of one picosecond and is accompanied with thermal effects that heat up the surrounding area.

The first report of using femtosecond lasers to determine the surface damage threshold of fused silica as a function of laser pulse duration was published in 1994 [48] by the University of Michigan, USA. At Harvard University, this technology was used to explore new ways of high-density three-dimensional binary data storage by Glezer *et al.* in 1996 [49]. However, in the same year, a new era of integrated optics fabrication was started by the group of Hirao in Kyoto, Japan. Here, Davis *et al.* [38] studied the effects of sub-picosecond pulses focused through a microscope objective into various transparent glasses to form optical waveguides. A titanium sapphire laser emitting 120 fs pulses at a wavelength of 810 nm with a repetition rate of 200 kHz induced a permanent refractive index increase of 0.001 - 0.035 in pure and Ge-doped fused silica. This remarkable discovery led to an entirely new research field of femtosecond laser direct-writing (FLDW).

Femtosecond laser direct-writing involves many parameters that determine the type and amount of the refractive index change. Laser parameters play an important role such as wavelength, repetition rate, pulse duration, pulse energy and polarisation, but the focusing conditions, the translation velocity of the stage and the properties of the glass are also important. With this many free variables it is rather difficult to develop one common fabrication procedure that can be applied to every material. Each material therefore has to be studied individually in order to fabricate high quality and low-loss optical waveguides.

This chapter provides a background of the femtosecond laser direct-writing technique. It reviews different writing geometries and the mechanisms involved in creating permanent refractive index changes. Furthermore, the different modification regimes using high and low repetition rates are explained. These topics are described in more detail in the review article by Gross *et al.* [50] and the book *Femtosecond Laser Micromachining* by R. Osellame, G. Cerullo and R. Ramponi [51].

## 2.1 Writing geometry

The key advantage of FLDW is the capability of forming 3-dimensional waveguide devices whereas traditional photolithography is limited to planar fabrication. To fabricate these devices, a computer-controlled translation stage moves the glass sample, controlling the three-dimensional writing path. It translates the glass through the focal volume of the laser with a precision on the order of nanometers. This offers a wide range of devices to be produced, from simple straight waveguides [52] to more complex structures such as 3-dimensional beam combiners [53] and photonic lanterns [54].

Two basic geometrical writing arrangements for optical waveguides are applied in FLDW: longitudinal and transverse writing, shown in Figure 2.1.

For longitudinal writing, the sample is moved either away or towards the inscribing laser beam. This gives the waveguide structure a circular shape attributed to the laser beam's circular symmetric Gaussian intensity profile. One major drawback of the longitudinal writing method is the limitation of the waveguide length to the working distance of the focusing objective. For a typical air objective with a numerical aperture (NA) of 0.4, the working distance is about 5 mm. To solve this problem, slower focusing objectives with a NA of $\sim$0.2 are used, but they require high laser peak powers to provide the intensity needed for optical breakdown. This can lead to Kerr self-focusing (Section 2.2.3), resulting in filaments

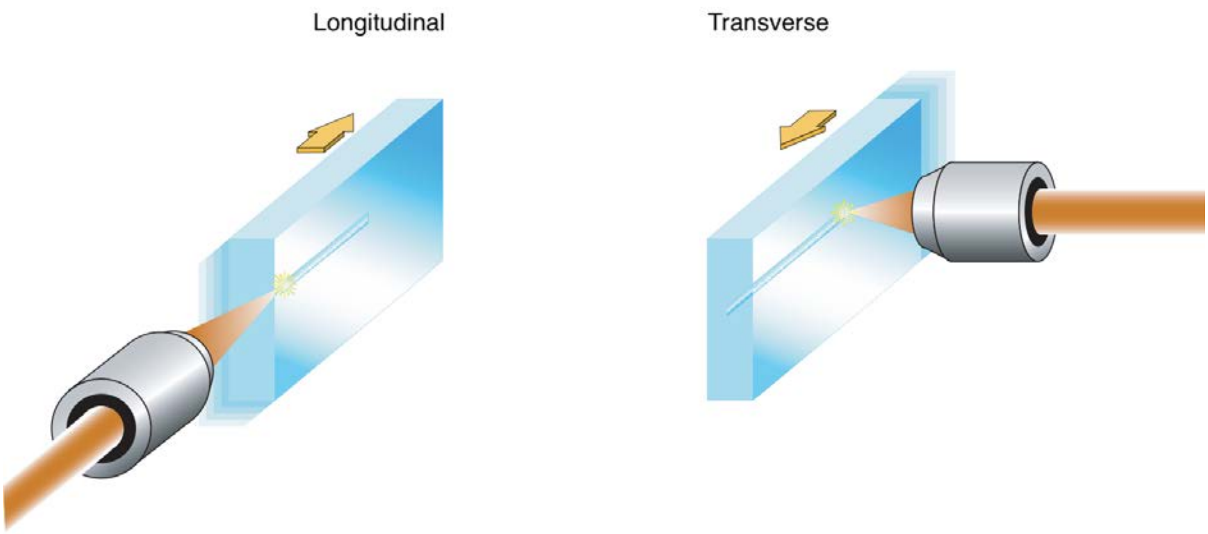


FIGURE 2.1: Schematic of longitudinal (left) and transverse (right) laser inscription in transparent bulk material [51].

of several hundred micrometers in the axial direction [55].

For the transverse writing method, the sample is moved perpendicular to the inscribing laser beam. The waveguide length is thus no longer limited by the working distance of the focusing objective. This flexibility made transverse writing the most commonly used method nowadays in femtosecond laser direct-writing setups. The writing depth of up to several millimeters provides enough flexibility to create 3-dimensional structures. One challenge of the transverse writing method however, is to create circular waveguides. The typically asymmetric waveguide cross section can be explained as follows: The dimension of the waveguide perpendicular to the incident laser is given by twice the beam waist $\omega_0$. The dimension along the laser propagation direction, is determined by twice the Rayleigh length $z_R = \pi\omega_0^2/\lambda$ [56] that exceeds the size of the beam waist by $n/\mathrm{NA}$ with $n$ being the refractive index of the glass. The large asymmetry of the waveguide can lead to elliptical modes that poorly couple into circular fibres. For a low refractive index ($n = \sim 1.5$) glass the asymmetry can be mitigated by using oil immersion objectives (NA $> 1$). For improved waveguide symmetry in glass with a high refractive index such as gallium lanthanum sulphide (GLS, $n \sim 2.4$), it is useful to apply additional beam-shaping techniques or the multiscan method described in Section 2.4.

## 2.2 Femtosecond laser-material interaction

In order to permanently modify the material, electrons need to be excited and their energy transferred to the material lattice. Linear absorption of an incident laser beam would require high energy UV photons to bridge the gap between the valence and the conduction band. However, single photon effects have very limited penetration depth due to the linear nature of the absorption. In FLDW, lower energy photons in the near-infrared are used, typically centered around 800 nm and 1064 nm. Here, the high intensity of focused femtosecond laser pulses results in strong nonlinear absorption in the bulk of a transparent dielectric. The process of FLDW can be divided into three main steps: free electron plasma formation through nonlinear excitation mechanisms, relaxation of energy and modification of the material.

### 2.2.1 Nonlinear excitation mechanisms

Nonlinear photoionisation is strongly dependent on the laser's wavelength and intensity that triggers multiphoton or tunnelling ionisation processes [57, 58]. Furthermore, strong avalanche photoionisation takes place with increasing pulse durations.

#### Nonlinear photoionisation

Femtosecond lasers in the infrared are unable to provide single photons with sufficient energy to directly promote an electron from the valence into the conduction band for most common glasses with bandgaps in and below the visible region. It requires simultaneous absorption of multiple photons to provide the energy for the ionisation process (Fig. 2.2 left). To capture enough energy, the number of simultaneously absorbed photons $k$ has to be equal to or larger than the bandgap of the material $E_g$ divided by the photon energy

$$kh\omega > E_g \,, \tag{2.1}$$

with the frequency of light $\omega$ and Planck's constant $h$. For GLS glass with a band gap energy of 2.6 eV it takes a minimum of two photons from a 800 nm laser pulse to fulfil

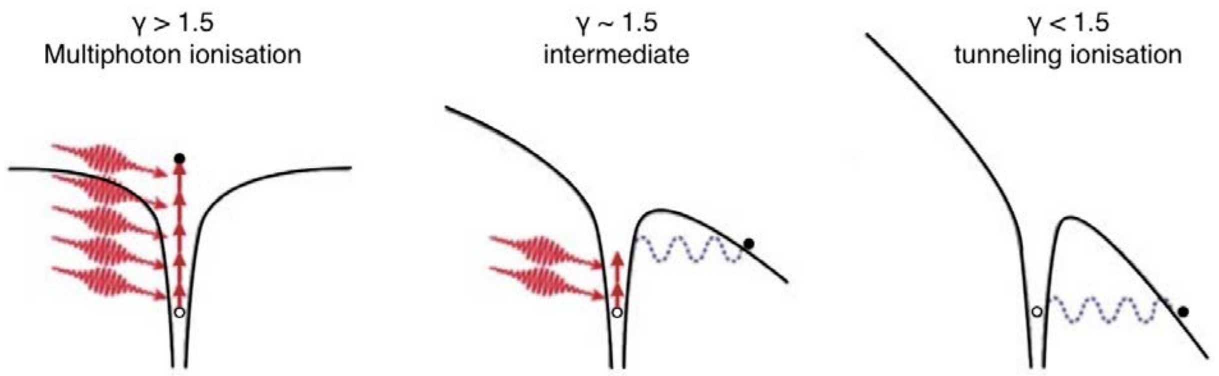


FIGURE 2.2: Nonlinear photoionisation processes during femtosecond laser inscription include multiphoton ionisation (left), tunnelling ionisation (right) or an intermediate regime (center) depending on the laser frequency and intensity [57].

this requirement. For high laser frequencies and low intensities, the multiphoton ionisation regime dominates the ionisation process. The tunnelling ionisation regime takes over at high intensities [59] with very little influence from the laser frequency [60]. A strong electric field of the laser suppresses the Coulomb barrier that ties a valence electron to its parent atom. This allows the electron to tunnel through the shorter barrier to become free (Fig. 2.2 right). The transition from multiphoton to tunnelling ionisation is expressed by the Keldysh parameter $\gamma$ [59]

$$\gamma = \frac{\omega}{e}\left[\frac{mcn\varepsilon_0 E_g}{I}\right]^{1/2} \tag{2.2}$$

with the reduced charge and mass of the electron $e$ and $m$, respectively, the material's refractive index $n$, the vacuum speed of light $c$, the permittivity of free space $\varepsilon_0$ and the laser intensity at the focus $I$. The photoionisation is dominated by multiphoton ionisation for $\gamma > 1.5$ and by tunnelling ionisation for $\gamma < 1.5$. An intermediate state is found for $\gamma \sim 1.5$ with both regimes contributing to the ionisation process (Fig. 2.2 center).

### Avalanche photoionisation

The energy from several photons of the laser field can also be absorbed linearly by a free electron in the conduction band (Fig. 2.3 left). Once the free electron has gained sufficient energy to bridge the band gap, additional energy is potentially transferred to a different electron via impact ionisation as shown in Figure 2.3 (right). These two excited electrons can subsequently promote new electrons into the conduction band after undergoing further energy absorption.

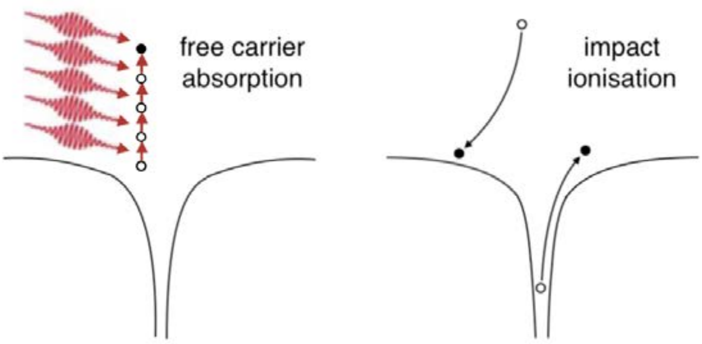


FIGURE 2.3: A free electron in the conduction band can absorb multiple photons from a laser pulse.

This avalanche process can result in exponential growth of the plasma density $N$

$$\frac{dN}{dt} = \eta(E)N \tag{2.3}$$

with an ionisation rate $\eta$ that depends on the laser's electric field strength. The avalanche process is started through seed electrons mainly provided by tunnelling and multiphoton ionisation but also by ionised impurities and defects and by thermal excitation. Avalanche ionisation is stronger for pulse durations of a few hundred femtoseconds and longer [57] while pulse durations below 200 fs are too short to cause significant avalanche ionisation [61].

### 2.2.2 Modification regimes

In general, after generating a free electron plasma via photoionisation, tunnelling, and avalanche processes, the energy is transferred to the lattice of the glass network via electron-phonon coupling. However, the time needed for femtosecond laser pulses to be absorbed is shorter than the energy transfer to the material, typically on the order of ∼1 ps. The fast energy deposition leads to lattice heating and material modifications that are decoupled from the ionisation process [58]. One can divide the typically observed modifications into three different types:

Firstly, a smooth refractive index change [62] is observed at low pulse energies when the melted glass in the focal spot cools down quickly from high temperatures. Secondly, a birefringent refractive index change appears at intermediate pulse energies [63–65] while thirdly, a void formation occurs at high pulse energies due to microexplosions [66]. Shock waves are created after the electron releases its energy, leaving less dense or hollow cores behind.

Not all of these phenomena appear in every material. The modification depends on a great number of exposure parameters such as the pulse duration, pulse energy, repetition rate, translation velocity, wavelength, etc. Material properties such as thermal conductivity, band-gap energy and others are also important factors influencing the type of modification.

#### Smooth refractive index change

The quality of FLDW waveguides depends on the uniformity of the modification that can lead to a smooth refractive index change with low propagation loss. Chan *et al.* [67] attributed the smooth refractive index change in fused silica to densification within the focal volume from rapid quenching of the melted glass as originally proposed by Davis *et al* [38]. Observations in glasses such as borosilicate and phosphate support this theory showing that a decrease in density during rapid quenching causes a negative refractive index change [68]. By contrast, stress modifications that are generated through shock waves upon impact of femtosecond laser pulses were shown to contribute minimally to the refractive index change [69]. Other studies showed that colour centers are responsible for modification carried out with kHz laser repetition rates, while densification occurs upon MHz irradiation [70, 71]. It is difficult to distinguish individual modifications given the number of variables that contribute to femtosecond laser direct-written waveguides. The influence of each modification varies from glass to glass and should rather be treated as an interplay of effects that form the refractive index change.

### Birefringent refractive index change

A permanent birefringent refractive index change has been demonstrated for fused silica waveguides fabricated with intermediate pulse energies [63]. It was predicted that an inhomogeneous optical breakdown generates nanoplasma that forms growing and self-organising nanoplanes [72] and has been accurately confirmed experimentally [73]. The periodic layers feature alternating refractive indices with a sub-wavelength period of $\lambda/2n$, called nanogratings, that are independent of the writing velocity. Shimotsuma *et al.* [64] and Hnatovsky *et al.* [73] showed that the orientation of inscribed nanogratings appears perpendicular to the polarisation of the inscribing laser (Fig. 2.4). This creates a birefringent behaviour that can be utilised for polarisation controlling waveguide retarders [74].

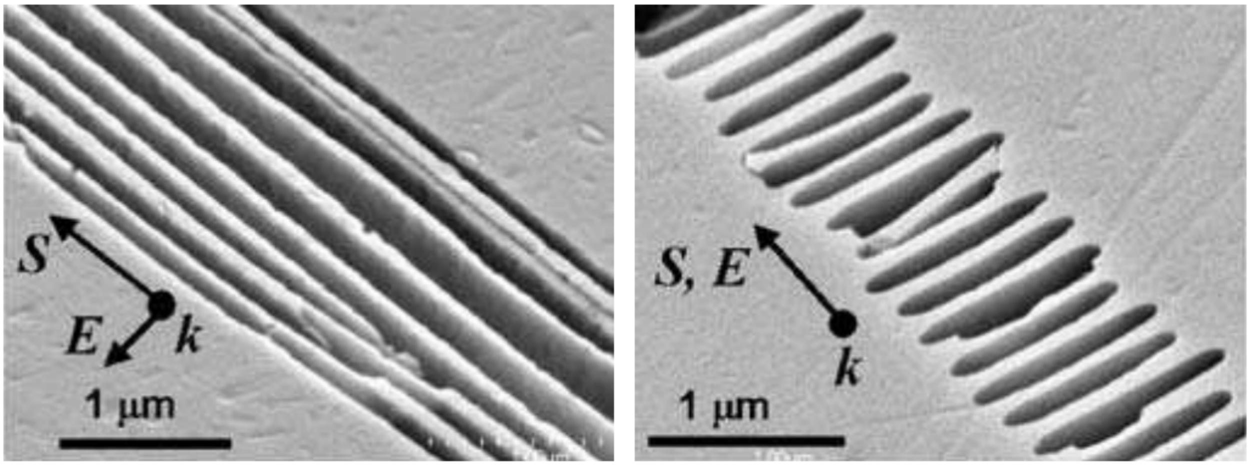


Figure 2.4: Secondary electron microscope images of polarisation-dependent nanostructures formed by transverse writing geometry [73] with linear polarisation perpendicular (left) and parallel (left) to the writing direction.

### Void formation

At high pulse energies the plasma pressure in the focal volume can exceed the internal pressure of the material (Young's modulus). It then generates shockwaves after the electrons have transferred their energy to the material lattice. Shockwaves propagate radially outwards and are depleted by the counteracting natural material pressure. The affected volume depends on the distance travelled by the shockwaves [66], before they convert into soundwaves. The affected volume is left behind with a less dense or even hollow core (void) while the surrounding area features an increase of refractive index [75]. These modifications cannot be used to form optical waveguides but have been investigated for other applications, such as data storage [49] and fiber Bragg gratings [76].

## 2.2.3 Kerr self-focusing

The material modifications explained thus far are based on high peak powers of femtosecond lasers. These high intensities can also lead to undesirable nonlinear Kerr self-focusing during waveguide fabrication as a response to the strong electric field $E$. Highly-nonlinear glasses such as GLS are especially prone to such modifications. Laser pulses that propagate through the material induce electric dipole moments and hence polarisation. The material response can be separated into a linear and a nonlinear term with the refractive index

$$n = n_0 + n_2 I \ , \tag{2.4}$$

where $n_0$ is the linear and $n_2$ is the nonlinear refractive index. $I$ is the intensity of the laser field given by

$$I = \frac{1}{2} n_0 \epsilon_0 c_0 \left( |E|^2 \right) \ . \tag{2.5}$$

Due to the intensity distribution of a Gaussian beam, the nonlinear refractive index change is also of Gaussian shape. As long as $n_2$ is positive, the center of the beam has a higher refractive index compared to the surrounding area. This refractive index variation forms a positive lens that focuses the beam inside the glass depending on the peak power. With a high laser peak intensity, the pulse collapses if the critical power $P_c$ for Kerr self-focusing is exceeded [77]

$$P_c = \alpha \frac{\lambda_0^2}{4\pi n_0 n_2}\ , \tag{2.6}$$

where $\alpha = 1.8962$ is the intensity profile factor for a Gaussian beam and $\lambda_0$ is the vacuum wavelength. If nonlinear ionisation mechanisms form a free electron plasma in the material, the plasma will behave like a diverging lens counteracting the Kerr self-focusing. An equilibrium between these two conditions leads to a filamentary propagation that produces unwanted axially elongated structures. Filaments in GLS glass are illustrated in Figure 2.5 (left) while Figure 2.5 (right) shows a comparison of waveguides fabricated in the cumulative heating regime below the critical power peak for Kerr self-focusing.

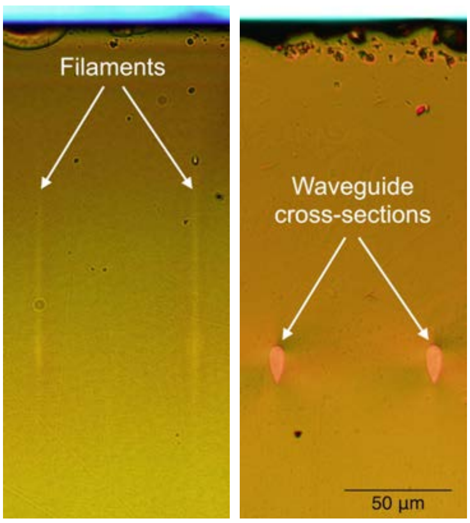


Figure 2.5: Left: Filamentation in GLS due to high peak power and a very low NA of the focused laser beam. Right: As a comparison, cross-sections of GLS waveguides inscribed in the cumulative heating regime with low peak intensities.

These effects can be minimised by tightly focusing the inscription laser beam using objectives with a high NA. Optical breakdown can thus be achieved with peak powers below the critical power for Kerr self-focusing. A value of $n_2 = 3 \times 10^{-18}$ [$m^2/W$] was reported for GLS by Hughes [40] for a wavelength of 700 nm. The corresponding $n_0 = 2.4277$ can be derived from the Sellmeier equation (5.1). Applying Equation (2.6), the critical power for Kerr self-focusing is calculated to be 10.2 kW. Since the nonlinear refractive index decreases with wavelength, the critical power for self-focusing at the 800 nm laser wavelength lies slightly above this value. This low critical power for Kerr self-focusing shows the high sensitivity of GLS to nonlinear effects compared to other glasses such as fused silica or ZBLAN. Both of these glasses are able to withstand peak powers in the order ~2.5 MW at 800 nm.

## 2.3 Repetition rate regimes

Femtosecond laser direct-writing can be divided into two fabrication regimes: high repetition rate (thermal) and low repetition rate (athermal) (Fig. 2.6). In the low repetition rate regime, pulse repetition rates ~1 kHz are applied with common Ti:Sapphire femtosecond laser systems. The heat caused by a single laser pulse in the focal volume diffuses within ~1 $\mu$s [79] before the next pulse arrives (Fig. 2.6 bottom left). This implies that every single pulse modifies the material independently. In this regime, air objectives with a low NA are typically used to focus the laser beam into the material. As mentioned in Section 2.1, the confocal parameter and the Gaussian beam waist give the structure its elliptical cross-section. Several methods can be used to produce more symmetric structures which are discussed in Section 2.4. To achieve a continuous structure, the single modified regions must sufficiently overlap which limits the translation velocity of the computer-controlled stages.

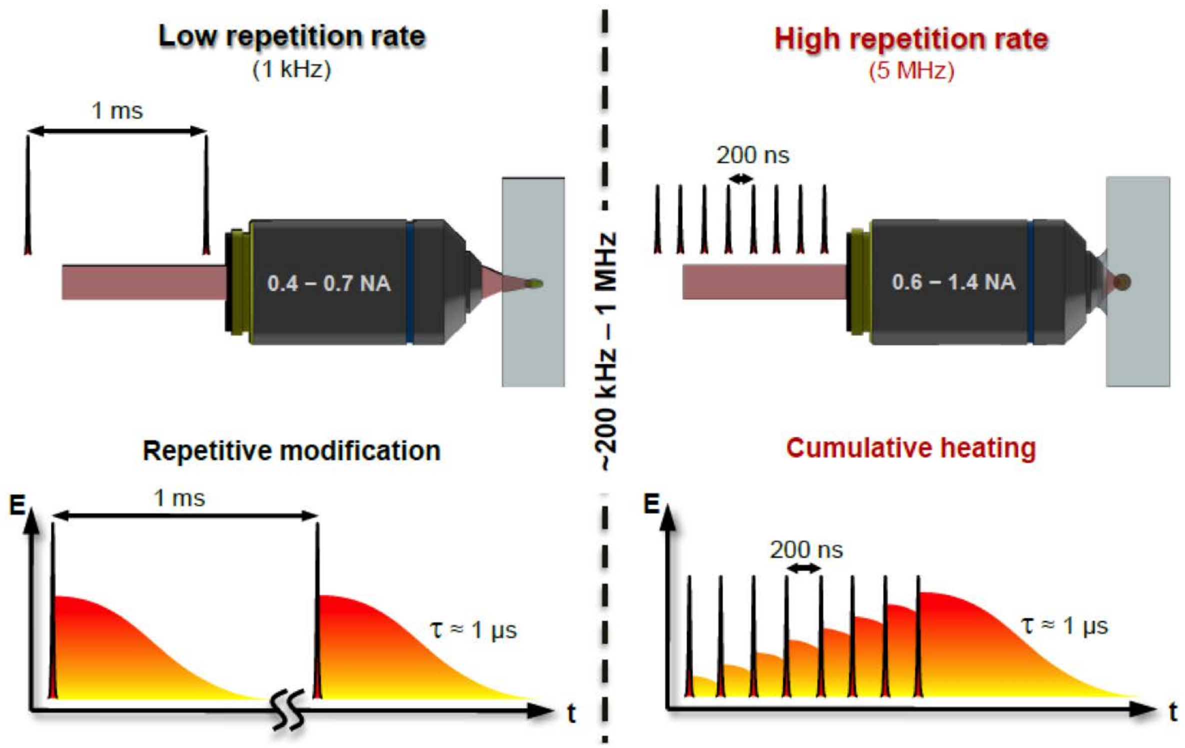


FIGURE 2.6: Femtosecond laser direct-writing can be applied in two different regimes. At low repetition rates, every single pulse creates a permanent material change within the focal volume. At high repetition rates, heat accumulation occurs and causes the material to melt far beyond the focal volume of the focused laser [78].

A typical translation velocity of 1.5 mm/min is used for 1 kHz repetition rate systems [41] leading to a total fabrication time of more than 6.5 minutes for a 1 cm long waveguide. With a higher repetition rate, a considerably higher translation velocity can be chosen compared to the low repetition regime. The velocities typically exceed 600 mm/min and result in a shorter fabrication time of 1 s for a 1 cm long waveguide compared to 6.5 minutes for a waveguide of the same length. At repetition rates >100 kHz, depending on the material, the time between each single pulse is reduced to the point where heat in the focal spot of the laser does not have sufficient time to diffuse (Fig. 2.6 bottom right). The temperature increases with each consecutive pulse and accumulates around the focal volume. The heated area expands further as the temperature rises until the melting point is reached and material changes appear. Once the laser pulses are turned off or moved past the heated area, rapid quenching occurs and forms a highly amorphous structure. These structures exceed the dimensions of the focal spot with a homogeneous distribution in all directions. Using a high NA microscope objective in this regime allows for a circular waveguide cross-section. The size of the waveguide can be adjusted by changing the translation velocity and pulse energy in order to deposit more or less energy per unit volume. As a result, no beam-shaping techniques are necessary to obtain symmetric waveguides.

## 2.4 Waveguide cross-section control

The cross-section and hence the refractive index profile is one of the most important parameters of a waveguide and defines the number and properties of supported modes. Elliptical modes, usually the product of asymmetric cross-sections, lead to coupling losses while weakly confined modes lead to high bending loss in curved waveguides. Waveguide fabrication in the thermal regime can naturally lead to a circular waveguide cross-section for single scans of the laser beam. The athermal regime on the other hand requires different approaches for controlling the cross-section. Two common approaches are the slit beam-shaping method and the multiscan technique. Beam shaping methods aim to manipulate the inscribing laser beam while the multiscan technique uses multiple passes across the sample to form a symmetric cross-section.

### 2.4.1 Slit beam-shaping technique

The beam waist of a focused laser pulse has a direct dependence on the NA of the focusing optic and is described as

$$2\omega_0 = \frac{2f\lambda}{\pi w\,(f)} \approx \frac{2\lambda}{\mathrm{NA}\pi} \quad , \tag{2.7}$$

with $w_0$ being the beam waist radius, $w\,(f)$ the radius of the beam at the objective, $f$ the focal length of the focusing objective, $\lambda$ the wavelength, $n$ the refractive index of the material and NA the numerical aperture of the focusing objective. The NA depends on both the focal length and the beam diameter illuminating the focusing objective. The NA can be reduced in the plane perpendicular to the sample's translational direction by inserting a slit in the path of the inscribing beam at the back aperture of the objective (Fig. 2.7).

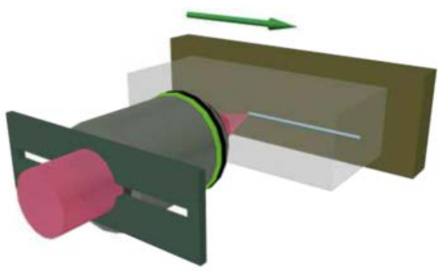

Figure 2.7: The slit beam-shaping technique uses a slit to shape the laser beam in one dimension. This way the numerical aperture of the inscribing laser can be tuned to provide a circular focus cross-section that translates into a circular waveguide [80].

This means that the ratio of the beam waist and therefore the symmetry of the waveguide is controlled by the slit width. Ams *et al.* [81] successfully inscribed symmetric structures in phosphate glass by applying the slit beam-shaping technique. The slit dimension is calculated with

$$\frac{W_y}{W_x} = \frac{\mathrm{NA}}{n}\sqrt{\frac{\ln 2}{3}} \qquad \text{for} \qquad W_x > 3W_y \quad , \tag{2.8}$$

where NA is given by

$$\mathrm{NA} \approx \frac{f}{W_x} \quad , \tag{2.9}$$

and $W_y$ is the width of the slit, $W_x$ is the diameter of the laser beam before the slit, $f$ is the objective focal length and $n$ is the refractive index of the material. Figure 2.8 shows a calculated intensity distribution in the YZ-plane for two focused beams where both beams propagate through a glass of $n = 1.54$. The circular Gaussian beam (Fig. 2.8 a) shows an elliptical energy distribution (Fig. 2.8 b) in the focal region. A 500 $\mu$m slit before the objective leads to a truncated beam (Fig. 2.8 c) with an almost symmetrical energy distribution (Fig. 2.8 d) in the YZ-plane.

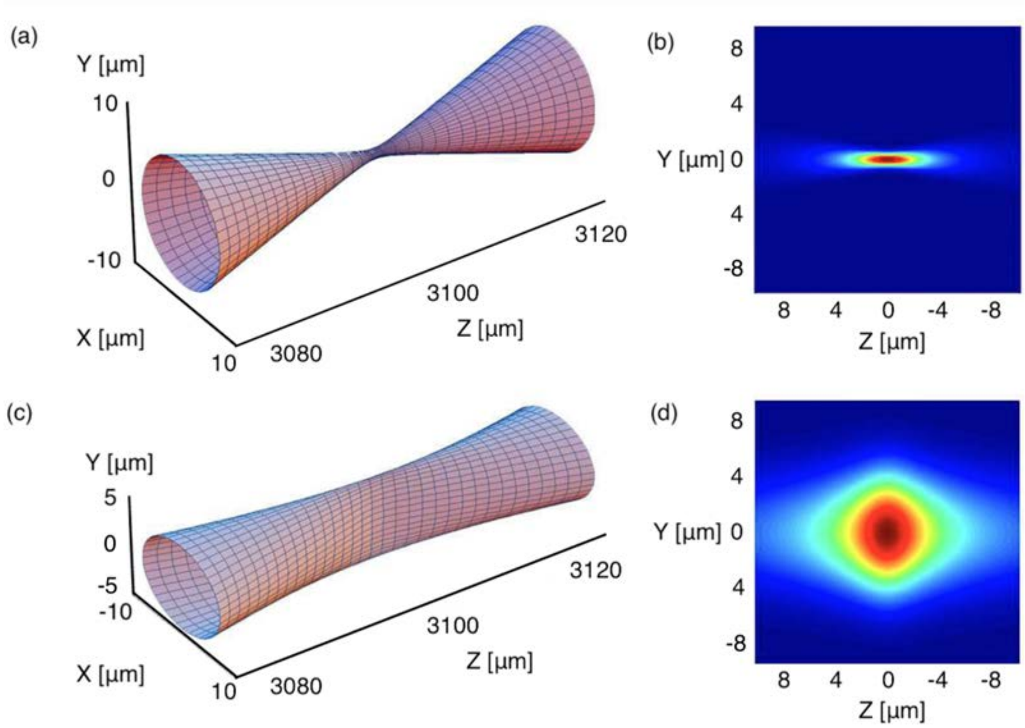


FIGURE 2.8: Image (a) and (b) show the beam profile and energy distribution in the YZ-plane without using a slit while (c) and (d) show the beam profile and energy distribution in the YZ-plane using a 500 $\mu$m slit orientated parallel to the X-axis [81].

### 2.4.2 Multiscan technique

The multiscan method [82] takes advantage of the asymmetric energy distribution at the focal region. As Figure 2.9 illustrates, the desired waveguide structure is created by scanning the sample multiple times transversely (Y-direction) through the focal spot. Several tracks with an elliptically shaped structure are placed next to each other (X-direction) usually with a slight overlap.

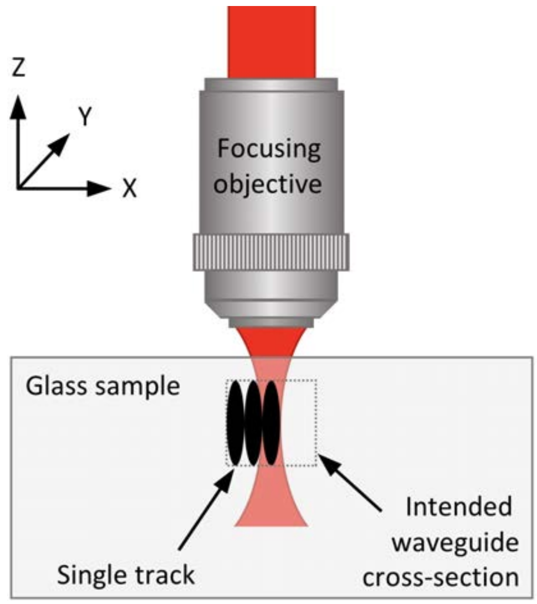


FIGURE 2.9: Principle of the multiscan technique [83]. Single scans are inscribed along the Y-direction at a depth Z. Several tracks are placed next to each other in X-direction, usually with a slight overlap, until the desired cross-section is reached.

A disadvantage compared to other methods is that each individual track prolongs the fabrication time. This technique however, features the advantage of having precise control over the waveguide dimensions. The height can be adapted by varying the pulse energy, translation velocity or the effective numerical aperture of the focusing objective. The width on the other hand is defined by the number of scans and the chosen step size or overlap. Thus, symmetric waveguides with quasi-rectangular shapes can be inscribed. The multiscan technique is mainly used in the low repetition regime [83] but has successfully been applied in the intermediate regime [84]. It is widely used with a variety of glasses that led to waveguides with a propagation loss as low as 0.12 dB/cm as reported by Nasu *et al.* [85] in fused silica.

Low losses may be explained by the very low peak intensity applied and could thus reduce the number of absorbing and scattering defects.

### 2.4.3 Spherical aberration

When using high numerical aperture objectives, spherical aberrations become critical. The aberration arises from the refractive index mismatch at the air-glass interface. Figure 2.10 shows the refraction on a glass sample with a refractive index of $n > 1$. With a relatively high NA, the focal spot *P0* of light ray *L0* lays above the focal spot *P1* of light ray *L1*. This results in an elongated focal area with the distance *d1*. The spherical aberration of the objective in air is indicated by the dashed lines of light rays *L0* and *L1* where its elongated focal area *d0* is smaller than *d1*. The distortion of the laser beam thus leads to a focal spot with a larger area and asymmetric energy distribution. This causes a decrease in peak intensity and influences the shape of the waveguide. The distortion becomes more severe the larger the refractive index difference between the sample and the immersion medium.

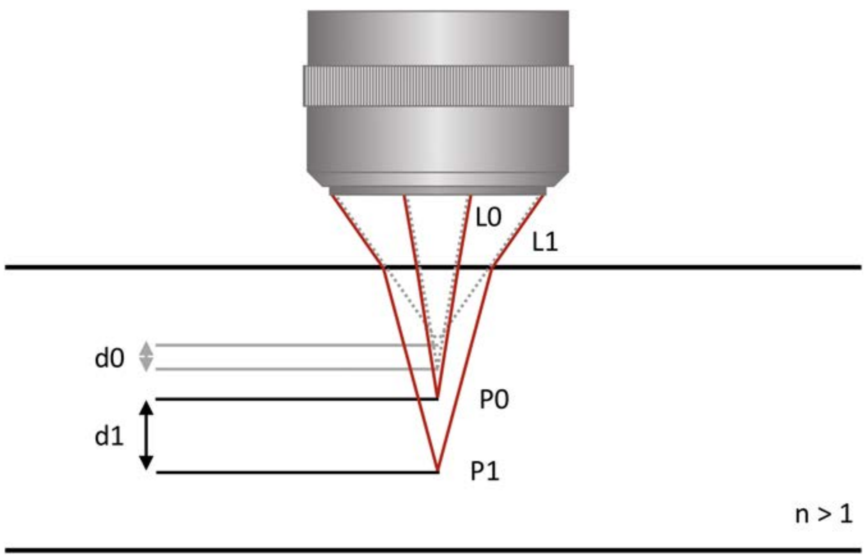


FIGURE 2.10: Refraction of light rays as they enter a glass sample. Spherical aberration occurs at the glass-air interface for any difference in refractive index between the immersion medium and the sample. The focal spot is thus distorted and leads to an elongated modification.

Most commercial microscope objectives are used for biological applications. They are corrected for spherical aberrations when imaging through standard microscope slides of 170 $\mu$m thickness with a refractive index of $n = 1.518$. The refractive index changes with different materials and the writing depths may be adjusted depending on the structure requirements. If any of these two parameters change, the correction of the objective is ineffective and thus leads to spherical aberration. By changing the writing depth while using a high NA objective, a deviation of a few microns can decrease the peak intensity significantly. This limits the capability for creating three dimensional structures. Using low NA objectives results in a broader distribution of the peak power across the focused beam that marginally changes for different depth. However, a higher peak power is necessary in order to modify the material, which often exceeds the critical power for catastrophic self-focusing (Sec. 2.2.3). Therefore, a compromise has to be made regarding high and low NA. The aberration can be mitigated by using oil immersion microscope objectives where oil with a refractive index of $n = 1.518$ fills the space between sample and objective. These objectives have NAs of >0.8 which limits the inscribing depth due to their short working distance of typically $\sim$200 - 450 $\mu$m.

A limited number of objectives are on the market that are equipped with an adjustable correction collar. Although this feature allows for operating at different focusing depths, this correction is static and limits the 3D capabilities of femtosecond laser direct-writing when deviating from the focusing depth corrected for aberration. Alternatively, adaptive optics can be used to correct for spherical aberrations. This requires a real-time feedback system that images the waveguide from the side during inscription via phase contrast microscopy and corrects the length of the inscription to compensate for occurring aberrations [86]. A different approach was reported where the intensity of the plasma generated by the focused laser beam was used as a feedback to maintain a homogeneous inscription at different depths [87].

# 3

# Experimental methods

This chapter outlines the experimental methods and the equipment used for fabricating and characterising integrated optical waveguides and photonic devices in gallium lanthanum sulphide (GLS) glass. It contains a description of the pre- and post-processing of the samples, performed by the author, and details of the femtosecond laser fabrication facility. The fabricated components are visually inspected with an optical microscope and their physical size determined. The propagation loss of optical waveguides is measured for monochromatic light at 3.39 $\mu$m and 4 $\mu$m using the Fabry-Perot method and the spectral response of photonic components is in turn measured on a separate broadband test bed for a wavelength range of 3 - 5 $\mu$m. Moreover, this chapter introduces the methods to understand structural changes of the material upon femtosecond laser exposure. Material bond changes are investigated via Raman spectroscopy while ion migration is examined with an electron probe micro-analyser. The refractive index change is determined by exploiting the micro-reflectivity method.

## 3.1 Sample preparation

The GLS glass samples were kindly provided by Dan Hewak from the University of Southampton with dimensions of 50 mm $\times$ 10 mm $\times$ 1 mm with the top and bottom surfaces polished. Samples are cut on a dicing machine to a desired length before the waveguide inscription. Waveguide inscriptions that start at edge of glass samples form tapers caused by refracted laser light at the sample edge. Hence, waveguide inscriptions need to begin 100 $\mu$m away from the edge inside the glass sample. As a consequence, the glass edges then need to be ground back to expose the waveguide's end-faces. A subsequent polishing step minimises coupling losses and is mandatory to determine the mode-field diameter and especially the propagation loss utilising the Fabry-Perot method (Section 3.3.4). Dicing as well as grinding and polishing of the samples is a challenging and slow process due to the brittle nature of this soft glass.

### 3.1.1 Dicing

The glass samples are fixed in place on a 10 cm glass disc with sticky wax and the assembly is then placed on the vacuum chuck of a water-cooled SYJ-400 CNC dicing machine from the MTI Corporation (Fig. 3.1 left). Silicone high vacuum grease (Dow Corning) placed between the two surfaces seals the vacuum. The computer-controlled dicing saw uses a 100 mm diameter and 0.3 mm thin diamond blade operating at 4000 rpm. The glass is cut into 1 mm thin, 10 mm wide and 8 - 15 mm long pieces under a slow float of water to provide cooling. A slow feed rate of 4 mm/min is chosen to prevent the glass from chipping or cracking. After debonding from the glass disc on a hot plate, the glass pieces are put inside a falcon tube with acetone and placed into an ultrasonic bath to remove wax residuals.

### 3.1.2 Grinding and polishing

After fabricating waveguides in GLS glass, the samples need to be prepared for grinding and polishing. The soft edges of the samples tend to crack and chip upon mechanical pressure during the process and need to be protected. To have sufficient support, microscope cover

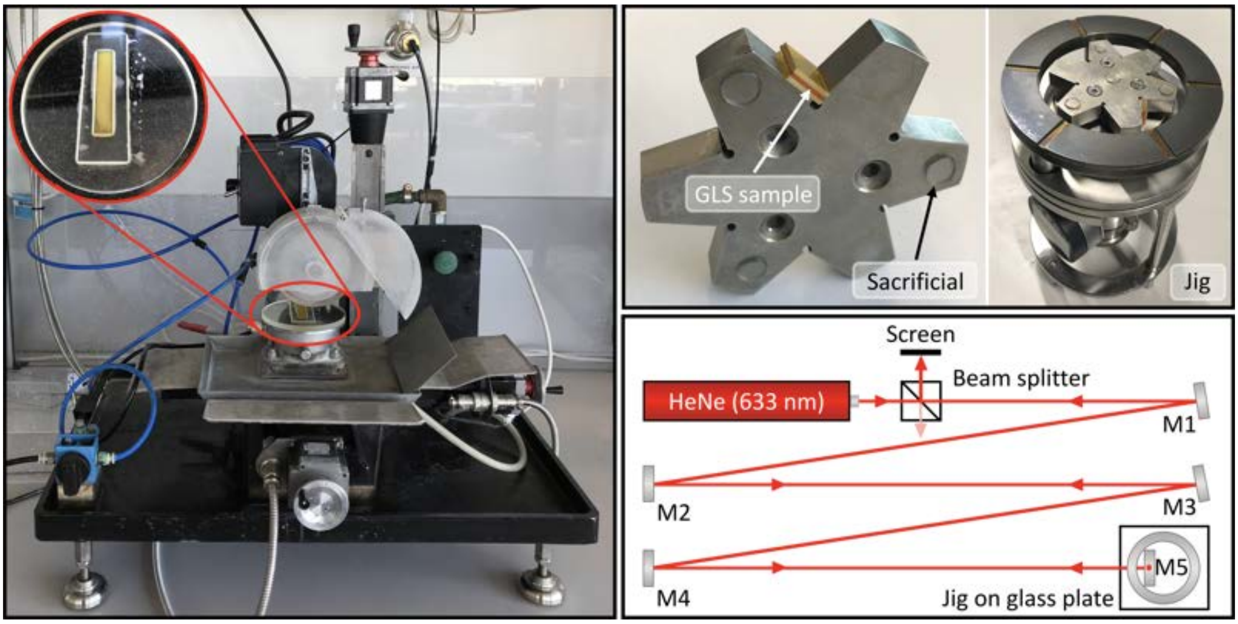


Figure 3.1: Left: Glass samples of 5 cm length are bonded with sticky wax to a glass disc (inset) and placed on the vacuum holder of a CNC dicing machine to be cut into various sizes. Right: Alignment setup (bottom) for squaring up the grinding and polishing jig with a star mount (top) holding a GLS sample 'sandwiched' by microscope cover slips.

slips with a thickness of 0.17 mm are glued with blocking UV adhesive NBA107 (Norland Products) on both top and bottom surfaces, lining up with the sample's end-faces. The assembly in turn is glued under 365 nm UV light to a metal star mount (Fig. 3.1 right) with a slightly stronger adhesive (NOA61, Norland Products) to withstand the high mechanical stress. The star mounts are available in thicknesses from 5 to 30 mm and are chosen to expose both ends of the sample on the flat side of the mount. Glass sacrificials of 1 mm thickness are stacked onto the flat side of the star using the UV adhesive to provide an even level across the mount for smooth material removal during grinding and polishing. The star is mounted to a Logitech PP5 jig (Fig. 3.1 right) and offers the advantage that it can be flipped to grind and polish the second facet without having to de-bond and re-bond the sample.

The angular alignment of the mount (Fig. 3.1 bottom) is crucial to ensure that the end-faces of the glass are perpendicular to the waveguides. The light of a HeNe laser is back reflected from both the sacrificial glued to the center of the downwards pointing star mount and the glass plate bearing the jig. A path length of 3.6 m is created by folding the beam over five silver mirrors (M1-M5), which enables an angular resolution of the system of approximately 1 arcmin. The reflection of the laser beam from the glass plate thus provides a reference beam that travels back along the beam path and is projected onto a white screen by a 50/50 beam splitter. The light reflected from the star mount is adjusted with three alignment screws from the jig to follow the same path as the reference beam until both overlap on the screen.

Like the process of dicing, the mechanical stress during grinding and polishing must be chosen carefully to avoid damaging the glass. At the expense of time, the jig allows for adjustment of the downward force experienced by the glass while shear forces can be reduced by decreasing the rotational speed of the grinding or polishing plate.


FIGURE 3.2: Left: grinding is carried out on a flatness-controlled Logitech PM5 machine using a 25 $\mu$m or 5 $\mu$m $Al_2O_3$ particle abrasive to remove excess material from the GLS glass sample. Right: the ground sample on the PP5 jig is placed on a polyurethane foam pad on a Logitech PM5 machine and lapped for ~60 minutes on a NaOH diluted colloidal silica slurry for an optical quality surface finish.

The actual grinding process is carried out in two steps: firstly, coarse grinding with 25 $\mu$m grit $Al_2O_3$ abrasive for fast removal of excess material followed by a fine grinding with 5 $\mu$m grit abrasive to smooth the surface. Each abrasive is inserted into an auto feed cylinder and mixed with reverse osmosis filtered water to form a dispensable solution. These cylinders are positioned on top of a PM5 Logitech (or preceding model PM4) lapping machine (Fig. 3.2 left) to constantly dispense the solution onto a rotating 30 cm diameter cast iron plate. The plate carries both a flatness monitor and the PP5 jig which is equipped with a digital micrometer gauge to measure the amount of material removed. The monitor is priorly calibrated against a granite surface and offers a permanent flatness control throughout the procedure. Each device is held in place on the cast iron plate by a metal fork.

The equipment is thoroughly cleaned after both the first and the second step to prevent any cross-contamination between the abrasives and the solutions used for the following polishing process. The flatness monitor is removed, and the cast iron plate is replaced by a polyurethane foam pad. The abrasive is exchanged for a colloidal silica slurry (Ultra-Sol 500S) with an average particle size of 70 nm and a NaOH solution for dilution (Fig. 3.2 right). The end-facets feature an optical quality finish after ∼60 minutes of polishing on each side. Approximately 12h are needed for the star mount to rest in an acetone-filled beaker in order to dissolve the applied adhesive. The samples may be retrieved, after only 4h if the beaker is placed in an ultrasound bath.

## 3.2 Femtosecond laser fabrication setup

This section describes in detail the state-of-the-art fabrication facility for waveguides and optical components in dielectric materials. The system consists of a high power oscillator (HPO), alignment optics and a 3-axis air bearing translation stage. The equipment is installed on an optical table with air suspension and is located in a temperature-controlled basement laboratory.

### 3.2.1 High power oscillator

A mode-locked titanium doped sapphire (Ti:sapphire) femtosecond oscillator (Femtosource XL500, Femtolasers GmbH) is the starting point of the inscription setup. Short pulses of <50 fs pulse duration are emitted at a center wavelength of 800 nm (Fig. 3.4 left) with a

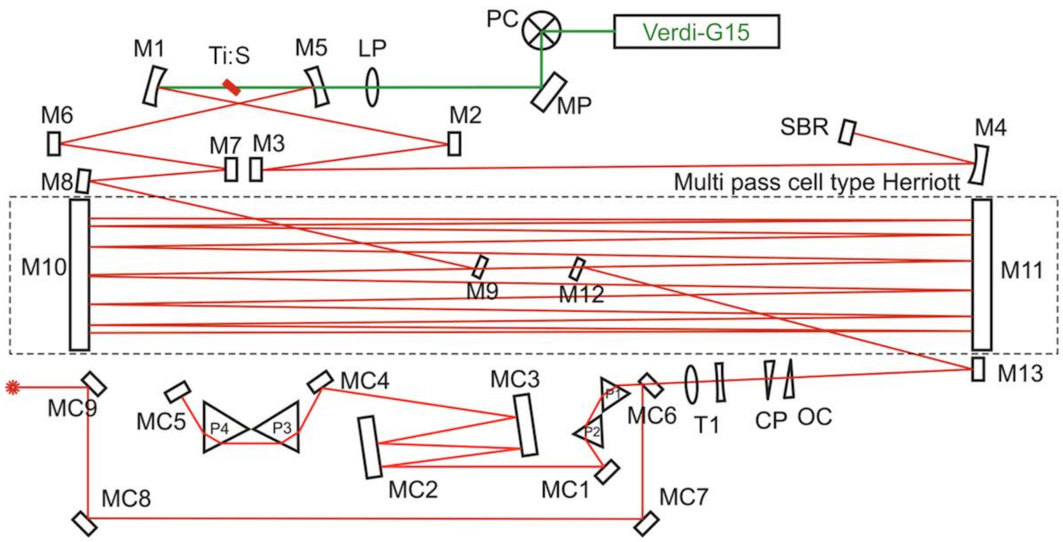


FIGURE 3.3: Internal structure schematic of the HPO (Femtosource XL500) with Verdi-V5 as the diode pump laser, Ti:S as the laser crystal and M# as mirrors [88].

repetition rate of 5.1 MHz. The pulses gain a maximum energy of 550 nJ which equals 11 MW in peak power and an average power of 2.75 W. The heart of the laser (Fig. 3.3) is the Ti:sapphire crystal which is pumped by a 15 W optically-pumped semiconductor laser (Coherent Verdi-G15, 532 nm). The crystal sits in an isolated dry-air chamber to avoid the occurrence of condensation on its surface. It is cooled to -32°C with a Peltier device in order to counteract the heat generated through high pump powers and to avoid thermal lensing effects. The short arm of the X-folded cavity terminates in a saturable Bragg reflector to

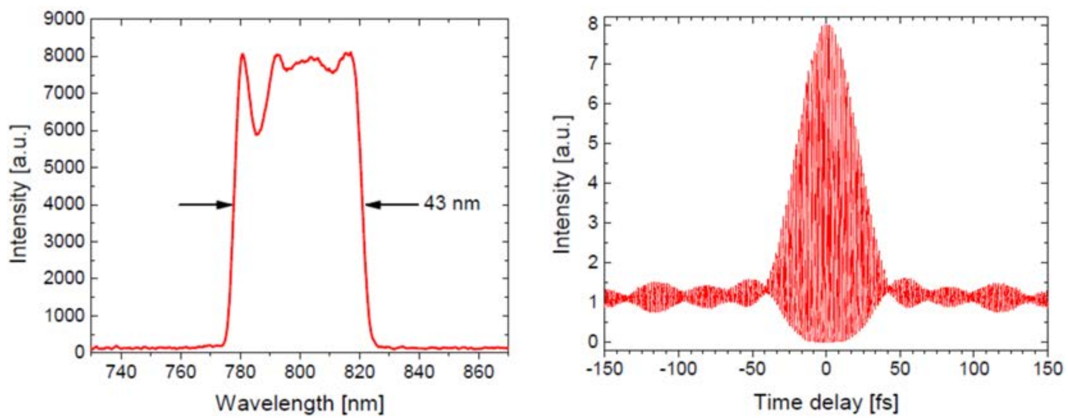


FIGURE 3.4: Output spectrum of the HPO with typically steep edges due to a chirped pulse (left) and corresponding interferometric autocorrelation (right). Image credit [78].

stabilise the mode-lock operation while the longer arm extends the cavity length to 30 m with a multi-pass cell. This leads to a decrease in repetition rate with a simultaneous increase in laser pulse intensity. It also causes the pulse to stretch due to group velocity dispersion. This behaviour is compensated by a compressing delay line of 1.5 m that consists of 2 prism pairs P1/P2 and P3/P4. The latter pair offers the flexibility of adjusting the pulse duration, measured with an auto-correlator (Fig. 3.4 right) by simply translating it in or out of the beam path.

### 3.2.2 Alignment setup

Once the laser light is coupled out of the HPO it follows a series of optical alignment tools until it reaches the focusing objective (Fig. 3.5). A beam stabiliser (1) closely follows the exit of the housing to account for the internal drift inside the laser cavity. It consists of two picomotor-driven mirrors for large offsets and two fast piezo mirrors for fine adjustments in a closed loop, accompanied with corresponding picometer drivers (New Focus, Inc.). The beam passes through a variable attenuator (Aerotech ADR75) on a rotational stage (2) fitted with a $\lambda = 800$ nm zero-order half-wave plate. It enters a periscope (3) formed by two polarising beam splitter cubes in reflection which additionally cleans the beam from light of unwanted polarisation. The light travels at a new height of 50 mm towards a demagnifying 3:1 telescope (4) after being reflected off a silver mirror by 90°. The 1 mm diameter beam continues through a 3 mm aperture rubidium titanyl phosphate ($RbTiOPO_4$) Pockels cell (Leysop Ltd., UK) (5) for high speed switching at MHz rates. This enables external tuning of the pulse repetition rate by picking pulses of any integer division of the fundamental 5.1 MHz. It allows the facility to operate in both a thermal and an athermal regime by setting the appropriate laser repetition rate (MHz vs kHz - Sec. 2.3) resulting in different modifications of the glass network.

The beam is expanded after the Pockels cell with any one of five different telescopes (6) available in ascending magnifications (1:2.5, 1:3, 1:3.5, 1:4, 1:5). Hence, the illumination of the focusing microscope objective at the final stage ranges from 3 - 6 mm in diameter and determines the effective numerical aperture. The polariser (7) and polarised beam splitter

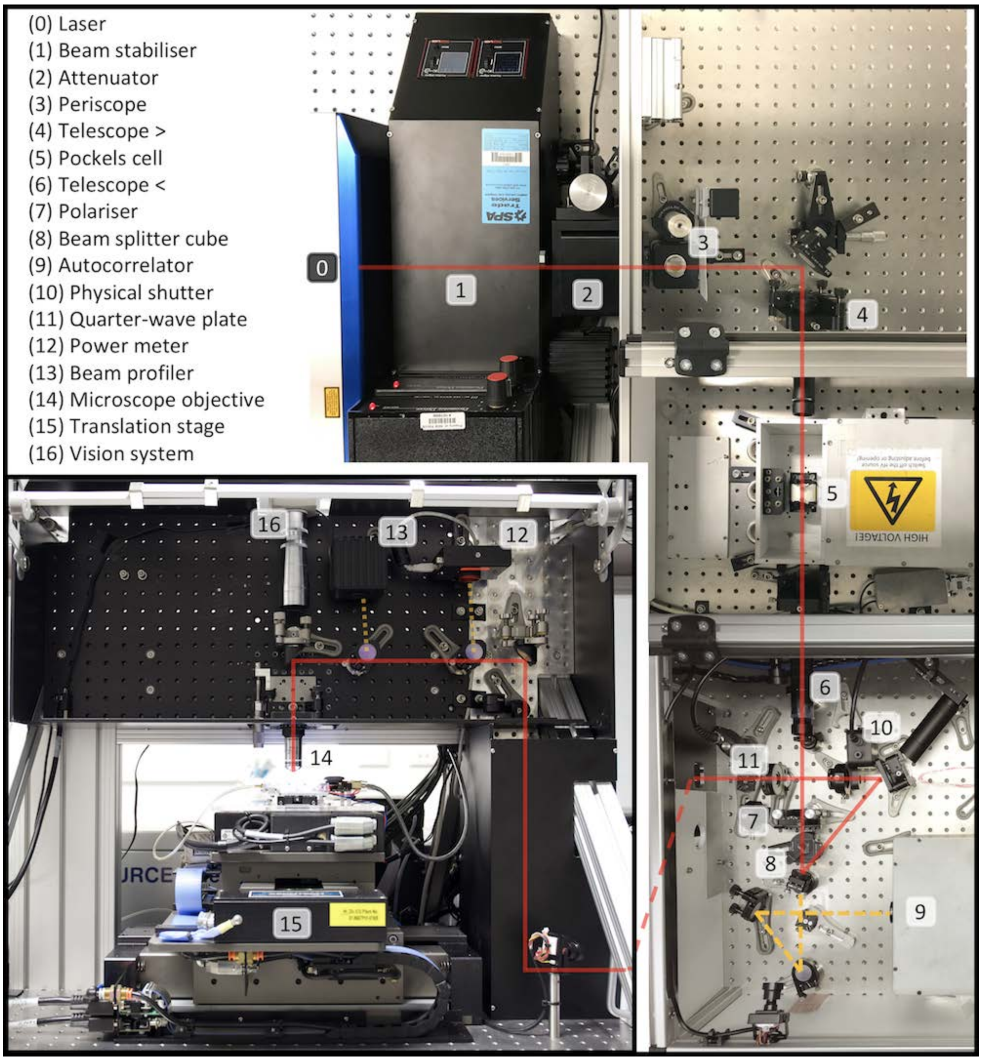


FIGURE 3.5: Femtosecond laser direct-writing alignment setup. Laser pulses travel through a series of alignment optics and characterisation devices (1-13) before they are focused by a microscope objective (14) into the glass sample located on a three-axis translation stage (15).

cube (8) are aligned by using their back reflection to pass through the center of an iris. The position of the rotatable polariser is set to have the beam splitter cube reflect unwanted pulses onto a safety screen if zero voltage is applied across the Pockels cell. If high voltage is applied, the pulses pass through the beam splitter cube onto a turning mirror on a magnetic mount. This mirror can temporarily be removed to open a path for characterising the laser pulses on an autocorrelator (9). The magnetic mirror and a second turning mirror reflect the beam through a physical shutter (10) and second iris, a tool used for aligning the microscope objective and to line up the beam perpendicular to the translation stage. The last element before the periscope is a quarter-wave plate (11) which changes linear polarisation into circular polarised light.

The beam is reflected twice within the periscope before it again travels parallel to the optical table in a horizontal encasement. Two available mirrors can be flipped into the beam path to direct the light onto a Spiricon LW230 beam profiler (12) to measure the beam dimensions or to a Thorlabs power meter (S142C, 350-1100nm) (13) to obtain the average power. A 45° dichroic mirror for near-IR wavelengths finally reflects the beam downwards towards the inscribing objective (14). The objective is screwed into a tip/tilt and X/Y translation holder and centered with respect to the beam and squared to the 3-axis translation stage (15). The stage carries a back illuminated vacuum chuck that permits viewing the fabrication process in real time with an overhead vision system (16) through the visible light transmissive dichroic mirror. The system consists of a 15 cm f4.5 Wollensak Raptar lens and a Sony low light colour CCD CCTV camera.

### 3.2.3 Microscope objective

The working distance of the objective is an important factor for the fabrication of intricate 3D waveguide circuits. The Olympus 100× Plan N objective has a working distance of 150 $\mu$m and an NA of 1.4 when immersed in oil. The high NA allows for the inscription of more symmetric structures compared to a microscope objective with a lower NA as discussed earlier. Taking Snell's Law into account, the inscription depth ranges from the surface of the material down to ∼241 $\mu$m (Equ. (3.1)). It must be noted that at a critical writing depth, a specific amount of energy is reflected off the sample and focuses onto the front surface of the objective. This Fresnel reflection can potentially cause permanent damage depending on the applied pulse energy. GLS glass with a refractive index of $n_{GLS} = 2.3931$ at $\lambda = 800$ nm and immersion oil with $n_{medium} = 1.51$ reflects around 5.1% of the incident light, calculated from Equation (3.5). The critical depth is at a distance of 75 $\mu$m between sample and objective which equals half of the working distance of the Olympus objective and corresponds to a writing depth of ∼119 $\mu$m calculated from

$$f_{\mathrm{depth}} = z \cdot \frac{n_{\mathrm{GLS}}}{n_{\mathrm{oil}}}\,, \tag{3.1}$$

with $f_{\mathrm{depth}}$ as the focal depth inside the material, $z$ as the lateral distance of the objective to the sample and $n_{\mathrm{GLS}}$ and $n_{\mathrm{oil}}$ as the refractive indices for GLS glass and immersion oil, respectively.

### 3.2.4 Translation stages

A set of Aerotech linear stages (Fig. 3.5 (14)) are used to move the glass sample through the incident laser light focused by the microscope objective. These stacked stages enable translation in XYZ-directions in order to fabricate 3-dimensional optical devices. An air bearing Aerotech ABL2000 linear stage is the foundation of the setup and is responsible for translation along the X-axis. A second Aerotech air bearing linear stage model ABL1000 sits on top and controls the Y-axis with both stages featuring a travel range of 100 mm. The final Aerotech WaferMax Z lift stage with a mechanical bearing controls the Z-axis over a travel range of 5 mm, where in practice the microscope objective limits the working depth to a maximum of 150 $\mu$m. The stage velocities are limited to 3000 mm/min on the X- and Y-axis and to 240 mm/min for the Z-axis, with an encoder resolution of 62.5 pm and 32.6 pm, respectively. A mirror mount is installed on top of the lift stage carrying a 70×80 mm vacuum chuck to hold the sample in place. The mount is used to align the tip/tilt of the sample's top surface parallel to translation stages.

An Aerotech U500 Ultra PCI motion controller drives the stages by interpreting a numerical control programming language (G-code) entered in the form of scripts in the A3200 Motion Composer software (v6.02.001 - Aerotech, Inc.). It further drives the mechanical bearing Aerotech ADR75 rotary stage with a zero-order half-wave plate as part of the variable attenuator described in Section 3.2.2.

## 3.3 Device characterisation

Device characterisation plays an important role in order to understand and improve their behaviour. This is accomplished through determination of their properties such as dimension, losses and chromaticity. The fabricated devices are visually inspected, and their physical size measured using an optical microscopy. The propagation loss of optical waveguides can be measured at 3.39 $\mu$m and 4 $\mu$m via the Fabry-Perot method. The spectral response of photonic components like Y-splitters and couplers are measured on a separate broadband test bed for a wavelength range of 3 - 5 $\mu$m.

### 3.3.1 Differential interference contrast microscopy

The first step after fabrication is to examine the waveguides visually for a continuous and smooth modified region along the writing direction of the laser. The optical characterisation is carried out on an Olympus IX81 light transmission microscope equipped with a Olympus DP72 camera and differential interference contrast (DIC) optical components (Fig. 3.6). DIC is a technique attributed to Georges Nomarski in 1955 to enhance the contrast of transparent specimens by converting optical path differences into intensity differences.

In a DIC microscope, light from a semi-coherent source passes through a polariser followed by a modified Wollaston prism. The prism consists of two quartz wedges glued together which splits the polarised beam into two orthogonal diverging beams. The following condenser focuses the beams into the specimen where the beams travel with a slight transversal offset and experience different optical path lengths. This difference originates from either a difference in refractive index or thickness of the sample. Microscope objectives with 10$\times$, 20$\times$, 40$\times$, 100$\times$ and 150$\times$ are available, where each objective requires a different prism selectable from a revolving turret on the condenser. The objective recombines the two beams and removes the shear causing interference in a second Wollaston prism. Any phase shift between the beams results in elliptical or circular polarisation that passes through the final polariser (analyser) oriented orthogonally to the first polariser, while linear polarised light is simultaneously blocked. The recombined beam is observed as a variation in intensity and colour either through eyepieces or captured digitally by a camera. A three-dimensional

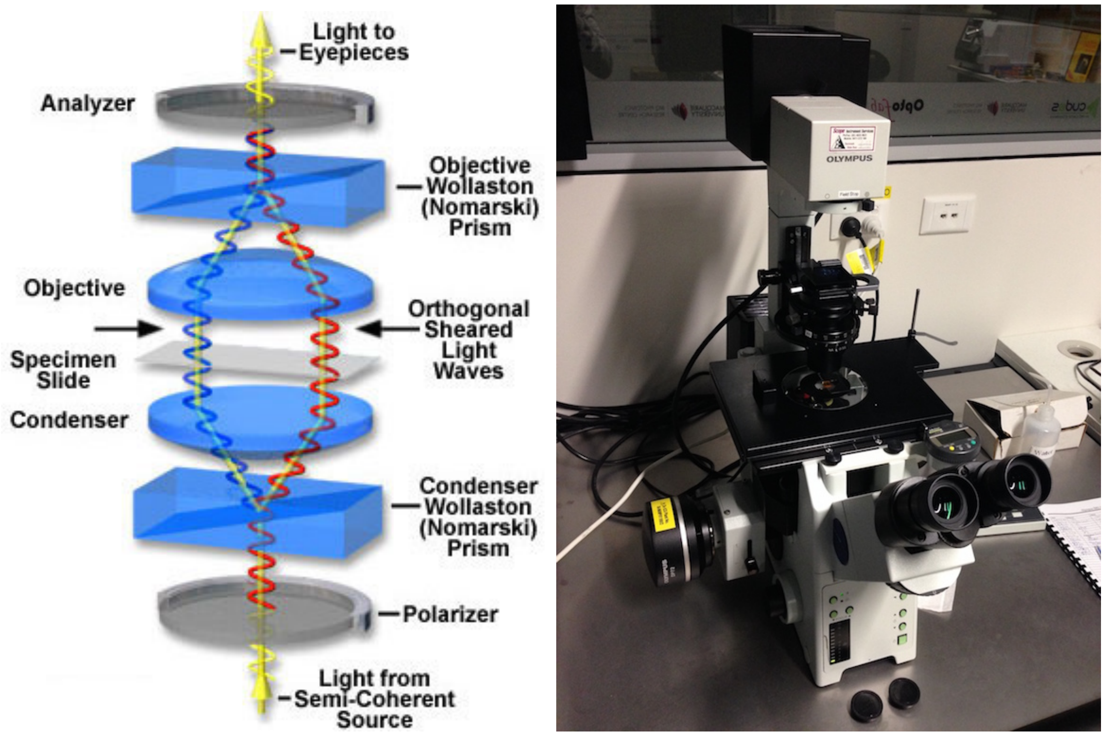


FIGURE 3.6: Left: Differential interference contrast schematic [89]. Right: Olympus IX81 microscope.

appearance of a waveguide is given by bright and dark areas (Fig. 3.7) where its physical parameters can be determined using the accompanying software. Additionally, the perpendicularity of waveguides compared to the sample edge can be measured with an accuracy of $\pm 0.5°$.


FIGURE 3.7: DIC microscope image of waveguides written in GLS glass (top view).

### 3.3.2 Micro-reflectivity

The refractive index of a waveguide can be obtained by measuring the Fresnel reflectivity of an optically polished surface [90]. A 2-dimensional reflectance profile is converted into a refractive index profile using the Fresnel equation (3.2) with $R$ being the reflectance of a local position and $n$ the refractive index,

$$n = \frac{1+\sqrt{R}}{1-\sqrt{R}}\,. \tag{3.2}$$

The experimental setup employs a single-mode fibre-coupled super luminescence diode (SLD, $\lambda = 822$ nm, 20 nm FWHM) with an integrated isolator that prevents back reflections from entering the light source and causing power fluctuations. The output of the SLD is connected to Port 1 of a 50/50 4-port single-mode fiber splitter (Fig. 3.8) and transmitted to Port 2. Light emerging from Port 2 is sent onto a silicon photodiode (PD1). The signal on PD1 is converted to a voltage using a 50 k$\Omega$ variable resistor (PR1) and serves as a reference to

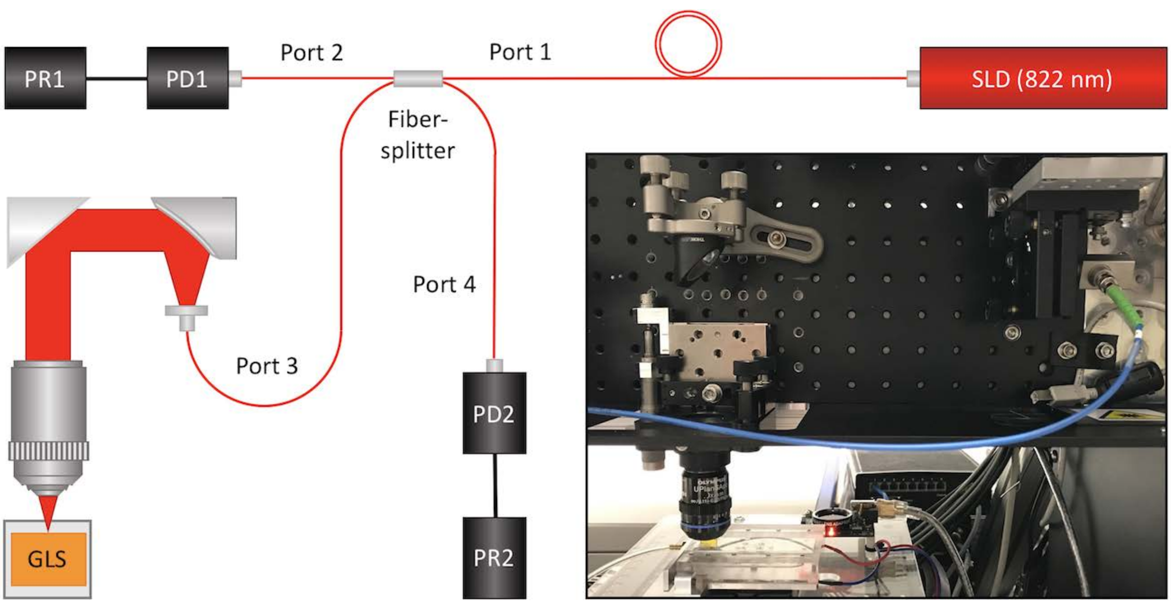


FIGURE 3.8: Micro-reflectivity setup. Light from an SLD is transmitted through a fiber splitter and focused with a microscope objective after collimation. The Fresnel reflection of the glass surface is transported back through the system and converted into a voltage signal with a photodiode (PD2). Changes in local refractive index change are thus recorded as a change in voltage while the sample is scanned. A second photodiode (PD1) monitors the power fluctuation of the source.

monitor power fluctuations of the light source. Light from Port 3 is collimated using an off-axis parabola fibre collimator and directed horizontally to a 90° turning mirror that reflects the light downwards to an Olympus 60× microscope objective (LUCPlanFL N, NA 0.7). A feature of this objective is the large 4.2 mm back aperture that compensates for any drift in pointing that otherwise potentially crops the amount of back reflected light. The 3.5 mm $1/e^2$ diameter Gaussian beam is focused to a spot with a diameter of 1 $\mu$m onto the glass sample. The sample is placed on a tip/tilt adjustable vacuum holder mounted on the same 3-axis air-bearing stage (Aerotech) used for waveguide inscriptions. The reflected light travels back through the objective, the collimator and the fiber splitter and is detected using another identical silicon photo diode (PD2) at Port 4 of the splitter. The generated photo current is then converted to a voltage using a 1 MΩ variable resistor (PR2). All fibre optic connectors in the setup are of APC type to reduce return reflections. The Aerotech A3200 motion controller is used for data acquisition, converting the photo diode signals with 16 bit precision.

To verify the correct operation of the system, a commercial G652D single-mode fiber (unknown manufacturer) with similar standards as an SMF-28e (Corning) and an 8.2 $\mu$m core diameter was scanned (Fig. 3.9). The other end of the fibre was mechanically broken and immersed in an index-matching adhesive to prevent back reflections. Maintaining the focus of the beam on the surface of the sample is challenging but essential for acquiring the correct

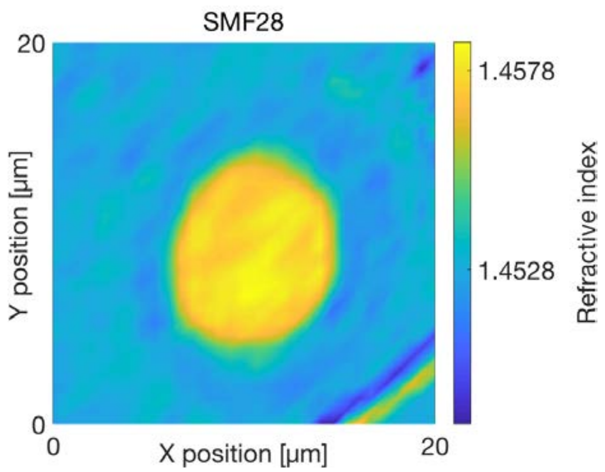


FIGURE 3.9: Micro-reflectivity map of an optical fiber end-face which serves as a reference measurement. The index change $\Delta n = 0.005$ is similar to a Corning SMF-28e.

amount of back reflection [91]. Stage and/or sample tilt can lead to depth variation as well as additionally changing contours of the sample. A coarse depth scan was performed for three corners of the area of interest to determine the slope in the X- and Y-direction. The translation stage followed this slope while mapping an area of 20×20 $\mu$m with ∼650 nm step size. For every spatial point a finer depth scan in the Z-direction was performed with a focusing step size of 150 nm over a 1.5 $\mu$m distance. The highest reflection value was determined by a 4th order polynomial fit through the recorded voltage data (0 - 9 V) of the Z-scan [91]. This approach also efficiently compensates for any temperature-induced mechanical drift over the several hours required to take a two dimensional map. For verification and error analysis, the fiber was moved 62× to a reference point in the bulk between acquisitions with a standard deviation of 0.063%, which is an equivalent to a 32 dB suppression of the fluctuation noise versus the detected signal. Such a high suppression is difficult to obtain but has been demonstrated with $<$ 30 dB [92] and even $<$ 35 dB [91] using very stable LEDs.

The reference scan was set as the value $n = 1.4528$ for the cladding of the fiber and served as a normalising factor. The voltage signal was corrected for SLD fluctuations and converted to a relative refractive index change by using the Equation (3.2). The average refractive index across the fiber core of 1.4578 (Fig 3.9) corresponds to a refractive index difference of $\Delta n = 0.005$ or 0.34%, which closely matches the value of 0.36% obtained from the data sheet of a Corning SMF-28e fiber. This value lies well above the deviation of the reference scans and thus within an acceptable signal-to-noise ratio.

### 3.3.3 Device losses

The amount of light lost in transmission through an optical device is called insertion loss (IL) and gives information about its quality. It is defined as the ratio between the measured power before ($P_{\text{in}}$) the input and at the output ($P_{\text{out}}$) of the device. This value can be expressed in decibels (dB) as

$$\mathrm{IL}_{\mathrm{dB}} = 10 \cdot \log_{10}\left(\frac{P_{\text{out}}}{P_{\text{in}}}\right) . \tag{3.3}$$

Insertion losses can be broken down into three main components: Fresnel (FL), coupling (CL) and propagation losses (PL).

$$\mathrm{IL_{dB}} = \mathrm{FL_{dB}} + \mathrm{CL_{dB}} + \mathrm{PL_{dB}} \,. \tag{3.4}$$

Fresnel losses occur at the end-facets of the device due to different refracting indices of two mediums like glass ($n_{\text{glass}}$) and typically air ($n_{\text{medium}}$) at a specific wavelength.

$$FL_{dB} = 10 \cdot \log_{10}\left[1 - \frac{(n_{\text{glass}} - n_{\text{medium}})^2}{(n_{\text{glass}} + n_{\text{medium}})^2}\right] \,. \tag{3.5}$$

Each GLS - air interface reflects 0.7 dB, or 15.3% of the incident light due to the high index contrast of $n_{\text{glass}} = 2.2832$ [93] and $n_{\text{medium}} = 1$ at 4 $\mu$m wavelength. Additional losses occur when injecting light into a waveguide with mismatching transverse electric fields $E_1$ and $E_2$. This coupling loss can be calculated from the mode overlap integral and has to be considered for each interface.

$$CL_{dB} = -10 \cdot \log_{10}\left[\frac{\left|\int E_1 E_2 \cdot \mathrm{dxdy}\right|^2}{\int {E_1}^2 \cdot \mathrm{dxdy} \int {E_2}^2 \cdot \mathrm{dxdy}}\right] \,. \tag{3.6}$$

The $1/\mathrm{e}^2$ mode-field diameter is extracted by applying a Gaussian fit using a MATLAB script to the recorded frames as part of the Fabry-Perot loss measurement in Section 3.3.4.

The most crucial parameter for an optical device performance is the propagation loss where scattering and absorption attenuate the output signal and decrease the contrast of interferometric circuits. Keeping these losses low is the greatest challenge in femtosecond laser direct-writing. A common method for low refractive index glasses is to record the insertion loss for identical waveguides of different lengths. This can be achieved by either fabricating different waveguides with equal writing conditions or using a long sample that is cut back several times after determining the insertion loss. The only variable is the propagation loss which is derived from the slope of a set of measurements. This method is prone to inaccuracy due to different qualities of the waveguide end-facets and constant realignment of the waveguides leading to insertion errors.

An accurate method for measuring the propagation loss, independent from the coupling efficiency is the Fabry-Perot technique. In particular high refractive index materials form a strong Fabry-Perot cavity due to the air-glass interface at the end-faces of the waveguide, which act like mirrors. Periodically varying the transmittance of monochromatic light results in a fringe pattern with the contrast being a function of propagation loss. The variation can either be achieved by sweeping the wavelength of the laser or changing the length of the waveguides through thermal expansion. As the propagation loss decreases, the fringe contrast increases which, unlike most techniques, improves the accuracy of the measurement. The spectral transmission for coherent light equals [94]

$$T = \gamma \frac{e^{-\alpha \mathrm{L}}\left(1 - R_1\right)\left(1 - R_2\right)}{\left(1 - e^{-\alpha \mathrm{L}}\sqrt{R_1 R_2}\right)^2 + 4\sqrt{R_1 R_2}e^{-\alpha \mathrm{L}}\sin^2\phi} \,, \tag{3.7}$$

where $\gamma$ is the coupling efficiency, $\alpha$ is the propagation loss, $L$ is the length of the sample in cm and $R_1$ and $R_2$ are the end-face reflectivities of the glass. The reflectivity equals the Fresnel reflection as given by Equation (3.5) and the phase delay in the cavity per roundtrip is given by [94]

$$\phi = \frac{2\pi}{\lambda} 2 L N_{\mathrm{eff}} \,, \tag{3.8}$$

where $N_{\mathrm{eff}}$ is the effective index of the mode and $\lambda$ is the wavelength of light. The minimum and maximum intensity transmitted through the glass is used to calculate the fringe contrast [95]

$$K = \frac{I_{\mathrm{max}} - I_{\mathrm{min}}}{I_{\mathrm{max}} + I_{\mathrm{min}}} \,. \tag{3.9}$$

With the fringe contrast one can calculate the propagation loss [94]

$$\alpha\left[\frac{\mathrm{dB}}{\mathrm{cm}}\right] = -\frac{4.34}{L}\ln\frac{1-\sqrt{1-\mathrm{K}^2}}{\mathrm{K}\sqrt{\mathrm{R}_1\mathrm{R}_2}} \,. \tag{3.10}$$

Repeated measurements and measurements at several lengths $L$ give additional precision. The above derivation applies for waveguides perfectly perpendicular to the sample's end-faces. Small angular deviations cause an imperfect back coupling of the mode into the waveguide and results in a decreased fringe contrast and accuracy of the propagation loss measurement. The loss of back-coupled light due to the angular deviation can be calculated from

$$AL_{dB} = 42.8\left(\frac{n\rho}{\lambda}\theta\right)^2 \,, \tag{3.11}$$

where $\lambda$ is the wavelength, $\rho$ is the full-width intensity of the Gaussian mode at $1/\mathrm{e}^2$, $n$ is the refractive index and the angular deviation is $\theta$ in radians. The angular deviation of all fabricated waveguides in this project is measured using the DIC microscope (Section 3.3.1) to be $0°$ with a low resolution of $> 0.5°$. Equation (3.10) therefore gives an upper boundary and thus an overestimated loss value.

### 3.3.4 Fabry-Perot test bed

The propagation loss of single-mode waveguides is measured using the afore described Fabry-Perot method [96, 97]. The requirement is high quality polished end-faces (Sec. 3.1.2) of the GLS samples to achieve a high fringe contrast. In addition, a free space arrangement prevents the formation of external etalons between two flat surfaces that could occur between glass and optical fibers. The test bed (Fig. 3.10) is equipped with a 4 $\mu$m Quantum Cascade laser (Daylight Solutions - 21040) and a 3.39 $\mu$m Helium-Neon laser (REO-4018). Both sources feature a narrow linewidth and as a consequence a long coherence length [98], which makes

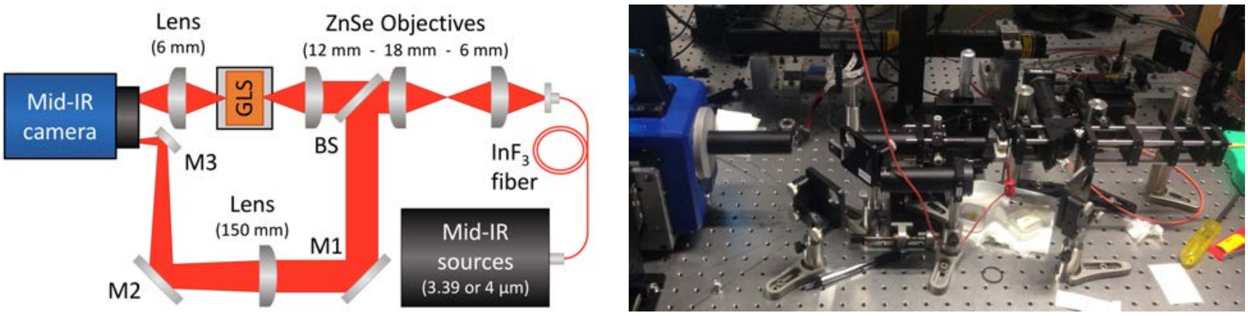


Figure 3.10: Left: Schematic layout of the propagation loss measurement test bed. Monochromatic light of either 3.39 or 4 $\mu$m wavelength is coupled into a GLS single-mode waveguide. The output is monitored and recorded with a mid-infrared camera while the glass is heated. The fringe contrast of the periodically changing transmission is used to precisely derive the propagation loss value. Right: Image of the described Fabry-Perot test-bed.

them ideal for interrogating waveguides.

Either of these sources can be connected to a free-space Thorlabs cage-setup with an indium-fluoride single-mode fibre (Thorlabs - $InF_3$). The setup contains three consecutive zinc-selenide objectives ($ZnSe_{f=6mm}$, $ZnSe_{f=18mm}$ and $ZnSe_{f=12mm}$) to collimate and refocus the light into the glass waveguides. An integrated vacuum chuck on top of a 5-axis stage holds the waveguide sample in place. A wire-wound resistor (5W, 22 $\Omega$) is placed on the top surface of the sample and connected to a power supply providing 5 V and a current of 1 A. A thermally conductive pad is placed in between the sample and the resistor to aid the conduction of heat and expose the glass to $\sim$100°C temperature. This causes the light to travel through a constantly extending waveguide resulting in a sinusoidal power transmittance. The output is imaged with a black diamond lens ($L_{f=6mm}$) onto a mid-infrared indium-antimonide detector (InSb) (FLIR SC7000, 1 - 5 $\mu$m) where 150 frames are recorded. The propagation loss is calculated from the average contrast of successive minima and maxima of the resulting $\sim$6 fringes, each with $\sim$25 data points to provide a high resolution. Each measurement is carried out twice before the sample is cleaned and flipped to launch light into the waveguide in the opposite direction. Presented loss values are the average of four measurements to ensure high reproducibility of the results. A broadband $CaF_2$ beam-splitter plate (BS) is installed before the third objective followed by a plano-convex lens ($L2_{f=150mm}$) and a set of mirrors (M1 - M3) to reflect part of the laser light directly onto a free area on the detector. This reference signal is used to compensate for any laser power fluctuations. A polariser can optionally be inserted before the beam-splitter in order to measure polarisation-dependent losses.

The waveguide mode profile is extracted from the recorded frames which allows for the calculation of the mode-field diameter in the vertical and horizontal direction based on the intensity at $1/e^2$.

### 3.3.5 Spectral response test bed

A second free space setup is assembled to determine the spectral response of Y-splitters and directional couplers (Fig. 3.11). A Tungsten emitter (Thorlabs SLS202, 0.45 - 5.5 $\mu$m) as well as the previously mentioned Helium-Neon laser (REO-4018, 3.39 $\mu$m) form the interrogating light sources. The tungsten source is connected to an indium fluoride ($InF_3$) multimode fiber (0.28 - 4.5 $\mu$m) while the HeNe source is connected to a zirconium fluoride ($ZrF_4$) single-mode fiber (3.2 - 5.5 $\mu$m). Each fiber end is held in a X/Y translation cage mount to align the output to an off-axis parabola (OAP1 and OAP2) with the aid of a shear plate. The advantage of OAPs lies in achromatic collimation from a broadband point source to avoid chromatic dispersion. Both beams are combined in a pellicle beam splitter and simultaneously focused into the glass sample using a calcium-fluoride lens $CaF_{2\,(f=20mm)}$. The output is collimated by a black diamond lens $BD_{2\,(f=6mm)}$. The sample is held vertically

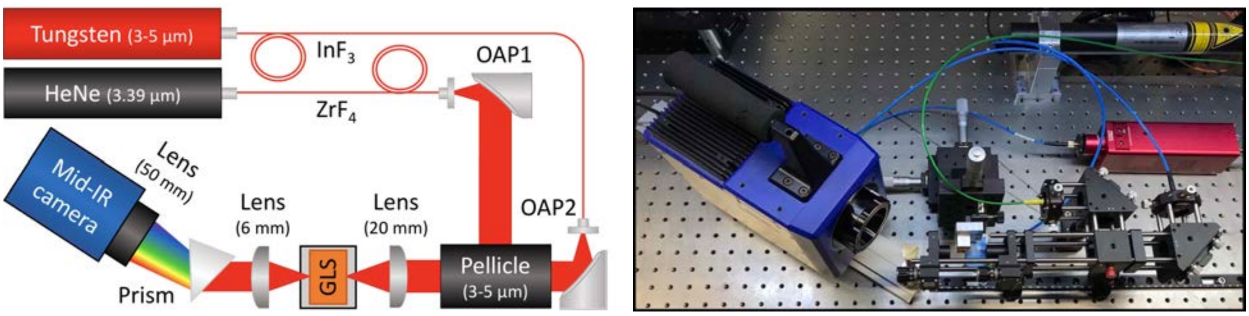


FIGURE 3.11: Left: Broadband measurement test bed. Light from a broadband tungsten and a reference helium-neon source are simultaneously injected into a Y-splitter or directional coupler and the output spatially dispersed. The spectrum of each arm is used to determine the wavelength-dependent power splitting ratio (3.75 - 4.25 $\mu$m). Right: Photo of the used setup.

on a vacuum chuck mounted on a 5-axis stage. This way, the outputs of couplers and Y-junctions run from top to bottom. This allows for the beams to be spectrally dispersed by a triangular CaF prism with an apex angle of 60° without overlapping on the mid-infrared detector (FLIR SC7000, 1 - 5 $\mu$m). The setup is surrounded by 5 mm thick acrylic glass that reduces fluctuations in the thermal background of the measurements. An internal camera function then subtracts remaining background noise before light sources are switched on for each measurement that allows for a SNR of >300. A last background adjustment is performed on the actual measurement to counter stray light. Eight data point in close vicinity to the imaged output are averaged and the value subtracted from each measured pixel. Each of the output powers is then vertically integrated and calibrated using the laser's sharp peak at 3.39 $\mu$m and the atmospheric $CO_2$ absorption dip at 4.26 $\mu$m. Illuminating 46 pixels over this wavelength band gives a spectral resolution of 19.33 nm. The exact sub-pixel position is determined by the peak of a Gaussian and a 4th order polynomial fit, respectively. Afterwards, an extrapolation is applied to provide a total of 1000 data points to resample the outputs over the exact same wavelength grid. Both signals are hereafter overlapped and their splitting ratio left/(left+right) calculated.

## 3.4 Material analysis

The section introduces the methods used to analyse the bulk of GLS glass and the structural changes upon femtosecond laser exposure. A spectrophotometer and FTIR-spectrometer reveal the absorption bands of the bulk glass while Raman spectroscopy is used to uncover material bond changes in inscribed waveguides. To understand ion migration processes, a series of electron probe micro-analysers are used while the refractive index change is determined with a micro-reflectivity setup.

### 3.4.1 Spectrophotometer and FTIR-spectrometer

The transparency of dielectrics is an important parameter that determines whether the material is suitable for femtosecond laser direct-writing at 800 nm and for Raman analysis.

The spectral absorption can be quantified with the aid of a spectrophotometer where light of a known wavelength passes through a material of known thickness and is compared to a reference beam. The Varian Cary 5000 (Fig. 3.12 left) covers the range between 175 - 3300 nm in two different wavelength windows, below 800 nm (UV-Vis) or above (NIR) using different detectors, light source and gratings. A deuterium arc UV source (below 350 nm) and a tungsten halogen visible source with a quartz window are available to either operate with a 1200 lines/mm (UV-Vis) or a 300 lines/mm (NIR) grating to produce monochromatic light. A beam splitting chopper alternately directs the light to the sample or to the reference path by either reflection off a mirrored segment or transmission through the 'gap' segment. A third, matt surface segment is used to block the beam when the grating moves to the next wavelength while simultaneously taking dark measurements. The change in grating causes a step in the absorption data around 800 nm. The sample sits vertically in the beam path (Fig. 3.12 insets) with a 3 mm aperture similar to the reference beam. Both beams are measured with a R928 photomultiplier tube (UV-Vis) detector or a thermo-electrically cooled lead sulphide (PbS) photocell (NIR) and their intensities compared. The resolution is limited to <0.05% for UV-Vis and <0.2% for NIR light.

A Fourier-transform infrared (FTIR) spectrometer Nicolet iS10 from Thermo Scientific (Fig. 3.12 right) is used to measure the spectral absorption in the mid-infrared. A silicon-carbide element emits infrared radiation between 2 - 25 $\mu$m when heated to about 1200 K with

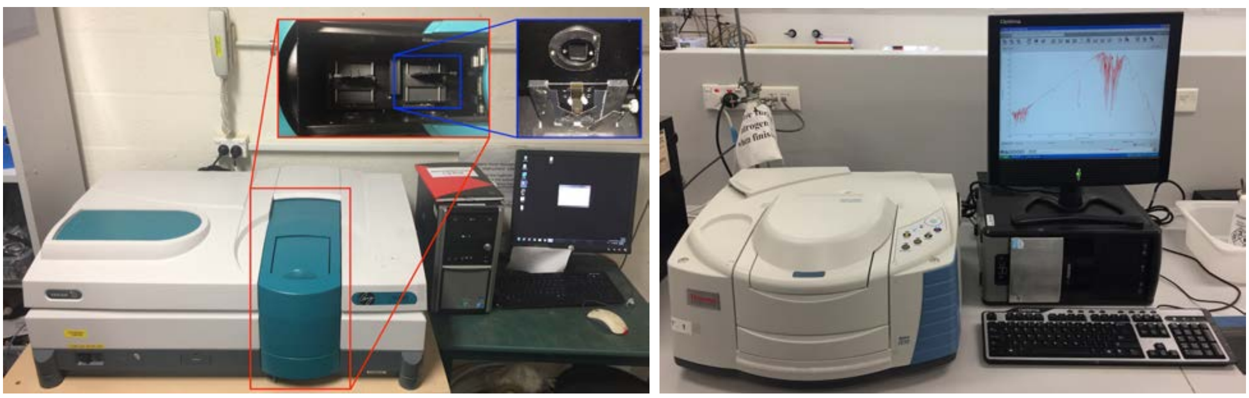

FIGURE 3.12: The Varian Cary 5000 Spectrophotometer (left) is used to determine the transmission spectrum of GLS glass in the visible and near infrared while a Nicolet iS10 Fourier transform infrared spectroscope from Thermo Scientific (right) measures the transmission in the mid-infrared.

a similar output as a blackbody source. The light passes through a Michelson-Interferometer [99, 100] with the resulting interferogram signal accompanied by a reference laser beam. The beams reach the sample that sits vertically in the beam path using the same holder as the spectrophotometer. The form of the interferogram is modulated by absorption bands present in the material which provides a broadband absorption spectrum and uncovers molecules with a dipole moment change. The interferogram is captured by a pyro-electric detector and unravelled using a fast Fourier transform (FFT).

### 3.4.2 Raman spectroscopy

Raman spectroscopy is a non-contact and non-destructive technique that can identify substances and assess crystallinity, stress and orientation by analysing inelastic scattering of laser light. This inelastic scattering was theoretically predicted by Adolf Smekal in 1923 and demonstrated experimentally by Kariamanickam S. Krishnan and Chandrasekhara V. Raman in 1928, where Raman received the Nobel prize for this discovery.

The Raman effect is an inelastic process between photons and molecules that results in a frequency shift of scattered photons [101]. Monochromatic light that is incident on a polarisable molecule induces an electric dipole moment which deforms the molecule. Because of this periodic deformation caused by the oscillating electromagnetic wave, the molecule starts vibrating and is transformed into an oscillating dipole with a certain frequency. If energy from an incident photon is transferred to a molecule in the ground vibrational state, the photon experiences a shift to a lower frequency, called the Stokes frequency (Fig 3.13 left), while the molecule is elevated to higher vibrational state. By contrast, a photon with anti-Stokes frequency gains energy from a higher order vibrational state molecule which shifts its wavelength to a higher frequency and the molecule returns to its ground state. This inelastic process only occurs to a small percentage of the incident light while the majority is scattered in an elastic process (Rayleigh scattering). Rayleigh scattering does not involve energy exchanges and thus the scattered light remains at the same frequency as the incident light.

The Raman spectrum is represented as the intensity of scattered light versus wavenumber, the inverse of wavelength. The Raman shift in wavenumbers can be calculated with

$$\Delta\omega = (\frac{1}{\lambda_0} - \frac{1}{\lambda_1}) \tag{3.12}$$

where $\lambda_0$ is the excitation wavelength, $\lambda_1$ is the Raman wavelength and $\Delta\omega$ is the Raman shift given in $cm^{-1}$ which expresses a value that is independent of the excitation wavelength. The peak position of the Raman shift is associated with a specific vibrational mode of each molecule included in the analysed material and can be seen as a molecular fingerprint. The more crystalline the investigated material is, the narrower the Raman peaks are due to their highly ordered structure. Alternatively, the more amorphous the material is, the broader the peaks are. Raman measurements therefore make it possible to identify the material and structural composition as well as stresses and strains.

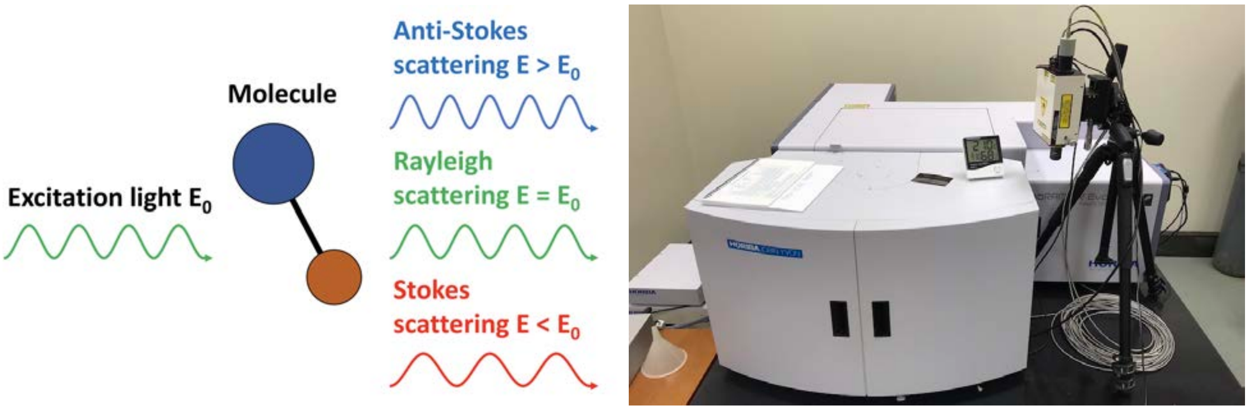


FIGURE 3.13: Left: Raman and Rayleigh scattering of light by molecules. Right: Raman device Horiba Jobin Yvon Labram Evolution.

Raman measurements are taken with a Horiba system (Jobin Yvon Labram Evolution) equipped with four different laser sources (473, 532, 633 and 785 nm). The laser light is internally directed to a motorised 3-axis stage and focussed by one of four different microscope objectives (10×, 20×, 50× and 100×) onto the surface of the sample (Fig. 3.13 right). The backscattered light is passed through a holographic notch filter that removes Rayleigh scattering but allows Stokes and anti-Stokes shifted light to pass. The following spectrometer consists of interchangeable 600 or 1800 groove/mm gratings and a CCD camera. For the purpose of analysing GLS glass, the combination of the 633 nm helium-neon laser, a 100× Olympus objective (MPlanN, 0.9 NA) and the 1800 groove/mm grating gives a spectral resolution of ~0.25 cm$^{-1}$ and a ~1 $\mu$m spatial resolution. The operating software LabSpec6 records dark frames before the initial measurement and adjusts the background automatically. A MATLAB script applies pseudo-Voigt functions to deconvolve the final Raman spectrum into its individual Raman bands. A pseudo-Voigt function is a linear combination of a Gaussian and a Lorentzian function, where both functions share the same peak maximum, peak position and full width at half maximum of the peak (FWHM). Each of the $N$ pseudo-Voigt profiles are weighted by the shape factor $\mu$ (0 - 1) which shifts the profile either to a Gaussian (0) or Lorentzian (1). The recorded Spectrum $I$ is fitted to

$$I_{fit}\left(\nu\right) \;=\; \sum_{n=1}^{N} A_n \,\left(\mu_n \frac{w_n}{\left(\nu-\nu_n\right)^2+w_n^2} + \left(1-\mu_n\right) e^{-ln(2)\cdot(\nu-\nu_n)^2/w_n^2}\right). \tag{3.13}$$

where $\nu$ is the Raman shift, $A_n$ is the amplitude of the Raman band $n$, $w_n$ the half width at half maximum (HWHM) and $\nu_n$ the center position of the Raman mode. The area under a Raman peak is a measure of strength for each individual Raman band and can be calculated by

$$Area \;=\; A_n \,\left(\mu_n \pi w_n + \left(1-\mu_n\right)\, w_n \sqrt{\frac{\pi}{ln\left(2\right)}}\right) \tag{3.14}$$

### 3.4.3 Electron probe micro-analyser

Micro-analysis is used to identify chemical elements within or on the surface of a sample, and their spatial distribution. The electron probe micro-analyser (EPMA) follows the principle of a scanning electron microscope (SEM) and uses a high-energy electron beam to generate X-rays, visible light and secondary electrons upon impact on solid materials. This gives information about fluorescence, the morphology of the investigated material and the

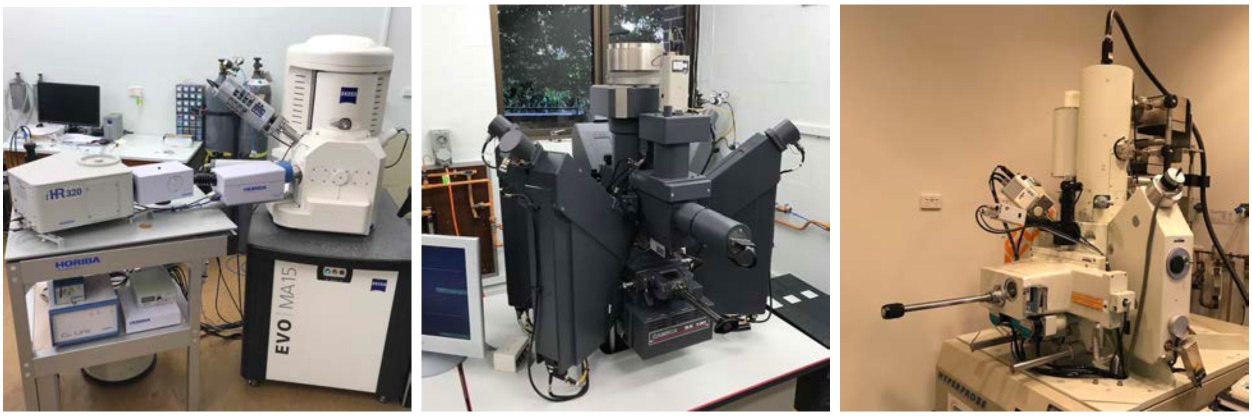


FIGURE 3.14: Devices used to analyse the elemental composition of waveguide cross-sections inscribed in GLS glass. The devices (left to right) are a Zeiss EVO MA15 SEM (with EDS), Cameca SX100 SEM (with WDS) and a Jeol JXA-8500F Hyperprobe (with EDS and WDS).

concentration of elements on a microscopic scale.

The material needs to have a flat and polished surface to avoid impurities that could disturb the electron-sample interaction. Dielectrics are natural insulators and need to be coated with a conducting carbon layer in an evaporative deposition chamber. After the coating, the glass is fixed on a holder and put into electrical contact using conductive tape. This assembly is loaded into a sample chamber of the EPMA with a motorised 3-axis stage and pumped until high vacuum is obtained to prevent interference from contaminative molecules.

Waveguide cross-sections are investigated on three different EPMA devices shown in Figure 3.14. The first device is a Zeiss EVO MA15 SEM equipped with an Oxford Instruments X-Max SDD energy-dispersive spectrograph (EDS). The second device used is a Cameca SX100 EPMA with five different wavelength-dispersive spectrographs (WDS). Each spectrograph holds a different crystal for the detection of different elements. Both the Zeiss and the Cameca use a tungsten filament for generating the electron beam. The last device is a Jeol JXA-8500F Hyperprobe that features both an EDS and WDS. It generates electrons with a field emission gun that offers a smaller beam diameter of ~5 - 25 nm compared to a ~1 $\mu$m diameter of a tungsten filament.

Electrons generated in an EPMA with energies of 5 - 30 keV are condensed and focused through electromagnetic lenses down to the chamber where they impact on the sample surface to produce a variety of signals (Fig. 3.15 right). Electrons are scattered by atoms in an elastic

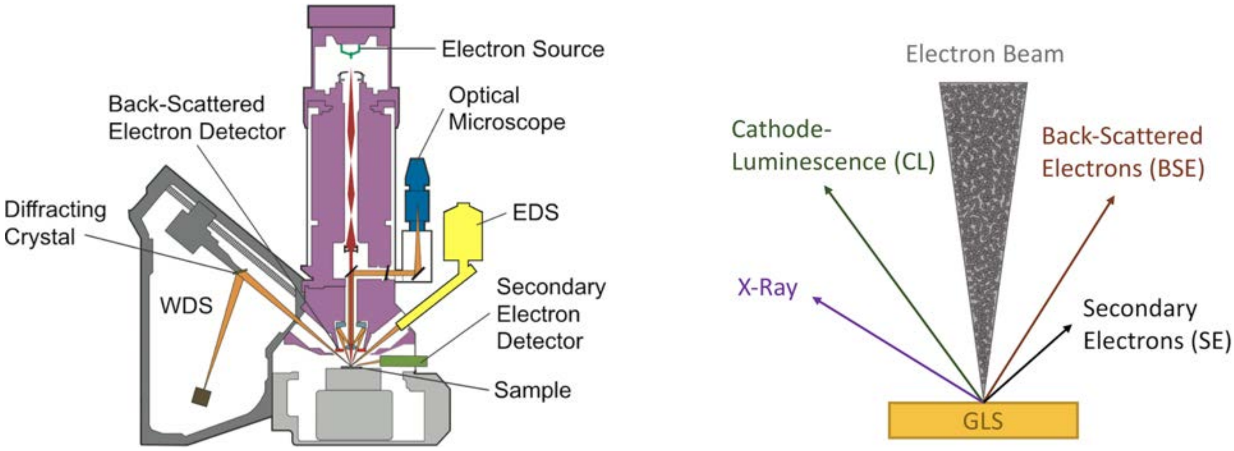


Figure 3.15: Left: Internal setup of an EPMA for detection of back-scattered electrons (BSE), secondary electrons (BSE) and X-rays (EDS and WDS). Right: The electron beam of an electron probe micro-analyser (EPMA) generates a variety of signals upon impact on the investigated material. X-rays are predominantly used to create 2-dimensional elemental maps.

process and measured by an internal back-scattered electron (BSE) detector [102]. The greater the atomic number of an atom the higher the probability of collision with an electron simply due to the larger diameter of that atom. The number of electrons produced during elastic scattering is proportional to the average atomic number of the material. Consequently, a generated compositional map suggests that higher intensities are found in areas with a greater average atomic number and lower intensities for areas with a smaller average atomic number [103].

The electron beam also interacts with electrons of the material in an inelastic process, rather than with the atom. This interaction results in rejection of the negatively charged electrons and deceleration of the incoming electrons from the incident beam. If the energy of an impacting electron is sufficiently large, an electron can be pushed out of the atoms outer electron orbit and overcome the surface energy barrier. These slow moving electrons are called secondary electrons (SE) [104] and are attracted to a positively charged detector. Their primary use is to form topography images of the sample surface.

Inelastic scattering also occurs in discrete orbitals of the atoms. An electron ejected from an inner orbit leaves behind a vacancy that is filled by a higher orbit electron. By returning to a lower energy state, this electron releases excess energy in form of X-ray radiation which is characteristic for each individual element. This radiation is analysed by energy-dispersive

spectrographs (EDS) [105] and wavelength-dispersive spectrographs (WDS) [104].
EDS systems contain an electron trap to ensure only X-rays are directed by a collimator towards a silicon crystal or silicon-drift detector. The detector is cooled with liquid nitrogen to minimise electrical noise. Electron-hole pairs that are created in the detector by the dissipated energy of X-rays move towards electrodes located on the opposite side of the detector. The charge is converted to a voltage signal and processed by a pulse processor that removes noise and discriminates between energies of individual X-rays, even if they arrive simultaneously.
WDS systems use an analytic crystal with a specific lattice spacing to direct X-rays generated on the sample's surface to a gas proportional counter. X-rays that encounter the analytic crystal are reflected according to Bragg's law. The law determines the incident angle for X-rays of one particular wavelength that is reflected onto the detector. Consequently, only one wavelength and its corresponding element can be detected at a time but can be altered by changing the angle of the crystal relative to the sample. Since the sample and the analytical crystal are fixed in their constellation for each element, the gas detector needs to be moved in order to capture the reflected X-rays. An incoming photon ionises the gas and produces an electron avalanche which results in a countable current pulse on an axial anode.
Typically, both spectrographs, EDS and WDS, are found in an EPMA connected via long tubes, and are meant to complement each other. EDS is usually used for quick elemental scans and the findings are used to calibrate the WDS. The WDS achieves a more precise chemical analysis due to a significantly higher peak resolution. The detection limit for a WDS is typically 50 - 100 ppm for quantitative analyses with an accuracy in the order of 1%.

# 4

# Optical waveguides

This chapter leads in with a review of femtosecond laser direct-writing (FLDW) in mid-infrared chalcogenide glasses using different fabrication regimes and geometries. Next, a summary is provided for the work undertaken in developing near-infrared optical waveguides in GLS during my Master of Science degree. The main objective of this chapter, however, lies in the development of low-loss single-mode optical waveguides in GLS glass for the mid-infrared wavelength range. Multiscan waveguides in the athermal regime and cumulative heating waveguides in the thermal regime are contrasted against each other. For the theoretical background of optical waveguides, please refer to established reference books such as [106] and [107].

Optical waveguides for the mid-infrared wavelength range are the basis of the proposed integrated photonic nulling interferometer for the astronomical L-band. Although it is possible to produce excellent low-loss waveguides in the visible and near-infrared range with FLDW [85, 108], the mid-infrared region still lags behind. To be compatible with on-sky operations, optical waveguides need to feature a high refractive index contrast to prevent bending losses, round mode-fields for a high coupling efficiency and low intrinsic losses. Different materials have been investigated from crystalline $Bi_4Ge_3O_{12}$ [109] and lithium niobate [110] to amorphous materials such as fluoride [43] and chalcogenide glasses [111] with some more and some less promising results. The response of each individual glass to the focused femtosecond laser pulses determines the ideal waveguide geometry. A common differentiation between FLDW waveguides in glass or crystals is simply called Type I and Type II [112]. These terms were originally established by Archambault *et al.* [113] for the classification of fiber Bragg gratings fabricated with a low and a high index contrast. The adaptation into FLDW however led to several new interpretations of the two types. Most authors refer to Type I as waveguides with a purely positive refractive index change while they refer to Type II as stress waveguides. Even a third, Type III, was introduced to cover negative refractive index changes in the form of depressed cladding waveguides [114]. Other authors have since reduced the definition of Type I to a positive and Type II to a negative refractive index change [115]. An interesting discussion about the definition of different types is given by Gross *et al.* [116].

However, in terms of waveguide geometry it is important to first identify whether the refractive index change induced is positive or negative. Furthermore, the shape can be correlated with the refractive index of the glass where high refractive index glasses tend to form asymmetric shapes due to spherical aberations [117]. An extension for the classification of waveguide structures was presented by Arriola *et al.* [39] on glasses suitable for mid-infrared waveguide inscriptions. The most common approaches are illustrated in Figure 4.1.

The top row is associated with a positive index change. P1 refers to a single scan modification most commonly fabricated in the thermal regime or by using beam-shaping methods in the athermal regime. P2 shows the extension of the core around the center and can be divided into modifications that are either separated (expanded core) [118, 119] or overlapped (rosette

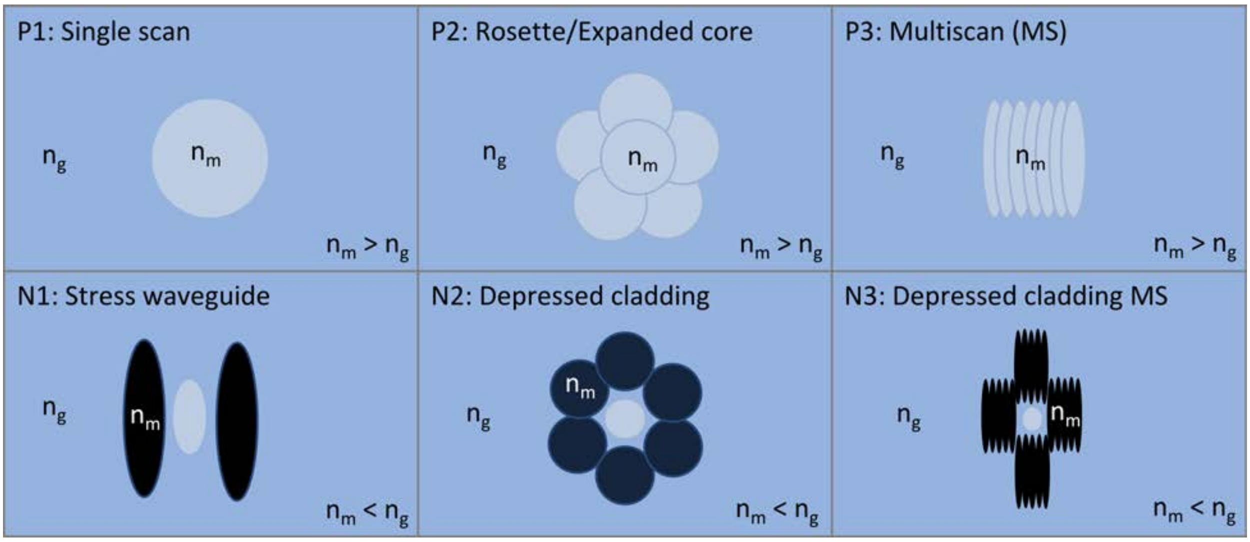


FIGURE 4.1: The applicable waveguide geometry depends on the material and its response to the irradiating laser. The change in refractive index $n_m$ can be positive (P1 - P3) as well as negative (N1 - N3) compared to the refractive index of the surrounding bulk glass. These changes are independent from the thermal or athermal writing regime. Image courtesy of [39].

pattern). P3 combines multiple overlapping modifications in one dimension fabricated using the athermal regime also known as the multiscan technique [83].

The bottom row of Figure 4.1 shows geometries for cases where the refractive index change of the glass is negative. N1 is known as a stress waveguide [120, 121] and consists of two tracks that create a stress-induced higher refractive index region between them. N2 and N3 are called depressed cladding waveguides where a series of negative refractive index modifications surrounds an unmodified core region. This can either be achieved using single scans, a rosette pattern in the thermal regime (N2) [43] or by using the multiscan technique in the athermal regime (N3).

Positive refractive index modifications usually exhibit shorter fabrication times compared to negative refractive index-based waveguides because less material has to be exposed to the femtosecond laser. Additionally, it is challenging to design couplers and hence an interferometric device using depressed cladding waveguides due to their complex design.

Chalcogenide glasses are the most promising material for mid-infrared photonics due to their compatibility with FLDW and their high transmission at longer wavelengths. This class of glasses consists of at least one element of the 16th group of the periodic table: either sulphur, selenium or tellurium [122]. These elements can be covalently bonded to network former such as As, Ge, Sb, Ga, Si or P to enable a wide range of possible stoichiometries. Early work on thermal waveguide inscriptions started with bulk glass and thin films of arsenic selenide ($As_2Se_3$) [123], arsenic sulphide ($As_2S_3$) [124] and a combination of both ($As_{40}S_{30}Se_{30}$, $As_{24}S_{38}Se_{38}$) [123]. The observed positive refractive index changes ranged from weak to strong in the order of $10^{-4}$ - $10^{-2}$ [124, 125]. Other authors found a high positive refractive index change in the center of $As_2S_3$ waveguides and an even higher negative refractive index region surrounding the core [126]. The introduction of additional germanium to sulphur-based glasses has shown to influence the magnitude but also the sign of the refractive index change and allows tailoring of these parameters by varying the content [115, 127, 128]. Replacing the toxic component arsenic with gallium led to one of the most researched chalcogenide glasses: gallium lanthanum sulphide.

As of early of 2016 at the beginning of this project, the lowest reported propagation loss for FLDW mid-infrared waveguides was 0.8 dB/cm [129] at 3.39 $\mu$m in GLS with slightly elliptical mode profiles. An elliptical mode profile causes coupling losses when light is coupled into the chip from round apertures such as the primary mirror of a telescope. Moreover, the low propagation loss value is still relatively high for waveguides as a base for astrophotonic devices with the intention of on-sky operation.

The lowest propagation loss for FLDW waveguides was achieved in zirconium fluoride glass (ZBLAN, $ZrF_4$-$BaF_2$-$LaF_3$-$AlF_3$-NaF) with 0.29 dB/cm at 4 $\mu$m [43]. However, a weak negative refractive index change of the depressed cladding waveguides (N2) led to large mode-field diameters of $\sim$60 $\mu$m causing immense coupling losses between the chip and optical fibers.

GLS responds with a positive refractive index change to femtosecond laser irradiation and was studied using cumulative heating (P1) in the thermal regime as well as applying the multiscan technique (P3) and the slit beam-shaping (P1) in the athermal regime [117]. GLS optical waveguides have a high potential to be further improved and used as a platform for mid-infrared photonics. This work is summarised in the next sections.

## 4.1 Previous near-infrared study on GLS glass

The preceding work of my six month Master of Sciences thesis project provided a me with a background of femtosecond laser direct-writing in GLS glass. During this time, I studied the inscription of single-mode waveguides for the near-infrared wavelength range at 1.55 $\mu$m. The thermal and athermal regimes were explored for laser repetition rates between 1 kHz and 5.1 MHz. Three different techniques were exploited to fabricate waveguides: cumulative heating in the thermal regime and both multiscan and slit beam-shaping in the athermal regime. The inscribed structures were characterised for their physical shape and size, refractive index change, mode-field diameters and their propagation loss. A brief summary about this work is given below whereas more details can be found in [117]. Table 4.1 provides a comparison of the individual inscription techniques suitable for waveguide fabrication in GLS and highlights their advantages and disadvantages.

The slit beam-shaping in the athermal regime created strong Kerr self-focusing induced filaments for short femtosecond laser pulses. By stretching the pulse to 1.5 ps, circular waveguide structures were achieved with a single scan (Fig. 4.2 right). Multiple overpasses of the same waveguide improved the refractive index contrast up to $\Delta n = 0.006 \pm 0.001$, an approximation based on the Petermann formula [130] rather than a direct measurement. This simultaneously reduced the mode-field diameter (MFD) to $8.3 \pm 0.8$ $\mu$m at 1.55 $\mu$m which

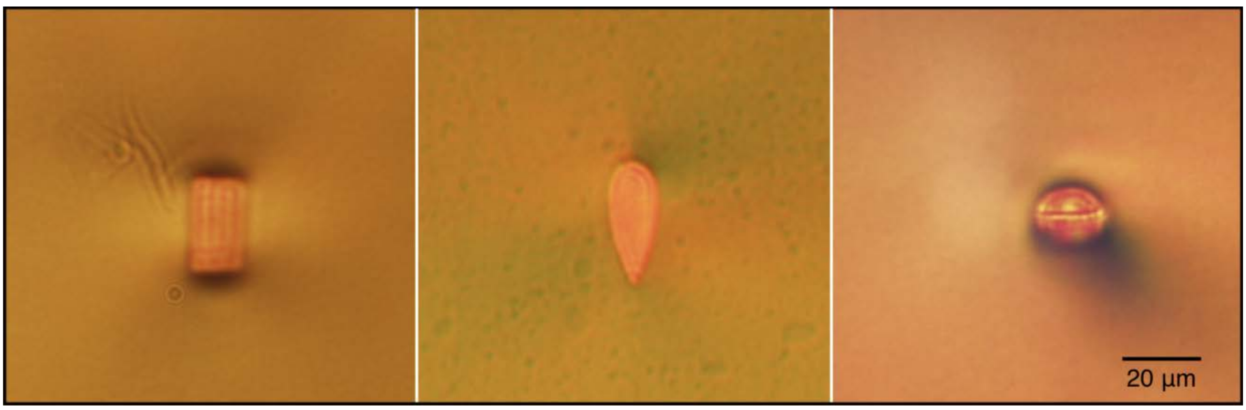


FIGURE 4.2: Bright-field images of multiscan, cumulative heating and slit beam-shaping waveguides (left to right).

| | **Thermal** | **Athermal** | |
|---|---|---|---|
| | **Cumulative heating** | **Slit beam-shaping** | **Multiscan** |
| Index contrast Δn | 0.005 ± 0.001 | 0.006 ± 0.001 | 0.004 ± 0.001 |
| Mode-field diameter (at 1.55 $\mu$m) | 9.3 ± 0.8 $\mu$m | 8.3 ± 0.8 $\mu$m | 10.1 ± 0.8 $\mu$m |
| Propagation loss | 1.82 ± 0.07 dB/cm | 2.01 ± 0.12 dB/cm | 2.56 ± 0.09 dB/cm |
| Flexibility in size and shape | average | average | high |
| Fabrication velocity | high | low | average |
| Susceptibility to Kerr non-linearity | low | high | low |

TABLE 4.1: Comparison between three different techniques for waveguide inscription in GLS glass.

is significantly smaller compared to a standard Corning SMF-28 with an MFD of 10.4 $\mu$m for the same wavelength. The lowest propagation loss was found to be 2.01 ± 0.12 dB/cm, measured on a free space Fabry-Perot test bed. For this technique, the waveguide size is dependent on the focusing conditions. Accordingly, it requires lower NA focusing and thus high peak intensities to enable the formation of waveguide cross-sections large enough to guide light in the mid-infrared wavelength range. This increases the Kerr self-focusing effect and makes waveguide inscription using the slit beam-shaping technique challenging and less suitable for exploring the fabrication of mid-infrared waveguides in GLS.

The athermal multiscan technique on the other hand offers great control over the waveguide size in terms of width and height. The width is easily controlled by the amount of laterally-stacked waveguide tracks while the height is controlled by a combination of inscription pulse energy and translation velocity, resulting in a rectangular shape (Fig. 4.2 left). This technique enables the use of high NA objectives (Olympus Plan N 100×, NA 1.25) and femtosecond laser pulses that in turn reduce the event of Kerr self-focusing. It was found that increasing the laser repetition rate from 255 kHz to 1020 kHz decreased the propagation loss to 2.56 ± 0.09 dB/cm. A waveguide MFD as small as 10.1 ± 0.8 $\mu$m was found and a lower refractive index contrast of $\Delta n = 0.004 \pm 0.001$ compared to the slit beam-shaping waveguides (Tab. 4.1).

Finally, a high repetition rate of 5.1 MHz was applied to fabricate waveguides in the thermal regime using a high NA objectives (Olympus Plan N 100×, NA 1.25). The shape resembles an inverted teardrop (Fig. 4.2 center) attributed to spherical aberrations. The waveguide size is controlled by the pulse energy and/or translation velocity, but always features an asymmetric waveguide shape. This leads to rather elliptical mode profiles with the smallest average diameter being 9.3 ± 0.8 $\mu$m with a corresponding index contrast of $\Delta n$ = 0.005 ± 0.001. The lowest propagation loss of 1.82 ± 0.07 dB/cm was found for the lowest translation velocity of 100 mm/min in combination with the highest pulse energy possible before exceeding the waveguide size for single-mode behaviour. The thermal regime thus features the lowest propagation loss waveguides with the shortest fabrication time. Moreover, the thermal regime is less susceptible for Kerr self-focusing compared to slit beam-shaping technique in the athermal regime.

## 4.2 Mid-infrared optical waveguides in GLS

The previous section has shown that the slit beam-shaping method introduces Kerr nonlinearity effects that intensify with lower NA objectives. Lower NA objectives however are required to increase the cross-section of the waveguides in order to guide light in the mid-infrared wavelength range. As a result, and due to the excessive fabrication time, the study using the slit beam-shaping technique was not extended in this thesis.

Waveguides were fabricated on the mode-locked Ti:sapphire femtosecond oscillator inscription facility introduced in Section 3.2. The laser emits pulses of $<$ 50 fs at a wavelength of 800 nm with an average output power of 2.4 W. An oil immersion objective with an effective NA of 0.9 was used to focus the laser pulses 180 $\mu$m below the surface of the glass chip. Inscriptions in the thermal regime using high repetition rates are contrasted in terms of propagation loss and mode-profiles against waveguides fabricated in the athermal regime using low repetition rates.

### 4.2.1 Athermal fabrication regime - multiscan technique

The multiscan technique (Sec. 2.4.2) in the athermal regime [85] was investigated using four different repetition rates: 425, 510, 728 and 1020 kHz. Each repetition rate was studied with pulse energies varying from 30 to 120 nJ and translation stage velocities between 100 and 1125 mm/min. Each waveguide consists of 15 individual tracks across the sample, each with a transversal offset of 400 nm. This created a 6 $\mu$m wide structure similar to previous multiscan studies in GLS glass [129]. Sample translation velocities were chosen between 100 - 1025 mm/min to ensure similar pulse densities (41, 61, 122 and 255 pulses/$\mu$m) for all laser repetition rates. The use of higher pulse energies was enabled for the fabrication of single-mode waveguides by lowering the repetition rate. This led to Kerr self-focusing which created largely elongated cross-sections (Fig. 4.3).

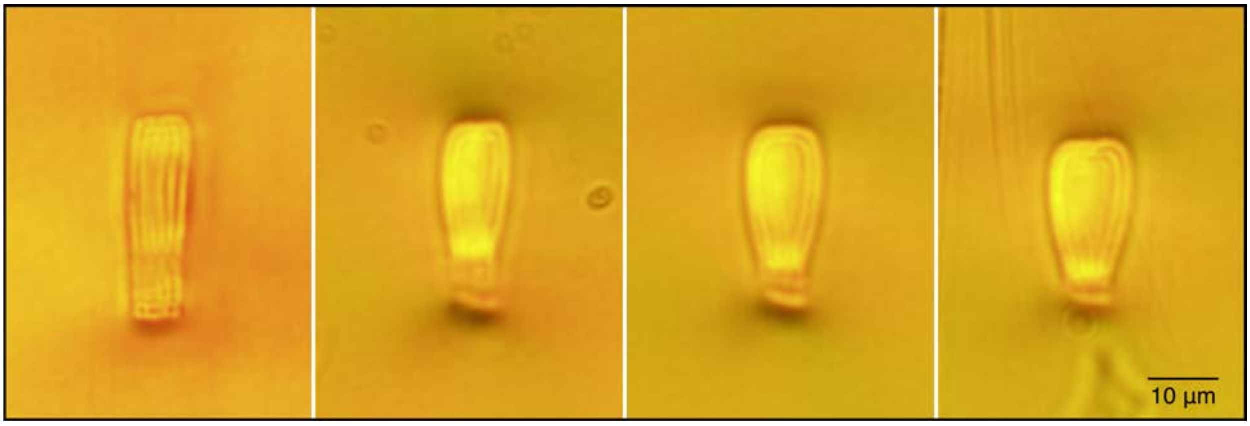


FIGURE 4.3: Images of the lowest loss multiscan waveguides each fabricated at a different repetition rate: 425, 510, 728 and 1020 kHz (left to right). Each waveguide consists of 15 partially overlapping tracks. A growing heat diffusion effect with increasing repetition rate but similar pulse density can be observed.

The mode-field diameter (MFD) of each inscription was determined at 3.39 $\mu$m wavelength and is illustrated in Figure 4.4. The increase in repetition rate from 425 to 1020 kHz led to a general decrease in average mode-field diameters. Furthermore, increasing the pulse energy at each repetition rate slightly increased the waveguide cross-section in the vertical dimension. The higher pulse energies caused a higher refractive index change that in turn reduced the size of the guided mode. The general trend showed an additional decrease in

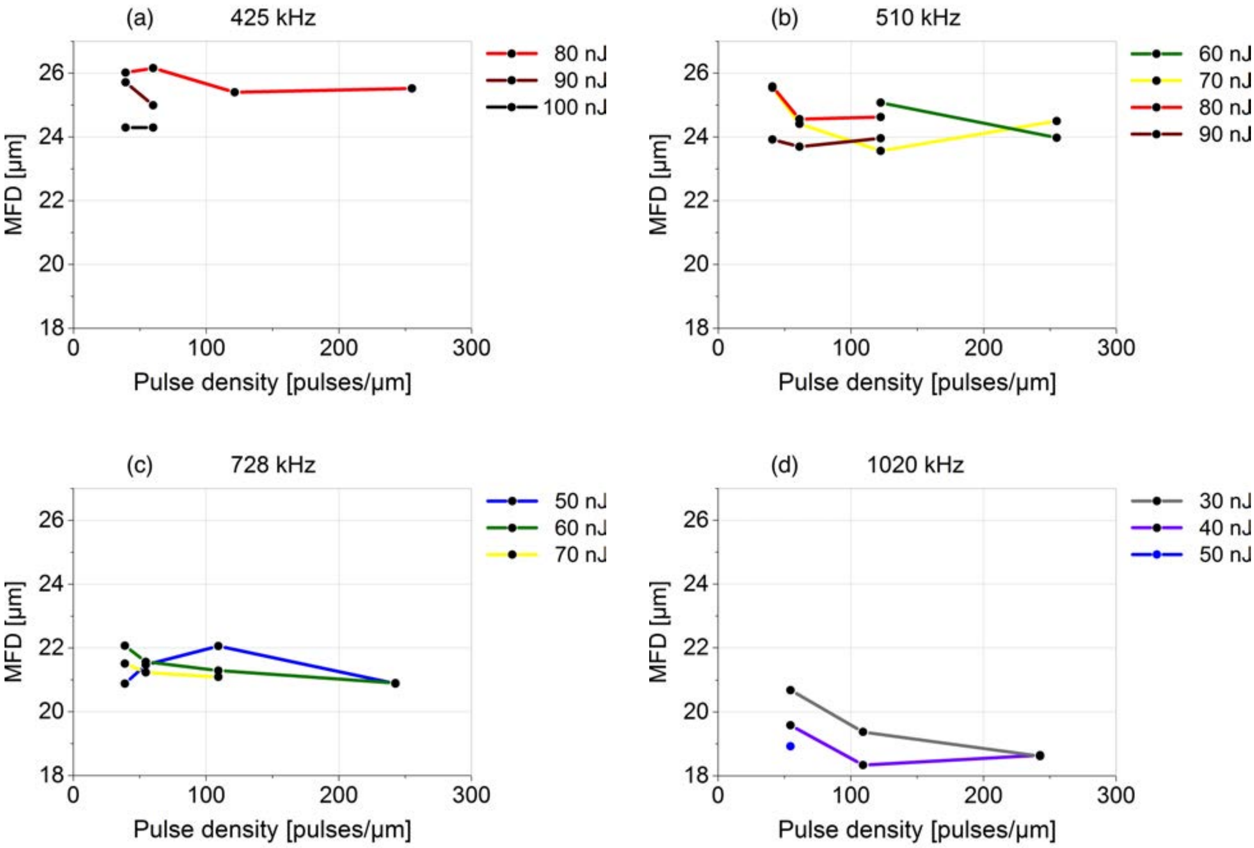


Figure 4.4: Mode-field diameters at 3.39 $\mu$m for sets of multiscan waveguides fabricated between 30 and 120 nJ with 10 nJ pulse energy increments at repetition rates of 425, 510, 728 and 1020 kHz. The smallest mode-field diameter of 18.3 $\mu$m was found for the highest repetition rate 1020 kHz and 40 nJ pulse energy.

mode-field diameter for higher pulse densities.

The smallest MFD of 18.3 $\mu$m was found for the waveguide inscribed with a repetition rate of 1020 kHz and a pulse energy of 40 nJ. This waveguide showed a much higher mode-confinement than waveguides reported for 3.39 $\mu$m with an average MFD of 24.5 $\mu$m [129] and 25.4 $\mu$m [131]. Both authors used the same multiscan approach in GLS glass with the difference that a repetition rate of 500 kHz was applied, rather than 1020 kHz. This in turn is consistent with the measurements in Figure 4.4(b) where similar mode-field diameters are shown.

The propagation loss for each multiscan waveguide was measured on the Fabry-Perot test bed at 3.39 $\mu$m wavelength. The measurements showed that the lowest propagation loss for each repetition rate (425, 510, 728 and 1020 kHz) was achieved with the highest pulse density and pulse energy (Fig. 4.5). Comparing waveguides fabricated with the same pulse density and pulse energy, a reduction in propagation loss can be seen when increasing the repetition rate (e.g. the same colour coded graphs in Fig. 4.5).

This observation implies that at even higher repetition rates lower pulse energies can be applied that potentially lead to a lower propagation loss. The cross-sections of the lowest

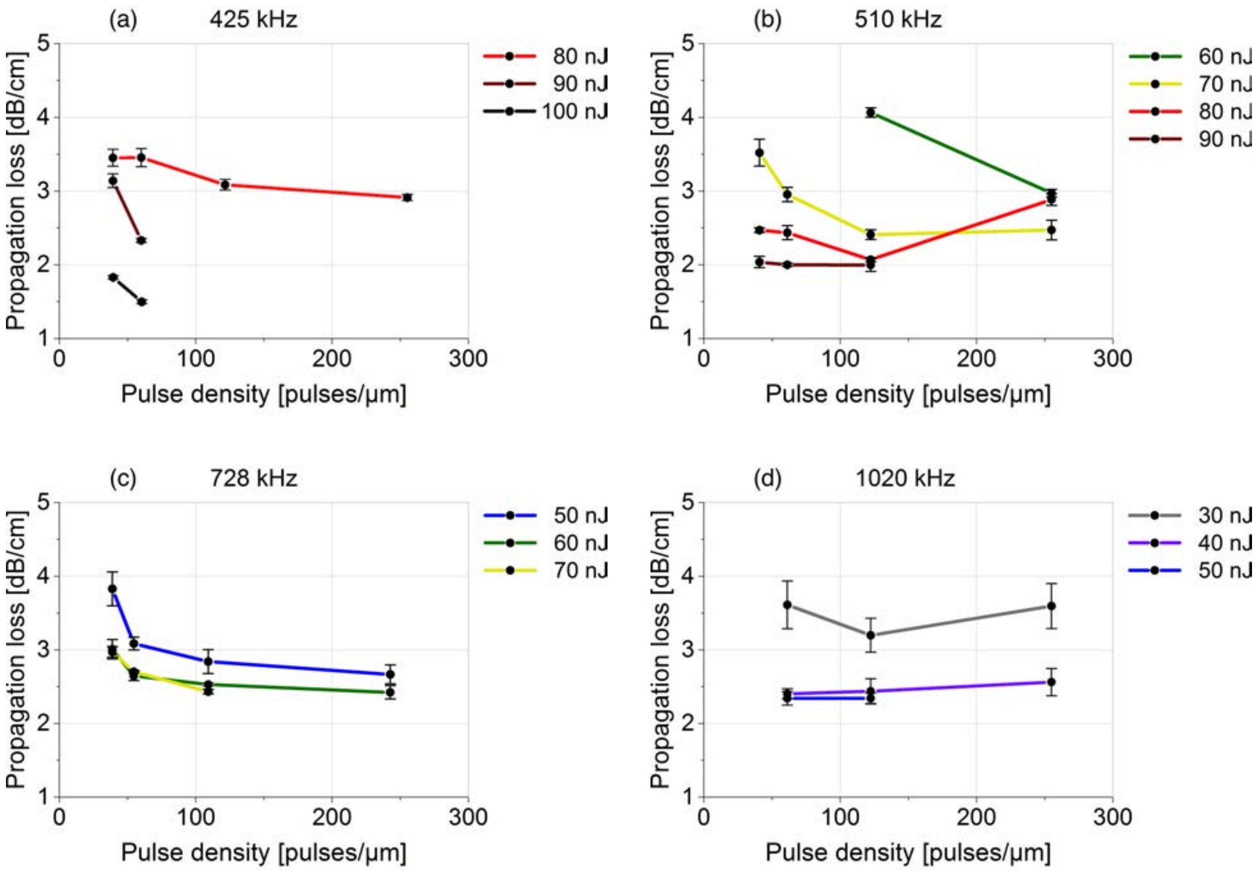


FIGURE 4.5: Multiscan waveguides at repetition rates of 425, 510, 728 and 1020 kHz were investigated for their propagation loss. The lowest propagation loss of 1.5 ± 0.03 dB/cm was found for the lowest repetition rate 425 kHz and 100 nJ pulse energy.

propagation loss waveguide at each repetition rate are shown in Figure 4.3. The cross-sections underpin the growing heat diffusion effect, distinguishable by an expanding teardrop-shape for increasing repetition rates (left to right). While waveguides inscribed with 425 kHz appear to be created strictly in the athermal regime, waveguides inscribed with higher repetition rates show contribution of cumulative heating. The increase in repetition rate led to a greater deposition of energy inside the glass per unit time and thus stronger thermal diffusion where an intermediate state between a purely athermal modification and cumulative heating was reached. Cross-sections with a small contribution of cumulative heating were also shown in GLS multiscan waveguides [129] inscribed with 500 kHz and 31 - 250 pulses/$\mu$m. Their shape and physical size in the vertical and horizontal is very similar to the demonstrated waveguides in this work inscribed with 510 kHz, 41 - 255 pulses/$\mu$m and similar pulse energies. This implies that eightfold longer pulses of 400 fs and the longer wavelength of 1030 nm of the inscribing laser has only little influence on the structure and the cumulative heating contribution.

The lowest propagation loss of 1.5 $\pm$ 0.03 dB/cm was found for the strictly athermally inscribed waveguide at 425 kHz with 100 nJ and 61 pulses/$\mu$m and a relatively large MFD of 24.3 $\mu$m. This highlights the fact that a smaller MFD is not correlated with a lower propagation loss whereas a stronger confinement could have been expected. The propagation loss was remeasured for this waveguide with a polariser inserted into the beam path before the light injection. A polarisation dependent loss (PDL) of 0.24 $\pm$ 0.02 dB/cm was found with a higher loss for horizontally polarised light. This technique is inherently prone to PDL [54, 132] due to the nature of the multiple scan fabrication that results in an inconsistently smooth refractive index change throughout the waveguide.

Inscription parameters below a 425 kHz repetition rate were tested but resulted in weak modifications of the glass and were therefore insufficient to guide light at 3.39 $\mu$m. Waveguides fabricated with pulse energies larger than 50, 70, 90 and 100 nJ for 1020, 728, 510 and 425 kHz, respectively, supported more than one mode in the vertical dimension at 3.39 $\mu$m. The positive correlation between the decrease in propagation loss and an escalating cumulative heating effect due to the higher energy deposition inside the glass will be further examined in the next section.

### 4.2.2 Thermal fabrication regime - cumulative heating

The thermal regime was explored for the fabrication of cumulative heating waveguides in order to allow heat diffusion to be the predominant source of material index change. To reach the cumulative heating regime, higher repetition rates are required as demonstrated numerically and experimentally by Eaton *et al.* [133]. The advantage of heat accumulation effects are to allow for the formation of more symmetrical optical waveguides [79, 134].

Both McCarthy *et al.* [135] and Hughes *et al.* [56] demonstrated waveguides in GLS fabricated in the thermal regime with a teardrop-shaped cross-section. Two distinct regions were determined: a dark inner core and a surrounding positive outer shell. This generated an overall positive refractive index change compared to the bulk of the material and allowed the guidance of the fundamental mode to span across the entire structure. The teardrop-shape can be attributed to the nonlinear absorption of the femtosecond laser pulses in the elongated region along the irradiated axis caused by spherical aberrations. The internal melting of the glass due to cumulative heating was investigated in more detail by Miyamoto *et al.* [136] as well as Hughes *et al.* [137]. Interestingly, McCarthy *et al.* used similar laser parameters for their inscriptions as well as pulse energies and the same repetition rate of 500 kHz as previously used by Arriola *et al.* [129] and Tepper *et al.* [131] for the athermal regime. The main difference that led to the purely thermal regime was the 10 - 20× lower translation velocity that allowed for applying 625 - 2500 pulses/$\mu$m.

In order to apply higher translation stage velocities for faster fabrication times, a higher repetition rate can be applied. Here, the laser's initial repetition rate of 5.1 MHz was utilised for waveguide inscription compared to the lower kHz-regime associated with the multiscan technique. This parameters enabled a pulse density of 3060 pulses/$\mu$m. The translation velocity was set to 100 mm/min which lead to the best results in the previous GLS studies for the near-infrared wavelength range, summarised in Section 4.1.

Applying pulse energies between 8 and 13 nJ resulted in single track waveguides with a width of 5.5 to 9.8 $\mu$m at a depth of 180 $\mu$m below the surface of the glass. Even though the focusing objective was immersed in oil ($n$ = 1.518) during fabrication, the high refractive index difference compared to GLS at 800 nm ($n$ = 2.3931) led to spherical aberrations and thus to teardrop-shaped waveguides (Fig. 4.6 right). The waveguide width was found to be the benchmark in order to precisely replicate mode-field values and the propagation loss. The lowest propagation loss of 0.47 ± 0.01 dB/cm was found for a waveguide width of 7.5 $\mu$m at 3.39 $\mu$m (Fig. 4.6 left). The corresponding mode-field dimension of 22.9×24.7 $\mu$m ± 0.1 $\mu$m featured an elliptical shape. The lowest propagation loss of any multiscan waveguide fabricated in this work however only exhibited a minimum propagation loss of 1.5 ± 0.03 dB/cm at 3.39 $\mu$m even though it featured similar physical and mode-field dimensions in the vertical and horizontal like the single cumulative heating modification.

The entire set of single modifications showed an asymmetric physical aspect ratio of approximately 1:2.5 in the horizontal:vertical that caused elliptical mode-field diameter ratios of 0.83 - 0.93. This asymmetry potentially increases bending losses for curved waveguides and causes coupling losses from round apertures.

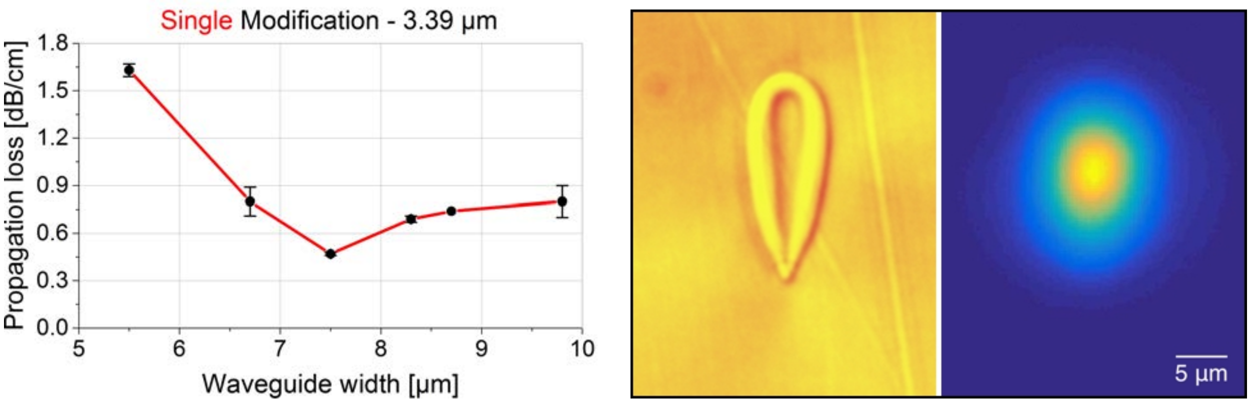


Figure 4.6: Propagation losses at 3.39 $\mu$m wavelength for waveguides with a certain structure width fabricated in the thermal regime (left). These loss values are significantly lower compared to those of waveguides fabricated with the multiscan method. A 7.5 $\mu$m waveguide width offers the lowest propagation loss with 0.47 ± 0.01 dB/cm. The corresponding teardrop-shaped cross-section features an elliptical mode profile (right).

The waveguide core was therefore extended in the horizontal dimension by adding an adjacent waveguide track. A set of nine waveguides was inscribed, where each waveguide consisted of two tracks with different separations. The inscription parameters were chosen to be the same as the lowest propagation loss single-track waveguide with a 7.5 $\mu$m width. A further reduction in propagation loss for a wide range of different waveguide widths was found, illustrated in Figure 4.7 (left). These loss values remained consistently low for structure widths between 11.6 $\mu$m and ~15 $\mu$m, where the two parallel inscribed tracks stopped overlapping. The reduced refractive index contrast and imperfect guidance due to the unmodified center region between the tracks likely contributed to a higher propagation loss. The lowest propagation loss value of 0.33 ± 0.02 dB/cm was obtained for a waveguide with a 12.3 $\mu$m width where the shell regions of both tracks perfectly overlapped. The mode-field of this waveguide showed a strong confinement but still slightly elliptical diameters 19.7×22.1 $\mu$m ± 0.1 $\mu$m in the horizontal and vertical direction (Fig. 4.7 right).

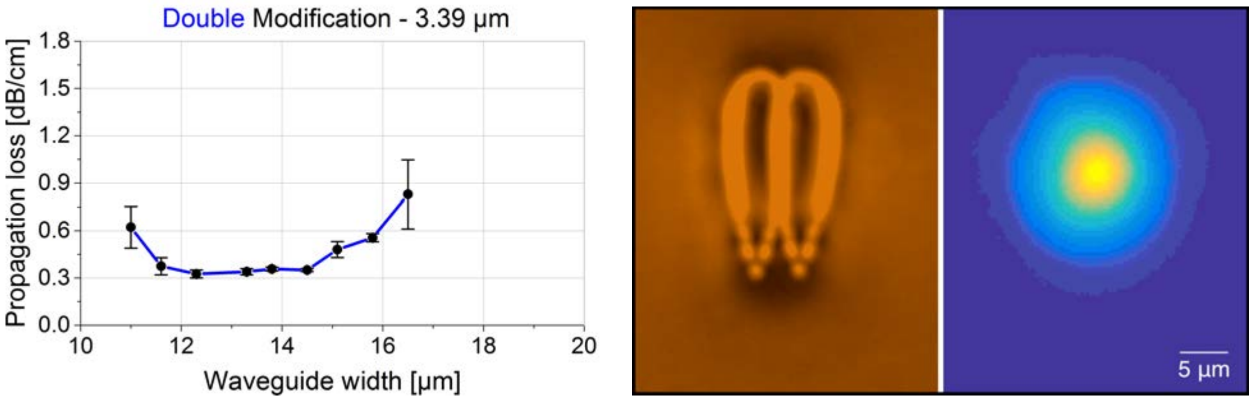


FIGURE 4.7: Double modifications with two adjacent tracks were inscribed with different separations to extend the waveguide width. This led to a decrease in propagation losses at 3.39 $\mu$m (left) for a wide range of waveguide widths where the lowest value was 0.33 ± 0.02 dB/cm. The corresponding cross-section still featured a slightly elliptical mode profile (right).

The lowest loss value of 0.33 ± 0.02 dB/cm compares favourably to other reports in GLS at 3.39 $\mu$m wavelength with 0.25 ± 0.05 dB/cm however, fabricated using the multiscan technique [138]. The authors in [138] investigated the effect of physical dimension on the propagation loss. The width of the waveguide was determined by the amount of overlapping scans with the same spacing while the height was controlled by the applied pulse energy of the inscribing laser. It was found that a width of 12 $\mu$m was decisive for a low-loss performance which is of the same order of magnitude of the demonstrated cumulative heating waveguide with a width of 12.3 $\mu$m. To create this structure, 40 parallel scans were inscribed at a velocity of 60 mm/min. The fabrication time is thus 33× longer than the time needed to fabricate a cumulative heating double modification.

Due to the achieved low propagation losses, the cumulative heating waveguides were further developed for single-mode operation at 4 $\mu$m. First, the existing single modifications were examined and showed an improved guidance for waveguides with a width between 8.3 and 9.8 $\mu$m (Fig. 4.8) in contrast to 3.39 $\mu$m (Fig. 4.6 left). Rayleigh scattering decreases at longer wavelengths and thus potentially helped the loss reduction to 0.29 $\pm$ 0.06 dB/cm, while the internal material attenuation at both wavelengths is negligibly small (<0.3 dB/m) [93]. The mode-profile of 23.7$\times$27.2 $\mu$m is highly asymmetric but features a lower ellipticity than cumulative heating waveguides in GLS as demonstrated by McCarthy *et al.* [135]. These reported waveguides have a mode-profile of 19.3$\times$27.2 $\mu$m at 3.85 $\mu$m wavelength. One potential reason for the lower ellipticity is the higher numerical aperture objective used for fabrication, and another reason is the writing depth of only 180 $\mu$m rather than 240 $\mu$m. A deeper writing depth shows a stronger effect of spherical aberrations.

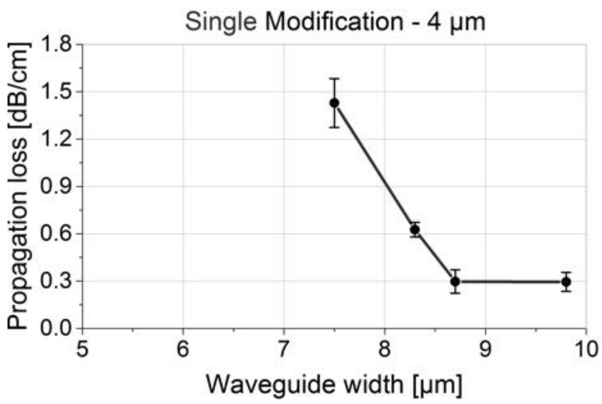


Figure 4.8: Propagation losses at 4 $\mu$m for cumulative heating single modifications. The increase in waveguide width reduced the propagation losses down to 0.29 $\pm$ 0.06 dB/cm.

In order to fabricate cross-sections equal in the vertical and horizontal dimension and thus obtain circular mode-fields, three single tracks were inscribed sequentially with the same center-to-center spacing of 2.65 to 6.15 $\mu$m at 0.7 $\mu$m increments. An almost linear decline in propagation loss was observed for increasing waveguide widths as seen previously for the single modifications. This resulted in a propagation loss as low as 0.22 $\pm$ 0.02 dB/cm (Fig. 4.9 left) near the threshold to multimode behaviour in the horizontal dimension. The error bars in Figure 4.9 reflect the minimum and maximum deviation of subsequent inscriptions in two supplementary samples within a 4 week interval, resulting in precise replicas.

The writing order of the three waveguide-forming tracks was chosen sequentially from left to right. Different writing orders were tested such as right to left, left-right-center and center-right-left, where every attempt featured the same propagation loss and mode-field diameters. The cross-section of the lowest loss triple modification has a physical size of 19.4×19.8 $\mu$m where the three tracks overlap only in their shell regions. The round mode profile of 22.3×22.6 $\mu$m ± 0.1 $\mu$m shows the lowest ellipticity of ∼0.99 for all presented waveguides.

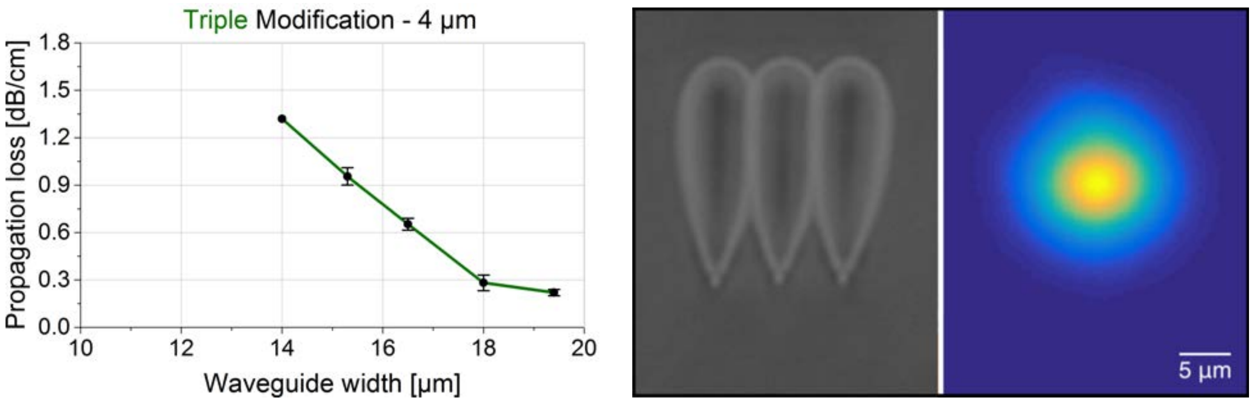


FIGURE 4.9: Propagation losses at 4 $\mu$m for cumulative heating triple modifications (left). The lowest loss waveguide with 0.22 ± 0.02 dB/cm features an almost 1:1 cross-section with symmetric mode-field dimensions of 22.3×22.6 $\mu$m.

The findings are consistent with previous studies by Gross *et al.* [43] who achieved a propagation loss value of 0.29 ± 0.03 dB/cm in mid-infrared fluorozirconate (ZBLAN) glass at 4 $\mu$m. However, the depressed cladding waveguide (N2) potentially sustains a great bending loss due to a large MFD. The ∼2.5× larger MFD of the waveguide compared to mid-infrared optical fibers leads to additional coupling losses between the two.

A higher mode confinement compared to ZBLAN waveguides was achieved by Masselin *et al.* [139] in germanium-based chalcogenide glass (GeS-$_2$Ga$_2$S$_3$-CsCl) fabricating multicore waveguides. A multicore waveguide is an expanded core geometry (P2) fabricated using FLDW. Single-mode guidance was demonstrated with a propagation loss as low as 0.2 dB/cm at 4.5 $\mu$m.

In comparison to the athermally inscribed waveguides described in Section 4.2.1, the hybrid approach between multiscan and cumulative heating with three tracks featured a lower polarisation dependent loss of <0.1 dB/cm, lowest propagation loss for vertical polarisation, while no PDL was found for single track waveguides. Even though the lowest loss multiscan waveguide for 3.39 $\mu$m wavelength can be inscribed with a higher velocity, it still requires 15 scans and thus takes twofold longer to inscribe compared to the cumulative heating double modification method. Table 4.2 summarises the important parameters of the presented multiscan and cumulative heating waveguides.

| | $\lambda$ | **Cumulative heating (single)** | **Cumulative heating (double/triple)** | **Multiscan** |
|---|---|---|---|---|
| MFD (h×v) | | 22.9×24.7 $\mu$m | 19.7×22.1 $\mu$m | 16.9×22.6 $\mu$m |
| Propagation loss | 3.39 $\mu$m | 0.47 ± 0.01 dB/cm | 0.33 ± 0.02 dB/cm | 1.5 ± 0.03 dB/cm |
| PDL | | below resolution | <0.1 dB/cm | 0.24 ± 0.02 dB/cm |
| MFD (h×v) | | 23.7×27.2 $\mu$m | 22.3×22.6 $\mu$m | — |
| Propagation loss | 4 $\mu$m | 0.29 ± 0.06 dB/cm | 0.22 ± 0.02 dB/cm | — |
| PDL | | below resolution | <0.1 dB/cm | — |
| Fabr. time (1 cm) | | 6 s | 12 - 18 s | 22 s |

Table 4.2: Comparison of the lowest loss cumulative heating and multiscan GLS waveguides at 3.39 and 4 $\mu$m wavelengths.

Waveguide fabrication in the cumulative heating regime is a less common approach for GLS or other chalcogenide glasses. Their high refractive index and the associated spherical aberration during FLDW causes an asymmetric waveguide cross-section that results in an elliptical mode profile. By combining three cumulative heating waveguides with the multiscan technique it was possible to fabricate waveguides with a propagation loss as low as 0.22 ± 0.02 dB/cm and a round mode profile. Further investigations on these structures and material changes are presented in the following Chapter 5.

# 5

# Structure analysis of optical waveguides

The following chapter provides a deeper understanding of gallium lanthanum sulphide glass and its structural change upon femtosecond laser exposure. The general structure of the glass is discussed followed by a detailed investigation of the waveguides fabricated in the thermal regime, demonstrated in Section 4.2.2. The refractive index change was measured with a micro-reflectivity setup explained in Section 3.3.2. Raman microscopy laid the groundwork for understanding the structural changes within the glass network, supplemented by Electron Probe Micro-Analysis (EPMA,) namely energy dispersive spectroscopy (EDS) and wavelength dispersive spectroscopy (WDS).

## 5.1 Gallium lanthanum sulphide glass

Crystalline and amorphous materials can be distinguished by the long and short-range order of their constituent atoms, ions or molecules, as the short-range order of amorphous solids have many thermal, mechanical and optical properties useful for photonic applications. Out of the many glass types classified by their constituent elements, classic chalcogenide glasses are a family of glasses obtained by combining group III - V elements with chalcogens such as sulphur, tellurium and selenium but excluding oxygen. Well known for their IR transmitting properties, chalcogenide glasses are one of the most favoured glasses for mid-infrared photonic applications.

The glass investigated in this work (Fig. 5.1 inset), gallium lanthanum sulphide (GLS), was discovered by Loireau-Lozach *et al.* [140] in 1976. GLS has a light orange colour, attributable to the band-gap of 2.6 eV ($\lambda$ = 475 nm). This non-toxic glass, in contrast to arsenic chalcogenides, has a high thermal resistance due to its high glass transition temperature $> 500°$C. Compared to common silica glass, it features a higher refractive index, as shown in (Fig. 5.1), for the wavelength range between 0.5 - 10 $\mu$m. The refractive index is described by a 3-term Sellmeier equation

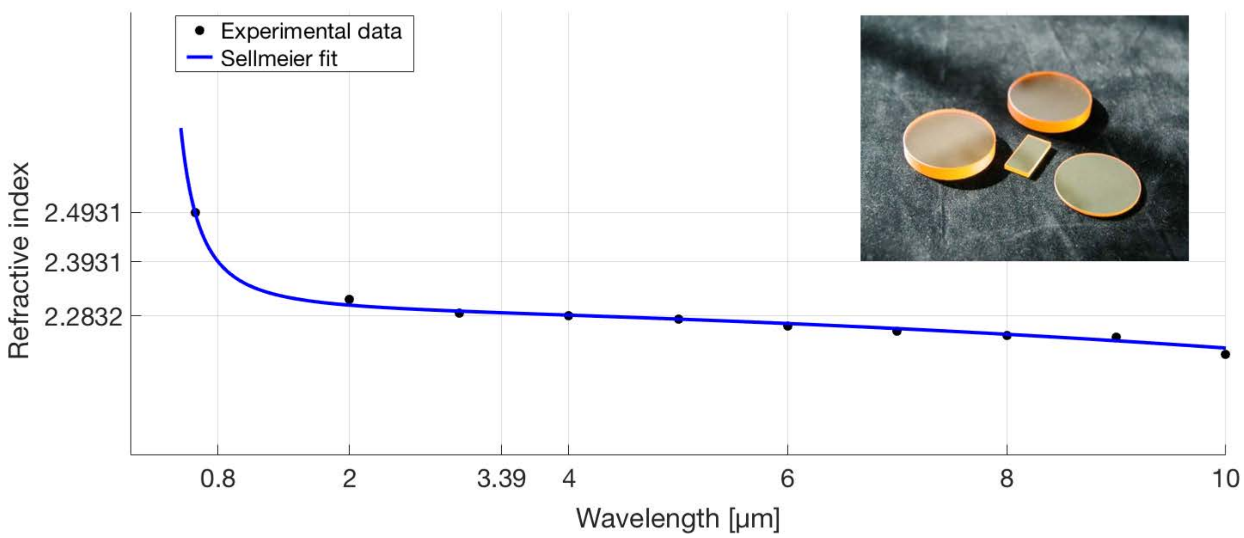


FIGURE 5.1: The Sellmeier fit provides the refractive index for GLS glass at different wavelengths up to 10 $\mu$m. Inset: Image of GLS glass samples (Credit: ChG Southampton Ltd).

$$n(\lambda) = \sqrt{1 + \frac{B_1\lambda^2}{\lambda^2 - C_1} + \frac{B_2\lambda^2}{\lambda^2 - C_2} + \frac{B_3\lambda^2}{\lambda^2 - C_3}} \tag{5.1}$$

determined using a nonlinear curve fit to a number of experimentally measured points with the coefficients $B_1 = 227.914$, $B_2 = 2.12767$, $B_3 = 2.12903$, $C_1 = 66945.7$, $C_2 = 0.063941$ and $C_3 = 0.063941$. The experimental data for the fit was taken from [93]. Two refractive indices of importance are 2.3931 at the inscription wavelength of 800 nm and 2.2832 at the design wavelength of 4 $\mu$m for optical waveguides.

The third order nonlinear response of GLS is large under a strong electromagnetic field due to the high hyperpolarisability of sulphide ions. The nonlinear refractive index of $300 \times 10^{-20}$ m$^2$/W is two orders of magnitude higher than silica at 700 nm wavelength [40].

The raw transmission of GLS glass was measured with a Cary 5000 (Varian) spectrophotometer (blue line) and a Nicolet iS10 (Thermo Scientific) Fourier-transform infrared (FTIR) spectrometer (black line) with a 1 mm thick sample (Fig. 5.2). The transparency begins in the visible range around 460 nm and extends up to 13 $\mu$m, far beyond the capability of fluoride and silica glasses. The step at 840 nm occurs when changing to a different internal

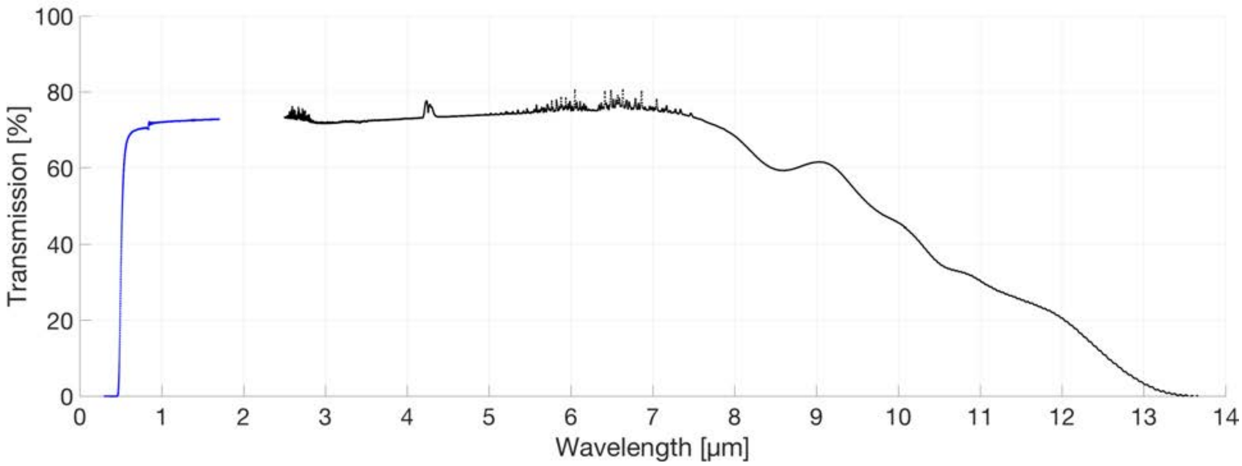


Figure 5.2: The optical transmission of a 1 mm thick GLS sample from the visible to the infrared range was measured in air with a spectrophotometer (blue) and in vacuum with an FTIR spectrometer (black). The transparency starts at ∼460 nm and ends at ∼13.5 $\mu$m. The transmission data has not been corrected for Fresnel reflections of approximately 30% which means that GLS glass features an almost 100% transmission between 700 nm - 7 $\mu$m.

grating of the spectrophotometer in order to measure longer wavelengths. The spectrum is not corrected for Fresnel reflections of around 30%. This means the internal transmission is close to 100% from 700 nm to about 7.5 $\mu$m, after which a linear decline in transmission starts. For the wavelength range from ~3 - 6 $\mu$m the absorption losses are less than 0.02 dB/cm.

The GLS glass used in this work has a composition of $70Ga_2S_3$:$30La_2S_3$. The crystalline structure of $Ga_2S_3$ (Fig. 5.3) is considered to be the fundamental base unit for GLS glass.

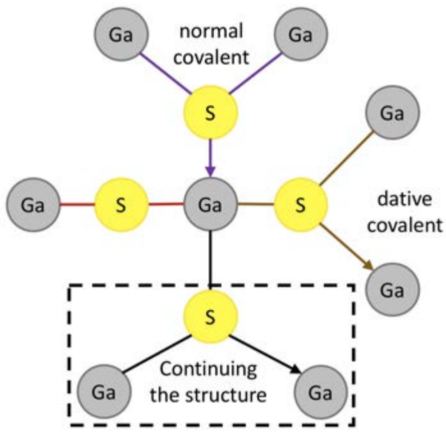


FIGURE 5.3: Crystalline structure of $Ga_2S_3$ with two sulphur atoms, each connected to three gallium atoms and one sulphur atom is connected to two gallium atoms.

Two sulphur atoms are each connected to three gallium atoms (brown and purple) and one sulphur atom is connected to two gallium atoms (red). Of the three covalent bonds of Ga-S, one is a dative bond (marked as an arrow). A dative bond is where only one of the constituent atoms provides both electrons for covalent bonding rather than mutual.

Since $Ga_2S_3$ only exists in a crystalline state, network modifiers like $La_2S_3$ and $La_2O_3$ are added to the melt to facilitate vitrification during the quenching process [141]. During glass formation, $La_2S_3$ introduces sulphur anions ($S^{2-}$) that break the dative bonds and replace the sulphur atoms in the $Ga_2S_3$ crystal (Fig. 5.4).

An $S^{2-}$ anion is linked with the gallium atom in such a way that the environment of the network forming gallium tetrahedra $GaS_4$ remains unchanged but forms a negative cavity. This negative cavity is compensated by an incoming network modifying $La^{3+}$ cation (or again by a gallium atom) [141]. Sulphur anions as well as negative cavities are transient states and

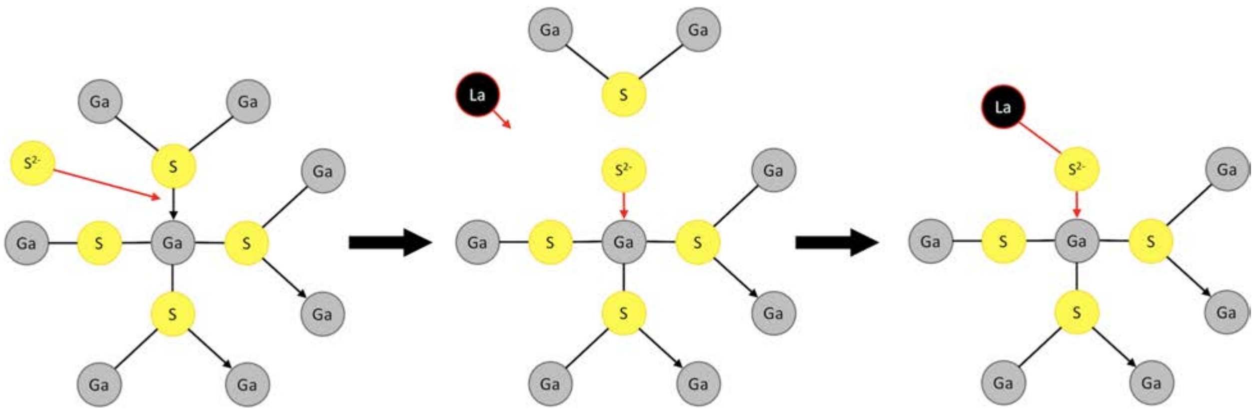


Figure 5.4: Structural change of $Ga_2S_3$ by introducing $La_2S_3$. $S^{2-}$ anions replace sulphur in dative bonds, creating negatively charged tetrahedra. The new environment allows $La^{3+}$ cations to connect.

only present during the glass forming process. The average bond length for Ga-S is reported to be 2.27 Å for both amorphous and crystalline environments [141], whereas La-S has an average bond length of 2.93 Å.

The typical way to fabricate GLS glass was to add a low percentage of lanthanum oxide $La_2O_3$ during the glass melting process [111]. The introduced oxygen anions $O^{2-}$ behave the same way as the $S^{2-}$ anions in Figure 5.4 and replace sulphur in the dative covalent bonds. This allows $La^{3+}$ cations to bind with oxygen and sulphur atoms where oxygen has a higher affinity to bond than S. The oxide impurities aid the glass formation due to high resistance to crystallisation by hybridisation and formation of an extended glass network that increases the quality of the glass. However, impurities like oxygen and water can lead to absorption and scattering losses and need to be kept to a minimum. In 2015 the group of Dan Hewak at the University of Southampton improved the fabrication process of GLS where no additional LaO is used as a precursor (Dan Hewak personal communication). Since the new fabrication method has been patented and the intellectual properties are protected, no further description can be made.

## 5.2 Refractive index change

The refractive index profile of FLDW waveguides provides insights of their guiding properties and formation mechanisms. These profiles are often complex due to the arbitrary core geometries and are more challenging to measure than conventional cylindrical fibers. High refractive index glass adds an additional level of difficulty since well established techniques, such as the refracted near-field method, are limited to glasses of $n < 1.7$. Neither the 2-dimensional refractive index profile nor the structural integrity of waveguides inscribed in GLS glass are clearly understood to date. Attempts to provide quantitative and qualitative information using quantitative phase microscopy resulted in a 1-dimensional line profile [137] while ellipsometric measurements were unsuccessful [40].
A test with monochromatic light of 633 nm and 808 nm showed multimode guiding character anywhere in the shell of single and triple track waveguides originally designed for a 4 $\mu$m wavelength (Fig. 5.5 center and right). This behaviour is identical to observations by Hughes *et al.* [56] and proves that the bright regions in the bright-field microscope image (Fig. 5.5 left) correspond to a local increase in refractive index. This means that the surrounding bulk and the central core must have a lower refractive index.

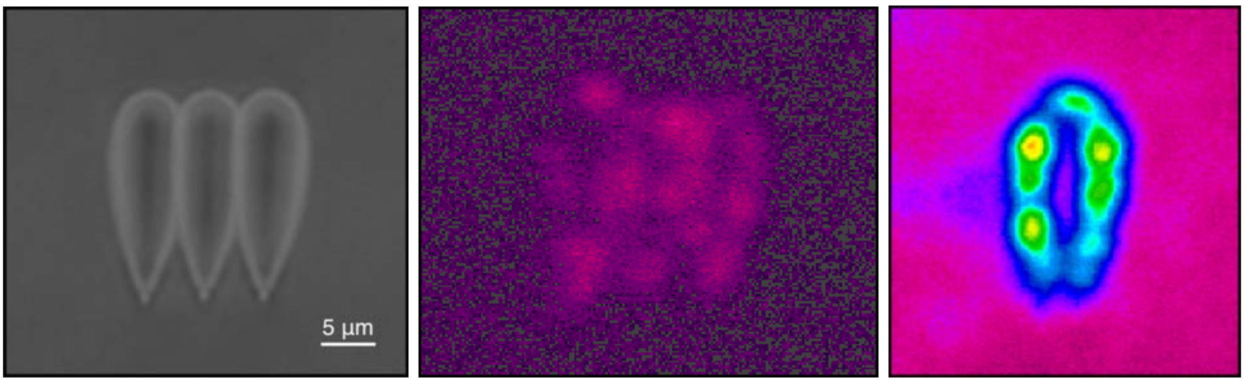


FIGURE 5.5: Bright-field microscope image of a triple waveguide (left). Single (right) and triple (center) waveguides show guiding capability only in the shell region when illuminated with 633 nm and 808 nm monochromatic light, respectively.

To confirm these results experimentally, a micro-reflectivity [92] measurement system was set up (Sec. 3.3.2) to map the cross-section of the waveguides. The Fresnel reflection from the highly polished surface can be linked to the refractive index of the glass using the

Fresnel formula. The back surface of the GLS sample was polished at a 45° angle to avoid back reflections from the waveguide end. The light from a narrow bandwidth 822 nm SLD (< 25 nm) was used to scan a 35×35 $\mu$m area with a ∼0.65 $\mu$m step size. The resulting map in Figure 5.6 (left) shows a high refractive index in the shell on the right-hand side with $\Delta n$ ∼0.03 while the left site of the waveguide structure shows a lower refractive index than the bulk with $\Delta n$ ∼ -0.03. Interestingly, rotating the sample by 180° shows that the reflectivity increases and decreases for different parts of the shell depending on the positioning (Fig. 5.6 right). Even though the surface might still be slightly tilted after the alignment, the effect should be marginally low. Eickhoff *et al.* [90] calculated the change in reflectivity to be only 0.001% or $10^{-5}$ for misalignment angles as large as 4°. The rotation, however, should not affect the refractive index map and thus requires further investigation of the surface profile.

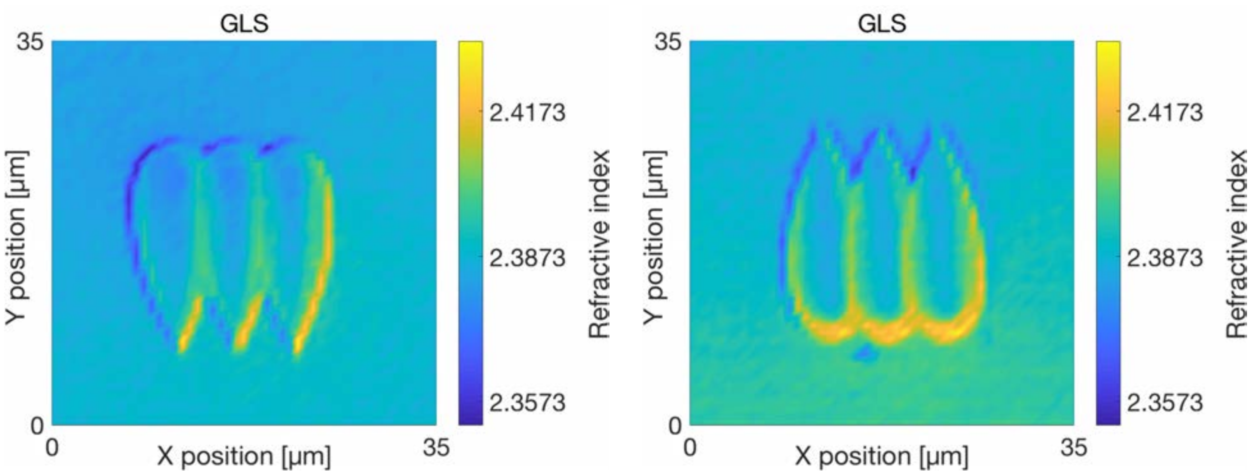


Figure 5.6: Two micro-reflectivity measurements of the same GLS glass waveguide for two different orientations. The contradictory results point out an irregular surface flatness that leads to inaccurate results.

In order to understand these arbitrary reflections, a topological map was taken using a white-light interferometer (Fig. 5.7 left). The map confirmed a mismatch in flatness between the waveguide and the bulk of the glass. Indents of up to 0.026 $\mu$m deep can be found in the core of the waveguide. A horizontal line profile through the center of the waveguide is shown in Figure 5.7 (right). The undercut is associated with the polishing process of the glass chip's end-faces using a colloidal silica particle slurry with a pH value of 10.

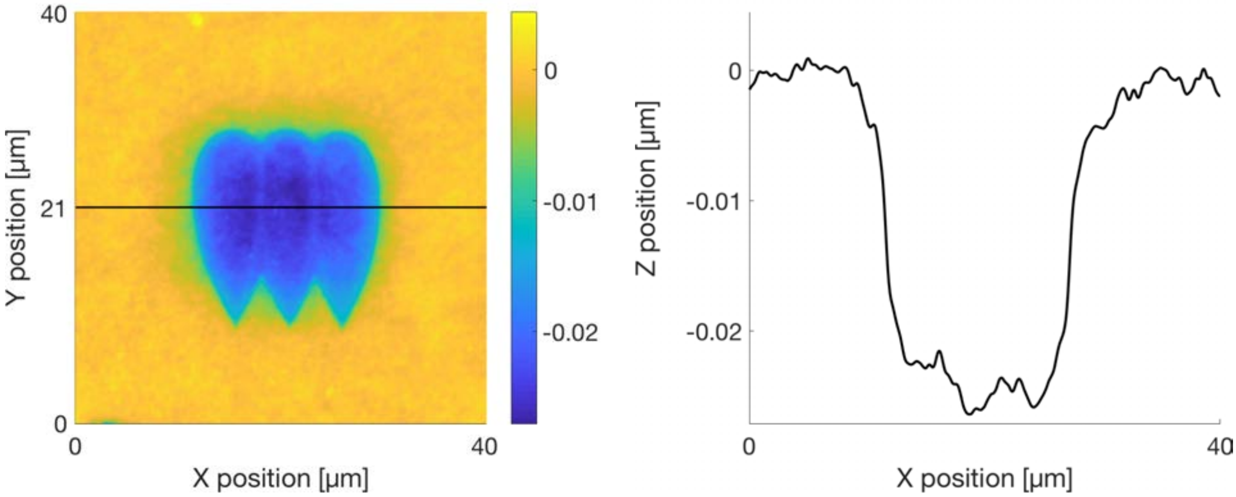


FIGURE 5.7: Left: Topographical map of a GLS triple waveguide's cross-section measured on a white-light interferometer. The dark areas show the degree of indentation caused my mechanical grinding and polishing of the sample's end-faces. Right: The graph shows the depth at the center of the waveguide (horizontal line).

It is difficult to determine the origin of the surface indentation and the contribution associated with the lapping hardness. This term is defined as the removed volume of material under fixed processing conditions. It depends on the mechanical properties of the material such as elastic (Youngs modulus), plastic (Knoop hardness) and fracture parameters [142]. These parameters are potentially affected by the laser irradiation and lead to a faster material removal under chemical-mechanical polishing. This implies either a change in hardness or chemical etch-rate.

To change the polishing conditions, silica polishing slurry was replaced by a 0.5 $\mu$m monocrystalline diamond suspension in a water solution with a pH value of 7.5 (Eminess technologies, Ultra-Sol STD0.5$\mu$50M). As a result, the undercut was avoided at the cost of the surface quality containing deep and random micro-scratches (Fig. 5.8).

The refractive index $n = 2.3873$ of the bulk was determined at 822 nm with the Sellmeier Equation (5.1). The easily visible refractive index increase in the shell region of the waveguide has an average value of $n = 2.4031$ and thus a contrast of $\Delta n_{\text{shell}} = 0.0158 \pm 0.0010$ compared to the bulk of the glass. The waveguide core features a refractive index of $n = 2.3933$ and thus a $\Delta n_{\text{core}} = 0.0060 \pm 0.0014$. The waveguide structure, including

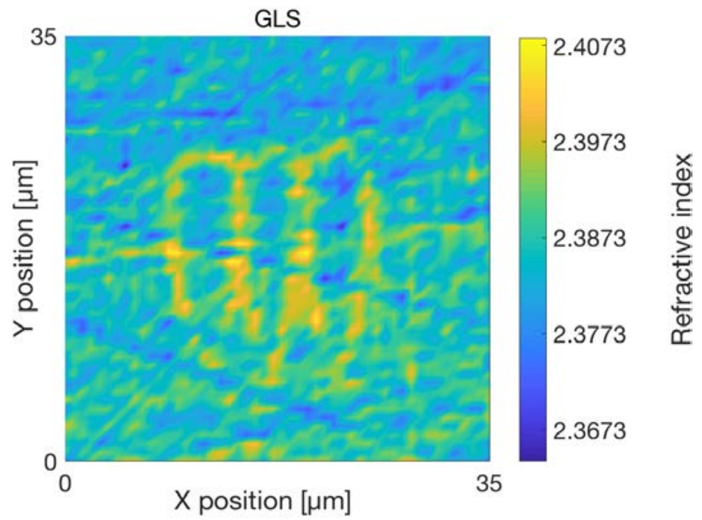


Figure 5.8: The micro-reflectivity map features a higher noise level due to decreased surface quality when polishing with a diamond suspension. This polishing approach provided a flat surface suitable for micro-reflectivity measurements. A higher refractive index of $\Delta n_{\text{shell}} = 0.0158 \pm 0.0010$ was found in the shell region of the waveguide compared to the bulk of the glass.

core and shell, has an overall refractive index of 2.4001 resulting in a refractive index change of $\Delta n_{\text{waveguide}} = 0.0128 \pm 0.0009$. The micro-reflectivity map shows significantly more noise than the previous scans due to the decreased surface quality. The standard deviation of the background is $\Delta n_{\text{noise}} = 0.0056$ from the refractive index of the bulk glass. This value is two orders of magnitude higher compared to the $\Delta n = 0.00003$ background noise measured for the silica polished waveguide.

A refractive index change was previously reported for multiscan waveguides in GLS glass at 10.4 $\mu$m wavelength [53]. The mode-field diameter and physical size of the waveguide was used to estimate a $\Delta n = 0.012$ using a finite element software (COMSOL). Other chalcogenide waveguides in GeAsS [118] or $GeS_2$-$Ga_2S_3$-CsCl [39] are usually reported with an estimated refractive index contrast of $\Delta n = 0.001$ - $0.007$ at 1.55 $\mu$m. Other high refractive index changes of $\Delta n = 0.015$ for FLDW phosphate glass waveguides [143] were estimated based on measurements of the NA of the waveguides.

To further investigate the origin of the refractive index change, Raman spectroscopy and EPMA were used. The sample was therefore again polished with the silica slurry to provide a high surface quality since the undercut has no effect on all downstream measurements.

## 5.3 Raman analysis

To gain a better understanding of femtosecond laser direct-written (FLDW) waveguide formation in the cumulative heating regime, a 2-dimensional Raman map of the waveguide's end-face was taken with a Horiba Jobin Yvon system. An excitation wavelength of 633 nm was used, which lies above the absorption edge of the material (Fig. 5.2).

The microscope image in Figure 5.9 (left) shows a laser direct-written waveguide with three central inverted teardrop-shaped structures (core) each with a surrounding bright zone (shell). This area was covered by a 25×28 $\mu$m region (Fig. 5.9 right) and scanned with 1 $\mu$m steps that allow for the analysis of changes in the uniformity of the material and provides insights into density, composition, stress and crystallinity.

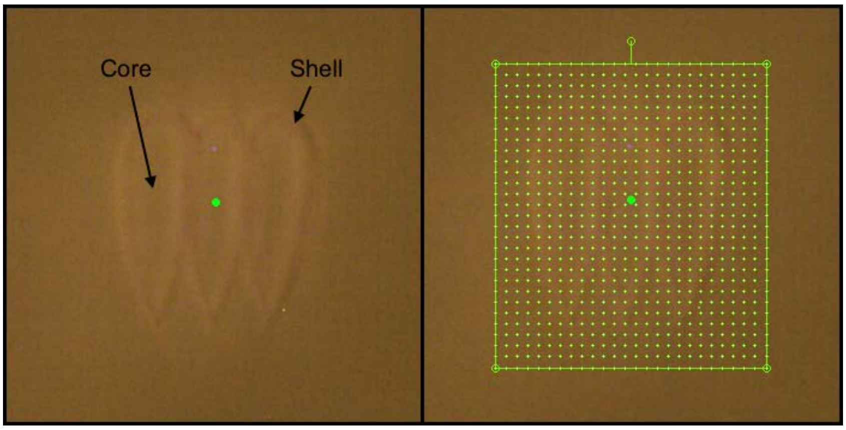


FIGURE 5.9: Left: Microscope image of the end-face of a GLS waveguide triple waveguide. Right: The end-face is mapped on a Raman device with 1 $\mu$m resolution.

Even though measurements are taken confocally, the back of the sample was ground and polished with a 45° angle to prevent light from coupling into the waveguide and reflecting back into the Raman system. This was done to avoid the back reflected light being interpreted as an increase in Raman intensity due to a local modification. The Raman spectrum was taken between 0 - 600 cm$^{-1}$. The edge filter used to block the excitation wavelength and Rayleigh scattered light before entering the spectrometer prevented obtaining a Raman response below 75 cm$^{-1}$. Therefore, this region is neglected for the following analyses. Figure 5.10 shows the Raman spectrum of the GLS bulk glass (black line) that is deconvolved with a pseudo-Voigt curve fit revealing six distinguishable peaks. These peaks are used as a reference and compared with the shift in peak position, full width of the peak at half maximum (FWHM) and intensity of the waveguide area.

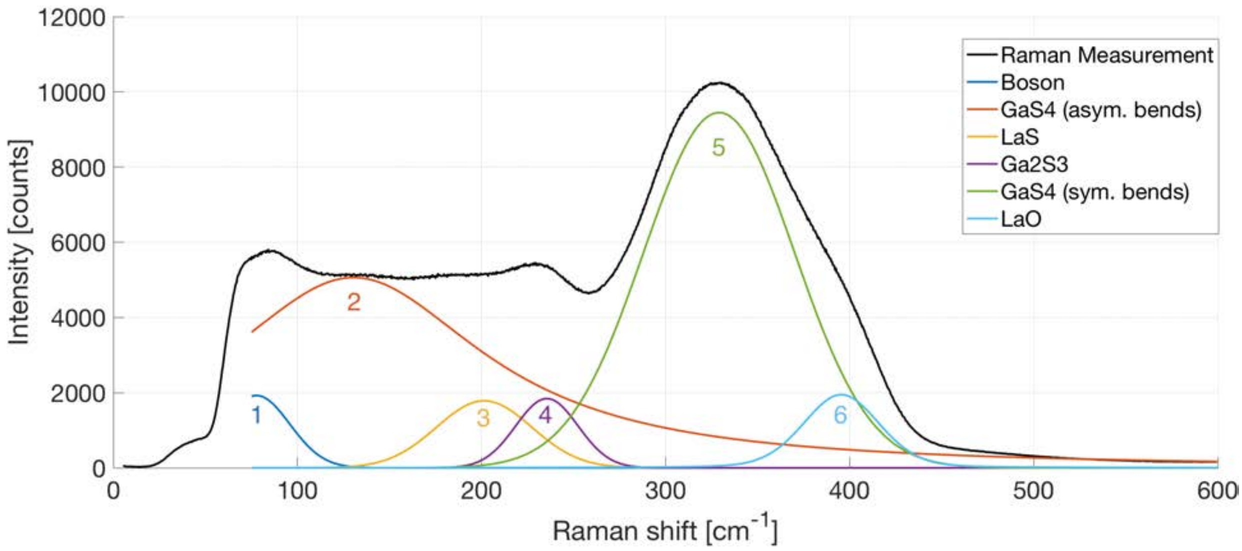


Figure 5.10: Deconvolved Raman spectrum of bulk GLS glass. The two main peaks at 131 cm$^{-1}$ (2) and 329.5 cm$^{-1}$ (5) are attributed to the main network former $GaS_4$ (symmetric and asymmetric bands).

Previous Raman analysis of FLDW waveguides in the cumulative heating [56] and athermal multiscan regime [144] were unsuccessful in detecting variations between the bulk and the waveguide region.

The Raman measurement (Fig. 5.10) shows a Boson peak [145] at 77.3 cm$^{-1}$. It provides information about the vibrational density of states (VDOS) which is sensitive to local density fluctuations [146]. The Boson peak is present in any amorphous material regardless of its constituents or stoichiometry and is observed in the low frequency region between 0 - 100 cm$^{-1}$. Its origin is a well debated topic and is mostly controversial. Here we only make use of its response to the physical properties of the material.

The 2-D map in Figure 5.11 (top left) shows a shift of the Boson peak to lower wavenumbers for the shell region with a magnitude 1.3 cm$^{-1}$ compared to the bulk. The core regions on the other hand feature isolated patches with a similar wavenumber as the bulk and has in average a shift less than 0.5 cm$^{-1}$ to lower wavenumbers. A shift of the peak to higher wavenumbers suppresses the low vibrational energy modes of the Boson peak as densifications occurs, experimentally demonstrated by Inamura *et. al* [147]. In other words, a lower wavenumber (Fig. 5.11 top left) and hence a lower frequency is an indication for a low density zone, supported by previous studies based on vitreous silica [147]. Studies have also shown that low density zones experience an intensity enhancement [148] that is associated with the distribution of free volume, evident from comparing Figure 5.11 (top left) and Figure 5.11 (bottom). Strong glass-forming systems are expected to have higher relative intensities of the Boson peak [149] which we observed for the waveguide shell region in Figure 5.11 (bottom).

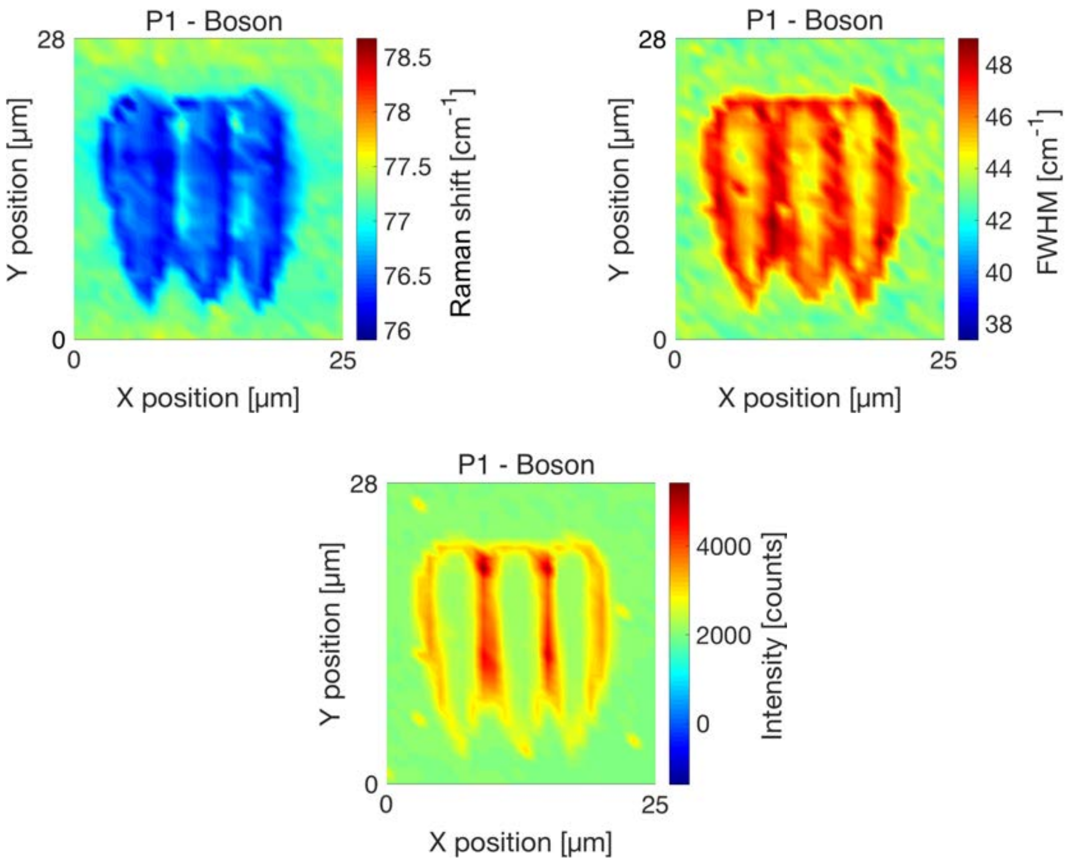


FIGURE 5.11: The three figures describe the Boson peak found in the Raman spectrum at 77.3 $cm^{-1}$. Peak shifts (top left) to lower wavenumbers and a broadening (top right) together with an increased intensity (bottom) are associated with low density zones.

The increase in FWHM of the Boson peak (Fig. 5.11 top right) in the shell region (4.5 $cm^{-1}$) is caused by activating lower vibrational energy modes in agreement with previous reports [147]. Similar results were reported by Boolchand *et al.* [150] where so-called low frequency floppy modes increased in the vicinity of the Boson peak when the concentration of chalcogens, sulphur in this case, in a chalcogenide glass was increased. This indicates an enriched sulphur area in the shell of the waveguide where a low density and higher refractive index are caused by sulphur ion migration processes initiated by a higher electronic polarisability compared to the bulk.

The $GaS_4$ network formers are the strongest bonds and can be found at 131.0 cm$^{-1}$ (asymmetric stretching mode) and 329.5 cm$^{-1}$ (symmetric stretching mode) as reported by Nemec *et al.* [151]. The Raman peak of the symmetric $GaS_4$ mode shifts to higher wavenumbers by 0.5 cm$^{-1}$ and 3 cm$^{-1}$ in the core and the shell, respectively (Fig. 5.12 top left). An increased width of the peak by 4.0 - 5.0 cm$^{-1}$ in both regions (Fig. 5.12 top right) is attributed to a wider range of bond lengths and bond angles and hence reflects the strong structural change in the material already indicated by the map of the Boson peak. In general, this can be

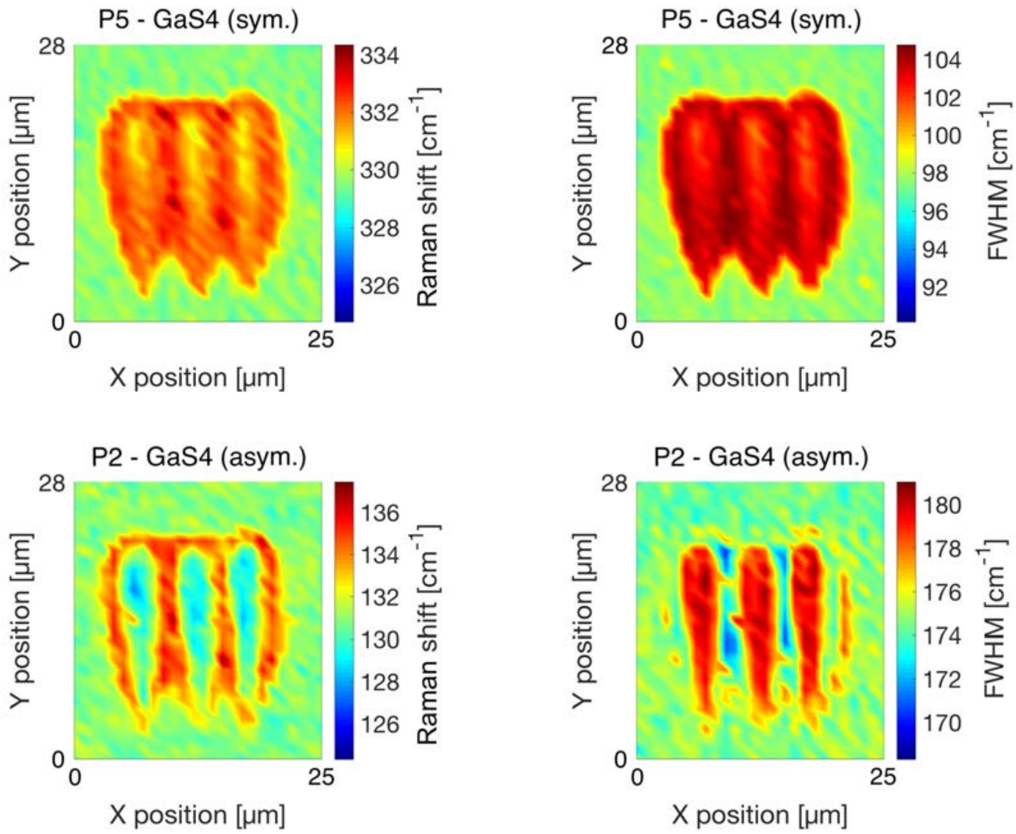


Figure 5.12: Peak 2 and 5 in the Raman spectrum at 130 cm$^{-1}$ and 329.5 cm$^{-1}$ belong to the symmetric (top) and asymmetric (bottom) vibrating bonds of the main network former $GaS_4$. Particularly, the increase in Raman shift and FWHM of $GaS_4$ symmetric bonds proves a strong structural change due to laser irradiation during the waveguide fabrication process.

seen as an improved glass structure with a larger long-range order. This is supported by an increase of $GaS_4$ (symmetric and asymmetric) bonds in the core with a simultaneous decrease of $Ga_2S_3$ bonds derived by the comparison of the ratio between these bonds across the waveguide region. This forms an even more vitreous material then the bulk glass.

The same positive peak shift of 3 $cm^{-1}$ in the shell and shift in FWHM in the core of up to 5 $cm^{-1}$ was found for asymmetric $GaS_4$ modes (Fig. 5.12 bottom left and right). The core on the other hand exhibits a decrease in frequency by 3.5 $cm^{-1}$ as well as a 4 $cm^{-1}$ decrease in width of the peak in the region where two shells overlap.

The peak position at 235.2 $cm^{-1}$ is identical with the $Ga_2S_3$ crystalline Raman signal and was reported to disappear during glass formation [152]. The peak width is broader compared to its crystalline counterpart and indicates a distorted crystalline-like unit. Its presence proves a low efficiency of $S^{2-}$ anions to break the Ga-S dative bonds [153] to form $GaS_4$ tetrahedra, as demonstrated in Figure 5.4. The mapping of this Raman band (Fig. 5.13 left) shows a minor decrease of 1.5 $cm^{-1}$ in the core and an even smaller increase in the shell region ($< 0.5$ $cm^{-1}$). The shift to a longer wavenumber means that the bond length between Ga - S is reduced and oscillates with a higher frequency. This makes space to accumulate a higher volume of sulphur that combines with gallium. Another reason for the reduction in bond length of Ga - S could be due to sulphur replacing oxygen atoms without changing the network geometry. Since sulphur is a larger sized atom than oxygen, the bonds have to

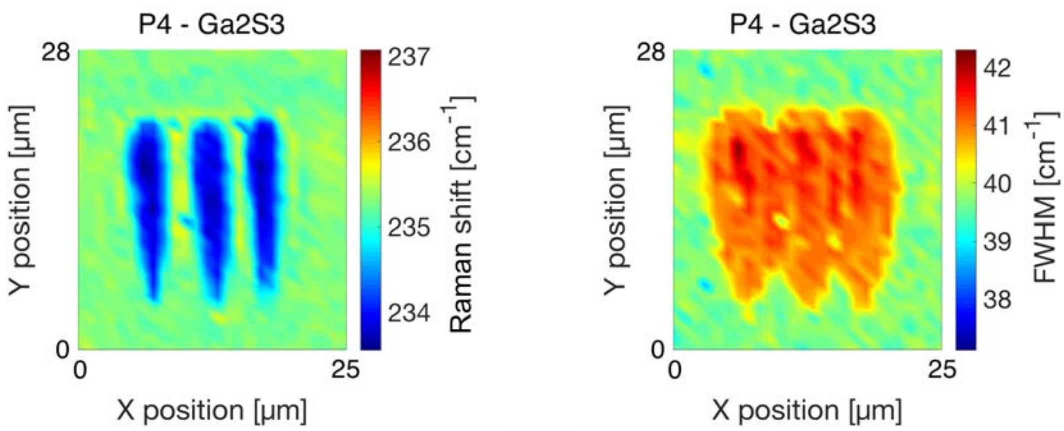


FIGURE 5.13: The fourth peak in the Raman spectrum is associated with $Ga_2S_3$. The peak shifts towards lower wavenumbers (left) due to decreasing bond length and broadening in FWHM (right) over the waveguide cross-section.

become shorter. This migration leads to a broadening of the $Ga_2S_3$ peak (Fig. 5.13 right) across the entire waveguide structure.

La-S bending modes are found at 201.5 $cm^{-1}$ and La-O bending modes at 395.7 $cm^{-1}$ [154]. The latter is assumed to have formed due to small oxide impurities from the raw materials, atmospheric oxygen or hydroxyl impurities, during fabrication. Missing Ga-O combinations suggest that they are either not Raman active or that oxygen is surrounded exclusively by two or three lanthanum atoms. The 2D map of the intensity ratio between La-O and La-S supports the theory of sulphur-oxygen ion migration (Fig. 5.14). It shows an enriched sulphur region in the shell (GLS) and a slight oxygen enriched region in the core, known as gallium-lanthanum-sulphur-oxide (GLSO).

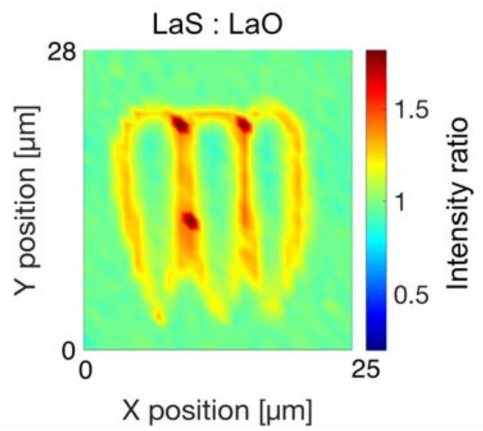


Figure 5.14: The ratio between La-S and La-O underpins the ion migration of sulphur into the waveguide shell region.

Fluorescence signals were found in the bulk glass centered around 4550 $cm^{-1}$ ($\sim$889 nm) for a 633 nm excitation wavelength. Compared to the maximum count of $\sim$10,000 in Raman signal, a low peak intensity of $\sim$62 counts was consistent for the bulk and the waveguide area. This shows the glass has very few defect sites such as non-bridging oxygen.

Previous reports show that GLS glass has a lower density (4.03g/$cm^3$) than GLSO (4.26g/$cm^3$) [155, 156], wheras the lower density is related to a higher refractive index of the glass. According to the Wemple equation [156]

$$n^2 - 1 = \frac{E_d E_0}{E_0^2 - E^2}, \tag{5.2}$$

the refractive index $n$ decreases with increasing average electronic band gap $E_0$ and/or decreasing electronic oscillator strength $E_d$, where $E$ is the photon energy. This was proven to be accurate for GLS compared to GLSO glass, where GLSO shows a lower electronic oscillator strength and a lower refractive index [156]. However, these two glasses form an exception since other chalcogenide, oxide and fluoride glasses have a lower electronic oscillator strength. The larger oscillator strength of GLS is related to the greater number of $S^{2-}$ ions with a higher electronic polarisability compared to $Ga^{3+}$, $La^{3+}$ and $O^{2-}$ ions [157]. This means that for femtosecond laser direct-written structures, a large sulphur polarisability results in a higher refractive index in the shell that forms the guiding region.

To recap, the Boson peak reveals a large Raman shift to lower wavenumbers for the shell region, whereas the core undergoes a minor shift to higher wavenumbers. A shift to lower wavenumbers generally indicates low density zones due to the activation of low frequency floppy modes with an increase in FWHM of the Boson peak in the shell region. This can be explained by migration of sulphur atoms forming a GLS rich region where the density is lowered, and refractive index is higher due to their larger electronic polarisability. This is supported by a map of the intensity ratio between LaO and LaS, where the latter increases in the shell region.

## 5.4 Electron probe micro-analysis

To spatially map the indicated migration of sulphur and oxygen, electron probe micro-analysis (EPMA) was used for qualitative and quantitative elemental analyses of waveguide structures inscribed in GLS. The aim was to identify chemical elements within or on the surface of a sample as well as their spatial distribution. It provides information about ion migration processes but also gives an insight into the surface topology. The sample used for this study was ground and polished with the conventional polishing method (Sec. 3.1.2). The elemental mapping was carried out with EDS and WDS detectors attached to various SEM systems (Sec. 3.4.3). The initial characterisation was done on a Zeiss EVO MA15 Scanning electron microscope with an EDS attachment. Figure 5.15 (left) shows the backscattered electron (BSE) image acquired using 15 kV and 1 nA. A line scan through the center of the waveguide clearly shows the migration of sulphur atoms towards the bright zones.

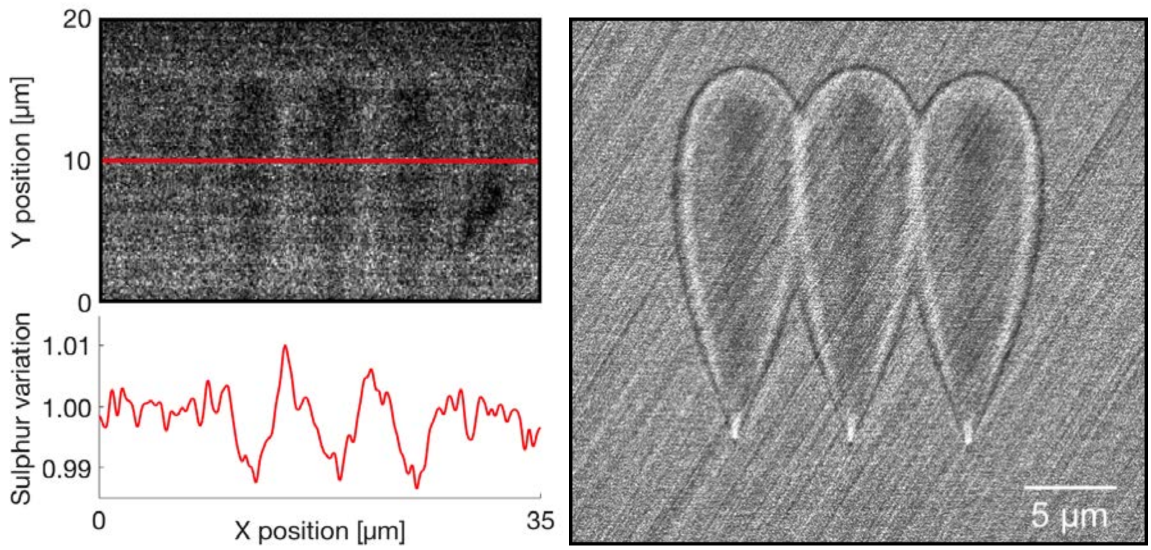


Figure 5.15: Left: Backscattered electron image of the waveguide structure taken with a Zeiss EVO MA15 EDS and below a sulphur K$\alpha$ variation trend line across the structure, normalised to the bulk. Brighter areas in the shell indicate larger atoms whereas smaller atoms are seen in darker regions of the core. The spikes in the trendline are evidence of an increase in sulphur quantity in the shell areas and an increase of oxygen in the core of the waveguide. Right: The BSE imaged with a JEOL JXA-8500F Hyperprobe with significantly higher resolution.

To obtain better quality data a JEOL JXA-8500F Hyperprobe was used. This instrument is equipped with a field emission gun SEM with a WDS attachment that is capable to detect and measure the concentration of light elements down to Beryllium (atomic number 4), with detection limits better than <0.05%. This device provided the best electron imaging with a clear secondary electron (Fig. 5.16) and backscattered imaging interpretation (Fig. 5.15 right) of the waveguide acquired with 15 kV and 10 nA excitation.

The backscattered electron image shows the defined bright sulphur shell region and the dark oxygen rich core regions as well as a narrow oxygen rich region seen as a dark line surrounding the structure. This illustrates that sulphur atoms migrated more efficiently into the shell from the modified zone compared to the unmodified zone.

Secondary electrons demonstrated a smooth topographical variation along the contours whereas the backscattered electrons show a high and low Z-contrast between the core and shell. These variations are associated with the undercut of the sample during grinding and polishing explained in the previous section.

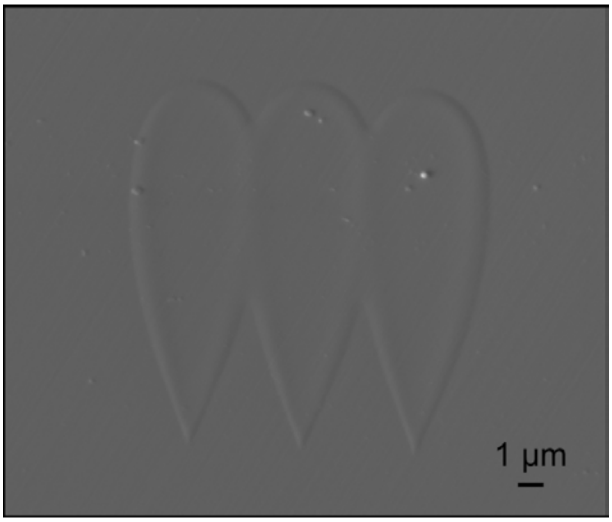


FIGURE 5.16: Secondary electron (SE) image of a triple waveguide structure. Changes along the contours of the waveguide are seen as darker and brighter regions and suggest that the surface suffers from topological variations.

Fernandez *et. al* [158] reported a dual regime of ion migration with dependence on the laser irradiation energy in phosphate glasses. It was experimentally demonstrated that lighter and heavier elements are subject to migration processes as a result of applying low and high laser fabrication energies, respectively. This is accociated with an element-dependent activation energy related to their atomic mass [159]. Since the elemental mapping did not show any evidence of Ga or La migration, it could be extrapolated that we could see only the migration of light elements (sulphur with 32.06 u) whereas heavy elements like Ga (69.723 u) and La (138.91 u) are inert due to the low inscription energy of 13 nJ.

Further measurements on waveguides fabricated between 10 and 70 nJ pulse energy were inconclusive (Fig. 5.17 waveguides left to right) which means that these energies were also not sufficient to induce heavy elements to migrate.

This is supported by the consistent morphology of the structure across the pulse energy range as further evidence that there is no heavy element migration unlike seen in [158]. Higher energies were not applied since 70 nJ caused cracking of the glass spanning across the structure up to the surface of the chip.


Figure 5.17: Single track waveguides inscribed with 10 - 70 nJ pulse energy (left to right). The triple waveguide structure on the far left serves as a size comparison. The last waveguide to the right caused cracks beginning from the structure up to the surface of the glass.

Measurements with 15 - 25 kV and 15 - 25 nA were used in previous glass studies to identify gallium as well as lanthanum [159]. Using these parameters were unsuccessful and confirmed a homogeneous distribution of gallium and lanthanum in the waveguide region. Hence it excludes the migration of both elements into the waveguide shell. A measurement of the bulk glass using 10 kV and 5 nA revealed a 1 - 1.5 wt% (weight percent) oxygen content. This is in agreement with the oxygen content found in the Raman measurements in the form of La-O bonds.

Nevertheless, mapping the minuscule sulphur rich area using EPMA is difficult due to the spatial resolution of the electron beam. Sulphur and oxygen are light elements with densities of 2.07 and 1.57 kg/m$^3$, respectively. The lighter an element is, the larger the investigated analytical area will be for a certain electron energy. This area increases with increasing electron energy. Wu *et al.* [160] successfully studied the K-shell ionisation cross-sections of sulphur under a 7 - 30 kV electron impact. In case of the field emission gun of the JEOL Hyperprobe, these electron energies correspond to an area of $\sim$1.2 - 14 $\mu$m$^2$ for oxygen and $\sim$0.95 - 11 $\mu$m$^2$ for sulphur. The sulphur concentration is evident only in the narrow shell, less than 1 $\mu$m thin. However, the probability is high that the resolving power is exceeded and through averaging across accumulated data, the contrast is reduced.

To conclude, sulphur migration into the shell of a cumulative heating triplet waveguide in GLS glass was demonstrated with the aid of Raman spectroscopy. The elemental EDS mapping showed supporting evidence of compositional changes via backscattered electrons. Brighter regions in the shell prove the migration of heavier elements while darker regions in the core confirms the presence of lighter elements. Since a low waveguide fabrication energy was applied, only sulphur could have migrated into the shell region and oxygen into the core. This explanation is supported by WDS measurements where no relocation of lanthanum and gallium was observed.

# 6

# Nulling interferometer

With the new inscription approach of three overlapping waveguide tracks developed in Chapter 4 Section 4.2.2, we intend to create an on-chip device similar to the beam combiner designs of Haguenauer *et al.* [28] and Benisty *et al.* [33]. With reduced intrinsic waveguide losses, the device will be capable of being operated at ground-based observatories. The fabrication parameters used are 5.1 MHz repetition rate, 100 mm/min translation speed and 13 nJ pulse energy for every component of the following device.

The layout in Figure 6.1 shows a 2-port nulling interferometer with two single-mode inputs that are spaced 500 $\mu$m apart in order to deploy a 1-dimensional V-groove fiber array or a silicon-based micro-lens array for injection. Single-mode waveguides have the advantage of spatially filtering collected starlight and thus removing all existing phase errors [22]. The waveguides evolve into cosine S-bend shaped asymmetric Y-splitters that feed 50% of the

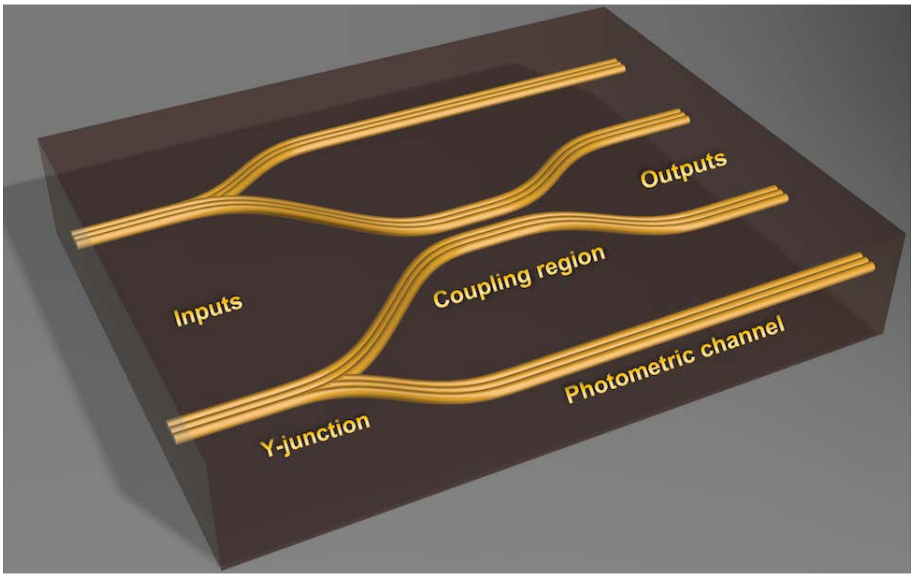


FIGURE 6.1: Two Y-splitters at the front-end of the two-port nulling interferometer GLS chip feed the starlight into two outer photometric and two inner interferometric channels. The inner channels fan into a 50/50 coupling region devised for a 4 $\mu$m center wavelength for interferometric interaction. Starlight is nulled as a result of destructive interference whereas additional light detected at the output is associated with a potential extrasolar planet in the vicinity of the star.

starlight to the outer power monitoring lines and the residual light into the inner interferometric channels. The purpose of these two interferometric channels is to destructively recombine the stellar light on-axis with the telescope to reveal an off-axis companion. This requires a half-wave shift in one of the arms introduced before entering the interferometric region. This can be achieved by offsetting the optical path length either off-chip via adaptive injection [161] or through an on-chip thermo-optic solution [162]. Any additional light in the 'null' of the star might be associated with a revolving exo-planet near the star. These faint signals are detected in the so-called null output channel while the starlight itself is found in the anti-null output channel. The four outputs are separated by 250 $\mu$m to allow the use of an aforementioned V-groove array holding the ends of optical fibers that connect the chip with a mid-infrared detector. The following sections describe the fabrication and characterisation of the individual components, namely S-bends, Y-splitters and couplers, for an on-chip nulling interferometer designed for 4 $\mu$m wavelength. Different coupler designs such as symmetric and asymmetric directional couplers as well as multimode interference couplers (MMI) are presented and contrasted against each other. The extinction ratio of asymmetric directional couplers and MMIs were measured at the University of Cologne, Germany, under my supervision.

## 6.1 S-bends

S-bend shaped waveguides play an important role in optical Y-splitters and directional couplers. In Y-splitters, they branch from one into two single-mode waveguides, splitting the power equally, whereas S-bends in directional couplers bring single-mode waveguides into close proximity for interferometric interaction. The overall interferometer performance relies on employing single-mode waveguide components with a low total structure loss. This loss can be decomposed for S-bend shaped step-index waveguides into radial and transition losses (Fig. 6.2).

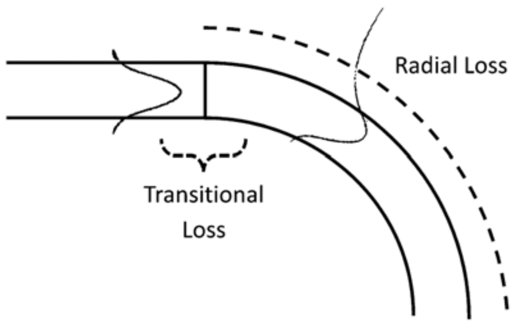


FIGURE 6.2: A waveguide mode experiences a transition power loss at straight-bend and bend-bend interfaces, and radial loss inside the bends due to limited guidance of the shifted mode in the outer region of the waveguide [163].

The mode in a bend shifts away from the center of the waveguide where the wavefront experiences an increase in refractive index. The mode travels towards the outside of the waveguide where it leaks into an unconfined space known as the caustic region. The radius of curvature function $R(s)$ with the S-bend profile $y(x)$ can be expressed as

$$R(s) = \frac{\left(1 + y\prime(x)^2\right)^{3/2}}{|y\prime\prime(x)|} \tag{6.1}$$

where $s$ is the incremental length with the S-bend of a bend radius $R$. The radial loss $\Gamma_{\mathrm{R}}$ over the S-bend length $S$ is given by [163]

$$\Gamma_{\mathrm{R}} = \exp\left(-\int_{S}^{0} \alpha\left(R\left(s\prime\right), s\prime\right) \mathrm{d}s\prime\right) \tag{6.2}$$

with the integration of the radial attenuation coefficient given by $\alpha(R, s)$. The mismatch between the mode in a straight and bent part of the waveguide as well as the mismatch between bends of opposite curvatures both cause transition loss at their interfaces. The loss at each interface can be calculated by the mode overlap integral known from Equation 3.6 in Chapter 3.

The transition loss is usually the limiting factor for well-designed S-Bend as radial loss can be prevented by adjusting the minimum bend radius through increase of the S-Bend length. This on the other hand increases the propagation loss for the final design. The radii of curvature vary for different types of S-bend designs with the same total length (Fig. 6.3). Two inverted radial arcs feature the highest bending radius but in turn suffer from transition loss at the start and end of the bend but more dramatically at the turning point. The cosine S-bend suffers from the same transition loss at the start and end of the bend as the inverted arcs

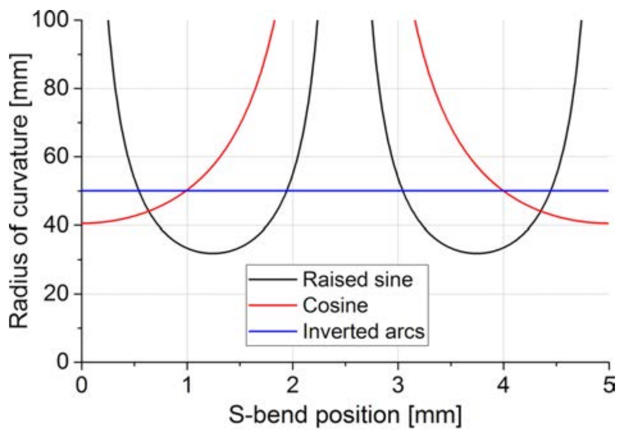


FIGURE 6.3: Comparison of calculated radii of curvature for three S-bend designs with a length of 5 mm and 125 $\mu$m lateral offset. Two inverted arcs offer the highest bending radii but in turn suffer from high transition loss at the inflection point. The cosine design shows the best compromise between low transition loss and high bending radii.

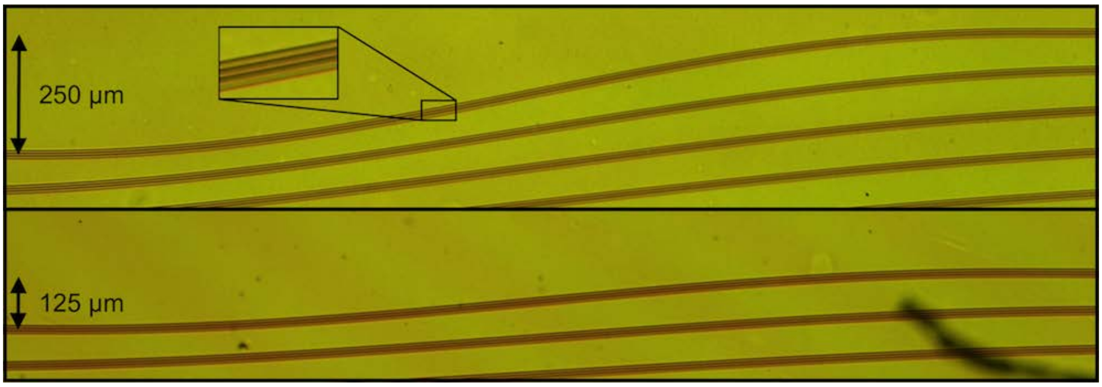


Figure 6.4: Top view of cosine S-bend waveguides fabricated in the cumulative heating regime (triple modification).

but experiences a lower radial loss than raised-sine shape S-bends [163]. More importantly, the latter has a higher potential for premature power transfers at the end of the two S-bends because of the large $R$ and thus very gradually transitions into the straight section of a directional coupler. The two interferometric waveguides hence need to be spaced apart with a greater distance which in turn leads to a slower power transfer between arms. The cosine S-bend has a minimum radius at the start and end of the bend and has the advantage of a gradually changing curvature with a monotone change in the center that avoids coupling loss between the curved sections.

A wide range of minimum bending radii was investigated by fabricating cosine S-bends with lateral offsets of 125 and 250 $\mu$m and varying interaction lengths of 2 - 12 mm (Fig. 6.4). The S-bend inscription was performed using FLDW with circular polarisation that has been demonstrated to significantly decrease radial loss in fused silica glass over FLDW with linear polarisation [41]. The S-bend excess loss at 4 $\mu$m wavelength was determined by measuring the S-bend propagation loss on the Fabry-Perot test bed and subtracting the corresponding propagation loss value of straight reference waveguides inscribed before and after the set of S-bends. Both S-bend sets with different lateral offsets showed identical loss behaviour with negligible bending losses for bend radii >40 mm (Fig. 6.5).

Gross *et al.* [43] used a raised-sine S-bend design to inscribe zero-gap couplers in ZBLAN. While the propagation loss at 4 $\mu$m wavelength was as low as 0.3 dB/cm, the large bend radii of 313 mm still caused ~1 dB loss per S-bend. The estimated refractive index of

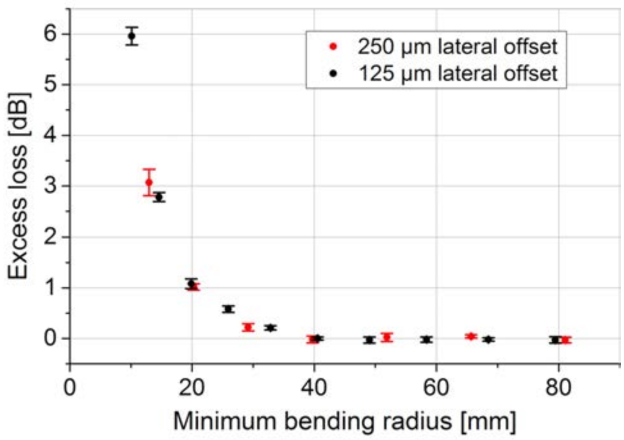


FIGURE 6.5: The experimental results of cosine S-bends show a negligible bending loss for bending radii larger than 40 mm at 4 $\mu$m wavelength. This results in S-bend lengths of ~5 and ~7 mm for 125 and 250 $\mu$m lateral offset S-bends, respectively.

$7 \times 10^{-4}$ played an important role as radial loss strongly depends on the wavelength and the mode confinement inside the waveguide. A larger refractive index difference $\Delta$n between the waveguide core and the surrounding bulk glass therefore allows for smaller radii of curvature.

The S-bends fabricated in this work with offsets 125 and 250 $\mu$m resulted in ~5 and ~7 mm lengths, respectively, for a minimum bend radius of 40 mm. S-bends with a length of 7 mm were also demonstrated by Diener *et al.* [164] as part of a multi-telescope beam combiner for the mid-infrared wavelength range. The much shallower raised-sine S-bends with 75 $\mu$m lateral offsets were demonstrated using the FLDW multiscan technique in GLS glass. Even though the corresponding minimum bending radius lies above 100 mm, the S-bends still suffered from a bending loss of ~0.5 dB per S-bend at 3.39 $\mu$m wavelength.

Further improvements to reduce radial and transition loss can be undertaken as numerically demonstrated by Ladouceur *et al.* [165]. The first initiative is to widen the bent waveguide sections which increases the confinement and reduces modal leakage and thus radial loss. The second step is to offset the straight waveguide equal to the offset of the mode created by the bend. This way the positions of the modes align and thus minimise the transition loss. A simple lateral offset by 10% of the waveguide width reduced the transition loss by more than 70%, for single-mode silica waveguides at 1.55 $\mu$m wavelength. The latter approach is especially suitable for the cosine design. Cosine S-bends do not suffer from transition loss in the center but instead at the start and end of S-bends if fabricated with small bending radii. This way, the minimum radius of curvature can be further reduced to shorten the S-bend length. Shorter S-bends lead to an overall shorter chip design that improves the total throughput.

## 6.2 Y-splitters

The first 1×2 Y-splitter using FLDW was demonstrated in fused silica in 1999 [166]. Since then, devices have been demonstrated as 1×N designs in various materials such as fused silica [167], lithium niobate ($LiNbO_3$) and [168] bismuth germanate ($Bi_4Ge_3O12$) crystals [109]. Liu *et al.* [169] even fabricated a splitting device in fused silica that uses seven cascading 1×2 Y-splitters to divide the light of one access waveguide eightfold. These devices operate in various wavelength regions from visible to mid-infrared for communication technologies to laser applications.

The aim of these single-mode devices is to equally split the injected light achromatically across the N output arms. A symmetric design is essential to achieve this goal. A homogeneous structure is simple to fabricate using lithography but difficult to accomplish employing FLDW. A single-mode Y-splitter consists of a stem and a tapered waveguide section with two diverging arms [170]. The sequential inscription of the Y-splitter arms leads to an overlap of waveguide tracks in the stem as illustrated in Figure 6.6 (top).

A consequently uneven power splitting was encountered by Færch et al. [171] in UV direct written symmetric Y-splitters. In symmetric splitters, the fundamental mode in the stem equally excites the fundamental modes in both arms. Here, the unbalanced power splitting ratio was believed to be caused by a lower refractive index of the second inscribed arm. The fundamental mode in the stem evolves across the junction more strongly into the fundamental mode of the branch with a more similar effective index and thus leads to an unbalanced power splitting [172]. By lowering the writing velocity of this arm, the refractive index was changed with the result of being able to finely tune the splitting ratio between 70/30 and 30/70 [171].

An interesting approach was conducted by Amorim *et al.* [173] to optimise FLDW Y-splitters in fused silica. Instead of overlapping the waveguide tracks, a lateral offset was introduced to separate the two diverging Y-splitter arms at the stem. The chromaticity successfully decreased with increasing separation, but so did the excess loss due to transition loss between the straight section and the branching point.

Both examples show that even though Y-splitters are symmetrical along their longitudinal axis, their splitting capability behaves asymmetricly due to sequentially inscribed waveguides. This emphasises the challenges of fabricating direct-written Y-splitters.

The proposed nulling interferometer chip design (Fig. 6.1) requires single-mode Y-splitters with a physically asymmetric design but symmetric splitting capability. This was accomplished using the S-bends developed in the previous section with 125 and 250 $\mu$m lateral offsets for the first and second arm, respectively. The two arms of the asymmetric Y-splitter designs (Fig. 6.6 top) differ significantly in refractive indices due to different changes in bending radii resulting in mismatching propagation constants [170, 174]. This refractive

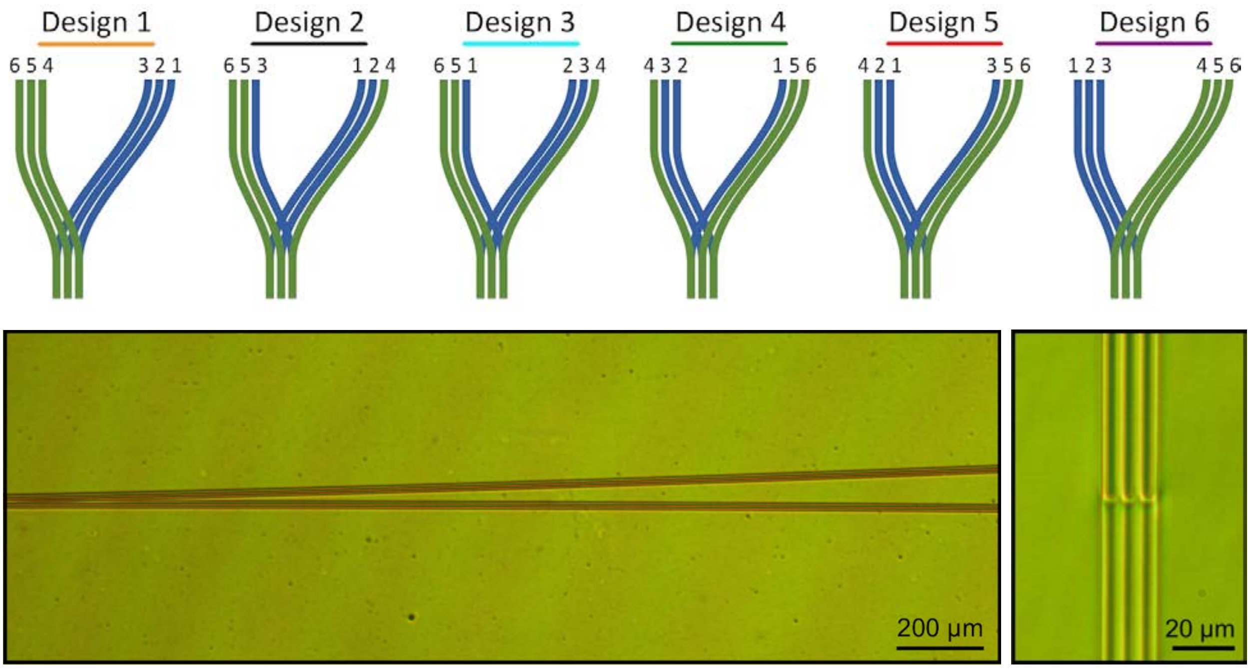


FIGURE 6.6: Top: Design of 6 different Y-splitters. The number at the end of each line indicates the writing order of the 6 tracks. Green lines indicate the overpassing tracks which influence the power splitting ratio. Bottom: Top view of a Y-splitter fabricated with 5.1 MHz repetition rate, 100 mm/min translation speed and 13 nJ pulse energy (left). The inscribing laser needs to overpass the stem in order to create the second arm of the Y-splitter. When switching on the laser before the point of divergence, an undesired defect is created causing scattering loss (right). Starting at the front-end of the chip to overwrite the straight and stem section is therefore most suitable.

index difference can be countered by exploiting the refractive index difference caused by the writing order of the waveguide tracks. The more similar the refractive indices of the arms are, the more equal the resulting splitting ratio will be.

The numbers on top of each design in Figure 6.6 (top) indicate the inscription order of the six tracks forming the Y-splitter. The sequential fabrication of the tracks leads to overpassing the first three tracks (blue) a second time (green) up to the branching point. The last three tracks form a more dominant pathway than the previous tracks and can therefore be altered in order to counter the imbalance in power splitting. The overpassed region includes both the stem and the straight section at the front-end of the chip. Care must be taken by choosing the starting point of the overpassing tracks. A starting position at the beginning of the stem results in a damage to the waveguide with an associated additional scattering loss (Fig. 6.6 bottom). Hence, the straight section has to be overpassed as well.

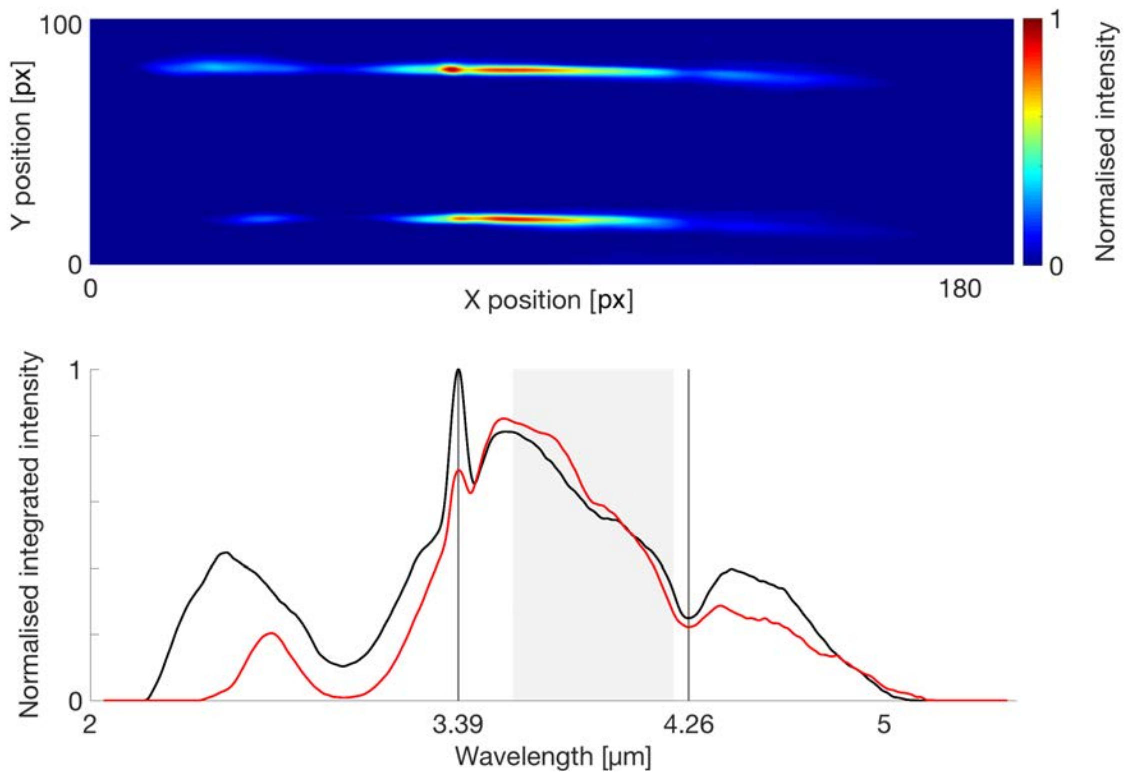


FIGURE 6.7: Top: Spectrally dispersed output modes of an asymmetric Y-splitter (design 6). Bottom: Vertical integration of each output over a ∼2 - 5.5 $\mu$m wavelength range. Reference points at 3.39 $\mu$m and 4.26 $\mu$m were used for scaling. An almost equal splitting ratio was found for the area of interest between 3.6 - 4.2 $\mu$m.

The power splitting ratios of the Y-splitters were measured with a broadband tungsten source on the spectral response test bed (Sec. 3.3.5). The transmitted light was spectrally dispersed using a triangular prism (Fig. 6.7 top). The simultaneously injected helium-neon laser light with 3.39 $\mu$m wavelength serves as a reference point as well as the $CO_2$ absorption dip at 4.26 $\mu$m. The power of each output mode was integrated vertically over 15 pixels (Fig. 6.7 bottom) across the scaled wavelength range of $\sim$2 - 5.5 $\mu$m. However, the area of interest lies between 3.6 $\mu$m and the end of the astronomical L-band at 4.2 $\mu$m (grey background). The splitting ratios for 6 designs were calculated with the output powers left/(left + right) over the 600 nm wavelength window, showing a gradual transition of transmission efficiency from one arm into the other (Fig. 6.8). The unevenness of the graphs reflect an uncertainty of $\sim$0.86%.

Designs 1 - 3 distribute a higher power ratio to the left arm with 125 $\mu$m lateral offsets, while designs 4 - 6 direct more light into the right arm with 250 $\mu$m lateral offsets. The orientation of the last two tracks decisively direct significantly more light to either arm. The left arm receives more light from the evolved mode in the stem but receives less light due to the waveguide writing order, resulting in an almost equal power splitting. In other words, the difference in refractive indices is well balanced between the arms.

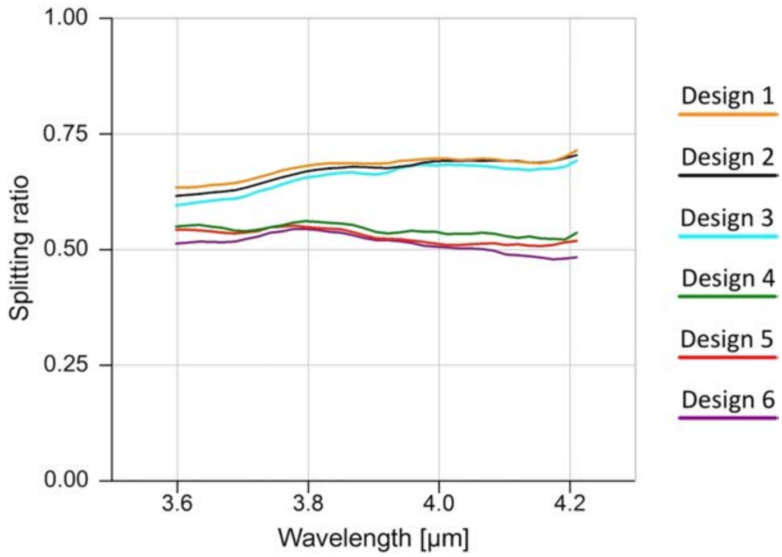


FIGURE 6.8: Power splitting ratios between the two arms (left/(left+right)) of the Y-splitter designs. The best spectral response in terms of equal power splitting over a 600 nm wavelength window was found for design 6.

Design 6 is closest to achromaticity and equal power splitting between 3.6 - 4.2 $\mu$m where the last three tracks inscribed lead into the arm with the larger lateral offset of 250 $\mu$m. A polarisation dependency was not found when characterising the Y-splitters with vertically or horizontally polarised light. The waveguide propagation loss and coupling loss was subtracted from the total measured throughput under broadband illumination. This way, the excess loss of the Y-splitters due to the branching point and overpassing of the stem was measured to be less than 0.5 dB for any design.

A more difficult approach was undertaken by Ren *et al.* [175] who fabricated Y-splitters in Ti:Sapphire crystals with depressed cladding based on the multiscan technique. The V-shaped splitting area design suffered from high excess losses of $\sim$3.3 dB at 1064 nm for the smallest divergence angle between the arms (0.5°). This underpins the importance of the design choice of the splitter since the refractive index change was reasonably high ($6\times10^{-3}$).

A cosine S-bend design is here preferred to mitigate transition loss as derived in the previous section. This was applied by Koo *et al.* [176] exploiting UV direct-written waveguides in PMMA-based copolymers. Y-Splitters with cosine bends facilitated a low 0.4 dB excess loss and a splitting ratio of $\sim$50% at 633 nm. This is very similar to the splitting ratio and excess loss achieved at 4 $\mu$m in GLS.

Demonstrations of mid-infrared 1×2, 1×3 and 1×4 Y-splitters in bismuth germanate [109] showed reasonably even splitting ratios with an additional excess loss of 0.3 dB at 4 $\mu$m wavelength. However, a >7 mm splitting length was necessary to achieve a 50 $\mu$m separation of the output arms. For greater separations of 125 $\mu$m and 250 $\mu$m, this would lead to a 17.5 and 35 mm length, respectively compared to the GLS cosine S-bend based Y-splitters of 5 and 7 mm for the same separation.

In summary, the otherwise negative aspect of sequentially inscribing waveguides was here utilised as an advantage. By balancing the asymmetry of the Y-splitter S-bends with the asymmetry of the waveguide inscription order, an achromatic 50/50 splitting response between 3.6 - 4.2 $\mu$m was demonstrated.

## 6.3 Directional couplers

This section is concerned with the theory behind coupled modes and discusses the fabrication and characterisation of FLDW symmetric and asymmetric directional couplers. The scope of directional coupler applications reaches from simple power splitters to Mach-Zehnder interferometer and ring-resonators over electro-optic switches. The heart of the photonic nulling interferometer in its simplest form is a 2×2 directional coupler that achieves a high interferometric extinction of polychromatic starlight. This requires an almost perfect 50/50 power splitting capability with either of the input arms to achieve a mid-infrared starlight suppression at a level of $10^{-5}$ to enable the detection of Earth-like planets revolving a sun-like star [177].

In this work we concentrate on two types of couplers: the symmetric and asymmetric directional couplers [178]. The symmetric coupler is formed by two identical waveguides that are brought in close proximity over a parallel section of length $L$, i.e. the interaction region (Fig. 6.9 left). It allows for an optical power transfer through optical tunnelling, also called evanescent coupling. The symmetry is given along the central lines in X- and Z-directions. The asymmetric coupler is by contrast only symmetric along its central line in X-direction. The waveguides in the interaction region have uniformly different propagation constants $\beta_i \neq \beta_j$. Such a difference can be achieved through a difference in widths and/or a difference in refractive indices. (Fig. 6.9 right).

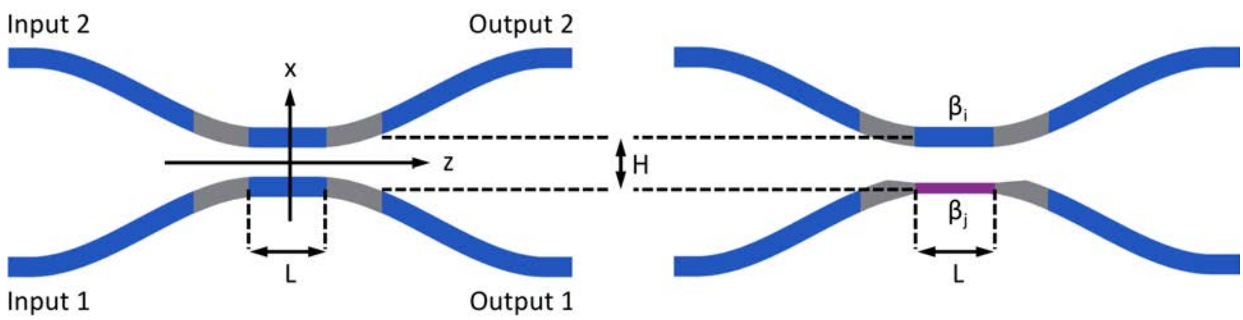


FIGURE 6.9: Directional symmetric (left) and asymmetric (right) coupler layouts with two input and two output ports. The grey S-bend zone contributes to the power transfer between waveguides even before the start of the interaction region $L$. Asymmetric couplers have different propagation constants, $\beta_i$ and $\beta_j$, in the coupling region due to different refractive indices or widths.

For simplicity, we first assume that the S-bend shaped input arms are uncoupled when we inject light into Input 1. The normal modes of each waveguide, $i$ and $j$, are then excited with equal phase and power at the beginning of the interaction region $L = 0$. In that region the modes travel with the propagation constants $\beta_i$ and $\beta_j$ where $\Delta\beta \simeq 0$

$$\Delta\beta = |\beta_i - \beta_j| \,. \tag{6.3}$$

The modes interfere as they propagate with the amplitude of each mode given as [179]

$$\psi_1 \;=\; \frac{1}{2}\left(e^{j\beta_i z} + e^{j\beta_j z}\right), \tag{6.4}$$

$$\psi_2 \;=\; \frac{1}{2}\left(e^{j\beta_i z} - e^{j\beta_j z}\right), \tag{6.5}$$

and the powers of the modes

$$P_1 \;=\; \psi_1\psi_1^* \;=\; \cos^2(\kappa z)\, e^{-\alpha_1 z}, \tag{6.6}$$

$$P_2 \;=\; \psi_2\psi_2^* \;=\; \sin^2(\kappa z)\, e^{-\alpha_2 z}, \tag{6.7}$$

with $\alpha$ as the exponential optical loss coefficient and $\kappa$ as the mode coupling coefficient representing the function of the mode tail shape inside the waveguides. If the modes are well confined, the overlapping mode tails only cause negligible perturbation of the weakly coupled approximation. The coupling coefficient is then given by the function

$$\kappa \;=\; \frac{2h^2\, qe^{-qH}}{\beta d\left(q^2 + h^2\right)} \tag{6.8}$$

where $\beta$ and $h$ are the propagation constants in the Z- and X-directions, $q$ is the extinction coefficient in the X-direction, $H$ is the separation and $d$ is the width of the waveguide.

The Equations (6.6) and (6.7) show the distinct phase difference of the two modes where the mode in waveguide 2 lags $\pi/2$ behind the mode in waveguide 1 when coupling into input 1. This leads to a phase relation that produces a continuous transfer of energy. An entire power transfer is completed at distance $z$ for $kz = \pi/2$ where the phase of mode 1 now lags behind the phase of mode 2 for $\pi/2 \leq kz \leq \pi$ and so on.

The coherent energy transfer arises from basic mechanisms of general field theory [180]. The dielectric material is polarised by the field in the initiating waveguide. Both field and polarisation are in phase with each other, even inside the volume between the waveguide structures due to the extended mode tails. Energy is generated if polarisation leads the field, while energy dissipation occurs if polarisation lags the field. Hence the name directional coupler, since it is not possible to couple energy into a backward wave in the initiating waveguide propagating in the Z-direction.

The wavelength dependent power transfer between the waveguides 1 and 2 changes therefore with the interaction length $L$ and can be described by coupled mode theory (CMT) [107, 181]. The normalised power splitting ratio at the outputs 1 and 2 is described as a sinusoidal function [182] with $P_{\text{bar}} = P_1$ and $P_{\text{cross}} = P_2$ for light coupled into waveguide 1 and vice versa using

$$\frac{P_{\text{cross}}(\lambda)}{(P_{\text{cross}}(\lambda) + P_{\text{bar}}(\lambda))} = \sigma(\lambda)^2 \sin^2\left(\frac{\kappa(\lambda)}{\sigma(\lambda)}L + \phi\right). \tag{6.9}$$

A non-negligible power transfer arises from the S-bends at the start and end of the coupling region, marked as a grey shaded area in Figure 6.9. The contribution is taken into account by the bending phase $\phi$ [183]. The dephasing term

$$\sigma(\lambda) = \left[1 + \left(\frac{\Delta\beta(\lambda)}{2\kappa(\lambda)}\right)^2\right]^{-1/2} \tag{6.10}$$

restricts the cross coupling ratio relative to the difference in propagation constants $\Delta\beta = |\beta_i - \beta_j|$ of the two parallel waveguides. The sequential fabrication of adjacent waveguides with FLDW can lead to a difference in propagation constants where the second waveguide is inscribed into a pre-modified stress region caused by a previously applied femtosecond laser irradiation [184]. Similarly, for an asymmetric coupler the waveguide width and/or refractive index is altered intentionally (Fig. 6.9) to feature different propagation constants. Consequently, the power distributions of the two modes are expressed as [107]

$$P_1(z) = \cos^2(gz)\, e^{-\alpha z} + \left(\frac{\Delta\beta}{2}\right)^2 \frac{\sin^2(gz)}{g^2} e^{-\alpha z} \tag{6.11}$$

and

$$P_2(z) = \frac{\kappa^2}{g^2} \sin^2(gz)\, e^{-\alpha z}, \tag{6.12}$$

with

$$g^2 \equiv \kappa^2 + \left(\frac{\Delta\beta}{2}\right)^2. \tag{6.13}$$

The power transfer still occurs but is incomplete since (6.11) does not yield a zero value for any $z$ as illustrated in Figure 6.10.

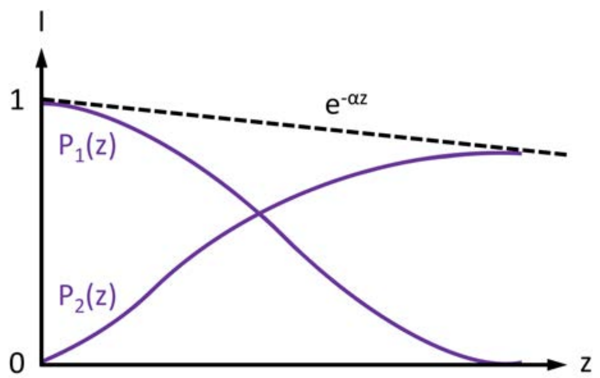


Figure 6.10: Theoretical power transfer between the waveguides 1 and 2 with different propagation constants $\Delta\beta$. The power transfer of $P_2$ appears incomplete by not reaching $I = 1$. This can be described by the term $e^{-\alpha z}$ (dotted line). Image derived from [107].

### 6.3.1 Symmetric directional couplers

The first report of a femtosecond laser direct-written two-port coupler appeared in 2001. Streltsov *et al.* [185] fabricated two closely spaced waveguides for a 633 nm wavelength in borosilicate glass, one straight and the other with two arcs and a straight middle segment. The study was extended by Minoshima *et al.* [186] by studying the effect of varying interaction length and waveguide separation using soda lime glass. It was finally Chen *et al.* [182] who reported a comprehensive study on symmetric and asymmetric couplers investigating the spectral response for a 400 nm wavelength window (1250 - 1650 nm) and engineering devices with wavelength-flattened response. The first directional coupler in GLS however was demonstrated at 3.39 $\mu$m wavelength by Arriola *et al.* [129] using raised sine S-bends. Similar to his approach, symmetric directional couplers were designed, fabricated and characterised in this study for their splitting ratio and chromaticity.
The proposed nulling interferometer chip design (Fig. 6.1) requires an asymmetric architecture for the symmetric coupler. The inputs and outputs are spaced 500 $\mu$m and 250 $\mu$m apart in order to attach a micro-lens array at the front end of the chip and a fiber coupler V-groove at the output. This design calls for cosine S-bends at the input with a7 mm length while the two S-bends at the output are 5 mm long. The four S-bends fan into the coupling region that was varied in length between 0 - 7.5 mm with incremental steps of 0.5 mm. The center-to-center separation on the other hand was fixed to either 21 or 26 $\mu$m (Fig. 6.11). Due to the waveguide separation in the coupling region, the lateral offsets become smaller by half of the separation compared to the designs with 250 and 125 $\mu$m offsets in Section 6.1. This improves the S-bend bending radius to a minimum of ~45 mm. However, this has neither a negative nor positive effect since no bending loss is expected above a minimum bending radius of 40 mm. The highest fabrication symmetry was accomplished by inscribing the tracks of the first waveguide sequentially from outside to inside followed by the second waveguide in the same order.

Since the polished end-faces of the glass are prone to form Fabry-Perot cavities, the chip was characterised using broadband light as described in Section 3.3.5. The splitting ratio for each coupler was extracted at three different wavelengths, 3.75, 4.00 and 4.25 $\mu$m. The

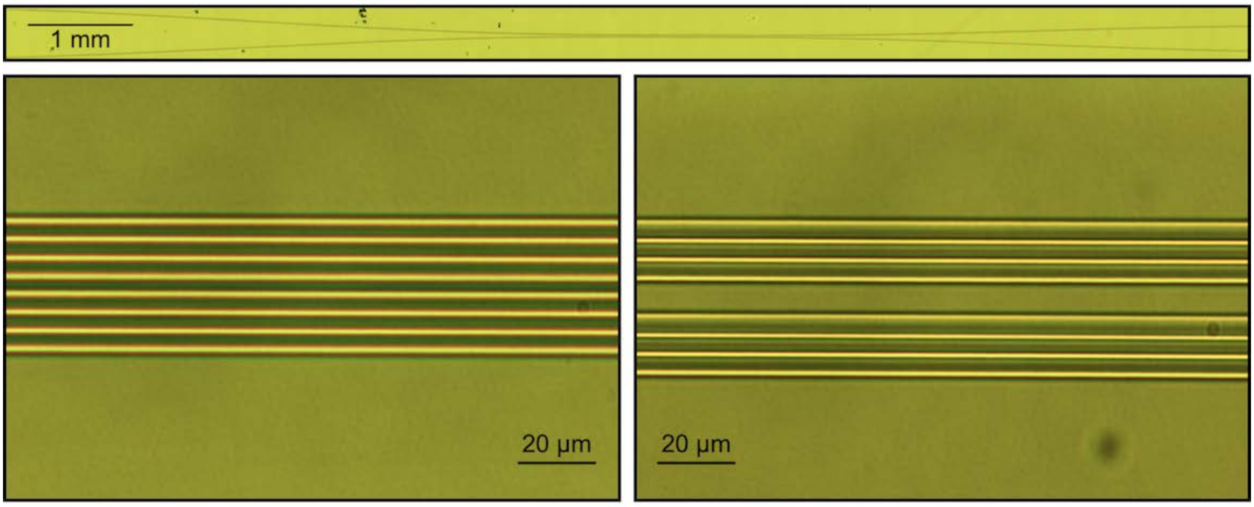


Figure 6.11: Top: View on a symmetric directional coupler with a 1 mm interaction length. The in- and output waveguides are spaced 500 $\mu$m and 250 $\mu$m apart, respectively. Bottom: Interaction region of a 21 $\mu$m (left) and 26 $\mu$m (right) separation.

experimental data was fitted with Equation (6.9) for the three wavelengths with a root mean square error (RMSE) of 3.4% - 4.8% for couplers with a 21 $\mu$m separation and a RMSE of 2.7 -2.8% for 26 $\mu$m separation couplers, summarised in Figure 6.12.

Couplers with a 21 $\mu$m separation show strong premature coupling in the S-bends where more than 70% of the light is transferred before the start of the interaction region due to their close vicinity. But despite the very small separation between the 19.4 $\mu$m wide waveguides, the coupling coefficient $\kappa$ of 0.69 - 0.71 rad/mm is relatively small compared to published values of 1 - 2.5 rad/mm [182]. These values underpin the very strong mode confinement obtained with cumulative heating waveguides. The result is a generally small overlap of the evanescent tails where a small $\kappa$ leads to a relatively slow power transfer. For longer wavelengths on the other hand, the electric field amplitude of the guided mode extends further into the bulk [187] which results in a marginally larger overlap of the evanescent tails. This is sufficient to foster the energy transfer illustrated by the uniform drift of the oscillatory period to higher frequencies.

An evidently small $\Delta\beta$ of 0.32 - 0.43 rad/mm between 3.75 and 4.25 $\mu$m wavelengths emphasises the small asymmetry between the closely spaced waveguides. These small propagation

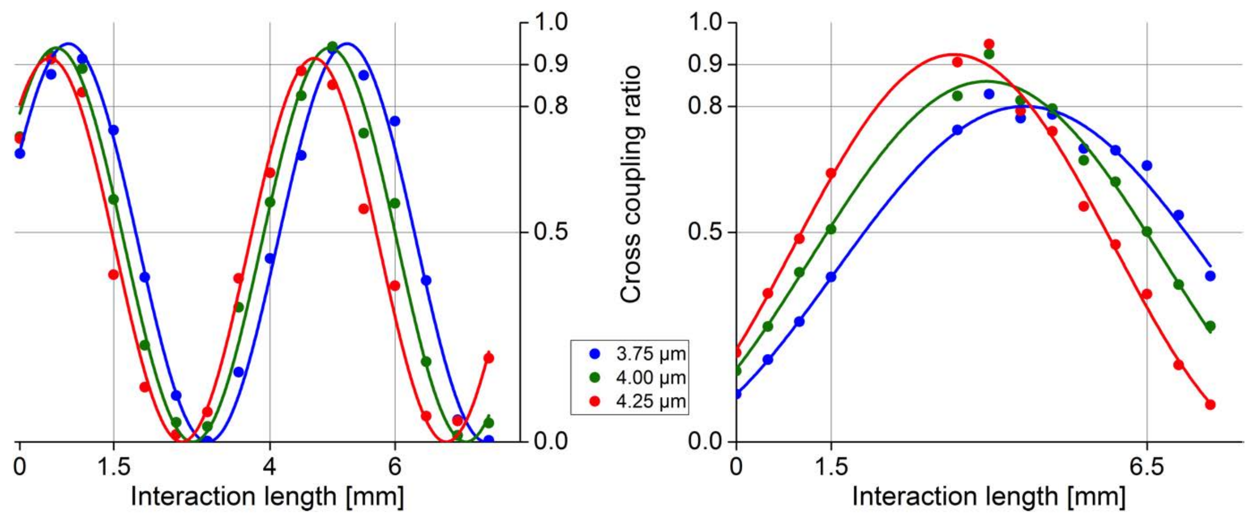


FIGURE 6.12: The cross coupling ratios at 4 $\mu$m reveal almost 50/50 power divisions for directional couplers with a 21 $\mu$m separation with lengths 1.5, 4 and 6 mm (left) and at 1.5 and 6.5 mm for couplers with a 26 $\mu$m separation (right). The smaller separation shows stronger coupling and therefore accelerated power transfer, but also causes strong premature coupling in the S-bends. The three investigated wavelengths (3.75, 4 and 4.25 $\mu$m) show different maximal cross coupling ratios, indicating a change of the dephasing term and hence a change in $\Delta\beta$.

constant offsets for thermally inscribed couplers are similar to the results for couplers fabricated in GLS using the multiscan method in the athermal regime presented by Diener *et al.* [184]. It is a sign for a similarly small stress field surrounding the waveguides. However, the dephasing $\sigma$ changes relative to changes in $\Delta\beta$ which in turn restricts the cross coupling ratio, as shown in Equations (6.10) and (6.9). Here, the maximum cross coupling ratios are 91.6 - 95% (Fig. 6.12 left). These are typical values, also reported by other authors for FLDW directional couplers with maximum cross coupling ratios of 92% and 90% for monochromatic light in GLS [129] and bismuth borate glass [108], respectively. The cause is, as stated above, the inscription of the second waveguide into a pre-modified area that leads to a different refractive index and hence a different propagation constant.

A similar dephasing for both coupler separations of 21 $\mu$m and 26 $\mu$m at 4.25 $\mu$m wavelength (red lines in Fig. 6.12) results in a comparable maximum cross coupling, but also illustrates that the dephasing has a higher influence on the dispersion when $\kappa$ remains small. Hence, it is beneficial to increase the coupling coefficient as high as possible by simply reducing the spacing between the waveguides in the coupling region.

A larger separation of 26 $\mu$m also leads to a greater distance between the pre-modified area and the second waveguide. As a result, $\Delta\beta$ decreases from 0.35 rad/mm for 21 $\mu$m separated couplers to 0.21 rad/mm for 26 $\mu$m separated couplers at 4 $\mu$m wavelength. The power transfer proceeds more slowly for the larger separation of 26 $\mu$m as a consequence of smaller coupling coefficients [181] $\kappa$ = 0.23 - 0.29. This is reflected in longer periodicities for power exchanges (Fig. 6.12 right). Equal power splitting ratios can be found at beat lengths of

$$0.5\,n + 0.25 \tag{6.14}$$

with $n \in \mathbb{N}_0$, where one beat length expresses the gradual transfer of light into the opposite waveguide and back. The 0.25 beat length for couplers with a 21 $\mu$m separation is located within the S-bends and before the coupling region due to premature coupling. The increase in separation from 21 $\mu$m to 26 $\mu$m reduced the bending phase from $\phi$ = 1.02 - 1.22 rad to 0.39 - 0.50 rad. This reduced the premature coupling and allowed for the identification of two 50/50 couplers at 0.25 (L = 1.5 mm) and 0.75 (L = 6.5 mm) beat lengths for a 4 $\mu$m wavelength (Fig. 6.12).

The chromaticity is illustrated as the difference between minimum and maximum cross coupling ratios within a 500 nm wavelength window where a desired achromaticity would be reflected as 0% variation across the wavelength band. Figure 6.13 shows that the dispersion at longer interaction lengths leads to an increase in chromaticity from 23.8% to 29.5%. Shorter interaction lengths are therefore preferred to achieve a more broadband device. In comparison, Tepper *et al.* [131] reported directional couplers inscribed in GLS glass with a chromaticity of 40% across a wavelength range of 3.1 - 3.6 $\mu$m. The athermally inscribed multiscan couplers feature raised-sine S-bends that induce strong premature coupling enhanced by only weakly guided modes. Thus, the S-bends hold the position of the 0.25 beat length which is the first 50/50 power splitting point. The large chromaticity is therefore mostly attributed to the operation at the 0.75 beat length with an additional chromatic dispersion from a long interaction length of 4 mm.

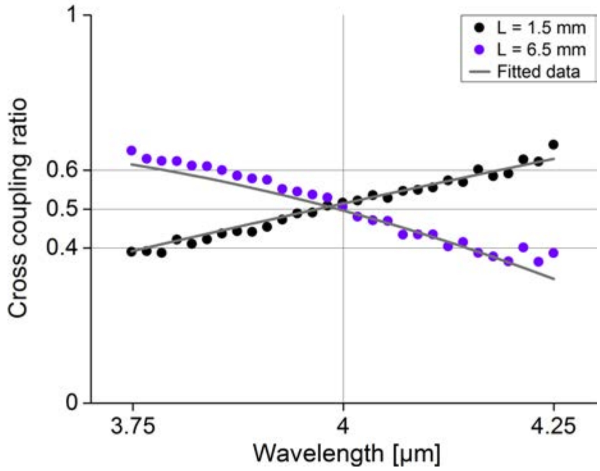


FIGURE 6.13: The slope of two 26 $\mu$m separated 50/50 couplers are shown. The interaction length of 1.5 and 6.5 mm correspond to a 0.25 (black) and 0.75 (purple) beat length. The progressing chromatic dispersion for couplers as a function of increasing length is illustrated by the increasing difference in maximum and minimum cross coupling ratios over a 500 nm wavelength window.

Better results were achieved by Tepper *et al.* [188] investigating a FLDW zero-gap coupler fabricated with depressed cladding and first demonstrated by Gross *et al.* [43]. The maximum and minimum cross coupling were measured to be 41% to 60% between 3.1 - 3.6 $\mu$m with a 50/50 crossing point at 3.3 $\mu$m. Even though these devices are usually inherently achromatic, the chromaticity of 19% can be attributed to the fabrication process.

In the case of FLDW symmetric couplers, it has been shown that a perfect symmetry cannot be realised due to the nature of sequentially inscribed waveguides. Nevertheless, a relatively flat wavelength response can be achieved in directional couplers by reducing the separation of the coupling region to a minimum. This minimum is found at a separation where the premature coupling in the S-bends is weak enough to allow the 0.25 beat length to be within the interaction length. Moreover, the interaction length needs to be as short as possible to reduce chromatic dispersion.

### 6.3.2 Asymmetric directional couplers

The previous section has shown that strong modal dispersion leads to a wavelength dependence of directional couplers. Introducing an asymmetry in one of the coupler arms can lead to a wavelength-flattened response. This asymmetry can be achieved for instance by changing the propagation constant $\beta_i$ or $\beta_j$ through altering the width or refractive index of the waveguide.

Chen *et al.* [182] demonstrated that shorter separations and lengths, proven by Equation (6.9), induce a wavelength-flattened response in asymmetric couplers. The minimally dispersive dephasing $\sigma$ can be balanced with the bending phase $\phi$ by reducing the waveguide separation utilising premature coupling in S-bends. Especially with small distances, the coupling coefficient $\kappa$ and the bending phase $\phi$ are expected to feature a strong opposing slope with little contribution of the dephasing $\sigma$. It was shown that any desired splitting ratio could be fabricated in boroaluminosilicate glass over a broad band of 1250 - 1650 nm.

A different way to improve the wavelength-flattened response was reported by Olivero *et al.* [189] by using the UV direct-writing technique. His approach was to introduce a high dephasing to limit the maximum power transfer to exactly 50%. At the maximum and minimum of the sinusoidal function, a balanced and opposing dispersion condition for $\kappa$ and $\phi$ terms is more likely to be met [182]. The result was an even power splitting between 1450 - 1750 nm.

The approach was therefore to test the effect of varying propagation constant differences $\Delta\beta$ in directional couplers. For simplicity, the coupler design from the previous section was changed to a 2×2 coupler with both an input and output waveguide separation of 125 $\mu$m. This reduced each S-bend length to 3.3 mm but also brought the opposing S-bends together earlier facilitating longer premature coupling. For that reason, a 26 $\mu$m coupling region separation was chosen to limit the dispersion contribution of $\phi$.

The asymmetry was introduced by changing the writing velocity of the laser since it alters width and refractive index of the waveguide simultaneously. This introduces a high $\Delta\beta$ which is useful in the case of short interaction lengths. The translation stages feature a high precision and repeatability and are thus preferred over tuning the inscribing pulse energy.

### Asymmetry induced by high translation velocities

Five sets of directional couplers were fabricated where each set consisted of eight couplers with different interaction lengths of 0 - 7 mm in 1 mm steps. The left waveguide, comprised of three tracks, was inscribed with 13 nJ and a 100 mm/min translation velocity resulting in a 19 $\mu$m wide structure. For the right waveguide, the translation velocity was changed to alter its width and refractive index and thus the propagation constant. An abrupt acceleration or deceleration would lead to an inaccurate performance of the translation stage, and more importantly to an instant change in waveguide width causing transitional loss at the interfaces. This was overcome by linearly changing the velocity over a 0.5 mm transition length, forming tapers in the S-bend before entering and exiting the coupling region (Fig. 6.9 right). Five velocities were tested, namely 100, 120, 200, 300 and 500 mm/min with the first set having an equal velocity for left and right inscribed tracks used for reference purposes.

The cross coupling ratios at 4 $\mu$m wavelength were extracted from light dispersed broadband measurements and fitted with root mean square errors (RMSE) between 0.9 - 2.6% to Equation (6.9). The solid lines represent the least-squares-error sinusoidal (Fig. 6.14 left). We established in the previous section that inscribed waveguides create a surrounding stress field considered as a pre-modified area [184]. In symmetric directional couplers, this led to a propagation constant difference and incomplete coupling (86.0%) even though both waveguide arms were inscribed with the same translation velocity of 100 mm/min. This means that the same inscription parameters cause a stronger modification of the glass since the area already experienced a small increase in refractive index and thus the guided mode exhibits a larger propagation constant. By increasing the inscription velocity at the second arm, less energy is deposited inside the glass. This can be observed when increasing the velocity to 120 and also 200 mm/min. The cross coupling increases to 91.0 and 93.5%, respectively, hence the dephasing term in Equation (6.10) increases. This causes $\Delta\beta$ first to decrease from 0.21 to 0.15 and 0.13 rad/mm before it rises again to 0.27 and 0.56 rad/mm for inscription velocities of 300 and 500 mm/min (Fig. 6.14 right). Diener *et al.* [184] discovered the same effect in neighbouring multiscan waveguides inscribed in GLS. The author showed that a small increase in writing velocity can lead to an equal $\beta_i$ and $\beta_j$ and hence eliminate the propagation

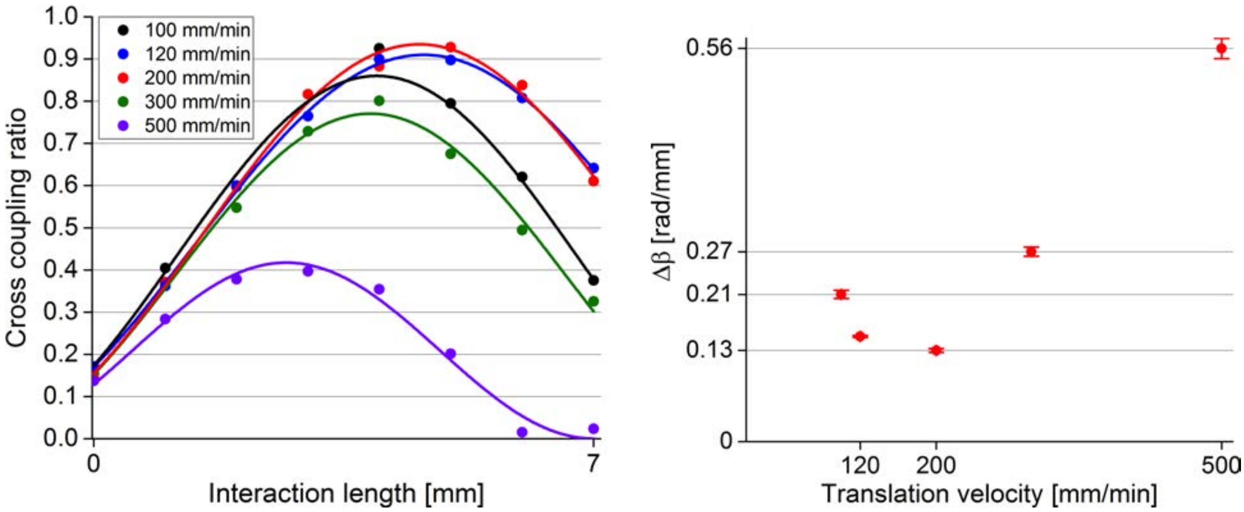


Figure 6.14: Left: The cross coupling ratios at 4 $\mu$m wavelength show the effect of incomplete coupling for asymmetric couplers. Surprisingly, the maximum cross coupling improved for 120 and 200 mm/min. Right: Responsible for the improved coupling is the reduction in propagation constant difference $\Delta\beta$ due to an improved balance between the pre-modified area and inscription parameters. Equal $\beta$ in both coupler arms should be found using an inscription velocity between 120 and 200 mm/min in the second arm.

constant difference at 3.39 $\mu$m. Therefore, a 100% power transfer should be attainable for the presented couplers with waveguides inscribed between 120 and 200 mm/min to achieve $\Delta\beta = 0$ rad/mm.

The strong mode confinement and the 26 $\mu$m separation are responsible for a generally small coupling coefficient $\kappa$. A coupler was presented in the previous symmetric coupler section with identical fabrication parameters (100 mm/min translation velocity). Both couplers feature an equal value for $\Delta\beta = 0.21$ rad/mm and nearly the same value for $\kappa = 0.24$ rad/mm as the current asymmetric coupler $\kappa = 0.23$ rad/mm at 4 $\mu$m. This emphasises a high repeatability of the presented devices. At 4 $\mu$m, $\kappa$ first decreases for 120 and 200 mm/min inscriptions before it increases again. This marginal increase from 0.23 to 0.25 rad/mm for a decreasing waveguide width is caused by a decline in mode confinement. The mode tail extends further into the bulk between the waveguides and accelerates the power transfer. This can be seen by the increasing frequency of power transfer for higher translation velocities of 300 and 500 mm/min (Fig. 6.14 left).

As we learned from Section 4.2.2, the propagation loss depends on the track separation and

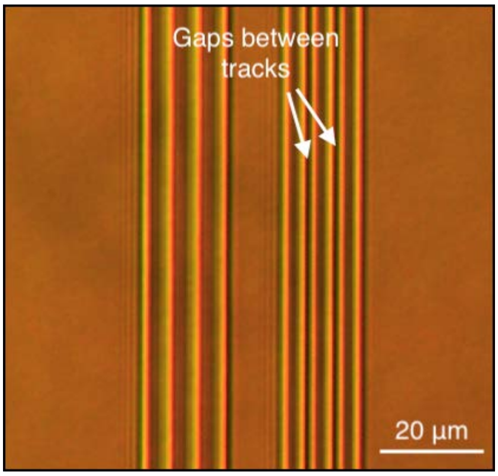


FIGURE 6.15: Waveguides fabricated with a translation velocity of 500 mm/min are reduced in width but also lack an appropriate overlap which introduces additional propagation loss.

increases for smaller waveguide diameters as present in the right waveguide in Figure 6.15. This waveguide inscribed at 500 mm/min has a width of 17 $\mu$m compared to a 19 $\mu$m of the first waveguide. More importantly, the three waveguide tracks stopped overlapping and exposed unmodified glass between the tracks. This not only increases the propagation loss to ∼0.5 dB/cm but also contributes to the decrease of the overall refractive index change and thus the propagation constant. This way we achieve the intended change in $\Delta\beta$ but at the expense of an additional ∼ 0 - 0.2 dB propagation loss for couplers with 0 - 7 mm interaction length. The additional loss can be a significant contribution to a device with a projected internal loss of <1 dB.

## Asymmetry induced by low translation velocities

This led to the conclusion to apply lower translation velocities in order to alter the waveguide width and refractive index to create the desired propagation constant difference $\Delta\beta$. Sets of couplers with a 26 $\mu$m separation and interaction lengths 0 - 7 mm in 1 mm steps were fabricated. The translation velocity of the first waveguide was kept at 100 mm/min while the velocity of the second waveguide was reduced from 75 to 55 mm/min with a 5 mm/min step size. A change in physical dimension was not distinguishable between the two waveguides inscribed with 100 and 55 mm/min using a DIC microscope, as it was for couplers with higher inscription velocities. However, the use of lower velocities was sufficient to cause a change in coupling behaviour. At 4 $\mu$m wavelength, this is reflected by a small gradual increase in $\Delta\beta$ from 0.24 to 0.32 rad/mm for decreasing translation velocities. This corresponds to a difference in refractive index $\Delta n$ = 1.5 - 2$\times 10^{-4}$ between the two arms of the coupler. Similarly, $\kappa$ increases from 0.26 to 0.34 rad/mm for decreasing translation velocities. Both parameters lead to an earlier described accelerated cross coupling with reduced maximum cross coupling ratio (Fig. 6.16 left). The cross coupling ratios were measured with an RMSE of 2.8 - 4.7% for wavelengths of 3.75 - 4.25 $\mu$m.

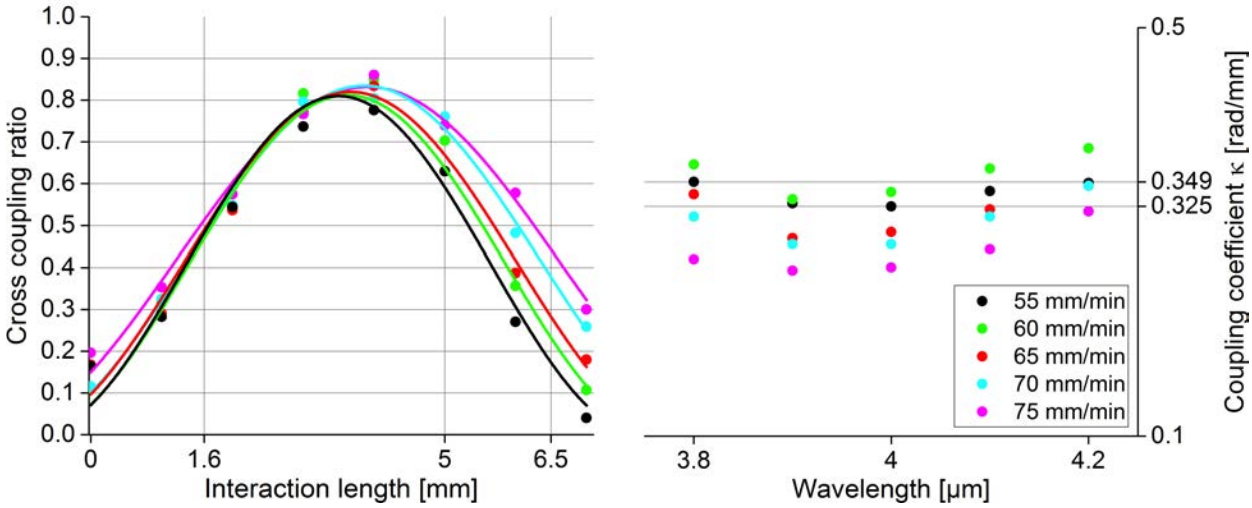


Figure 6.16: Left: Cross coupling ratio at 4 $\mu$m wavelength. Applying lower translation velocities introduces an increase in propagation constant difference $\Delta\beta$ and coupling coefficient $\kappa$ that both foster an accelerated power transfer but a decreased maximum cross coupling. Right: Couplers with the highest $\Delta\beta$ (lowest translation velocity) feature the lowest minimum-to-maximum $\kappa$ variation of 0.349 - 0.325 rad/mm. The general flat spectral response for all designs expresses a low contribution to the dispersion.

The aim of these asymmetric couplers is to counteract natural dispersion as the key to a wavelength-flattened behaviour. Three main factors influence the dispersion in conjunction: the dephasing $\sigma$, the coupling coefficient $\kappa$ and the bending phase $\phi$ [182].

Since we increase the propagation constant offset $\Delta\beta$ every time we reduce the inscription velocity from 75 - 55 mm/min, the dephasing term reduces as well according to Equation (6.10). The dispersion in form of the minimum-to-maximum of the maximum cross coupling ratios between 3.8 - 4.2 $\mu$m slowly increases from 11.8 - 15.3% with a decreasing inscription velocity (Fig. 6.17 left). This was expected since the amplitude is the square of the dephasing term $\sigma$. The coupling constant therefore must have a relatively flat chromatic response with a minimum-to-maximum $\Delta\kappa$ that improves linearly from 0.065 - 0.024 rad/mm for inscription velocities of 75 mm/min down to 55 mm/min (Fig. 6.16 right).

The coupling constant itself increases with lower inscription velocities and hence higher $\Delta\beta$. This highlights that a higher energy deposition in the glass volume during fabrication does not necessarily further increase the refractive index change. Instead, a weaker refractive index change leads to less confined modes that enhance the coupling.

Figure 6.16 (right) shows that $\kappa$ takes a slightly negative slope for shorter wavelengths that levels at approximately 3.95 $\mu$m and becomes positively sloped for longer wavelengths, as similarly seen for the maximum cross coupling ratio (Fig. 6.17 left).

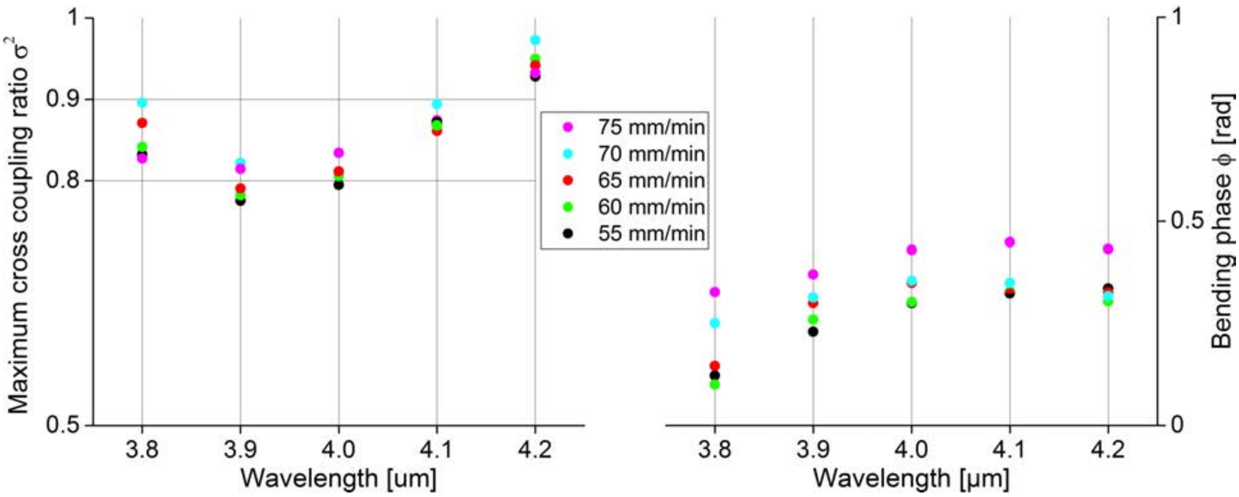


FIGURE 6.17: The maximum cross coupling ratio $\sigma^2$ (left) and bending phase $\phi$ (right) show opposing slopes between ~3.8 - 3.95 $\mu$m wavelengths that potentially cancel out the dispersion provided that $\kappa$ is wavelength independent (Fig. 6.16 right).

The change from a negative to a positive slope shows that the common misconception that $\kappa$ can only increase monotonically with $\lambda$ [178] was justifiably disproven by Chen *et al* [182] and also described by Eaton *et al.* [190]. Both authors explained the behaviour based on a symmetric coupler by analysing the functional form

$$\kappa = \frac{k_0(\lambda)^2}{2\beta_0(\lambda)} \iint_2 E_1(x,y)\, E_2(x,y)\, dxdy \tag{6.15}$$

with $k_0(\lambda)^2$ as the free propagation constant, $\lambda$ as the wavelength and $E_1$ and $E_2$ as the electric field distributions for coupler arm 1 and 2. Since the integral is applied over the second coupler arm, $E_1$ increases at longer wavelengths due to a weaker mode confinement in the second waveguide and hence stronger coupling. Due to the weaker mode confinement, $E_2$ simultaneously decreases since less light is carried in the center. This shows that $\kappa$ can also decrease with wavelength.

An opposite behaviour was found for $\phi$, exhibiting a positive gradient at shorter wavelengths and becoming flat or slightly negatively sloped after 4.1 $\mu$m wavelength (Fig. 6.17 right). Between ~3.8 - 3.95 $\mu$m, both graphs for $\kappa$ and $\sigma^2$ show the strongest opposing slopes against $\phi$ for the three lowest inscription velocities.

As a result, the dispersion is mostly equalised by the opposing slopes of $\kappa$ and $\phi$. Additional dispersion caused by the influence of $\Delta\beta$ is potentially counterbalanced as well by the opposite dispersion of the bending phase. For longer wavelengths, again opposite but dissimilar slopes are apparent that might only reduce rather than counteract the dispersion.

It is apparent from Figure 6.16 (left) that 50/50 power splitting ratios are located at around 1.6 and 6 mm interaction lengths for couplers with translation velocities of 65, 60 and 55 mm/min. The first location at a ~0.25 beat length has a wavelength dependent positive slope as shown for symmetric couplers in Figure 6.13. The introduced difference in propagation constant therefore amplifies the dispersion rather than preventing it. This is nicely illustrated in Figure 6.18 where a decrease in inscription velocity impairs the chromaticity from 30.9% to 37.8% and 40.0% with increasing dephasing. These values are much higher than the chromaticity of 23.8% for symmetric couplers between 3.75 - 4.25 $\mu$m.

Consequently, the 0.75 beat length was chosen to inscribe eleven couplers with a finer step size of 100 $\mu$m between 5.5 and 6.5 mm for each velocity. For simplicity, these couplers are hereafter referred to as C65, C60 and C55 where 65, 60 and 55 denote the inscription velocity in the second arm. At each velocity, three couplers were found that fulfil the requirements of equal power splitting at 4 $\mu$m wavelength and were investigated for their spectral response (Fig. 6.19).

The common, but reduced dispersion behaviour of mostly negatively sloped plots is shown by couplers with a translation velocity of 65 mm/min. These plots straighten further with

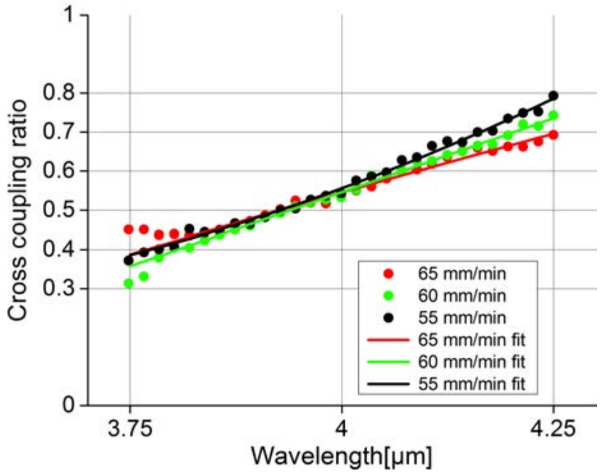


FIGURE 6.18: The slope of three 26 $\mu$m separated asymmetric couplers are shown with an interaction length of 2 mm that is close to 0.25 beat length. Lower inscription velocities lead to an increasing $\Delta\beta$ that amplifies the wavelength dispersion. This is illustrated over a 500 nm wavelength window by the increasing difference in maximum and minimum cross coupling ratios from 30.9% to 40.0%.

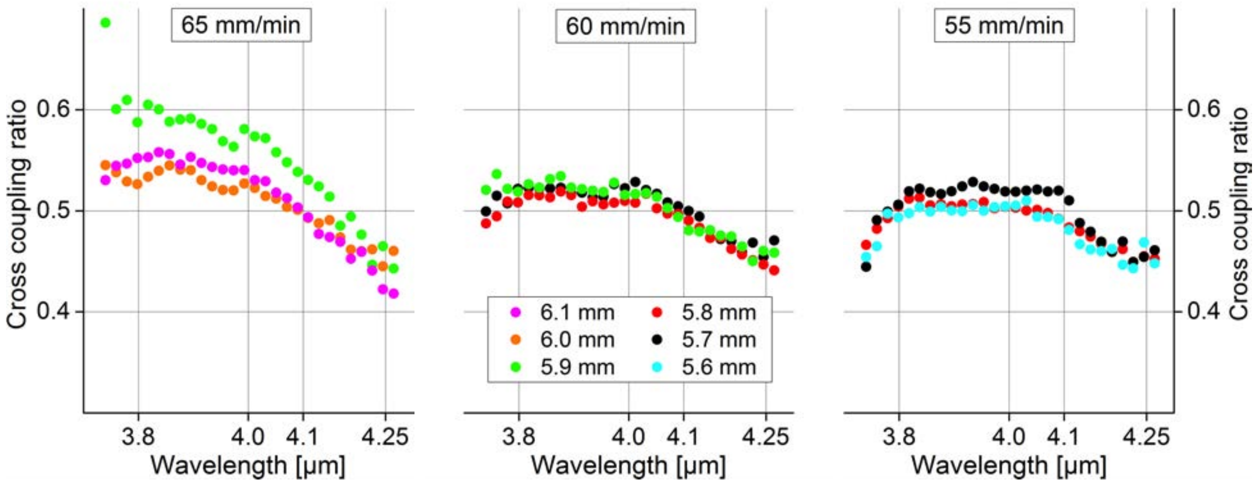


FIGURE 6.19: Cross coupling ratios for couplers with interaction lengths of 5.6 - 6.1 mm and different inscription velocities, 65, 60 and 55 mm/min. The flattest wavelength response with an even power splitting is given by the couplers fabricated with the lowest velocity over the wavelength window 3.8 - 4.1 $\mu$m.

lower inscription velocities, resulting in the flattest response for couplers inscribed with 55 mm/min. Here, interaction lengths of both 5.6 mm and 5.8 mm feature the closest to 50/50 power splitting between 3.8 - 4.05 $\mu$m wavelengths. The average cross coupling ratios of 50.2% and 50.6% have a standard deviation of only 0.3% from their average value. However, the greatest window with the flattest spectral response was obtained at a 5.7 mm interaction length. The 52.0% cross coupling over 300 nm from 3.8 to 4.1 $\mu$m also features a small deviation of 0.3%.

The results for the symmetrical couplers presented in the previous section differ significantly. A ~50/50 coupling ratio was achieved for 4 $\mu$m (Sec. 6.3.1, Fig. 6.13) with a peak-to-peak standard deviation greater than 3.7% within the 3.8 to 4.1 $\mu$m range. This is much larger compared to a standard deviation of 0.3% which makes symmetric couplers only conditionally suitable for interferometric measurements due to the lack of high broadband extinction capability.

It is also apparent that a broad wavelength-flattened response and almost equal power splitting is given by C60 in Figure 6.19 (center). The deviation of 0.6% from the average ~52/48 splitting for lengths of 5.7 and 5.8 mm is comparably small over the wavelength window of 3.75 - 4.05 $\mu$m. This tendency can be observed as well for couplers with the highest velocity. This implies that a smaller change in $\Delta\beta$ shifts the achromatic window to shorter wavelengths. In this case, the positive slope of $\phi$ is balanced by the combined and equally strong negative slopes of $\kappa$ and $\sigma^2$ compared to a C55 design. The latter faces a more dominant positive phase constant that overcompensates the dispersion and ends in a strong positive slope for wavelengths below 3.8 $\mu$m.

On the red side of the spectrum, it is noticeable that the slope of the flattest couplers become irreversibly negative at 4, 4.05 and 4.1 $\mu$m for C65, C60 and C55, respectively. For this particular range we should again take a closer look at the behaviour of the three parameters $\kappa$, $\phi$ and $\sigma^2$. The overall positive slopes of these parameters between ~4 - 4.25 $\mu$m for all three designs appear similar and slowly reverse the chromaticity and promote the natural modal dispersion. With the dephasing in the form of $\sigma^2$ having the same slope for all designs, the contribution to the dispersion is equally strong. However, the bending phase has a stronger slope and the coupling coefficient a weaker slope for C55 and vice versa for

C65. Given the circumstances in Figure 6.19, it indicates that after $\sigma^2$, $\kappa$ has a greater influence on the dispersion than $\phi$.

Especially with extremely small distances, $\kappa$ and $\phi$ are expected to feature a strong opposing slope that can cancel each other out with only a small contribution from the dephasing [182], and hence prevent dispersion. However, the asymmetric couplers in this work feature a flatter to a more positive slope for $\kappa$. Symmetric couplers with only a 21 $\mu$m separation also demonstrated positive slopes for $\kappa$ and $\phi$ attributed to the strong mode confinement of the waveguides. This shows the limitation of the coupler and implies that waveguides in the center of the coupler need to overlap for stronger coupling. Such overlap in turn represents a departure from the weakly coupled mode regime to the few mode interference domain resulting in zero-gap couplers.

Remeasuring the power splitting ratio at 4 $\mu$m wavelength with a polariser inserted revealed a polarisation dependency for C55 with a 5.6 mm interaction length (Fig. 6.20). Cross coupling ratios between 46.9 to 53.3 $\pm$ 0.6% were measured with a 10° step size of input polarisation, which deviated from the measurement of 50.5 $\pm$ 0.3% cross coupling for unpolarised light.

With relative phase shift $\pi$ between the two inputs and 50% power transfer from both input

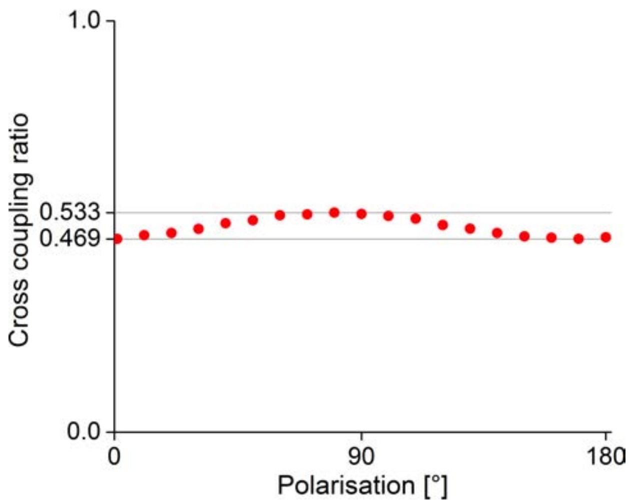


FIGURE 6.20: The cross coupling ratio at 4 $\mu$m wavelength as a function of the input polarisation angle for the asymmetric coupler C55 with a 5.6 mm interaction length shows a polarisation dependency deviating from 46.9 to 53.3 $\pm$ 0.6%.

modes into the adjacent waveguide, it will be possible to obtain efficient destructive interference in one output and constructive interference in the other for nulling interferometry. This can be demonstrated on an interferometric setup like a Michelson Interferometer. For this purpose, the asymmetric directional couplers were characterised at the University of Cologne in terms of their extinction ratio. The test bench is equipped with a super-continuum source (SCS, 3 - 5 $\mu$m) and a reference HeNe laser (3.39 $\mu$m) as shown in Figure 6.21. More details on the setup can be found in [131].

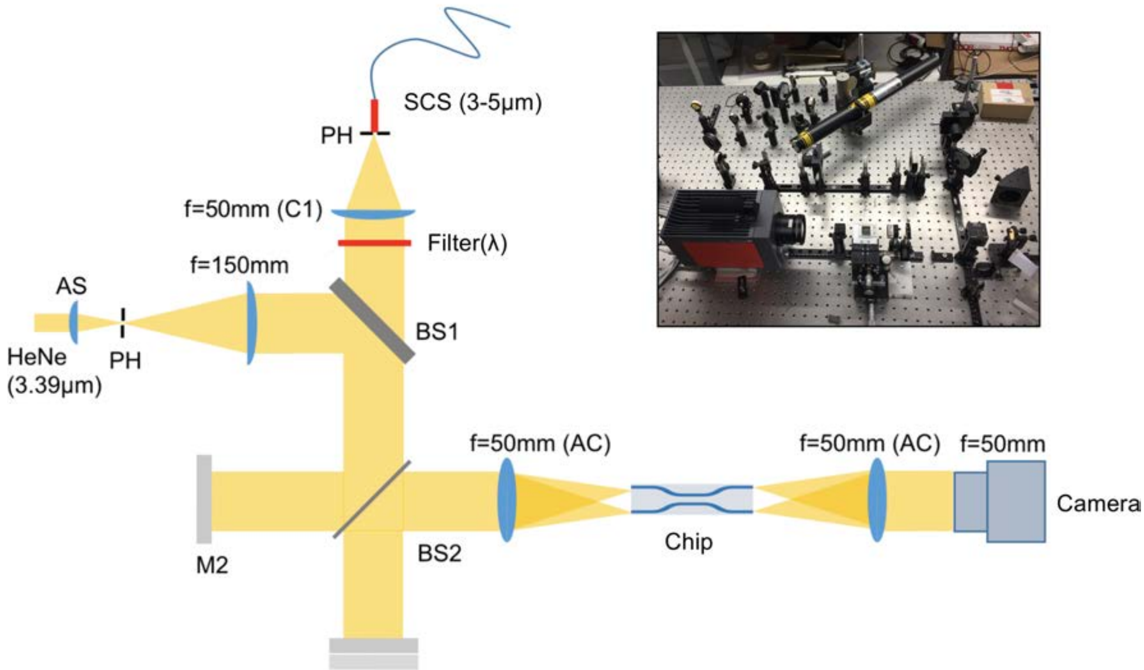


Figure 6.21: Michelson interferometer setup at the University of Cologne [131]. AC: achromat; AS: aspheric lens; BS1: thick beamsplitter; BS2: pellicle beamsplitter; C1, C2: collimators; M1, M2: flat mirrors; PH: pinhole.

Light from the SCS was simultaneously coupled into both input waveguides of a C55 with a 5.6 mm interaction length while the optical path length of one interferometer arm (M1) was scanned with a motorised translation stage. A narrow (LO171681) and a broad (SBP4136-001508) wavelength filter from Laser Components GmbH were both available to investigate the wavelength ranges 3.745 $\mu$m (69 nm FWHM) and 3.8 - 4.1 $\mu$m, respectively. With the broad wavelength filter a high extinction ratio of 98.79 $\pm$ 0.04% was achieved, using a fitted envelope function for the contrast of the interferogram in Figure 6.22.

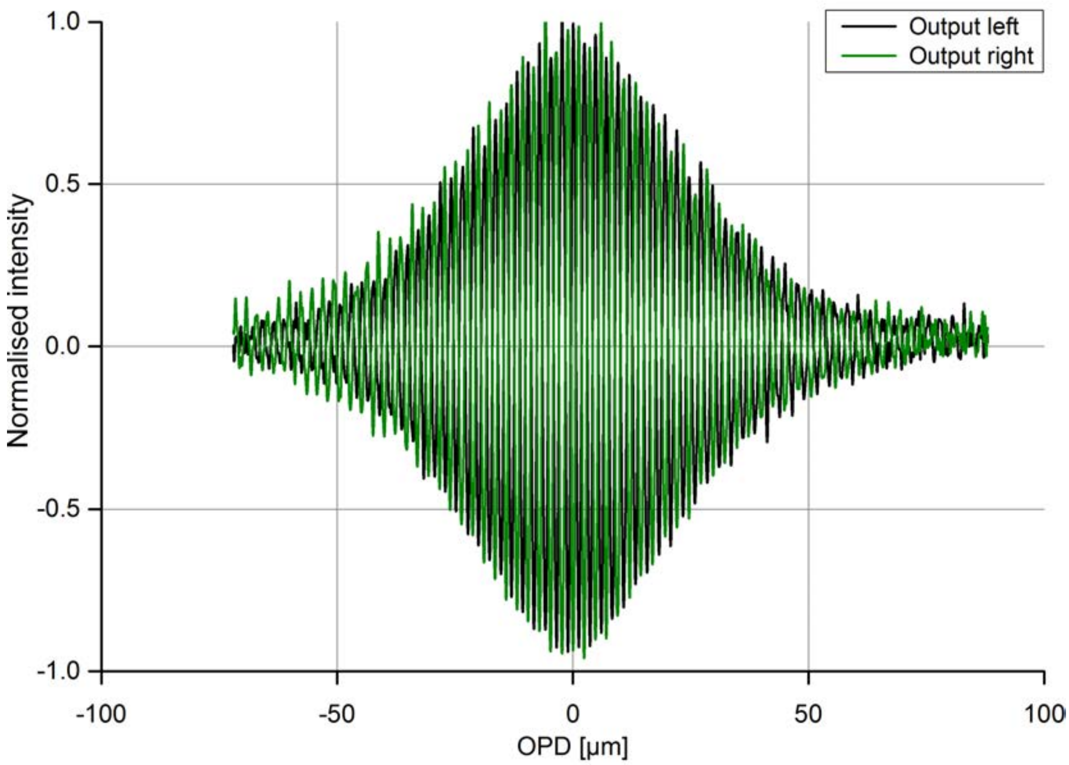


FIGURE 6.22: Experimental interferogram of the outputs of an asymmetric coupler for a wavelength range of 3.8 - 4.1 $\mu$m. A high extinction ratio of 98.79 $\pm$ 0.04 was measured.

Figure 6.19 shows that the splitting ratio at 4.1 $\mu$m is less ideal for high extinction due to a slight deviation of an even splitting ratio. Deploying the SCS with the narrowband filter (3.745 $\mu$m) even led to an extinction ratio of 99.3 $\pm$ 0.08%. However, this measurement was as well conducted outside the ideal splitting ratio window for this coupler between ~3.8 - 4.05 $\mu$m wavelength where an even higher extinction is achievable.

So far, several groups have reported high monochromatic contrasts in couplers for mid-infrared astronomical purposed, but these devices were not able to provide a reasonable broadband contrast [191]. Martin *et al.* [192] presented an on-chip double Mach-Zehnder concept with reverse Y-splitters with a very high extinction capability that depletes 99.98% of monochromatic light at 3.39 $\mu$m. However, a black body source (3.25 - 3.65 $\mu$m) then revealed dispersion and asymmetry inside the chip that only allowed a contrast of ~38% over the 400 nm window. Labadie *et al.* [193] achieved a lower interferometric contrast of 98.1%

at 10 $\mu$m with inverse Y-splitters as beam combiners, but demonstrated a highly stable performance with only 0.1% variation over a 5 h measuring period. The best broadband results were published by Tepper *et al.* [131] for symmetric directional couplers in GLS. Using an unpolarised broadband source, contrasts of 94.9% and 92.1% were given for 3.1 - 3.6 $\mu$m and 4.5 - 4.9 $\mu$m, respectively. The asymmetric directional couplers in this work exceed this performance with a highly achromatic extinction ratio of 98.79 $\pm$ 0.04% and represent the next step towards broadband mid-infrared astronomical interferometry.

The total throughput for a coupler with a total length of 12.3 mm was measured to be $\sim$47% (3.3 dB loss) for broadband light (3.75 - 4.25 $\mu$m) injected into either of the input waveguides. This throughput is an almost twofold improvement over other reports of FLDW directional couplers in GLS [131] for a similar wavelength range. A somewhat higher throughput of 58% was achieved for directional couplers in ZBLAN [188] since this glass only features a Fresnel loss of $\sim$4%. The majority of light for GLS chips is lost as Fresnel reflection with $\sim$15.3% at each air-glass interface. Even higher losses occur as coupling loss between the free space injection and the glass waveguide. The coupling efficiency between the Gaussian distribution of a single mode in a waveguide and the Airy-pattern of an optical beam and is at most 81% [194]. This miss-match and a miss-match in mode-field diameters contributes to an estimated coupling loss of 30% at the input interface, while the output interface only suffers from Fresnel loss. The insertion loss is estimated to $\sim$47% (2.75 dB) with a low propagation loss of 0.22 dB/cm. The discrepancy of $\sim$6% loss may be attributed to coupling losses. The measurement requires very precise coupling and unlike the Fabry-Perot measurement, the setup is not built to determine the losses as accurately. An additional uncertainty is given by the propagation loss that could be higher for light longer than the design wavelength of 4 $\mu$m. The throughput can be vastly improved applying anti-reflection coatings at the chip end-faces. Artemis Optical Ltd. offers thin film coating to reduce reflections from GLS glass surfaces to <1% [195]. Further improvements can be undertaken for more efficient broadband light injection into the chip using an off-axis parabola.

A summary and an associated Table 6.1 of the relevant parameters for directional couplers as well as multimode interference couplers is provided at the end of the following section.

## 6.4 Multimode interference couplers

Multimode Interference couplers (MMI) can be used as power splitters or as couplers with multiple inputs and outputs in a planar dimension as an alternative to directional couplers. Kenchington-Goldsmith *et al.* [196] even proposed a nulling interferometer that consists of three 2×2 MMIs, two of which are connected in parallel to a third. These devices are relatively small and compact with a low sensitivity to fabrication variations because of their simple design. The biggest advantages are their wavelength and polarisation insensitivity [197] that allows for broadband splitting and interferometric beam combination with high extinction ratios [196].

The operation of MMIs is based on the self-imaging principle, a characteristic of multimode waveguides where a single-mode input can create both single or multiple images along the direction of propagation [198–200]. Such a device typically has a number of single-mode input and output waveguides referred to as an N×M coupler (Fig. 6.23 left). The lateral dimension (width) is larger than the transverse dimension (height) and allows for multimode behaviour while the transverse direction is single-mode. It is assumed that these characteristics remain consistent throughout the device which allows the 3-dimensional waveguide to be reduced to a 2-dimensional step-index waveguide structure using the effective-index or the spectral-index method [201, 202].

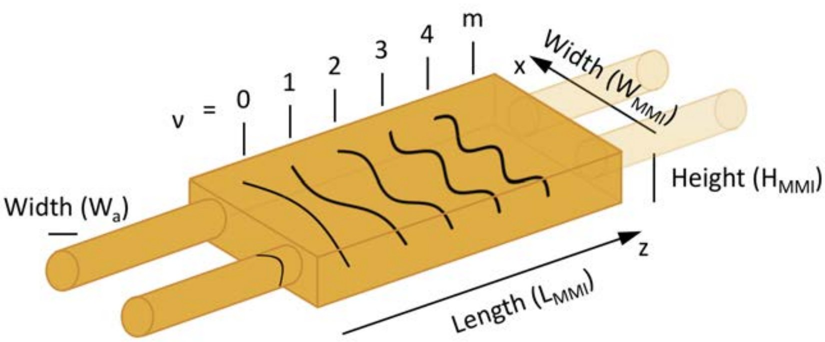


FIGURE 6.23: Schematic of a 3-dimensional two-port multimode interference coupler. A certain number of lateral modes $\nu$ can be found depending on the length $L_{MMI}$.

MMIs are commonly fabricated using lithographic processes to form ridge waveguide structures with core materials like $SiO_2$ [203] but also InP/InGaAsP [204, 205] as well as $Ge_{11.5}As_{24}Se_{64.5}$

for mid-infrared operations [206]. However, previous work by Watanabe *et al.* [207] showed a proof-of-concept for femtosecond laser direct-written 1×2 MMIs in fused silica for light in the visible spectrum. Long filaments were induced to form the width of the MMI whereas the distance of the transverse scanning laser determined the length. This research was later extended by Lui *et al.* [208] using the same material and method. Amorim *et al.* [209] used the multiscan technique in fused silica to fabricate two different designs of 1×2 MMIs that operate at 1550 $\mu$m. The MMI body was formed by several parallel tracks inscribed either parallel to the long side of the MMI or parallel to the short side of the MMI. Both approaches showed similar results in modal distribution. In our case, the latter architecture would not only require a significantly longer fabrication time due to a larger number of scans, but would also introduce additional losses due to scattering at the overlapping waveguide tracks.

The following mathematical description of MMIs and their wave propagation closely follows [202] and [210]. The effective refractive index of the core and cladding, or surrounding bulk material, is denoted as $n_c$ and $n_b$. The MMI multimode region supports $m$ lateral modes at the wavelength $\lambda_0$, $\nu = 0, 1, 2, ..., m-1$, with even modes referring to even numbers and odd modes referring to odd numbers (Fig. 6.23 right). The index $n_c$ can be linked to the propagation constant $\beta_\nu$ and the lateral wavenumber $k_{y\nu}$ by the dispersion equation

$$k_{y\nu}^2 + \beta_\nu^2 = k_0^2\, n_c^2 \tag{6.16}$$

with

$$k_0 = \frac{2\pi}{\lambda_0} \tag{6.17}$$

and

$$k_{y\nu} = \frac{(\nu+1)\,\pi}{W_{e\nu}} \tag{6.18}$$

where $W_e$ represents the effective width that considers the penetration depth of the mode field into the cladding material (Fig. 6.23). In cases of waveguides with a high enough contrast, particularly waveguides fabricated in GLS glass reported in this work, the penetration depth is assumed to be negligibly small so that $W_{e\nu} \simeq W_{\mathrm{MMI}}$. The propagation constant $\beta_\nu$ can be derived from Equation (6.16) - (6.18) applying a binomial expansion with $k_{y\nu}^2 \ll k_0^2\, n_c^2$

$$\beta_\nu \;\simeq\; k_0\, n_c \;-\; \frac{(\nu+1)^2\;\pi\,\lambda_0}{4n_c\, W_{\mathrm{MMI}}^2}\;. \tag{6.19}$$

This shows a roughly quadratic dependence for the propagation constants compared to the mode number $\nu$ in a step-index multimode waveguide. Each mode travels in the longitudinal (z) direction with a different propagation constant $\beta_\nu$ so that the beat length $L_\pi$ of the two lowest order modes is defined as

$$L_\pi \;=\; \frac{\pi}{\beta_0 \;-\; \beta_1} \;\simeq\; \frac{4n_c\, W_{\mathrm{MMI}}^2}{3\,\lambda_0}\;. \tag{6.20}$$

The MMI width $W$ and length $L$ depend on each other and thus constrain either of the dimensions. The propagation constant difference between the first order mode and the $\nu^{th}$ order mode can be written as

$$\beta_0 \;-\; \beta_\nu \;=\; \frac{\nu\,(\nu+2)\;\pi}{3\,L_\pi}\;. \tag{6.21}$$

The electric field of the mode $\nu$ experiences a phase rotation with respect to mode $\nu = 0$ as it propagates along the multimode waveguide region, where at the end of which the resulting phase is

$$\phi_\nu \;=\; \frac{\nu\,(\nu+2)\;\pi\, L_{\mathrm{MMI}}}{3\,L_\pi}\;. \tag{6.22}$$

As a consequence of the phase rotation, the input field is imaged as a single or multiples at certain positions along the propagation axis (z) that allows for the creation of M×N couplers by appropriately positioning exit waveguides to capture the optical power.

The input and output waveguides of width $W_a$ are assumed to only excite the lateral mode 0. The mode-field distribution is contained by the width $W_{\mathrm{MMI}}$ of the multimode section and is approximated by sinusoids

$$\psi_\nu\left(x\right) \;=\; \sin\left[\pi\left(\nu+1\right)\,\frac{x}{W_{\mathrm{MMI}}}\right]. \tag{6.23}$$

When only one input waveguide with a width $W_a$ is excited, the field profile at position $z = 0$ of the multimode section can be approximated as

$$\Psi\left(x,0\right) \;=\; \begin{cases} \sin\left[\frac{\pi\left(x - x_c + \frac{W_a}{2}\right)}{W_a}\right], & x_c - \frac{W_a}{2} < x < x_c + \frac{W_a}{2} \\ 0, & \text{otherwise} \end{cases} \tag{6.24}$$

whereas a weighted integration of the modes is defined as [202, 210]

$$\Psi\left(x,0\right) \;=\; \sum_{\nu=0}^{\infty} c_\nu\,\psi_\nu\left(x\right). \tag{6.25}$$

Incorporating Equation (6.22) into Equation (6.26) and excluding the common phase of the fundamental mode, the field profile $\Psi_{y,z}$ at a distance $z = L_{\mathrm{MMI}}$ is given by

$$\Psi\left(x, L_{\mathrm{MMI}}\right) \;=\; \sum_{\nu=0}^{m-1} c_\nu\,\psi_\nu\left(x\right)\exp\left[j\,\frac{\nu\left(\nu+2\right)\pi}{3\,L_\pi}\,L_{\mathrm{MMI}}\right]. \tag{6.26}$$

The types of images formed strongly depend on the exponent in Equation (6.26), the so-called shape factor and the modal excitation $c_\nu$. The latter are the Fourier series coefficients and serve as mode weights, obtained by a periodic odd function [210, 211]

$$\begin{aligned} c_\nu &= \frac{2}{W_{\mathrm{MMI}}} \int_{x_c - W_a/2}^{x_c + W_a/2} \sin\left[\frac{\pi\,(x - x_c) + \frac{W_a}{2}}{W_a}\right] \sin\left[\pi\,(\nu+1)\,\frac{x}{W_{\mathrm{MMI}}}\right] dx \\ &= \frac{4\,W_a}{\pi W_{\mathrm{MMI}} \left(1 - (\nu+1)^2 \left(\frac{W_a}{W_{\mathrm{MMI}}}\right)^2\right)} \cos\left[\pi\,(\nu+1)\,\frac{W_a}{2\,W_{\mathrm{MMI}}}\right] \sin\left[\pi\,(\nu+1)\,\frac{x_c}{W_{\mathrm{MMI}}}\right]. \end{aligned} \tag{6.27}$$

The current work aims for a 2×2 coupler which allows for a restriction to only excite certain modes. This can be achieved by simply adjusting the position of the input fields that lead to a shorter device length $L_{\mathrm{MMI}}$. Provided that

$$c_\nu = 0 \quad \text{for} \quad \nu = 2, 5, 8, ..., \tag{6.28}$$

two images are formed at

$$L = \left(\frac{p}{2}\right) L_\pi \tag{6.29}$$

with $p$ allowing only odd integers. This reduces the length factor in Equation (6.26) by three.

The ideal way is to position the entrance waveguides $1/6$ of $W_{\mathrm{MMI}}$ from the center of the multimode waveguide section [202]. This position allows an even symmetric field $\Psi(x, 0)$ to be launched, with modes fulfilling the requirements of Equation (6.28). The demonstrated MMIs in this work are based on the inscription parameters for low-loss triple waveguides in the cumulative heating regime, with a spacing of 5.25 $\mu$m between individual tracks. An almost perfect positioning of access waveguides is therefore achievable. A $1/6$ $W_{\mathrm{MMI}}$ positioning from the MMI center is equivalent to a positioning of the entrance waveguides at a position of $1/3$ from the MMI edge. Here, two images are formed at 0.5 $L_\pi$ based on the paired interference mechanism [202]. This is significantly shorter than the required length of 1.5 $L_\pi$ for arbitrary positions of the input waveguides. The MMI features 26 partially overlapping tracks with two access waveguides with a 47.25 $\mu$m center-to-center spacing. Each waveguide is situated 46.25 $\mu$m from its center to the outer edge of the slab. This allows for the smallest MMI width with a $\sim$ 1/3 positioning of the access waveguides which in turn leads to the shortest feasible design length to provide low propagation loss.

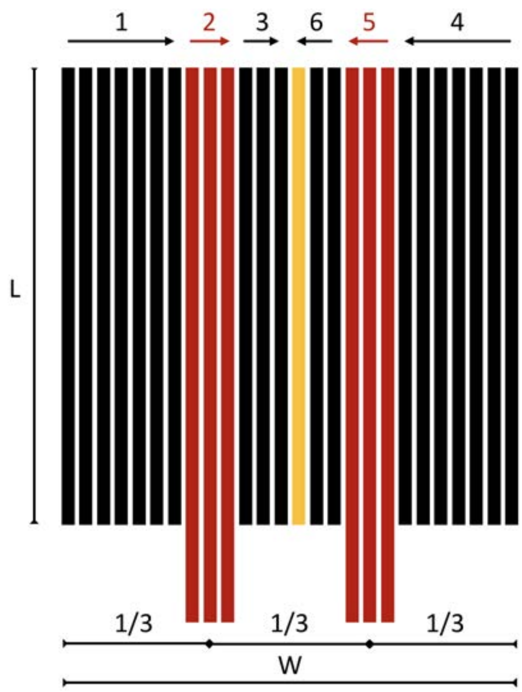


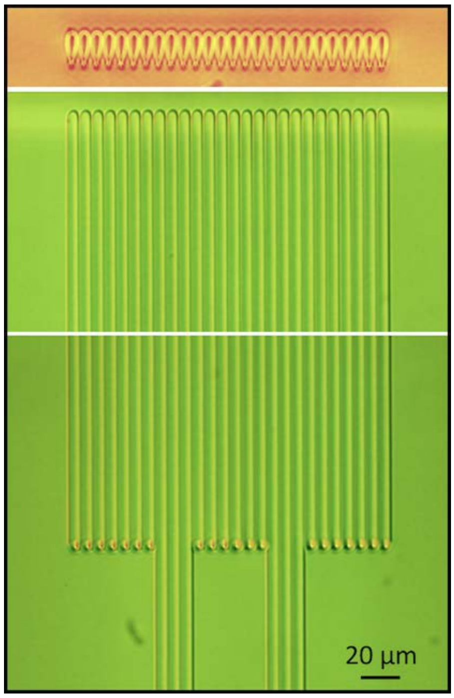


FIGURE 6.24: Left: The MMI design consists of 26 laterally stacked tracks of length L and width W with the last track inscribed being off-center (orange). Two input waveguides (red) are spaced evenly at 1/3 and 2/3 the width of the device. This design does not feature output waveguides in order to observe the output modes for different MMI lengths. Right: A microscope image of the end-face (orange) and top view of a fabricated MMI. The top view shows the start and end of the device sparing out the long middle section.

Assuming a $\Delta n_{\text{wavegiude}} = 0.0128 \pm 0.0010$ and a total width of 139.75 $\mu$m, a restricted MMI with a two-mode output requires a theoretical length of $\sim$7.5 mm as the shortest feasible design.

To keep the inscription symmetry as high as possible, the first half of the device, blocks 1 - 3, was fabricated from left to right while the second half, blocks 4 - 6, was fabricated from right to left (Fig. 6.24 left). Due to an even number, the last track inscribed was not at the center of the MMI and thus caused an asymmetry in the MMI slab. The length L of the slab (blocks 1, 3, 4 and 6) was varied between 6 - 10 mm with a 200 $\mu$m step size to investigate the interference process. The input waveguide lengths remained unchanged, reaching from edge to edge of the glass chip. Figure 6.24 (right) shows the top view of an MMI as well as the end-face of the output slab. The tracks were inscribed top to bottom creating small round areas of damage when the shutter blocked the laser beam. Both chip end-faces were ground and polished before the output slab was investigated.

To better understand and visualise the mode development across the MMI, the photonics device modelling software RSoft BeamProp (Fig. 6.25) was used. The left image shows the excitation and interference of several modes propagating along the Z-axis. The software predicts a 50/50 power splitting ration at ~8 mm lengths when injecting light at 4 $\mu$m into the right input waveguide. This deviates slightly from the calculated length of 7.5 mm using Equation (6.29). In addition, the simulation shows an excess loss of ~5% due to the mode-mismatch between the interference pattern and the output waveguides.

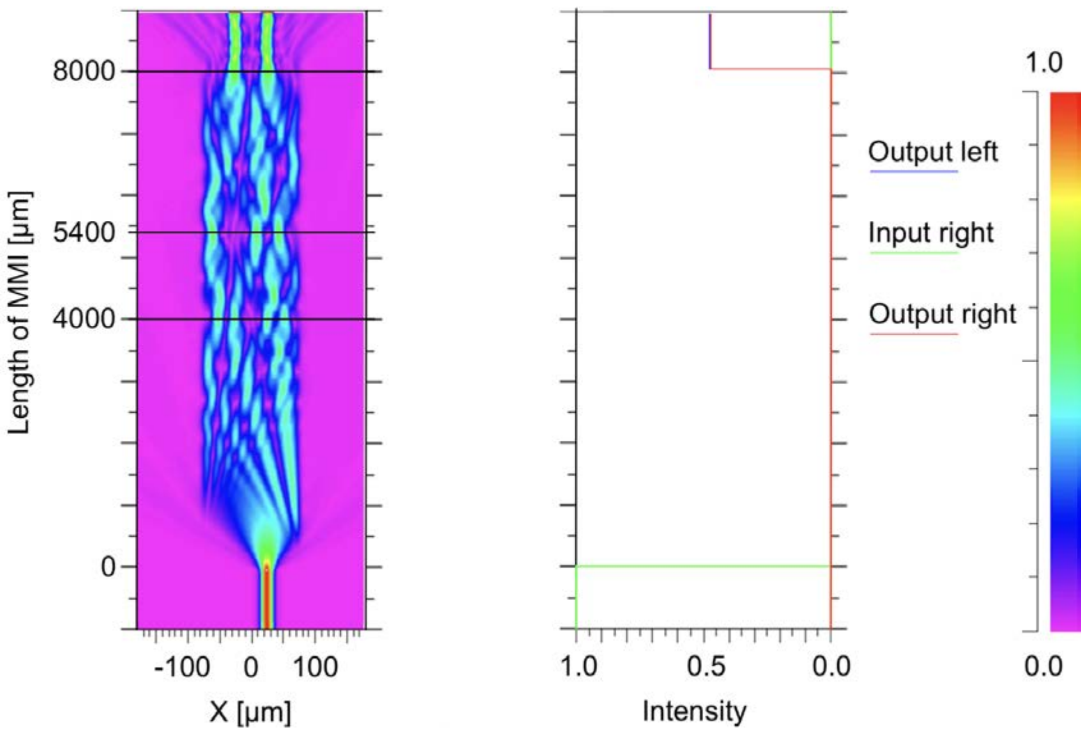


FIGURE 6.25: Simulation of a 2×2 MMI using RSoft BeamProp. With a given width of 140 $\mu$m, the length was simulated to be ~8 mm for a two mode output with a 50/50 power splitting ratio and ~5% excess loss.

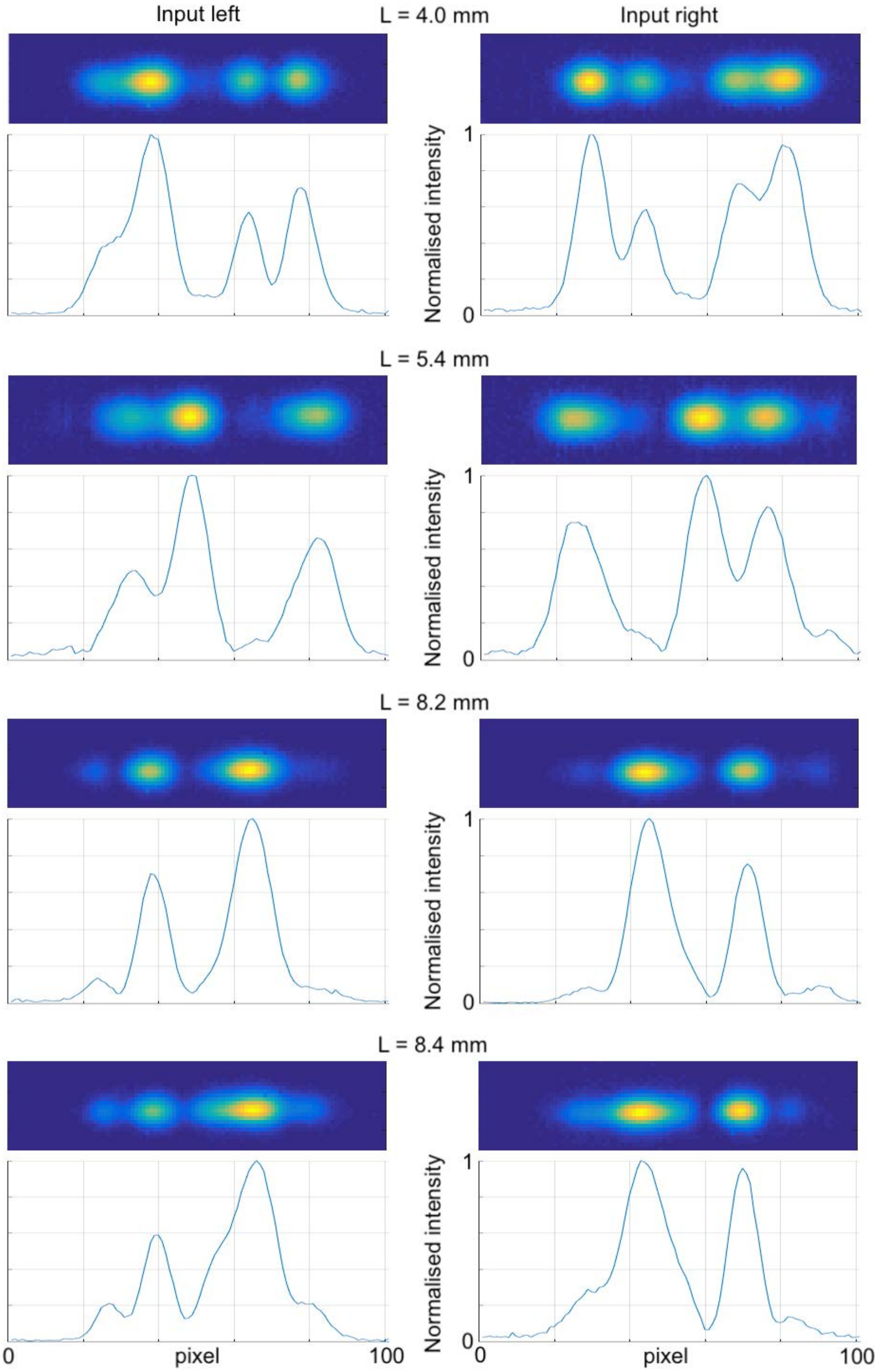


Figure 6.26: Measured output modes of MMIs with lengths 4, 5.4, 8.2 and 8.4 mm. An asymmetry is apparent when comparing the vertically integrated output power distribution of broadband light (3.75 - 4.25 $\mu$m) injected into the left and right inputs.

The fabricated MMIs were investigated under broadband illumination with a 4 $\mu$m center wavelength. The left and right columns in Figure 6.26 show the output modes of the slab as well as their power distributions when injecting light into the left and right access waveguides, respectively. The right column is in agreement with the simulation (horizontal lines Fig. 6.25 left), especially with the mode positions in X- and Z-directions where 4, 3 and 2-moded sections are indicated at 4.0, 5.4 and >8.0 mm. The experimental results however show an unequal behaviour when launching light into either the left or right input waveguide of the MMIs. Even though the mode position appears accurate, the intensity of the mode varies. The intensities were calculated by integrating a Gaussian fit applied to the measured modes. These values were subsequently used to determine the splitting ratios if output waveguides were present. The MMI with an 8.2 mm length features an identical splitting ratio of ~60/40 for light coupled into either of the input waveguides. The closest parity in power division however was found at a length of 8.4 mm for one input arm with significant difference for the other arm.

A possible cause for this splitting behaviour could be the last track inscribed which is off-center, highlighted orange in Figure 6.24 (left). Recalling from the previous Section 6.3.1, an inscribed waveguide modifies its surrounding area by creating a stress field. This leads to a refractive index difference between the first track and the track placed into the pre-modified region. Assuming that each of the sequentially written tracks is influenced only by the neighbouring modification, the last track of the device would experience a larger stress field caused by the two neighbouring tracks. The refractive index in this particular narrow strip differs from the rest of the MMI body and influences the mode development. Using only vertical or horizontal polarised light showed no effect and excluded errors through birefringence.

In order to guide the light at a two-mode output position, a set of MMIs was fabricated with exit waveguides mirroring the entrance waveguides. Research has shown that additional tapers help to funnel the light and thus improve the excess loss while simultaneously reducing the size of the MMI body [210]. The optimum taper width lies at approximately 33% of the MMI width but it was shown that the transmission only marginally decreases for taper widths down to 20% [196].

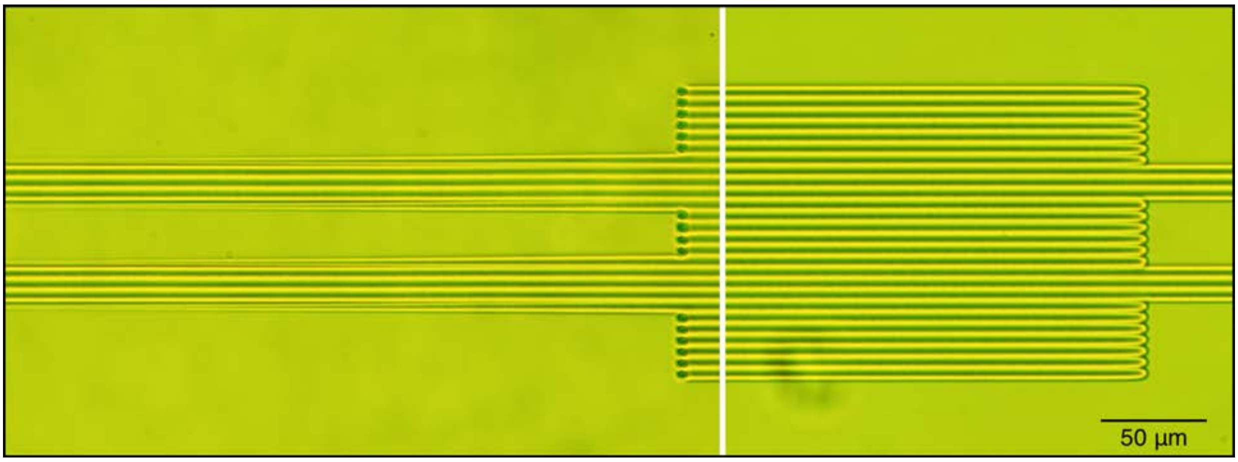


Figure 6.27: The second set of MMIs features two input and two output waveguides. The outputs were additionally provided with 500 $\mu$m tapers (left) by gradually decreasing the writing energy from 13 - 0 nJ. Pulse energies below 5 nJ are insufficient to change the glass index which causes the taper to fade at ~350 $\mu$m.

Based on the previous design (Fig. 6.24), the tracks to the left and right of each exit waveguide (block 2 and 5) were extended. A tapered region was formed by gradually decreasing the inscribing laser pulse energy from 13 - 0 nJ across a distance of 500 $\mu$m starting from the end of the slab. Since pulse energies below 5 nJ are insufficient to modify the material, the tapers fade beyond ~350 $\mu$m (Fig. 6.27). A taper width of 29.5 $\mu$m was achieved which corresponds to 21% of the MMI width and thus lies within the low transmission loss range. With the previous results in mind, the second set of MMIs was fabricated with lengths from 7.4 - 8.5 mm in 50 $\mu$m steps.

Devices between 7.90 and 8.25 mm show almost identical behaviour under broadband illumination (3.75 - 4.25 $\mu$m) indicating a high fabrication tolerance (Fig. 6.28). These dimensions also show that the MMIs are shorter by the approximate length of the taper as explained in [210]. The irregular power splitting before 7.9 mm and after 8.25 mm is due to a more chaotic power distribution of interfering, rather than pronounced modes coupled from the MMI body into the output waveguides.

The first set of MMIs (Fig. 6.26) has shown that a 50/50 splitting ratio was not achieved by coupling light in either of the input waveguides. The MMI lengths where two modes were expected showed small contributions attributed to other modes, evident as a shoulder in the intensity distribution plot of the modes. Adding exit waveguides led to suppression of

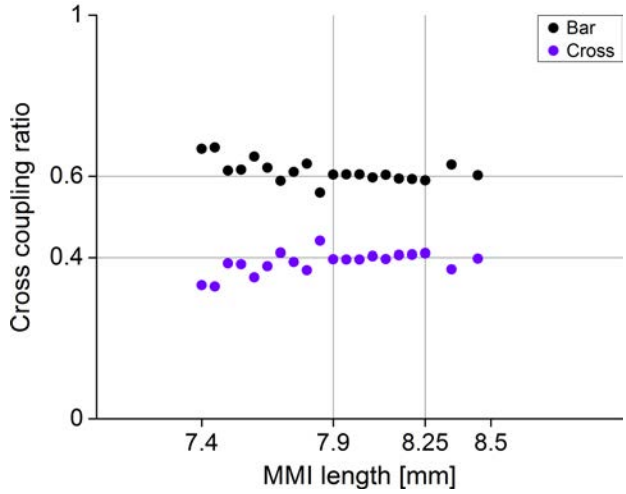


FIGURE 6.28: Cross coupling ratio for MMIs of different lengths for light injected into the left arm. A 60/40 splitting ration is evident over a 350 $\mu$m length for broadband illumination.

these modes in order to maintain single-mode behaviour. The result was a constant power splitting ratio over a broad 500 nm window at the expense of losses at the exit waveguide that contribute to stray light. Stray light can lead to a higher background noise when it reaches the detector and compromise interferometric measurements.

Figure 6.29 (left) presents the wavelength dependent cross coupling ratios for an MMI with

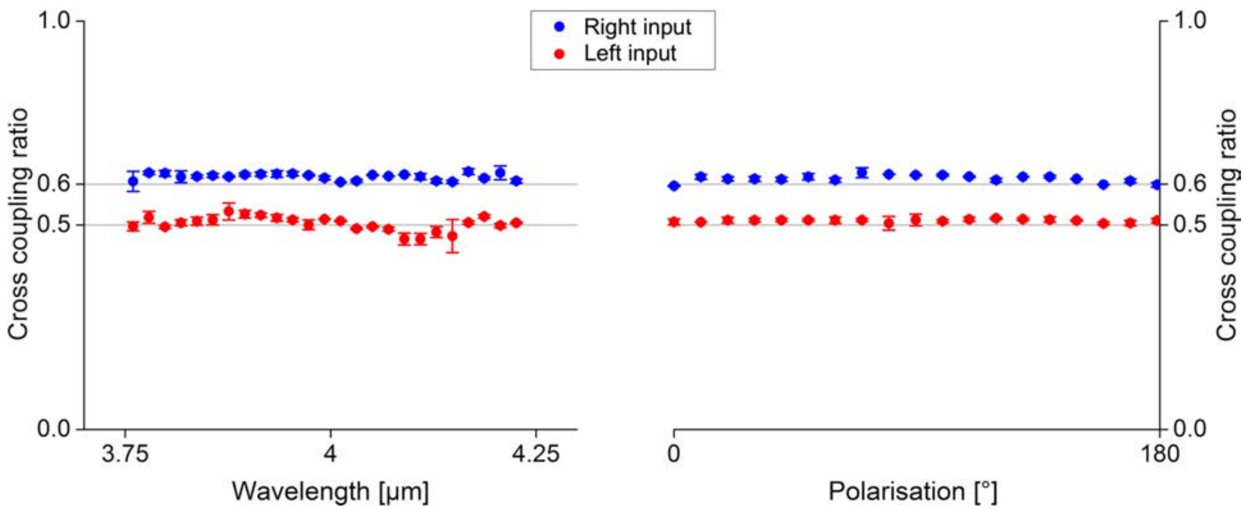


FIGURE 6.29: Left: Light coupled into the left arm of an 8.1 mm long MMI with output tapers led to a broad 50/50 power splitting ratio while light coupled into the right arm resulted in a ~62/38 power splitting ratio. The uneven behaviour arises from unhomogeneous fabrication of the MMI body. Right: The MMI shows no polarisation dependent splitting characteristics at 4 $\mu$m wavelength.

an 8.1 mm length. Injecting light into the right arm resulted in an average of 50.3/49.7 power splitting with a standard deviation of 1.7% over a 500 nm window (3.75 - 4.25 $\mu$m). Light coupled into the left arm was split 61.9/38.1 with a standard deviation of 0.8% across 500 nm. These ratios did not change when the chip was flipped to launch light from the other end into the device. By contrast, a similar cross coupling ratio of 50.2% was achieved for asymmetric couplers but only between 3.8 - 4.05 $\mu$m. These couplers show less coupling ratio variation of only 0.3% over this wavelength range compared to 1.7% for MMIs. A less broadband (3.9 - 4.2) but a $\sim$50/50 splitting ratio for both input arms of a $2\times2$ lithographically fabricated chalcogenide MMI was shown by Kenchington Goldsmith *et al.* [206].

A polarisation dependency for MMIs was not found for either arm measured over 180° in 10° steps at a 4 $\mu$m wavelength (Fig. 6.29 right). The polarisation on the other hand had a significant influence on splitting ratio of asymmetric directional couplers deviating 6.4% peak-to-peak from a 50.2/49.8 splitting ratio measured with unpolarised light.

The deviated position of the access waveguide from the ideal location plays a role in achieving a perfect power splitting behaviour and higher throughput. Nevertheless, the input dependent splitting ratio of the presented MMIs and the resulting imbalance potentially influence the interferometric capabilities. The MMIs were therefore characterised at the University of Cologne for their extinction ratio as were the previous asymmetric directional couplers. The contrast of the recorded interferogram using a super-continuum source (SCS) showed an extinction ratio of 96.81 $\pm$ 0.16% for wavelengths of 3.8 - 4.1 $\mu$m (Fig. 6.30). As expected, this value is lower than the 98.79 $\pm$ 0.04% extinction ratio of the asymmetric coupler due to the described left to right input imbalance.

Using the SCS with a narrow bandwidth filter on the other hand (3.745 $\mu$m, 69 nm FWHM) resulted in an almost identical extinction ratio of 99.35 $\pm$ 0.06% compared to 99.31 $\pm$ 0.08%. At this wavelength the asymmetric coupler no longer features a perfect 50/50 splitting ratio and is rather similar to the MMI. This also shows that non-perfect 50/50 splitting has little influence on the achievable extinction ratio. The interferometric measurements for MMIs are not corrected for background caused by high noise in the setup. The values therefore represent a minimum where the real extinction ratios are potentially higher.

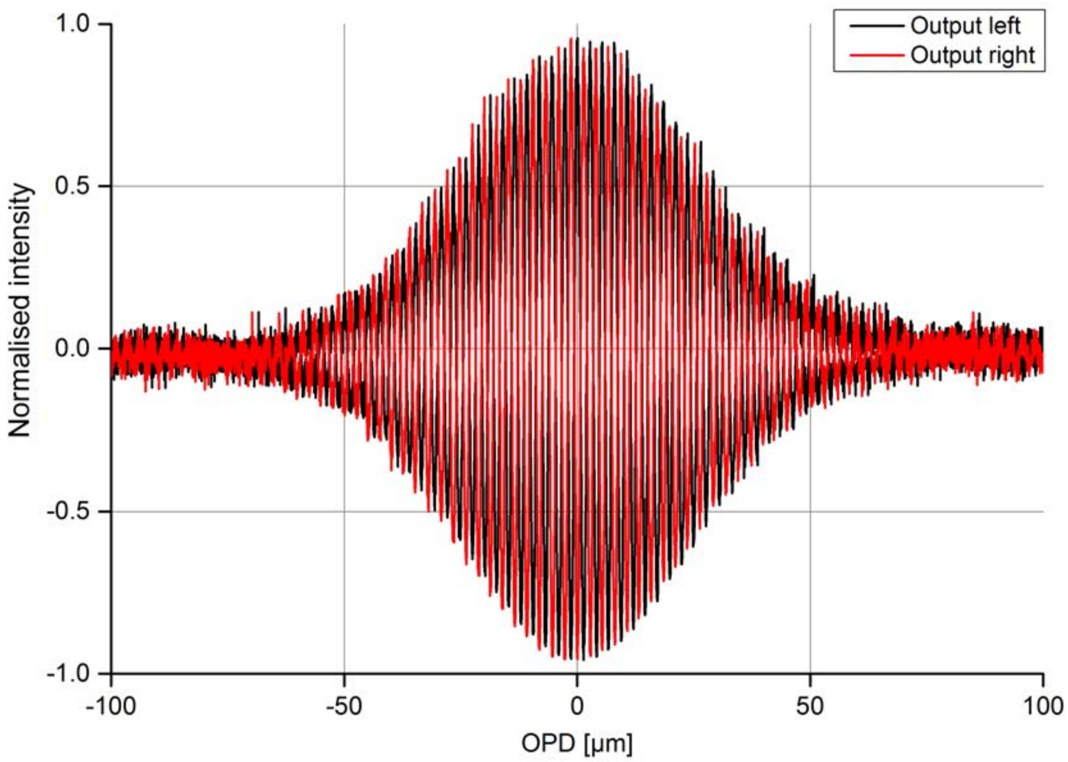


FIGURE 6.30: Experimental interferogram of the two outputs of an MMI for a wavelength range of 3.8 - 4.1 $\mu$m. An extinction ratio of 96.81 $\pm$ 0.16 was measured.

Simulations have shown that an extinction ratio of 99.9999% is attainable between 3.8 - 4.2$\mu$m [196]. Nevertheless, the ratios achieved in this work are still relatively high compared to experimentally demonstrated lithographic MMIs in the mid-infrared with 90% at 3.74 $\mu$m [212], 96.8% at 3.8 $\mu$m [213] and 99.8 - 99.9% at 3.39 $\mu$m [214] all for monochromatic light. For a direct comparison, the extinction ratio and other parameters of the symmetric, asymmetric and multimode interference couplers are summarised in Table 6.1.

The total device throughput for broadband light (3.75 - 4.25 $\mu$m) was measured to be ~16% (8 dB loss) and ~20% (7 dB loss) for light coupled into the left and right input waveguides, respectively. Better results were obtained for asymmetric directional couplers with ~47% throughput (3.3 dB loss). These values do not account for the Fresnel loss of ~15.3% at each glass-air interface and coupling losses of at least 30%. Assuming the MMI section has the same linear propagation loss of 0.22 dB/cm, the total insertion loss amounts to ~47% (2.75 dB). As a result, the remaining ~33% and ~37% are losses intrinsic to the MMI.

The majority of the loss is detected as stray light that originates from the mode-mismatch between the interference pattern and the output waveguide. Weaker modes that reach the end of the MMI body in the center are scattered and contribute to the stray light.

Introducing tapers at the output of the MMI body as well as revising their widths according to [210] would increase the throughput. Reported excess losses for lithographically fabricated MMIs with tapers range from similarly high excess losses in silicon-on-insulator MMIs at 3.74 $\mu$m wavelength [212] to much lower values of ∼1.6 dB (3.72 $\mu$m - 3.8 $\mu$m) [213] and ∼0.4 dB at 3.8 $\mu$m for MMIs in germanium-on-silicon [215]. In lithography, the side wall roughness plays an important role. A smooth side wall leads to a high internal reflection while a rough side wall causes scattering losses. Additionally, the propagation losses are usually relatively high (>1.5 dB/cm), however, the devices are relatively short (∼60 $\mu$m - 800 $\mu$m [206, 215]) which results in a relatively low total loss. The side walls of FLDW devices in the cumulative heating regime are assumed to be very smooth and provide perfect total reflection. A propagation loss of 0.22 ± 0.02 dB/cm aids to keep the losses low despite the long device length. The total length of such a device including input and output tapers amounts to ∼8.4 mm with access waveguides less than 50 $\mu$m apart. The narrow spacing needs to be enlarged in order to enable the use of micro-lens arrays or 1-dimensional optical fiber arrays. A 500 $\mu$m and 250 $\mu$m separation at the input and output, respectively, can be achieved by introducing cosine S-bend waveguides at both ends of the chip. The required S-bend lengths of ∼6.7 mm and ∼4.5 mm, however, would double the length of the MMIs to to 19.3 mm. This increases the contribution of the propagation loss to the device losses to ∼0.42 dB. However, S-bends would potentially help to eliminate parasitic stray light reflected and/or scattered from the ends of the MMI body.

## Summary

This chapter detailed the development of the key component for an on-chip nulling interferometer: S-bends, asymmetric Y-splitter and couplers. Different coupler designs were investigated namely symmetric and asymmetric directional couplers as well as multimode interference couplers (MMI).

S-bend shaped waveguides based on the low-loss triple modification were developed and found to feature a negligible bending loss if the minimum bending radius is kept above 40 mm. These S-bends were utilised to form asymmetric Y-splitters with 50/50 power division for the wavelength window 3.6 - 4.2 $\mu$m. This was achieved by balancing the asymmetry of the architecture with the asymmetry caused by the sequential inscription order of the waveguide tracks.

The sequential inscription order of FLDW devices prevented the fabrication of truly symmetric directional couplers due to an imbalance in propagation constants between the two coupler arms in the coupling region. This difference in $\Delta\beta$ can be compensated for by locally increasing the inscription velocity in the second inscribed arm to fabricate a truly symmetric coupler.

A summary of the relevant parameters of the directional couplers and MMIs are provided in Table 6.1.

| | **Symmetric coupler** | **Asymmetric coupler** | **MMI** |
|---|---:|---:|---:|
| Length | 1.5 mm | 5.6 mm | 8.4 mm |
| Length (incl. S-bends) | 13.5 mm | 17.6 mm | 19.3 mm |
| Achromatic window | 4 $\mu$m | 3.8 - 4.05 $\mu$m (250 nm) | 3.75 - 4.25 $\mu$m (500 nm) |
| Splitting ratio (of above window) | ~50/50 | 50.2/49.8 | 61.9/38.1 (left input)<br>50.3/49.7 (right input) |
| Deviation | >3.7% (3.8 - 4.05 $\mu$m) | 0.3% | 1.7% |
| Pol. dependent splitting | — | Yes (6.4%) | No |
| Total throughput | — | 47% | ~16% (left input)<br>~20% (right input) |
| Insertion loss | ~47% (2.75 dB) | ~47% (2.75 dB) | ~47% (2.75 dB) |
| Extinction (3.8 - 4.1 $\mu$m) | — | 98.79 ± 0.04% | 96.81 ± 0.16% |
| Extinction (3.745 $\mu$m) | — | 99.31 ± 0.08% | 99.35 ± 0.06% |
| Fabr. time (incl. S-bends) | 1 min 15 sec | 1 min 23 sec | 5 min 45 sec |

TABLE 6.1: Comparison between directional and multimode interference couplers.

An asymmetric coupler however requires a certain $\Delta\beta$ to obtain a wavelength-flattened coupling response. This $\Delta\beta$ was achieved by further increasing the waveguide inscription velocities which led to narrower waveguide widths and hence an increase in propagation loss.

Alternatively, decreasing the velocity in the second arm did not alter the waveguide width, but changed the refractive index sufficiently to reach a certain $\Delta\beta$. Here, an optimum balance between $\sigma^2$, $\phi$ and $\kappa$ was found to counter the natural wavelength dispersion of directional couplers. Asymmetric couplers with 55 mm/min feed rate used for the second arms showed broadband behaviour over 250 nm (3.8 - 4.05 $\mu$m) with only 0.3% standard deviation. For this wavelength window, a high 98.79% extinction ratio was shown by a coupler with a 50.2/49.8 splitting ratio. These results are superior to symmetric directional couplers which only features a $\sim$50/50 splitting at 4 $\mu$m and varied by >3.7% over the range of 3.8 - 4.05 $\mu$m. The fabrication time for both symmetric and asymmetric couplers is approximately 1:15 - 1:23 min. The fabrication time is similarly fast as demonstrated for UV direct-written asymmetric directional couplers [189] but without the required additional photosensitisation procedure before inscription.

The MMIs feature a greater achromaticity (3.75 - 4.25 $\mu$m) with a 50/50 splitting capability than asymmetric couplers but with a higher deviation of 1.7% from the average value. Nevertheless, the extinction ratio is still relatively high with 96.8 $\pm$ 0.16% for wavelengths of 3.8 - 4.1 $\mu$m compared to the asymmetric coupler with an extinction ratio of 98.79% over the same wavelength band. One drawback of the multimode interference couplers is the length and number of tracks that increase the fabrication time fourfold compared to directional couplers. The main drawback however is the unbalanced splitting behaviour between the input arms, but this can potentially be improved by changing the design to an uneven number of waveguide tracks, introducing more structural symmetry. Only the throughput is currently less than half compared to the asymmetric couplers due to internal scattering losses. However, the additional insensitivity of the MMI to polarisation and the broader achromatic window allow for more light to be used for a high interferometric performance. For the devices presented, one has to weigh the decision of higher device losses for a high bandwidth against higher throughput for a smaller bandwidth.

# 7

# Conclusion

Femtosecond laser direct-writing is a great alternative to the planar lithographic approach of developing optical waveguide-based mid-infrared photonics. This technology even offers the capability to from 3-dimensional circuits to accommodate a greater complexity of future devices. It is compatible with mid-infrared glasses, in particular gallium lanthanum sulphide. The advantage of this commercially available chalcogenide glass is the consistently high quality due to decades of manufacturing experience. The quality, and even more importantly the availability, is a crucial factor for the development of astrophotonic devices that allow for high reproducibility.

One of the key characteristics of astrophotonic devices are the intrinsic losses, in particular the waveguide propagation loss. Low losses are mandatory for on-sky operations. Not only does every captured photon carry valuable information, but it also determines the duration of the observation run which is directly connected to the operational costs. The development of low-loss optical waveguides deployable in the astronomical L'-band (3.6 - 4.26 $\mu$m) is therefore inevitable for interferometric devices with the goal of exo-planet detection.

This was demonstrated in Chapter 4 were cumulative heating fabrication was combined with the multiscan technique to create waveguides with a low propagation loss of $0.22 \pm 0.02$ dB/cm. This hybrid approach outperformed waveguides inscribed with either of these techniques individually. The round mode-fields are ideal to couple light from round apertures such as the primary mirrors of a telescopes into the chip with relatively low coupling losses.

These waveguides were investigated in more detail in Chapter 5 to understand their formation. It was proven with the aid of Raman spectroscopy and electron probe micro-analysis that migration of sulphur anions $S^{2-}$ were responsible for material modification in this three-element glass. This is an interesting discovery since usually cations are prone to ion migration processes, as opposed to the anions observed migrating here. The low pulse energies of the inscribing laser induced only light sulphur elements to move and were insufficient to overcome the element-dependent activation energy for lanthanum or gallium. The accumulation of sulphur rich areas created a relatively high refractive index contrast of up to $\Delta n_{\text{shell}} = 0.0158 \pm 0.0010$ in the shell region and an average refractive index contrast of $\Delta n_{\text{waveguide}} = 0.0128 \pm 0.009$ across the waveguide compared to the surrounding bulk glass. This in turn led to a strong mode confinement.

The heart of an on-chip nulling interferometer is the interferometric region were light is brought together for an interferometric interaction. This requires curved waveguides in the shape of cosine S-bends with a negligible bending loss, developed in Chapter 6. The relatively strong mode confinement allowed for tight bends with a minimum bending radius of 40 mm. These S-bend waveguides were used to form Y-splitters that will direct light towards the coupling region and also into power monitoring lines of the proposed nulling interferometer. These photometric channels are a beneficial feature to be used during on-sky observations. Knowing the power values in these channels provides an instantaneous insight of the power inside the individual waveguides in the coupling region. Hence, it is used to calibrate the contrast.

The simplest form of an interferometer is the two-port symmetric directional coupler. This coupler however is inherently chromatic and offers only limited interferometric performance.

The more broadband a coupler is, the more photons can be used at a time, which reduces the observation time. Another important parameter is the achievable destructive interference in form of the extinction ratio in order to diminish the high stellar flux and allows faint radiation from nearby companions to be detected. For that reason, asymmetric directional couplers and multimode interference couplers were developed both with high extinction ratios of up to 99.35±0.06% for nearly monochromatic light (3.745 $\mu$m) and up to 98.79±0.04% for a 300 nm window (3.8 - 4.1 $\mu$m) which is sufficient for on-sky testing in relatively short observation runs.

## Future work - the nulling interferometer chip

The 2-port nulling interferometer design presented at the beginning of the last chapter was the basis of the following prototype fabrication (Fig. 7.1 left). An additional design upgrade was undertaken to reduce the background noise caused by the chip itself. Stray light occurs at the front end of the chip due to a mode-mismatch between the waveguide and the light injected with a micro lens array (MLA). The stray light propagates through the chip and overlaps with the device outputs. This unguided stray light can cause interference and thus compromises measurements in stellar interferometers. This effect can be mitigated by integrating a side-step at the front end of the chip [216] to move the outputs and the coupling region out of the stray light cone (Fig. 7.1 right). The lenses of the silicon-based MLA (18-00284, Suss MicroOptics) have a pitch of 250 $\mu$m and are transparent between 1.2 - 10 $\mu$m. The focused beam with an NA = 0.19 results in a light cone with a half angle of 0.085 radians for the excess light when entering the GLS glass with a refractive index of $n$ = 2.2832 at 4 $\mu$m. The side-step thus needs to be larger than the area exposed by the light cone at the end of the chip.

A set of seven prototype nulling interferometers initially based on symmetric couplers were inscribed in a GLS glass sample based on the optimised low-loss waveguides. The two single-mode inputs were spaced 500 $\mu$m apart to deploy two non-neighbouring lenses of the MLA for injection in order to avoid cross-talk. The inputs take a 22.4 mm long and 2.5 mm wide side-step based on cosine S-bends developed in Section 6.1. These dimensions ensure a

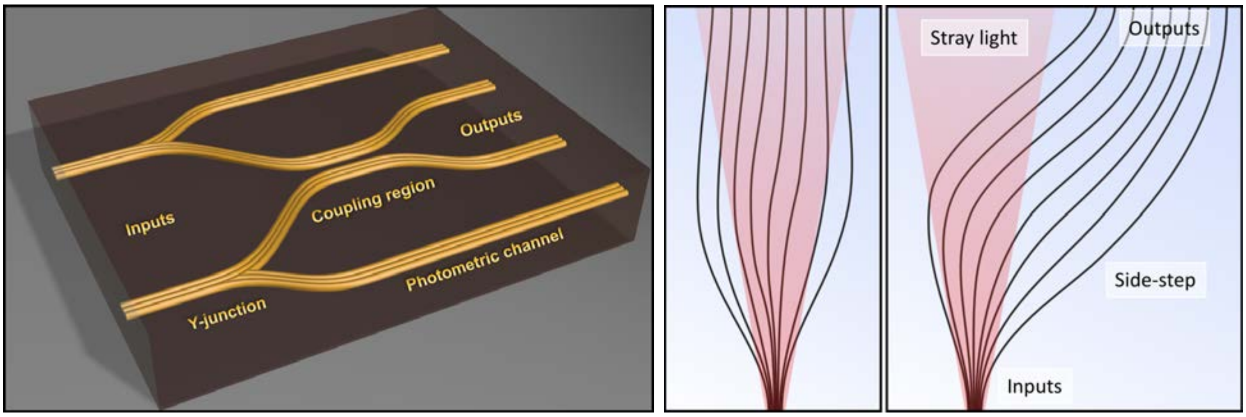


FIGURE 7.1: Left: Nulling interferometer chip design as described at the beginning of the chapter. Right: The diagrams show two pupil-remappers for astronomical applications [216]. The authors demonstrated a 'side-step' version to mitigate any interference effects of unguided light by simply moving the waveguide outputs outside the cone of the stray light (shown in red).

minimum bending radius of 40 mm to avoid bending losses. The ends of the side-steps branch into cosine S-bend shaped asymmetric Y-splitters presented in Section 6.2. Approximately 50% of the light is fed into the outer photometric channels for real-time power monitoring, while the residual light is directed to the interferometric coupling region. The seven devices feature symmetric couplers introduced in Section 6.3.1, with interaction lengths varying by 50 $\mu$m between 1.35 - 1.65 mm. The four outputs are separated by 250 $\mu$m that allow for connecting a V-groove fiber array to a mid-infrared detector. Figure 7.2 illustrates the fabricated chip with an individual device highlighted (red).

The additional side-step increased the length of the chip from 13.5 mm to 35.9 mm causing 0.8 dB in propagation loss. As a result, for entirely lossless directional couplers but with 0.5 dB excess loss for the Y-splitters, the internal loss of 1.3 dB exceeds the target of <1 dB for a chromatic interferometric device. However, implementing either an asymmetric directional coupler or a multimode interference coupler opens the door to broadband operation. This in turns allows for more photons to be used that can compensate for the additional loss for interferometric measurements. The 500 nm broadband window of an MMI is larger than the window of 250 nm for asymmetric couplers, but MMIs feature additional intrinsic losses. Hence, it depends on the magnitude of the target within the observation window. A strong but narrow bandwidth signal is better measured with an asymmetric coupler while weaker but broader signals can be better observed using an MMI based nulling interferometer. The detailed characterisation of the chip and optimisation using broadband couplers is a work in progress and detailed characterisation will be the subject to future work.


FIGURE 7.2: The photograph shows several nulling interferometers with different interaction lengths implemented on a single GLS chip. The red frame indicates a single device.

# List of publications

## Journal paper

- **T. Gretzinger**, S. Gross, A. Arriola, and M. J. Withford. *Towards a photonic mid-infrared nulling interferometer in chalcogenide glass.* submitted to Optics Express (2019).

- **T. Gretzinger**, T.T. Fernandez, S. Gross, A. Arriola, and M. J. Withford. *Role of ion migrations and structural reorganisations in femtosecond laser direct-written chalcogenide glass waveguides.* Arxiv (2018).

- A. Arriola, S. Gross, M. Ams, **T. Gretzinger**, D. Le Coq, R. P. Wang, H. Ebendorff-Heidepriem, J. Sanghera, S. Bayya, L. B. Shaw, M. Ireland, P. Tuthill, and M. J. Withford. *Mid-infrared astrophotonics: study of ultrafast laser induced index change in compatible materials.* Optical Materials Express **7**, 698-711 (2017).

- **T. Gretzinger**, S. Gross, M. Ams, A. Arriola, and M. J. Withford. *Ultrafast laser inscription in chalcogenide glass: thermal versus athermal fabrication* Optical Materials Express **5**, 2862-2877 (2015).

## Conference articles

- **T. Gretzinger**, T. T. Fernandez, S. Gross, A. Arriola, and M. J. Withford, ”Boson band vibrations aid refractive index mapping of waveguides in high index chalcogenide glass,” submitted to the European Conference on Lasers and Electro-Optics (CLEO), Munich, Germany (2019).

- **T. Gretzinger**, S. Gross, A. Arriola, T. T. Fernandez, D. Strixner, J. Tepper, L. Labadie, and M. J. Withford, ”Broadband mid-infrared directional and multimode interference couplers in GLS glass fabricated using femtosecond laser direct-writing,” submitted to the European Conference on Lasers and Electro-Optics (CLEO), Munich, Germany (2019).

- **T. Gretzinger**, S. Gross, A. Arriola, P. G. Tuthill, and M. J. Withford. *Progress on an astronomical on-chip nulling interferometer in the mid-infrared.* AS109-28, Astronomical Telescopes and Instrumentation, Austin, United States (2018).

- T. Lagadec, B. Norris, S. Gross, A. Arriola, **T. Gretzinger**, N. Cvetojevic, J. Lawrence, M. J. Withford, and P. G. Tuthill. *GLINT South: a photonic nulling interferometer pathfinder at the Anglo-Australian Telescope for high contrast imaging of substellar companions.* Proc. SPIE 10701, Optical and Infrared Interferometry and Imaging VI (2018), Vol. 10701, pp. 10701-10701-8. SPIE Astronomical Telescopes ans Instrumentation, Austin, Texas, United Stated (2018).

- **T. Gretzinger**, S. Gross, A. Arriola, P. G. Tuthill, and M. J. Withford. *Low-loss photonic Nulling Interferometer in the Mid-Infrared for Astronomical Applications.* JW4A.84, Frontiers in Optics (FiO), Washington, United States (2017).

- A. Arriola, B. Norris, N. Cvetojevic, S. Gross, **T. Gretzinger**, T. Lagadec, J. Lawrence, N. Jovanovic, O. Guyon, and M. J. Withford. *Measuring stellar diameters with a compact integrated photonic nulling interferometer in a 8 meter-class telescope.* CM_4_4, European Conference on Lasers and Electro-Optics (CLEO), Munich, Germany (2017).

- **T. Gretzinger**, S. Gross, A. Arriola, P. G. Tuthill, and M. J. Withford. *Towards an Ultrafast Laser Inscribed Astronomical Nulling Interferometer in the Mid-Infrared.* CK_P_15, European Conference on Lasers and Electro-Optics (CLEO), Munich, Germany (2017).

- A. Arriola, S. Gross, M. Ams, **T. Gretzinger**, D. Le Coq, R. Wang, H. Ebendorff-Heidepriem, J. Sanghera, S. Bayya, B. Shaw, M. Ireland, P. Tuthill, and M. J. Withford. *3D Photonics in the Mid-infrared: Parametric study of ultrafast laser inscribed waveguides for stellar interferometry.* BT3B.5, Photonics and Fiber Technology (ACOFT, BGPP, NP), Sydney, Australia (2016).

- **T. Gretzinger**, S. Gross, M. Ams, A. Arriola, and M. J. Withford. *Ultrafast laser waveguide inscription in Gallium Lanthanum Sulfide.* AM4C.5, Photonics and Fiber Technology (ACOFT, BGPP, NP), Sydney, Australia (2016).

- A. Arriola, S. Gross, **T. Gretzinger**, M. Ams, H. Ebendorff-Heidepriem, J. Sanghera, M. Ireland, P. Tuthill, and M. Withford. *Ultrafast laser inscribed waveguides for mid-infrared interferometry: Experimental study of suitable host materials.* CM_P_8, European Conference on Lasers and Electro-Optics (E-CLEO), Munich, Germany (2015).

# References

[1] M. Mayor and D. Queloz, "A Jupiter-mass companion to a solar-type star," Nature **378**, 355 (1995). 1

[2] "Exoplanet Catalogue," http://exoplanet.eu/catalog/ (2019). 1

[3] J. Wang, D. A. Fischer, T. Barclay, T. S. Boyajian, J. R. Crepp, M. E. Schwamb, C. Lintott, K. J. Jek, A. M. Smith, M. Parrish, K. Schawinski, J. R. Schmitt, M. J. Giguere, J. M. Brewer, S. Lynn, R. Simpson, A. J. Hoekstra, T. L. Jacobs, D. LaCourse, H. M. Schwengeler, M. Chopin, and R. Herszkowicz, "Planet Hunters. V. A Confirmed Jupiter-size Planet in the Habitable Zone and 42 Planet Candidates from the Kepler Archive Data," Astrophys. J. **776**, 10 (2013). 1

[4] D. Charbonneau, T. M. Brown, D. W. Latham, and M. Mayor, "Detection of Planetary Transits Across a Sun-like Star," Astrophys. J. Lett. **529**, L45 (2000). 1

[5] J. C. Guirado, J. E. Reynolds, J.-F. Lestrade, R. A. Preston, D. L. Jauncey, D. L. Jones, A. K. Tzioumis, R. H. Ferris, E. A. King, J. E. J. Lovell, P. M. McCulloch, K. J. Johnston, K. A. Kingham, J. O. Martin, G. L. White, P. A. Jones, F. Arenou, M. Froeschlé, J. Kovalevsky, C. Martin, L. Lindegren, and S. Söderhjelm, "Astrometric Detection of a Low-Mass Companion Orbiting the Star AB Doradus," Astrophys. J. **490**, 835 (1997). 1

[6] D. P. Bennett, S. H. Rhie, A. C. Becker, N. Butler, J. Dann, S. Kaspi, E. M. Leibowitz, Y. Lipkin, D. Maoz, H. Mendelson, B. A. Peterson, J. Quinn, O. Shemmer,

S. Thomson, and S. E. Turner, "Discovery of a planet orbiting a binary star system from gravitational microlensing," Nature **402**, 57 (1999). 1

[7] A. Wolszczan and D. A. Frail, "A planetary system around the millisecond pulsar PSR1257 + 12," Nature **355**, 145 (1992). 1

[8] W. J. Borucki, D. G. Koch, N. Batalha, S. T. Bryson, J. Rowe, F. Fressin, G. Torres, D. A. Caldwell, J. Christensen-Dalsgaard, W. D. Cochran, E. DeVore, T. N. Gautier, J. C. Geary, R. Gilliland, A. Gould, S. B. Howell, J. M. Jenkins, D. W. Latham, J. J. Lissauer, G. W. Marcy, D. Sasselov, A. Boss, D. Charbonneau, D. Ciardi, L. Kaltenegger, L. Doyle, A. K. Dupree, E. B. Ford, J. Fortney, M. J. Holman, J. H. Steffen, F. Mullally, M. Still, J. Tarter, S. Ballard, L. A. Buchhave, J. Carter, J. L. Christiansen, B.-O. Demory, J.-M. Désert, C. Dressing, M. Endl, D. Fabrycky, D. Fischer, M. R. Haas, C. Henze, E. Horch, A. W. Howard, H. Isaacson, H. Kjeldsen, J. A. Johnson, T. Klaus, J. Kolodziejczak, T. Barclay, J. Li, S. Meibom, A. Prsa, S. N. Quinn, E. V. Quintana, P. Robertson, W. Sherry, A. Shporer, P. Tenenbaum, S. E. Thompson, J. D. Twicken, J. V. Cleve, W. F. Welsh, S. Basu, W. Chaplin, A. Miglio, S. D. Kawaler, T. Arentoft, D. Stello, T. S. Metcalfe, G. A. Verner, C. Karoff, M. Lundkvist, M. N. Lund, R. Handberg, Y. Elsworth, S. Hekker, D. Huber, T. R. Bedding, and W. Rapin, "Kepler-22b: A 2.4 Earth-radius Planet in the Habitable Zone of a Sun-like Star," Astrophys. J. **745**, 120 (2012). 1

[9] N. Jovanovic, C. Schwab, N. Cvetojevic, O. Guyon, and F. Martinache, "Enhancing Stellar Spectroscopy with Extreme Adaptive Optics and Photonics," Publ. Astron. Soc. Pacific **128**, 1–15 (2016). 2

[10] B. I. Vasil'ev and O. Mannoun, "IR differential-absorption lidars for ecological monitoring of the environment," Quantum Electron. **36**, 801 (2006). 2

[11] L. Labadie and O. Wallner, "Mid-infrared guided optics: a perspective for astronomical instruments," Opt. Express **17**, 1947–1962 (2009). 3

[12] O. Absil, "Nulling Interferometry with IRSI- Darwin: Detection and Characterization of Earth-like Exoplanets," Ph.D. thesis, Université de Liège (2001). 3

[13] N. Madhusudhan, A. Burrows, and T. Currie, "Model Atmospheres for Massive Gas Giants with Thick Clouds: Application to the HR 8799 Planets and Predictions for Future Detections," Astrophys. J. **737**, 34 (2011). 3

[14] A. L. Kraus and M. J. Ireland, "LkCa 15: A Young Exoplanet Caught at Formation?" Astrophys. J. **745**, 5 (2012). 4

[15] R. N. Bracewell, "Detecting nonsolar planets by spinning infrared interferometer," (1978). 4

[16] E. Serabyn, A. Booth, M. Colavita, M. Creech-Eakman, S. Crawford, J. Garcia, R. Johnson Jr., E. Hovland, C. D. Koresko, E. Ligon, S. Martin, B. Mennesson, J. Moore, D. Palmer, C. Paine, M. Shao, M. Swain, R. Smythe, and G. Vasisht, "The Keck interferometer nuller: system architecture and laboratory performance," Proc.SPIE **5491**, 806 – 815 (2004). 4

[17] E. Serabyn, B. Mennesson, M. M. Colavita, C. Koresko, and M. J. Kuchner, "The Keck Interferometer Nuller," Astrophys. J. **748**, 55 (2012).

[18] B. Mennesson, R. Millan-Gabet, E. Serabyn, M. M. Colavita, O. Absil, G. Bryden, M. Wyatt, W. Danchi, D. Defrère, O. Doré, P. Hinz, M. Kuchner, S. Ragland, N. Scott, K. Stapelfeldt, W. Traub, and J. Woillez, "Constraining the Exozodiacal Luminosity Function of Main-sequence Stars: Complete Results from the Keck Nuller Mid-infrared Surveys," Astrophys. J. **797**, 119 (2014). 4

[19] D. Defrère, P. M. Hinz, B. Mennesson, W. F. Hoffmann, R. Millan-Gabet, A. J. Skemer, V. Bailey, W. C. Danchi, E. C. Downey, O. Durney, P. Grenz, J. M. Hill, T. J. McMahon, M. Montoya, E. Spalding, A. Vaz, O. Absil, P. Arbo, H. Bailey, G. Brusa, G. Bryden, S. Esposito, A. Gaspar, C. A. Haniff, G. M. Kennedy, J. M. Leisenring, L. Marion, M. Nowak, E. Pinna, K. Powell, A. Puglisi, G. Rieke, A. Roberge, E. Serabyn, R. Sosa, K. Stapeldfeldt, K. Su, A. J. Weinberger, and M. C. Wyatt, "Nulling

Data Reduction and on-Sky Performance of the Large Binocular Telescope Interferometer," Astrophys. J. **824**, 66 (2016). 5

[20] S. Martin, E. Serabyn, K. Liewer, F. Loya, B. Mennesson, C. Hanot, and D. Mawet, "The development and applications of a ground-based fiber nulling coronagraph," Proc. SPIE **7013**, 70131Y (2008). 5

[21] M. Ollivier and J. M. Mariotti, "Improvement in the rejection rate of a nulling interferometer by spatial filtering." Appl. Opt. **36**, 5340–6 (1997). 5

[22] B. Mennesson, M. Ollivier, and C. Ruilier, "Use of single-mode waveguides to correct the optical defects of a nulling interferometer." J. Opt. Soc. Am. A. Opt. Image Sci. Vis. **19**, 596–602 (2002). 5, 97

[23] J. P. Berger, K. Rousselet-Perraut, P. Kern, F. Malbet, I. Schanen-Duport, F. Reynaud, P. Haguenauer, and P. Benech, "Integrated optics for astronomical interferometry. II. First laboratory white-light interferograms," Astron. Astrophys. Suppl. Ser. **139**, 173–177 (1999). 5

[24] J. Bland-Hawthorn and P. Kern, "Astrophotonics: a new era for astronomical instruments," Opt. Express **17**, 1880–1884 (2009). 5

[25] J. Tepper, "Integrated optics beam combiners for mid-IR astronomical interferometry," Ph.D. thesis, University of Cologne (2017). 6

[26] R. Diener, S. Minardi, J. Tepper, S. Nolte, and L. Labadie, "All-in-one 4-telescope beam combination with a zig-zag array of waveguides," Proc. SPIE **990731**, 990731 (2016). 6

[27] P. Kern, F. Malbet, I. Schanen-Duport, and P. Benech, "Integrated optics single-mode interferometric beam combiner for near infrared astronomy," Integr. Opt. Astron. Interferom. eds. P. Kern F. Malbet pp. 195 – 203 (1997). 6

[28] P. Haguenauer, J. P. Berger, K. Rousselet-Perraut, P. Kern, F. Malbet, I. Schanen-Duport, and P. Benech, "Integrated Optics for Astronomical Interferometry. III. Optical Validation of a Planar Optics Two-Telescope Beam Combiner." Appl. Opt. **39**, 2130–2139 (2000). 6, 97

[29] J. P. Berger, P. Haguenauer, P. Kern, K. Perraut, F. Malbet, I. Schanen, M. Severi, R. Millan-Gabet, and W. Traub, "Integrated optics for astronomical interferometry IV. First measurements of stars," Astron. Astrophys. **376**, L31–L34 (2001). 6

[30] J.-P. Berger, P. Haguenauer, P. Y. Kern, K. Rousselet-Perraut, F. Malbet, S. Gluck, L. Lagny, I. Schanen-Duport, E. Laurent, A. Delboulbé, E. Tatulli, W. A. Traub, N. P. Carleton, R. Millan-Gabet, J. D. Monnier, E. Pedretti, and S. Ragland, "An integrated-optics 3-way beam combiner for IOTA," Interferom. Opt. Astron. II. Ed. by Wesley A. Traub . Proc. SPIE **4838**, 1099–1106 (2003). 6

[31] J. D. Monnier, W. A. Traub, F. P. Schloerb, R. Millan-Gabet, J.-P. Berger, E. Pedretti, N. P. Carleton, S. Kraus, M. G. Lacasse, M. Brewer, S. Ragland, A. Ahearn, C. Coldwell, P. Haguenauer, P. Kern, P. Labeye, L. Lagny, F. Malbet, D. Malin, P. Maymounkov, S. Morel, C. Papaliolios, K. Perraut, M. Pearlman, I. L. Porro, I. Schanen, K. Souccar, G. Torres, and G. Wallace, "First Results with the IOTA3 Imaging Interferometer: The Spectroscopic Binaries $\lambda$ Virginis and WR 140," Astrophys. J. Lett. **602**, L57 (2004). 6

[32] J.-B. Le Bouquin, J.-P. Berger, B. Lazareff, G. Zins, P. Haguenauer, L. Jocou, P. Kern, R. Millan-Gabet, W. A. Traub, O. Absil, J.-C. Augereau, M. Benisty, N. Blind, X. Bonfils, P. Bourget, A. Delboulbe, P. Feautrier, M. Germain, P. B. Gitton, D. Gillier, M. Kiekebusch, J. Kluska, J. Knudstrup, P. Labeye, J.-l. Lizon, J.-L. Monin, Y. Magnard, F. Malbet, D. Maurel, F. Ménard, M. Micallef, L. Michaud, G. Montagnier, S. Morel, T. Moulin, K. Perraut, D. Popovic, P. Rabou, S. Rochat, C. Rojas, F. Roussel, A. Roux, E. Stadler, S. Stefl, É. Tatulli, and N. Ventura, "PIONIER: a 4-telescope visitor instrument at VLTI," Astron. Astrophys. **535**, A67 (2011). 6

[33] M. Benisty, J.-P. Berger, L. Jocou, P. Labeye, F. Malbet, K. Perraut, and P. Y. Kern,

"An integrated optics beam combiner for the second generation VLTI instruments," Astron. Astrophys. **498**, 601–613 (2009). 7, 97

[34] GRAVITY Collaboration, R. Abuter, M. Accardo, A. Amorim, N. Anugu, G. Ávila, N. Azouaoui, M. Benisty, J. P. Berger, N. Blind, H. Bonnet, P. Bourget, W. Brandner, R. Brast, A. Buron, L. Burtscher, F. Cassaing, F. Chapron, É. Choquet, Y. Clénet, C. Collin, V. C. du Foresto, W. de Wit, P. T. de Zeeuw, C. Deen, F. Delplancke-Ströbele, R. Dembet, F. Derie, J. Dexter, G. Duvert, M. Ebert, A. Eckart, F. Eisenhauer, M. Esselborn, P. Fédou, G. Finger, P. Garcia, C. E. G. Dabo, R. G. Lopez, E. Gendron, R. Genzel, S. Gillessen, F. Gonte, P. Gordo, M. Grould, U. Grözinger, S. Guieu, P. Haguenauer, O. Hans, X. Haubois, M. Haug, F. Haussmann, T. Henning, S. Hippler, M. Horrobin, A. Huber, Z. Hubert, N. Hubin, C. A. Hummel, G. Jakob, A. Janssen, L. Jochum, L. Jocou, A. Kaufer, S. Kellner, L. Kern, P. Kervella, M. Kiekebusch, R. Klein, Y. Kok, J. Kolb, M. Kulas, S. Lacour, V. Lapeyrère, B. Lazareff, J. B. L. Bouquin, P. Lèna, R. Lenzen, S. Lévêque, M. Lippa, Y. Magnard, L. Mehrgan, M. Mellein, A. Mérand, J. Moreno-Ventas, T. Moulin, E. Müller, F. Müller, U. Neumann, S. Oberti, T. Ott, L. Pallanca, J. Panduro, L. Pasquini, T. Paumard, I. Percheron, K. Perraut, G. Perrin, A. Pflüger, O. Pfuhl, T. P. Duc, P. M. Plewa, D. Popovic, S. Rabien, A. Ramírez, J. Ramos, C. Rau, M. Riquelme, R. R. Rohloff, G. Rousset, J. Sanchez-Bermudez, S. Scheithauer, M. Schöller, N. Schuhler, J. Spyromilio, C. Straubmeier, E. Sturm, M. Suarez, K. R. W. Tristram, N. Ventura, F. Vincent, I. Waisberg, I. Wank, J. Weber, E. Wieprecht, M. Wiest, E. Wiezorrek, M. Wittkowski, J. Woillez, B. Wolff, S. Yazici, D. Ziegler, and G. Zins, "First Light for GRAVITY: Phase Referencing Optical Interferometry for the Very Large Telescope Interferometer," Astron. Astrophys. **94**, 1–23 (2017). 7

[35] M. M. Colavita, J. K. Wallace, B. E. Hines, Y. Gursel, F. Malbet, D. L. Palmer, X. P. Pan, M. Shao, J. W. Yu, A. F. Boden, P. J. Dumont, J. Gubler, C. D. Koresko, S. R. Kulkarni, B. F. Lane, D. W. Mobley, and G. T. van Belle, "The Palomar Testbed Interferometer," Astrophys. J. **510**, 505 (1999). 8

[36] G. Z. Mashanovich, M. M. Milošević, M. Nedeljkovic, N. Owens, B. Xiong, E. J.

Teo, and Y. Hu, "Low loss silicon waveguides for the mid-infrared," Opt. Express **19**, 7112–7119 (2011). 8

[37] N. Hô, M. C. Phillips, H. Qiao, P. J. Allen, K. Krishnaswami, B. J. Riley, T. L. Myers, and N. C. Anheier, "Single-mode low-loss chalcogenide glass waveguides for the mid-infrared," Opt. Lett. **31**, 1860–1862 (2006). 8

[38] K. M. Davis, K. Miura, N. Sugimoto, and K. Hirao, "Writing waveguides in glass with a femtosecond laser," Opt. Lett. **21**, 1729–1731 (1996). 8, 12, 18

[39] A. Arriola, S. Gross, M. Ams, T. Gretzinger, D. Le Coq, R. P. Wang, H. Ebendorff-Heidepriem, J. Sanghera, S. Bayya, L. B. Shaw, M. Ireland, P. Tuthill, and M. J. Withford, "Mid-infrared astrophotonics: study of ultrafast laser induced index change in compatible materials," Opt. Mater. Express **7**, 698–711 (2017). 9, 60, 61, 85

[40] M. A. Hughes, "Modified chalcogenide glasses for optical device applications," Ph.D. thesis, University of Southampton (2007). 9, 22, 79, 82

[41] M. Ams, G. D. Marshall, and M. J. Withford, "Study of the influence of femtosecond laser polarisation on direct writing of waveguides," Opt. Express **14**, 13158–13163 (2006). 11, 24, 101

[42] S. M. Eaton, M. L. Ng, J. Bonse, A. Mermillod-Blondin, H. Zhang, A. Rosenfeld, and P. R. Herman, "Low-loss waveguides fabricated in BK7 glass by high repetition rate femtosecond fiber laser," Appl. Opt. **47**, 2098–2102 (2008). 11

[43] S. Gross, N. Jovanovic, A. Sharp, M. Ireland, J. Lawrence, and M. J. Withford, "Low loss mid-infrared ZBLAN waveguides for future astronomical applications," Opt. Express **23**, 7946–7956 (2015). 11, 60, 61, 62, 74, 101, 116

[44] B. McMillen, B. Zhang, K. P. Chen, A. Benayas, and D. Jaque, "Ultrafast laser fabrication of low-loss waveguides in chalcogenide glass with 0.65 dB/cm loss." Opt. Lett. **37**, 3 (2012). 11

[45] P. Nandi, G. Jose, C. Jayakrishnan, S. Debbarma, K. Chalapathi, K. Alti, A. K. Dharmadhikari, J. A. Dharmadhikari, and D. Mathur, "Femtosecond laser written channel waveguides in tellurite glass," Opt. Express **14**, 12145–12150 (2006). 11

[46] W. Watanabe, S. Sowa, T. Tamaki, K. Itoh, and J. Nishii, "Three-Dimensional Waveguides Fabricated in Poly(methyl methacrylate) by a Femtosecond Laser," Jpn. J. Appl. Phys. **45**, L765—-L767 (2006). 11

[47] J. Thomas, M. Heinrich, P. Zeil, V. Hilbert, K. Rademaker, R. Riedel, S. Ringleb, C. Dubs, J.-P. Ruske, S. Nolte, and A. Tünnermann, "Laser direct writing: Enabling monolithic and hybrid integrated solutions on the lithium niobate platform," Phys. status solidi **208**, 276–283 (2011). 11

[48] D. Du, X. Liu, G. Korn, J. Squier, and G. Mourou, "Laserinduced breakdown by impact ionization in SiO2 with pulse widths from 7 ns to 150 fs," Appl. Phys. Lett. **64**, 3071–3073 (1994). 12

[49] E. N. Glezer, M. Milosavljevic, L. Huang, R. J. Finlay, T.-H. Her, J. P. Callan, and E. Mazur, "Three-dimensional optical storage inside transparent materials," Opt. Lett. **21**, 2023–2025 (1996). 12, 20

[50] S. Gross and M. J. Withford, "Ultrafast-laser-inscribed 3D integrated photonics: challenges and emerging applications," Nanophotonics **4**, 332–352 (2015). 13

[51] R. Osellame, G. Cerullo, and R. Ramponi, *Femtosecond laser micromachining: photonic and microfluidic devices in transparent materials*, vol. 123 (Springer Science & Business Media, 2012). 13, 14

[52] A. Ródenas and A. K. Kar, "High-contrast step-index waveguides in borate nonlinear laser crystals by 3D laser writing." Opt. Express **19**, 17820–33 (2011). 13

[53] A. Ródenas, J. McCarthy, N. D. Psaila, G. Brown, H. T. Bookey, R. R. Thomson, and A. K. Kar, "Mid-infrared photonics enabled by 3D laser writing chalcogenide glass," in "SPIE Secur. + Def.", (International Society for Optics and Photonics, 2012), p. 11. 13, 85

[54] R. R. Thomson, T. A. Birks, S. G. Leon-Saval, A. K. Kar, and J. Bland-Hawthorn, "Ultrafast laser inscription of an integrated photonic lantern," Opt. Express **19**, 5698–5705 (2011). 13, 69

[55] K. Yamada, W. Watanabe, T. Toma, K. Itoh, and J. Nishii, "In situ observation of photoinduced refractive-index changes in filaments formed in glasses by femtosecond laser pulses," Opt. Lett. **26**, 19 (2001). 14

[56] M. Hughes, W. Yang, and D. Hewak, "Fabrication and characterization of femtosecond laser written waveguides in chalcogenide glass," Appl. Phys. Lett. **90**, 131113 (2007). 14, 70, 82, 87

[57] C. B. Schaffer, A. Brodeur, and E. Mazur, "Laser-induced breakdown and damage in bulk transparent materials induced by tightly focused femtosecond laser pulses," Meas. Sci. Technol. **12**, 1784–1794 (2001). 15, 16, 17

[58] B. Stuart, M. Feit, S. Herman, A. Rubenchik, B. Shore, and M. Perry, "Nanosecond-to-femtosecond laser-induced breakdown in dielectrics," Phys. Rev. B **53**, 1749–1761 (1996). 15, 18

[59] L. V. Keldysh, "Ionization in the field of a strong electromagnetic wave," Sov. Phys. JETP **20**, 1307–1314 (1965). 16

[60] D. M. Simanovskii, H. A. Schwettman, H. Lee, and A. J. Welch, "Midinfrared Optical Breakdown in Transparent Dielectrics," Phys. Rev. Lett. **91**, 107601 (2003). 16

[61] A. Kaiser, B. Rethfeld, M. Vicanek, and G. Simon, "Microscopic processes in dielectrics under irradiation by subpicosecond laser pulses," Phys. Rev. B **61**, 11437–11450 (2000). 17

[62] K. Miura, J. Qiu, H. Inouye, T. Mitsuyu, and K. Hirao, "Photowritten optical waveguides in various glasses with ultrashort pulse laser," Appl. Phys. Lett. **71**, 3329 (1997). 18

[63] L. Sudrie, M. Franco, B. Prade, and A. Mysyrowicz, "Writing of permanent birefringent microlayers in bulk fused silica with femtosecond laser pulses," Opt. Commun. **171**, 279–284 (1999). 18, 19

[64] Y. Shimotsuma, P. Kazansky, J. Qiu, and K. Hirao, "Self-Organized Nanogratings in Glass Irradiated by Ultrashort Light Pulses," Phys. Rev. Lett. **91**, 247405 (2003). 19

[65] C. Hnatovsky, R. S. Taylor, P. P. Rajeev, E. Simova, V. R. Bhardwaj, D. M. Rayner, and P. B. Corkum, "Pulse duration dependence of femtosecond-laser-fabricated nanogratings in fused silica," Appl. Phys. Lett. **87**, 014104 (2005). 18

[66] S. Juodkazis, K. Nishimura, S. Tanaka, H. Misawa, E. Gamaly, B. Luther-Davies, L. Hallo, P. Nicolai, and V. Tikhonchuk, "Laser-Induced Microexplosion Confined in the Bulk of a Sapphire Crystal: Evidence of Multimegabar Pressures," Phys. Rev. Lett. **96**, 166101 (2006). 18, 20

[67] J. W. Chan, T. Huser, S. Risbud, and D. M. Krol, "Structural changes in fused silica after exposure to focused femtosecond laser pulses," Opt. Lett. **26**, 1726–1728 (2001). 18

[68] J. W. Chan, T. R. Huser, S. H. Risbud, J. S. Hayden, and D. M. Krol, "Waveguide fabrication in phosphate glasses using femtosecond laser pulses," Appl. Phys. Lett. **82**, 2371–2373 (2003). 18

[69] A. M. Streltsov and N. F. Borrelli, "Study of femtosecond-laser-written waveguides in glasses," J. Opt. Soc. Am. B **19**, 2496–2504 (2002). 18

[70] D. J. Little, M. Ams, P. Dekker, G. D. Marshall, and M. J. Withford, "Mechanism of femtosecond-laser induced refractive index change in phosphate glass under a low repetition-rate regime," J. Appl. Phys. **108**, 33110 (2010). 18

[71] D. J. Little, M. Ams, S. Gross, P. Dekker, C. T. Miese, A. Fuerbach, and M. J. Withford, "Structural changes in BK7 glass upon exposure to femtosecond laser pulses," J. Raman Spectrosc. **42**, 715–718 (2011). 18

[72] V. R. Bhardwaj, E. Simova, P. P. Rajeev, C. Hnatovsky, R. S. Taylor, D. M. Rayner, and P. B. Corkum, "Optically Produced Arrays of Planar Nanostructures inside Fused Silica," Phys. Rev. Lett. **96**, 57404 (2006). 19

[73] C. Hnatovsky, R. S. Taylor, E. Simova, P. P. Rajeev, D. M. Rayner, V. R. Bhardwaj, and P. B. Corkum, "Fabrication of microchannels in glass using focused femtosecond laser radiation and selective chemical etching," Appl. Phys. A **84**, 47–61 (2006). 19

[74] L. A. Fernandes, J. R. Grenier, P. R. Herman, J. S. Aitchison, and P. V. S. Marques, "Femtosecond laser writing of waveguide retarders in fused silica for polarization control in optical circuits," Opt. Express **19**, 18294–18301 (2011). 19

[75] E. N. Glezer and E. Mazur, "Ultrafast-laser driven micro-explosions in transparent materials," Appl. Phys. Lett. **71**, 882–884 (1997). 20

[76] N. Jovanovic, J. Thomas, R. J. Williams, M. J. Steel, G. D. Marshall, A. Fuerbach, S. Nolte, A. Tünnermann, and M. J. Withford, "Polarization-dependent effects in point-by-point fiber Bragg gratings enable simple, linearly polarized fiber lasers," Opt. Express **17**, 6082–6095 (2009). 20

[77] G. Fibich and A. L. Gaeta, "Critical power for self-focusing in bulk media and in hollow waveguides," Opt. Lett. **25**, 335 (2000). 21

[78] S. Gross, "Direct-write Mid-IR Waveguide Lasers," Ph.D. thesis, Macquarie University (2012). 23, 36

[79] C. B. Schaffer, J. F. García, and E. Mazur, "Bulk heating of transparent materials using a high-repetition-rate femtosecond laser," Appl. Phys. A Mater. Sci. Process. **76**, 351–354 (2003). 23, 70

[80] M. Ams, "Fabrication Of Optical Waveguide Devices In Bulk Materials Using Femtosecond Laser Pulses," Ph.D. thesis, Macquarie University (2008). 25

[81] M. Ams, G. Marshall, D. Spence, and M. Withford, "Slit beam shaping method for

femtosecond laser direct-write fabrication of symmetric waveguides in bulk glasses." Opt. Express **13**, 5676–5681 (2005). 25, 26

[82] P. Bado, A. Said, M. Dugan, T. Sosnowski, and S. Wright, "Dramatic improvements in waveguide manufacturing with femtosecond lasers," in "Natl. Fiber Opt. Eng. Conf. (NFOEC), Dallas, USA.", , vol. 1001 (2002), vol. 1001, p. 48108. 27

[83] J. Liu, Z. Zhang, C. Flueraru, X. Liu, S. Chang, and C. P. Grover, "Waveguide shaping and writing in fused silica using a femtosecond laser," IEEE J. Sel. Top. quantum Electron. **10**, 169–173 (2004). 27, 61

[84] N. D. Psaila, R. R. Thomson, H. T. Bookey, A. K. Kar, N. Chiodo, R. Osellame, G. Cerullo, G. Brown, A. Jha, and S. Shen, "Femtosecond laser inscription of optical waveguides in Bismuth ion doped glass," Opt. Express **14**, 10452–10459 (2006). 27

[85] Y. Nasu, M. Kohtoku, and Y. Hibino, "Low-loss waveguides written with a femtosecond laser for flexible interconnection in a planar light-wave circuit," Opt. Lett. **30**, 723–725 (2005). 27, 60, 66

[86] A. Jesacher, G. D. Marshall, T. Wilson, and M. J. Booth, "Adaptive optics for direct laser writing with plasma emission aberration sensing." Opt. Express **18**, 656–61 (2010). 29

[87] C. Mauclair, A. Mermillod-Blondin, N. Huot, E. Audouard, and R. Stoian, "Ultrafast laser writing of homogeneous longitudinal waveguides in glasses using dynamic wavefront correction," Opt. Express **16**, 5481–5492 (2008). 29

[88] Femto Lasers, "High energy oscillator operator's manual," Tech. rep., Coherent (2008). 36

[89] Olympus America, "Olympus Microscopy Resource Center — Differential Interference Contrast - Introduction," (2012). 42

[90] W. Eickhoff and E. Weidel, "Measuring method for the refractive index profile of optical glass fibres," Opt. Quantum Electron. **7**, 109–113 (1975). 43, 83

[91] Y. Park, N. H. Seong, Y. Youk, and D. Y. Kim, "Simple scanning fibre-optic confocal microscopy for the refractive index profile measurement of an optical fibre," Meas. Sci. Technol. **13**, 695–699 (2002). 45

[92] Y. Youk and D. Y. Kim, "A simple reflection-type two-dimensional refractive index profile measurement technique for optical waveguides," Opt. Commun. **262**, 206–210 (2006). 45, 82

[93] "GLS Infrared Transmitting Glass Datasheet," Tech. rep., University of Southampton (2015). 46, 73, 79

[94] C. Florea and K. A. Winick, "Fabrication and characterization of photonic devices directly written in glass using femtosecond laser pulses," J. Light. Technol. **21**, 246–253 (2003). 47, 48

[95] R. Regener and W. Sohler, "Loss in Low-Finesse Ti:LiNbO3 Optical Waveguide Resonators," Appl. Phys. B **147**, 143–147 (1985). 47

[96] G. Tittelbach, B. Richter, and W. Karthe, "Comparison of three transmission methods for integrated optical waveguide propagation loss measurement," Pure Appl. Opt. J. Eur. Opt. Soc. Part A **2**, 683–700 (1993). 48

[97] I. P. Kaminow and L. W. Stulz, "Loss in cleaved Ti-diffused LiNbO3waveguides," Appl. Phys. Lett. **33**, 62–64 (1978). 48

[98] L. S. Yu, Q. Z. Liu, S. A. Pappert, P. K. Yu, and S. S. Lau, "Laser spectral linewidth dependence on waveguide loss measurements using the Fabry-Perot method," Appl. Phys. Lett. **64**, 536–538 (1994). 48

[99] A. A. Michelson and E. W. Morley, "On the Relative Motion of the Earth and the Luminiferous Ether," Am. J. Sci. **4**, 333–345 (1870). 53

[100] R. S. Shankland, "The Michelson-Morley Experiment," Sci. Am. **211**, 107–115 (1964). 53

[101] C. V. Raman and K. S. Krishnan, "A new type of secondary radiation," Nature **121**, 501–502 (1928). 53

[102] D. H. Krinsley, K. Pye, S. Boggs, and N. K. Tovey, *Backscattered Scanning Electron Microscopy and Image Analysis of Sediments and Sedimentary Rocks* (Cambridge University Press, 2005). 57

[103] P. W. Hawkes and L. Reimer, *Scanning Electron Microscopy: Physics of Image Formation and Microanalysis*, Springer Series in Optical Sciences (Springer Berlin Heidelberg, 2013). 57

[104] L. Reimer, P. W. Hawkes, D. L. MacAdam, A. L. Schawlow, K. Shimoda, A. E. Siegman, T. Tamir, and H. K. Lotasch, *Scanning Electron Microscopy: Physics of Image Formation and Microanalysis*, Springer Series in Optical Sciences (Springer, 1998). 57, 58

[105] J. Goldstein, D. Newbury, D. Joy, J. Michael, N. W. M. Ritchie, and J. H. Scott, *Scanning Electron Microscopy and X-Ray Microanalysis* (Springer New York, 2017). 58

[106] J. D. Snyder, Allan W., Love, *Optical Waveguide Theory*, vol. 2 (Springer, 1983). 59

[107] R. G. Hunsperger, *Integrated Optics* (Springer, 2009), 6th ed. 59, 110, 111

[108] W. Yang, C. Corbari, P. G. Kazansky, K. Sakaguchi, and I. C. S. Carvalho, "Low loss photonic components in high index bismuth borate glass by femtosecond laser direct writing," Opt. Express **16**, 16215–16226 (2008). 60, 114

[109] R. He, I. Hernández-Palmero, C. Romero, J. R. V. de Aldana, and F. Chen, "Three-dimensional dielectric crystalline waveguide beam splitters in mid-infrared band by direct femtosecond laser writing," Opt. Express **22**, 31293–31298 (2014). 60, 103, 107

[110] H.-D. Nguyen, A. Ródenas, J. R. V. de Aldana, G. Martín, J. Martínez, M. Aguiló,

M. C. Pujol, and F. Díaz, "Low-loss 3D-laser-written mid-infrared LiNbO3 depressed-index cladding waveguides for both TE and TM polarizations," Opt. Express **25**, 3722–3736 (2017). 60

[111] D. Hewak, D. Brady, R. Curry, G. Elliott, C. Huang, M. Hughes, K. Knight, A. Mairaj, M. Petrovich, R. Simpson, and C. Sproat, "Chalcogenide glasses for photonics device applications," Photonic Glas. Glas. pp. 29–102 (2010). 60, 81

[112] J. Burghoff, C. Grebing, S. Nolte, and A. Tünnermann, "Efficient frequency doubling in femtosecond laser-written waveguides in lithium niobate," Appl. Phys. Lett. **89**, 81108 (2006). 60

[113] J.-L. . Archambault, L. Reekie, and P. S. J. Russell, "100% reflectivity Bragg reflectors produced in optical fibres by single excimer laser pulses," Electron. Lett. **29**, 453–455 (1993). 60

[114] M. D. Mackenzie, J. M. Morris, C. R. Petersen, A. Ravagli, C. Craig, D. W. Hewak, H. T. Bookey, O. Bang, and A. K. Kar, "GLS and GLSSe ultrafast laser inscribed waveguides for mid-IR supercontinuum generation," Opt. Mater. Express **9**, 643–651 (2019). 60

[115] C. D'Amico, C. Caillaud, P. K. Velpula, M. K. Bhuyan, M. Somayaji, J.-P. Colombier, J. Troles, L. Calvez, V. Nazabal, A. Boukenter, and R. Stoian, "Ultrafast laser-induced refractive index changes in Ge15As15S70 chalcogenide glass," Opt. Mater. Express **6**, 1914–1928 (2016). 60, 62

[116] S. Gross, M. Dubov, and M. J. Withford, "On the use of the Type I and II scheme for classifying ultrafast laser direct-write photonics," Opt. Express **23**, 7767–7770 (2015). 60

[117] T. Gretzinger, S. Gross, M. Ams, A. Arriola, and M. J. Withford, "Ultrafast laser inscription in chalcogenide glass: thermal versus athermal fabrication," Opt. Mater. Express **5**, 2862–2877 (2015). 60, 62, 63

[118] C. D'Amico, G. Cheng, C. Mauclair, J. Troles, L. Calvez, V. Nazabal, C. Caillaud, G. Martin, B. Arezki, E. LeCoarer, P. Kern, and R. Stoian, "Large-mode-area infrared guiding in ultrafast laser written waveguides in Sulfur-based chalcogenide glasses," Opt. Express **22**, 13091–13101 (2014). 60, 85

[119] P. Masselin and E. Bychkov, "Direct laser writing of a low-loss waveguide with independent control over the transverse dimension and the refractive index contrast between the core and the cladding," Opt. Lett. **41**, 3507 (2016). 60

[120] J. Siebenmorgen, K. Petermann, G. Huber, K. Rademaker, S. Nolte, and A. Tünnermann, "Femtosecond laser written stress-induced Nd:Y3Al5O12 (Nd:YAG) channel waveguide laser," Appl. Phys. B **97**, 251 (2009). 61

[121] L. A. Fernandes, J. R. Grenier, P. R. Herman, J. S. Aitchison, and P. V. S. Marques, "Stress induced birefringence tuning in femtosecond laser fabricated waveguides in fused silica," Opt. Express **20**, 24103–24114 (2012). 61

[122] B. J. Eggleton, B. Luther-Davies, and K. Richardson, "Chalcogenide photonics," Nat. Photonics **5**, 141–148 (2011). 62

[123] C. Lopez, K. Richardson, A. Zoubir, M. Richardson, A. Schulte, and A. Pope, "Photo-induced optical and physical property modifications in chalcogenide thin films by femtosecond irradiation," (CLEO). Conf. Lasers Electro-Optics, 2005. **1**, 74–76 (2005). 62

[124] O. M. Efimov, L. B. Glebov, K. A. Richardson, E. V. Stryland, T. Cardinal, S. H. Park, M. Couzi, and J. L. Brunéel, "Waveguide writing in chalcogenide glasses by a train of femtosecond laser pulses," Opt. Mater. (Amst). **17**, 379–386 (2001). 62

[125] A. Zoubir, M. Richardson, C. Rivero, A. Schulte, C. Lopez, K. Richardson, N. Hô, and R. Vallée, "Direct femtosecond laser writing of waveguides in As2S3 thin films," Opt. Lett. **29**, 748–750 (2004). 62

[126] O. Caulier, D. L. Coq, E. Bychkov, and P. Masselin, "Direct laser writing of buried waveguide in As2S3 glass using a helical sample translation," Opt. Lett. **38**, 4212–4215 (2013). 62

[127] L. Calvez, Z. Yang, and P. Lucas, "Composition dependence and reversibility of photoinduced refractive index changes in chalcogenide glass," J. Phys. D. Appl. Phys. **43**, 445401 (2010). 62

[128] J. P. Bérubé, S. H. Messaddeq, M. Bernier, I. Skripachev, Y. Messaddeq, and R. Vallée, "Tailoring the refractive index of Ge-S based glass for 3D embedded waveguides operating in the mid-IR region," Opt. Express **22**, 26103–26116 (2014). 62

[129] A. Arriola, S. Mukherjee, D. Choudhury, L. Labadie, and R. R. Thomson, "Ultrafast laser inscription of mid-IR directional couplers for stellar interferometry." Opt. Lett. **39**, 4820–4822 (2014). 62, 66, 67, 69, 70, 112, 114

[130] K. Petermann, "Constraints for fundamental-mode spot size for broadband dispersion-compensated single-mode fibres," Electron. Lett. **19**, 712–714 (1983). 63

[131] J. Tepper, L. Labadie, R. Diener, S. Minardi, J.-U. Pott, R. R. Thomson, and S. Nolte, "Integrated optics prototype beam combiner for long baseline interferometry in the L and M bands," Astron. Astrophys. **602**, 1–8 (2017). 67, 70, 115, 127, 129

[132] R. R. Thomson, H. T. Bookey, N. Psaila, S. Campbell, D. T. Reid, S. Shen, A. Jha, and A. K. Kar, "Internal gain from an erbium-doped oxyfluoride-silicate glass waveguide fabricated using femtosecond waveguide inscription," IEEE Photonics Technol. Lett. **18**, 1515–1517 (2006). 69

[133] S. M. Eaton, H. Zhang, M. L. Ng, J. Li, W.-J. Chen, S. Ho, and P. R. Herman, "Transition from thermal diffusion to heat accumulation in high repetition rate femtosecond laser writing of buried optical waveguides," Opt. Express **16**, 9443 (2008). 70

[134] K. Minoshima, A. M. Kowalevicz, I. Hartl, E. P. Ippen, and J. G. Fujimoto, "Photonic device fabrication in glass by use of nonlinear materials processing with a femtosecond laser oscillator," Opt. Lett. **26**, 1516–1518 (2001). 70

[135] J. E. McCarthy, H. T. Bookey, N. D. Psaila, R. R. Thomson, and A. K. Kar, "Mid-infrared spectral broadening in an ultrafast laser inscribed gallium lanthanum sulphide waveguide," Opt. Express **20**, 1545–1551 (2012). 70, 73

[136] I. Miyamoto, A. Horn, J. Gottmann, D. Wortmann, and F. Yoshino, "Fusion Welding of Glass Using Femtosecond Laser Pulses with High-repetition Rates," J. Laser Micro/Nanoengineering **2**, 57–63 (2007). 70

[137] M. A. Hughes, W. Yang, and D. W. Hewak, "Spectral broadening in femtosecond laser written waveguides in chalcogenide glass," J. Opt. Soc. Am. B **26**, 1370–1378 (2009). 70, 82

[138] G. E. Madden, D. Choudhury, W. N. MacPherson, and R. R. Thomson, "Development of low-loss mid-infrared ultrafast laser inscribed waveguides," Opt. Eng. **56**, 075102–1–075102–6 (2017). 72

[139] P. Masselin, E. Bychkov, and D. Le Coq, "Ultrafast Laser Inscription of High Performance Mid-Infrared Waveguides in Chalcogenide Glass," IEEE Photonics Technol. Lett. **1135**, 1–4 (2018). 74

[140] A. M. Loireau-Lozac'h, M. Guittard, and J. Flahaut, "Verres formes par les sulfures L2S3 des terres rares avec le sulfure de gallium Ga2S3," Mater. Res. Bull. **11**, 1489–1496 (1976). 78

[141] S. Benazeth, M. H. Tuilier, A. M. Loireau-Lozac'h, H. Dexpert, P. Lagarde, and J. Flahaut, "An EXAFS structural approach of the lanthanum-gallium-sulfur glasses," J. Non. Cryst. Solids **110**, 89–100 (1989). 80, 81

[142] T. S. Izumitani, "Optical glass," Am. Inst. Phys. p. 91 (1986). 84

[143] T. Toney Fernandez, P. Haro-González, B. Sotillo, M. Hernandez, D. Jaque, P. Fernandez, C. Domingo, J. Siegel, and J. Solis, "Ion migration assisted inscription of high refractive index contrast waveguides by femtosecond laser pulses in phosphate glass," Opt. Lett. **38**, 5248 (2013). 85

[144] R. Diener, G. Tabacchi, S. Nolte, and S. Minardi, "Structural modification of gallium lanthanum sulfide glass induced by ultrafast laser inscription," Proc. SPIE - Int. Soc. Opt. Eng. **10092**, 100920D (2017). 87

[145] V. K. Malinovsky and A. P. Sokolov, "The nature of boson peak in Raman scattering in glasses," Solid State Commun. **57**, 757–761 (1986). 87

[146] G. N. Greaves and S. Sen, "Inorganic glasses, glass-forming liquids and amorphizing solids," Adv. Phys. **56**, 1–166 (2007). 87

[147] Y. Inamura, M. Arai, M. Nakamura, T. Otomo, N. Kitamura, S. M. Bennington, A. C. Hannon, and U. Buchenau, "Intermediate range structure and low-energy dynamics of densified vitreous silica," J. Non. Cryst. Solids **293-295**, 389–393 (2001). 88

[148] G. N. Greaves, F. Meneau, O. Majérus, D. G. Jones, and J. Taylor, "Identifying Vibrations That Destabilize Crystals and Characterize the Glassy State," Science (80- . ). **308**, 1299–1302 (2005). 88

[149] V. N. Novikov and A. P. Sokolov, "Poissons ratio and the fragility of glass-forming liquids," Nature **431**, 961 (2004). 88

[150] P. Boolchand, R. N. Enzweiler, R. L. Cappelletti, W. A. Kamitakahara, Y. Cai, and M. F. Thorpe, "Vibrational thresholds in covalent networks," Solid State Ionics **39**, 81–89 (1990). 88

[151] P. Němec, V. Nazabal, M. Pavlišta, A. Moreac, M. Frumar, and M. Vlček, "Gallium-lanthanum-sulphide amorphous thin films prepared by pulsed laser deposition," Mater. Chem. Phys. **117**, 23–25 (2009). 89

[152] J. Flahaut and M. Guittard, "Rare-earth sulfide and oxysulfide glasses," Glas. Technol. **24**, 149–156 (1983). 90

[153] T. Schweizer, F. Goutaland, E. Martins, D. W. Hewak, and W. S. Brocklesby, "Site-selective spectroscopy in dysprosium-doped chalcogenide glasses for 13-m optical-fiber amplifiers," J. Opt. Soc. Am. B **18**, 1436 (2001). 90

[154] S. S. Chan and A. T. Bell, "Characterization of the preparation of Pd/SiO2 and Pd/La2O3 by laser Raman spectroscopy," J. Catal. **89**, 433–441 (1984). 91

[155] H. Takebe, D. J. Brady, D. W. Hewak, and K. Morinaga, "Thermal properties of Ga2S3-based glass and their consideration during fiber drawing," J. Non. Cryst. Solids **258**, 239–243 (1999). 91

[156] H. Yayama, S. Fujino, K. Morinaga, H. Takebe, D. W. Hewak, and D. N. Payne, "Refractive index dispersion of gallium lanthanum sulfide and oxysulfide glasses," J. Non. Cryst. Solids **239**, 187–191 (1998). 91, 92

[157] J. R. Tessman, A. H. Kahn, and W. Shockley, "Electronic Polarizabilities of Ions in Crystals," Phys. Rev. **92**, 890–895 (1953). 92

[158] T. T. Fernandez, M. Sakakura, S. M. Eaton, B. Sotillo, J. Siegel, J. Solis, Y. Shimotsuma, and K. Miura, "Bespoke photonic devices using ultrafast laser driven ion migration in glasses," Prog. Mater. Sci. **94**, 68–113 (2018). 94, 95

[159] T. T. Fernandez, B. Sotillo, J. Del Hoyo, J. A. Vallés, R. M. Vázquez, P. Fernandez, and J. Solis, "Dual regimes of ion migration in high repetition rate femtosecond laser inscribed waveguides," IEEE Photonics Technol. Lett. **27**, 1068–1071 (2015). 94, 95

[160] Y. Wu, Z. An, Y. M. Duan, and M. T. Liu, "Measurements of K-shell ionization cross-sections of S, Ca and Zn by 730keV electron impact," Nucl. Instruments Methods Phys. Res. Sect. B Beam Interact. with Mater. Atoms **268**, 2820–2824 (2010). 96

[161] T. Lagadec, B. Norris, S. Gross, A. Arriola, T. Gretzinger, N. Cvetojevic, J. Lawrence, M. Withford, and P. Tuthill, "GLINT South: a photonic nulling interferometer pathfinder at the Anglo-Australian Telescope for high contrast imaging of substellar companions," Proc. SPIE 10701, Opt. Infrared Interferom. Imaging VI **10701**, 10701–10701–8 (2018). 98

[162] Z. Chaboyer, A. Stokes, J. Downes, M. J. Steel, and M. J. Withford, "Design and fabrication of reconfigurable laser-written waveguide circuits," Opt. Express **25**, 33056–33065 (2017). 98

[163] K. L. Kruse and C. T. Middlebrook, "Fan-out routing and optical splitting techniques for compact optical interconnects using single-mode polymer waveguides," J. Mod. Opt. **62**, S1–S10 (2015). 99, 100, 101

[164] R. Diener, J. Tepper, L. Labadie, T. Pertsch, S. Nolte, and S. Minardi, "Towards 3D-photonic, multi-telescope beam combiners for mid-infrared astrointerferometry," Opt. Express **25**, 19262–19274 (2017). 102

[165] F. Ladouceur and P. Labeye, "A New General Approach to Optical Waveguide Path Design," J. Light. Technol. **13**, 481–492 (1995). 102

[166] D. Homoelle, S. Wielandy, A. L. Gaeta, N. F. Borrelli, and C. Smith, "Infrared photosensitivity in silica glasses exposed to femtosecond laser pulses," Opt. Lett. **24**, 1311–1313 (1999). 103

[167] S. Nolte, M. Will, J. Burghoff, and A. Tuennermann, "Femtosecond waveguide writing: a new avenue to three-dimensional integrated optics," Appl. Phys. A **77**, 109–111 (2003). 103

[168] J. Lv, Y. Cheng, W. Yuan, X. Hao, and F. Chen, "Three-dimensional femtosecond laser fabrication of waveguide beam splitters in LiNbO3 crystal," Opt. Mater. Express **5**, 1274–1280 (2015). 103

[169] T. Liu, A. R. Zakharian, M. Fallahi, J. V. Moloney, and M. Mansuripur, "Design of a compact photonic-crystal-based polarizing beam splitter," IEEE Photonics Technol. Lett. **17**, 1435–1437 (2005). 103

[170] M. Izutsu, Y. Nakai, and T. Sueta, "Operation mechanism of the single-mode optical-waveguide Y junction." Opt. Lett. **7**, 136–138 (1982). 103, 104

[171] K. Færch and M. Svalgaard, "Symmetrical waveguide devices fabricated by direct UV writing," IEEE Photonics Technol. Lett. (2002). 103

[172] J. D. Love and N. Riesen, "Single-, few-, and multimode Y-junctions," J. Light. Technol. **30**, 304–309 (2012). 103

[173] V. A. Amorim, J. M. Maia, D. Alexandre, and P. V. Marques, "Optimization of Broadband Y-Junction Splitters in Fused Silica by Femtosecond Laser Writing," IEEE Photonics Technol. Lett. **29**, 619–622 (2017). 103

[174] C. R. Doerr, M. Cappuzzo, E. Chen, A. Wong-Foy, L. Gomez, A. Griffin, and L. Buhl, "Bending of a planar lightwave circuit 2 2 coupler to desensitize it to wavelength, polarization, and fabrication changes," IEEE Photonics Technol. Lett. **17**, 1211–1213 (2005). 104

[175] Y. Ren, L. Zhang, H. Xing, C. Romero, J. R. V. de Aldana, and F. Chen, "Cladding waveguide splitters fabricated by femtosecond laser inscription in Ti:Sapphire crystal," Opt. Laser Technol. **103**, 82–88 (2018). 107

[176] J. . Koo, R. B. Williams, C. B. E. Gawith, S. P. Watts, G. D. Emmerson, V. Albanis, P. G. R. Smith, and M. C. Grossel, "UV written waveguide devices using crosslinkable PMMA-based copolymers," Electron. Lett. **39**, 394–395 (2003). 107

[177] R. D. Peters, O. P. Lay, and P. R. Lawson, "Mid-Infrared Adaptive Nulling for the Detection of Earthlike Exoplanets," Publ. Astron. Soc. Pacific **122**, 85–92 (2010). 108

[178] A. Takagi, K. Jinguji, and M. Kawachi, "Wavelength characteristics of (2x2) optical channel-type directional couplers with symmetric or nonsymmetric coupling structures," J. Light. Technol. **10**, 735–746 (1992). 108, 122

[179] T. Tamir, *Guided-Wave Optoelectronics* (Springer-Verlag Berlin Heidelberg, 1988). 109

[180] A. R. Von Hippel and A. S. Labounsky, *Dielectrics and Waves*, Artech House Microwave Library (Artech House, 1995). 110

[181] A. Yariv, "Coupled-Mode theory for guided-wave optics," IEEE J. Quantum Electron. **9**, 919–933 (1973). 110, 115

[182] W.-J. Chen, S. M. Eaton, H. Zhang, and P. R. Herman, "Broadband directional couplers fabricated in bulk glass with high repetition rate femtosecond laser pulses," Opt. Express **16**, 11470–11480 (2008). 110, 112, 113, 117, 121, 122, 126

[183] N. Takato, K. Jinguji, M. Yasu, M. Kawachi, and H. Toba, "Silica-Based Single-Mode Waveguides on Silicon and their Application to Guided-Wave Optical Interferometers," J. Light. Technol. **6**, 1003–1010 (1988). 110

[184] R. Diener, S. Nolte, T. Pertsch, and S. Minardi, "Effects of stress on neighboring laser written waveguides in gallium lanthanum sulfide," Appl. Phys. Lett. **112**, 111908 (2018). 111, 114, 118

[185] A. M. Streltsov and N. F. Borrelli, "Fabrication and analysis of a directional coupler written in glass by nanojoule femtosecond laser pulses," Opt. Lett. **26**, 42 (2001). 112

[186] K. Minoshima, A. M. Kowalevicz, E. P. Ippen, and J. G. Fujimoto, "Fabrication of coupled mode photonic devices in glass by nonlinear femtosecond laser materials processing," Opt. Express **10**, 645–652 (2002). 112

[187] R. Hereth and G. Schiffner, "Broad-Band Optical Directional Couplers and Polarization Splitters," J. Light. Technol. **7**, 925–930 (1989). 113

[188] J. Tepper, L. Labadie, S. Gross, A. Arriola, S. Minardi, R. Diener, and M. J. Withford, "Ultrafast laser inscription in ZBLAN integrated optics chips for mid-IR beam combination in astronomical interferometry," Opt. Express **25**, 20642 (2017). 116, 129

[189] M. Olivero and M. Svalgaard, "Direct UV-written broadband directional planar waveguide couplers." Opt. Express **13**, 8390–8399 (2005). 117, 145

[190] S. M. Eaton and P. R. Herrman, "Passive Photonic Devices in Glass," in "Femtosecond Laser Micromach.", (Springer Berlin Heidelberg, 2012), p. 185. 122

[191] A. Ródenas, G. Martin, B. Arezki, N. Psaila, G. Jose, A. Jha, L. Labadie, P. Kern, A. Kar, and R. Thomson, "Three-dimensional mid-infrared photonic circuits in chalcogenide glass." Opt. Lett. **37**, 392–394 (2012). 128

[192] G. Martin, S. Heidmann, J.-Y. Rauch, L. Jocou, and N. Courjal, "Electro-optic fringe locking and photometric tuning using a two-stage MachZehnder lithium niobate waveguide for high-contrast mid-infrared interferometry," Opt. Eng. **53**, 034101 (2014). 128

[193] L. Labadie, G. Mart, N. C. Anheier, B. Arezki, H. A. Qiao, B. Bernacki, and P. Kern, "A new step towards instrument miniaturization for mid-infrared interferometry," Astron. Astrophys. **531**, A48 (2011). 128

[194] M. Toyoshima, "Maximum fiber coupling efficiency and optimum beam size in the presence of random angular jitter for free-space laser systems and their applications," J. Opt. Soc. Am. A **23**, 2246–2250 (2006). 129

[195] "A World Leader In Optical Thin Film Coatings https://www.artemis-optical.co.uk," . 129

[196] H.-D. Kenchington-Goldsmith, N. Cvetojevic, M. Ireland, and S. Madden, "Fabrication tolerant chalcogenide mid-infrared multimode interference coupler design with applications for Bracewell nulling interferometry," Opt. Express **25**, 3038–3051 (2017). 130, 138, 142

[197] A. Maese-Novo, R. Halir, S. Romero-García, D. Pérez-Galacho, L. Zavargo-Peche, A. Ortega-Moñux, I. Molina-Fernández, J. G. Wangüemert-Pérez, and P. Cheben, "Wavelength independent multimode interference coupler," Opt. Express **21**, 7033–7040 (2013). 130

[198] H. F. Talbot, "Facts relating to optical science," London, Edinburgh, Dublin Philos. Mag. J. Sci. **9**, 401–407 (1836). 130

[199] O. Bryngdahl, "Image formation using self-imaging techniques," J. Opt. Soc. Am. **63**, 416–419 (1973).

[200] R. Ulrich and G. Ankele, "Self-imaging in homogeneous planar optical waveguides," Appl. Phys. Lett. **27**, 337–339 (1975). 130

[201] R. M. Knox and P. P. Toulios, *Integrated circuits for the millimeter through optical frequency range*, vol. 20 (1970). 130

[202] L. B. Soldano and E. C. M. Pennings, "Optical multi-mode interference devices based

on self-imaging: principles and applications," J. Light. Technol. **13**, 615–627 (1995). 130, 131, 133, 134

[203] Y. Shi and D. Dai, "Design of a compact multimode interference coupler based on deeply-etched SiO2 ridge waveguides," Opt. Commun. **271**, 404–407 (2007). 130

[204] P. A. Besse, M. Bachmann, H. Melchior, L. B. Soldano, and M. K. Smit, "Optical Bandwidth and Fabrication Tolerances of Multimode Interference Couplers," J. Light. Technol. **12**, 1004–1009 (1994). 130

[205] D. S. Levy, K. H. Park, R. Scarmozzino, R. M. Osgood, C. Dries, P. Studenkov, and S. Forrest, "Fabrication of Ultracompact 3-dB 2x2 MMI Power Splitters," IEEE Photonics Technol. Lett. **11**, 1009–1011 (1999). 130

[206] H.-D. Kenchington Goldsmith, N. Cvetojevic, M. Ireland, P. Ma, P. Tuthill, B. Eggleton, J. S. Lawrence, S. Debbarma, B. Luther-Davies, and S. J. Madden, "Chalcogenide glass planar MIR couplers for future chip based Bracewell interferometers," Proc. SPIE **990730**, 990730 (2016). 131, 141, 143

[207] W. Watanabe, Y. Note, and K. Itoh, "Fabrication of multimode interference waveguides in glass by use of a femtosecond laser." Opt. Lett. **30**, 2888–90 (2005). 131

[208] D.-Y. Liu, Y.-P. Li, H.-C. Guo, H. Yang, and Q.-H. Gong, "Transverse writing of multimode interference waveguides inside silica glass by femtosecond laser pulses," Chinese Phys. Lett. **25**, 2500–2503 (2008). 131

[209] A. V. O. Amorim, "Fabrication of Integrated Optical Devices in Fused Silica by Femtosecond Laser Direct Writing," Ph.D. thesis, Universidade do Porto (2016). 131

[210] M. T. Hill, X. J. M. Leijtens, G. D. Khoe, and M. K. Smit, "Optimizing Imbalance and Loss in 2x2 3-dB Multimode Interference Couplers via Access Waveguide Width," J. Light. Technol. **21**, 2305–2313 (2003). 131, 133, 138, 139, 143

[211] M. Bachmann, P. A. Besse, and H. Melchior, "General self-imaging properties in N x N

multimode interference couplers including phase relations," Appl. Opt. **33**, 3905–3911 (1994). 133

[212] M. M. Milošević, M. Nedeljkovic, T. M. Ben Masaud, E. Jaberansary, H. M. H. Chong, N. G. Emerson, G. T. Reed, and G. Z. Mashanovich, "Silicon waveguides and devices for the mid-infrared," Appl. Phys. Lett. **101**, 121105 (2012). 142, 143

[213] J. S. Penades, A. Ortega-Moñux, M. Nedeljkovic, J. G. Wangüemert-Pérez, R. Halir, A. Z. Khokhar, C. Alonso-Ramos, Z. Qu, I. Molina-Fernández, P. Cheben, and G. Z. Mashanovich, "Suspended silicon mid-infrared waveguide devices with subwavelength grating metamaterial cladding," Opt. Express **24**, 22908–22916 (2016). 142, 143

[214] M. Nedeljkovic, A. Z. Khokhar, Y. Hu, X. Chen, J. S. Penades, S. Stankovic, H. M. H. Chong, D. J. Thomson, F. Y. Gardes, G. T. Reed, and G. Z. Mashanovich, "Silicon photonic devices and platforms for the mid-infrared," Opt. Mater. Express **3**, 1205 (2013). 142

[215] M. Nedeljkovic, J. S. Penadés, C. J. Mitchell, A. Z. Khokhar, S. Stanković, T. D. Bucio, C. G. Littlejohns, F. Y. Gardes, and G. Z. Mashanovich, "Surface-grating-coupled low-loss ge-on-si rib waveguides and multimode interferometers," IEEE Photonics Technol. Lett. **27**, 1040–1043 (2015). 143

[216] B. Norris, N. Cvetojevic, S. Gross, N. Jovanovic, P. N. Stewart, N. Charles, J. S. Lawrence, M. J. Withford, and P. Tuthill, "High-performance 3D waveguide architecture for astronomical pupil-remapping interferometry," Opt. Express **22**, 18335–18353 (2014). 149, 150